University of Bath

UNIVERSITY OF BATH

PHD

Rational Design and Refinement of an Intracellular Derived Peptide: Deriving Potent Antagonists of Alpha-Synuclein Aggregation
(Alternative format thesis)

Meade, Richard

Award date:
2020

Awarding institution:
University of Bath

Link to publication

Alternative formats

If you require this document in an alternative format, please contact:
openaccess@bath.ac.uk

Download date: 11. May. 2021

Rational Design and Refinement of an Intracellular Derived Peptide: Deriving Potent Antagonists of Alpha-Synuclein Aggregation

Richard Mathew Meade
A thesis submitted for the degree of Doctor of Philosophy
University of Bath
Department of Biology and Biochemistry
August 2020

Table of Contents

Chapter 4:

Supporting information *108*

Chapter 5:

A Series of Helical α-synuclein Fibril Polymorphs Are Populated in the Presence of Lipid

Vesicles *116*

Chapter 5:

Supporting Information *123*

Chapter 6:

Refinement of an intracellular library-derived peptide inhibitor of alpha-synuclein

aggregation *131*

Thesis Abstract

Parkinson's disease (PD) is the second most prevalent neurodegenerative disease and is characterised by Lewy body deposits in the brains of suffers, which have been shown to consist of the protein alpha synuclein (αS), and membrane lipids. Previous research utilised an intracellular peptide screen of the residues 45-54 of αS, as this is where most early onset mutations reside, and selected a peptide, 4554W (KDGIVNGVKA). This peptide was shown to decrease αS aggregation, and rescue PC-12 cells from αS mediated toxicity.

Experiments were performed herein to deduce where along the αS aggregation pathway the 4554W peptide acted. It was found that the peptide inhibited primary nucleation of αS but exhibited no inhibitory effect on fibril elongation or secondary nucleation. An alanine scan was performed of 4554W to deduce the key mechanisms important for the interaction. It was found that the 4554W(K1A) and 4554W(N6A) substitutions exhibited increased. Following this truncation experiments of the C- and N-terminus were performed to determine their importance and the residue in position 1 was not required for the peptide's function. The final peptide optimised for this thesis is termed 4654W(N6A) (DGIVAGVKA). This represents a step forward to producing a novel peptide therapeutic targeted against PD and related synucleinopathies.

In addition to the peptide optimisation, a novel aggregate of αS was observed in the presence of lipid vesicles. These structures were much larger than any previously reported αS aggregates and may represent a novel therapeutically relevant conformation.

List of Abbreviations

AFM	atomic force microscopy
αS	alpha Synuclein
ATP	adenosine triphosphate
CPP	cell penetrating peptides
CD	Circular Dichroism
CryoEM	Cryogenic electron microscopy
DJ1	Daisuke-Junko-1 gene
DLB	Dementia with Lewy bodies
DLS	Dynamic light scattering
DHFR	Dihydrofolate reductase
DMPS	1,2-Dimyristoyl-sn-glycero-3-phospho-L-serine
EGCG	(-)-epigallocatechin
fOligomers	Oligomers produced from fibrils
FRET	Single molecule Forester Resonance Energy Transfer
HPLC	High Pressure Liquid Chromatography
HSPs	Heat-shock Proteins
IPTG	isopropyl-1-thio-D-galactopyranoside
LRRK2	Leucine rich repeat kinase 2
MSA	Multiple system atrophy
MTT	3-(4, 5-dimethylthiazol-2-yl)-2, 5-diphenyltetrazolium bromide
NAC	Non-amyloid component
NADH	Nicotinamide adenine dinucleotide
NMR	Nuclear Magnetic resonance
PBS	Phosphate buffered saline
PCA	Protein-fragment Complementation Assay
PD	Parkinson's disease
PDB	Protein data bank
PINK1	PTEN-induced putative Kinase 1
PICUP	Photo-induced cross-linking of unmodified proteins

PPI	Protein-protein interaction
PTM	Post translational modification
PTP	permeability transition pore
ROS	Reactive oxygen species
SEC	Size exclusion chromatography
SH-SY5Y	Human neuroblastoma cell line
SNCA	Alpha synuclein gene
ssNMR	solid state Nuclear Magnetic resonance
SNARE	SNAP Receptor
SUVs	Small unilamellar vesicles
TEM	Transmission electron microscopy
ThT	Thioflavin T
VPS35	vascular protein sorting 35 gene
wt	wild type

Chapter 1:

Introduction

1.1 Parkinson's Disease

Parkinson's disease was first described in the literature in over 200 years ago, in 1817, by James Parkinson in his article 'An Essay on the Shaking Palsy' (Parkinson, 1817), in which the disease was described as follows: -

'Involuntary tremulous motion, with lessened muscular power, in parts not in action and even when supported; with a propensity to bend the trunk forwards, and to pass from a walking to a running pace: the senses and intellects being uninjured.'

Following this seminal publication, most of the disorder of movement observations described remain attributed to the disease, and as a tribute the disease has become known, in modern times, as Parkinson's disease (PD). In recent times it has been observed that in addition to the disorder of movement, described by James Parkinson, the neurodegeneration associated with the disease can develop to include a range of non-motor symptoms, including cognitive dysfunction and depression, causing the sufferers to become passive and withdrawn, adding to the suffering caused by the disease (Dauer and Przedborski, 2003).

1.2 Prevalence

PD is the second-most prevalent neurodegenerative condition in the world, accounting for ~15%, and primarily affects older individuals. The condition is rare in individuals under the age of about 50 years old (Twelves, Perkins and Counsell, 2003), although early onset mutations are known to exist that can drastically reduce the age at which PD symptoms may appear. Prevalence of the disease rises sharply with age, and more than 3% of individuals above the age of 80 years old present PD symptoms (Pringsheim et al., 2014), with a higher incidence rate amongst men than women (Van Den Eeden et al., 2003).

A global trend of increasing life span due to modern advances in medicine means that more people will reach an age where they become susceptible to neurodegenerative diseases. It is estimated that in 1990 there were 2.0 - 3.0 million people living with PD (Feigin et al., 2019), increasing to 4.1 – 4.6 million by 2005 (Dorsey et al., 2007), and 5.0 – 7.3 million by 2016 (Feigin et al., 2019), and has been projected to rise to about 8.7 - 9.3 million by 2030 (Dorsey

et al., 2007). Due to the level of care required by individuals suffering from these diseases the socio-economic impacts and the burden of the heath care systems will be huge unless proactive steps are taken to reduce the prevalence of PD and related synucleinopathies (including multiple system atrophy and dementia with Lewy bodies).

1.3 Neuropathology and disease progression

The impairment of motor functions associated with PD are linked to loss of pigmented dopaminergic neurones within the substantia nigra (Halliday et al., 2011) a basal ganglia structure located in the mid brain. The loss of the dopaminergic neurones, and the spread of neuronal pathology is paired with the accumulation of Lewy body deposits, the pathogenic hallmark of the disease. These Lewy bodies have been found to be largely made up of the aggregated protein α-synuclein (αS) (Spillantini et al., 1997), a protein which has be implicated as the underlying cause of the disease onset.

The primary misfolding of αS, before neuronal toxicity occurs in the substantia nigra, is understood to occur via one of two potential portals. These are either the olfactory bulb, or in the gastrointestinal tract, with transmission occurring via the vagus nerve to the medulla oblongata (Liu, Chan and Stoessl, 2017).

Propagation of the neuropathology associated with the death of dopaminergic neurones in the substantia nigra is thought to spread in a prion-like mechanism, suggesting that once the initial αS aggregates have formed they then propagate and seed further misfolding of αS in adjacent neurones, transmitting the associated toxicity to other areas of the brain, linked to the progression observed in the disease symptoms, as can be measured by the Braak scale (Braak et al., 2003). In the early stages of the disease Lewy body pathology is restricted to the olfactory bulb and substantia nigra, causing only mild effects of PD, e.g. fatigue, depression and loss of smell (Braak stage I and II). The pathology then propagates towards the fore brain, as cell death starts to occur in the mid brain, presenting as the motor effects of PD, e.g. Bradykinesia and tremor (Braak stage III and IV), then finally spreads to the hind brain, affecting sensory perception and sleep, as cell death starts to occur in the frontal lobe causing

the cognitive impairment and dementia symptoms linked to the disease (Braak stage V and VI).
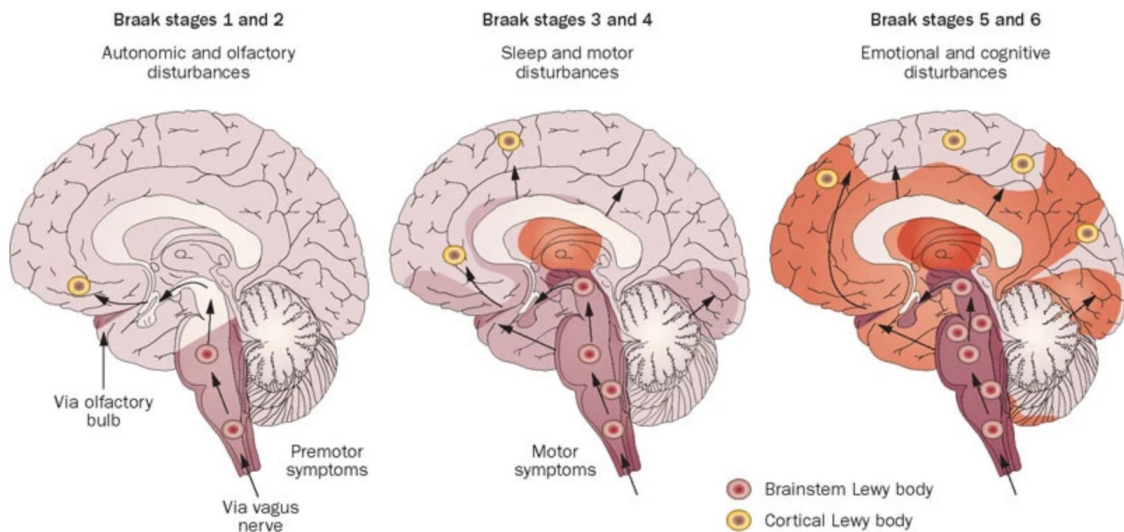
Figure 1.1: Neuropathology of PD, showing how the disease progression, measured by the Braak staging system, is linked to the progression of Lewy bodies throughout the brain. Initiation sites in either the olfactory bulb or in the medulla oblongata, via the vagus nerve, and progress into the cortical regions and hind brain in the later stages of the disease.
Image reproduced from (Doty, 2012)

1.4 Evidence for αS aggregation as the causal factor of PD

Presented here is a brief summary of how αS became implemented as the main causal factor of PD, and related synucleinopathies, over the past 30 years. This has had significant implications in enhancing our understanding of the disease. To avoid repetition this will be brief, and a complete, in depth, review of 'Alpha-Synuclein structure and Parkinson's disease - lessons and emerging principles' is presented in chapter 2 (Meade, R. M., Fairlie and Mason, 2019).

Almost a century following James Parkinson's essay describing the disease in 1817 (Parkinson, 1817), Fredrich Lewy described the cytoplasmic inclusions, now known as Lewy bodies, within the brains of deceased patients suffering from PD (Lewy, 1912). In 1990 an Italian American family (the Contursi Kindred) was described, showing inherited cases of early onset PD, presenting Lewy body pathology after autopsy (Golbe et al., 1990). The specific mutation leading to this early on-set form of the disease was found to be the autosomal dominant

substitution of an alanine to threonine in position 53 (A53T) of the SNCA gene on the long arm of chromosome 4 (Polymeropoulos et al., 1996; Polymeropoulos et al., 1997), encoding the gene for αS. Later that year, following on from the A53T discovery, Lewy bodies were found to be strongly immunoreactive for αS (Spillantini et al., 1997), suggesting that PD was likely an αS related disorder.

In the preceding years further autosomal dominant mutations in the SNCA gene have been found to cause familial PD. In addition to the original A53T mutation (Polymeropoulos et al., 1997) these include E46K (Greenbaum et al., 2005), H50Q (Ghosh et al., 2013; Rutherford et al., 2014), G51D (Lesage et al., 2013), A53E (Pasanen et al., 2014) and A30P (Kruger et al., 1998). These mutations in relation to recently published fibril structures are explored in chapter 2. Of important note to the aims of this thesis is the fact that 5 of the 6 mutations described occur in an eight amino acid region of the protein located between residues 46-53, implicating this as a key region involved in αS pathogenicity.

In addition to the early onset missense mutations described here there is a substantial and growing body of additional evidence implicating αS in PD pathology, including i) familial PD has been seen to occur when the SNCA gene is duplicated or triplicated (Singleton et al., 2003; Chartier-Harlin et al., 2004). The examples of triplication lead to a more severe form of PD than does duplication, highlighting the importance of intercellular concentrations of αS being a factor in the subsequent mis-folding into the toxic species leading to the disease phenotype. ii) synthetic αS rapidly aggregates into cytotoxic β-sheet rich fibrils similar to those found in Lewy bodies taken from recently deceased PD patients (Strohaker et al., 2019). iii) αS oligomers are seen to be toxic to therapeutically relevant cells in culture (Fusco et al., 2017).

1.5 αS and lipid interactions

Lewy bodies, the pathogenic hallmark of PD, have been shown not only to contain αS, as the predominant protein constituent, but also to contain a substantial lipid component (den Jager, 1969; Shahmoradian et al., 2019). Numerous *in vitro* experiments have indeed highlighted dramatic changes in αS structural morphology and aggregation kinetics in the presence of lipid vesicles (Lee, H.J., Choi and Lee, 2002; Burre, Sharma and Sudhof, 2015;

Galvagnion, C. et al., 2015; Meade, R. M., Fairlie and Mason, 2019). A striking recent experiment, using ultrastructural analysis, has revealed that most Lewy bodies (taken from post-mortem human brain samples from PD patients) contained clusters of membrane structures. At the core of the Lewy bodies these were coated with membrane bound forms of non-fibrillar αS, and only 20% of the Lewy bodies observed displayed large amyloid fibrils (longer than 25 nm) (Shahmoradian et al., 2019). This is leading to a new field of interest in the interactions of αS with lipid membranes, and improved understandings regarding how this may relate to the disease pathology.

Before aggregation occurs αS exists in solution as a random coil monomer, and the addition of lipid membranes has been shown to promote αS lipid binding and conversion into an α-helical conformation (Galvagnion, C. et al., 2015; Meade, R. M., Fairlie and Mason, 2019; Meade, Richard M., Williams and Mason, 2020). Moreover, the N-terminal lipid binding domain of αS is also the area where the early onset mutations occur in the SNCA gene (Jo et al., 2002; Zarranz et al., 2004; Appel-Cresswell et al., 2013; Ghosh et al., 2013; Ghosh et al., 2014; Brown et al., 2018), including the A30P mutation (Jo et al., 2002), which is not found to be important in the fibril structure hydrophobic zipper (Guerrero-Ferreira et al., 2018; Li, Y.W. et al., 2018; Meade, R. M., Fairlie and Mason, 2019), suggesting a strong link between αS lipid binding and pathogenicity. The binding of αS to pre-synaptic vesicle membrane has been postulated to be the native non-pathogenic function of αS within dopaminergic neurones, possibly promoting membrane curvature and modulating vesicle trafficking and neurotransmitter release by association with the SNARE complex (Burre et al., 2010).

αS is thought to interact with membranes via seven 'KTKEGV' imperfect repeat motifs (Maroteaux and Scheller, 1991). When folded into an 3/11 helix, the positively charged lysine residues interact with the negative headgroups of the membrane phospholipids (particularly negatively charged phospholipids, such as DMPS with its negatively charged serine residue attached to the head group), and the hydrophobic residues become buried in the fatty acid layer (Dettmer, 2018) . There is imperfect hydrophobicity in the fatty acid layer due to the placement of some of the polar residues (threonine and glutamine), and has been proposed that this can lead to an unstable, transient relationship of αS binding, and dissociation from

the membrane (Fanning, Selkoe and Dettmer, 2020) (see Fig 1.2). The concentration, and structural stabilisation, of αS monomers on the surface may well promote the aggregation of αS into stable oligomeric species, and it has been found that when αS dissociates from the membrane it can remain in its helical, multimeric form (Rovere et al., 2018). This may settle long running disagreement in the αS field centred around the existence of a native soluble helical tetrameric form of αS (Bartels, Choi and Selkoe, 2011). With one side of the argument suggesting that αS only exists in solution as a random coil monomer (Weinreb et al., 1996), and the opposing view suggesting that a helical tetramer of αS can be purified from cross-linked extracts from erythrocytes (Bartels, Choi and Selkoe, 2011). In light of recent findings, it could well be that both views are correct; the formation of the helical tetramer occurs on intracellular membranes, and this may then dissociate into the cytosol.
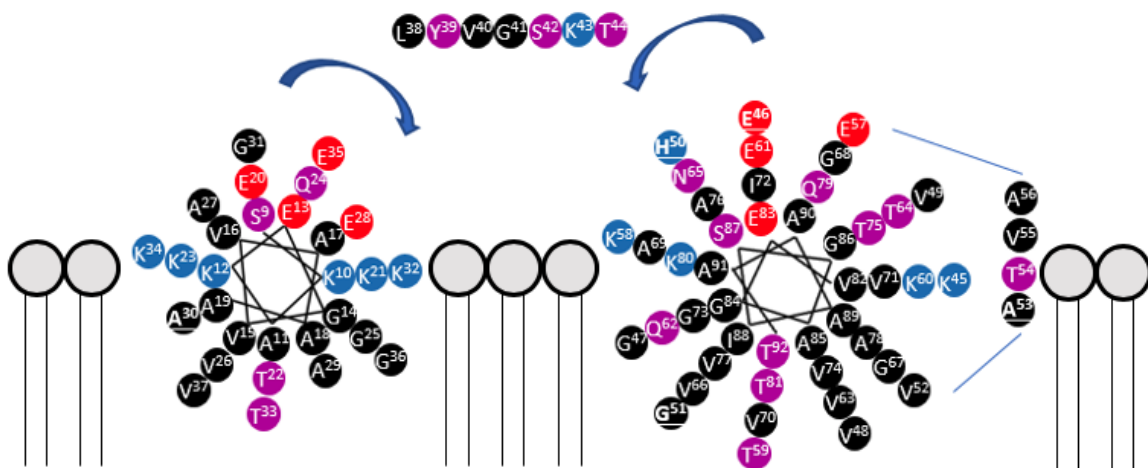
Figure 1.2: Proposed 3/11 (3 turns over 11 residues) helix model of αS bound to a lipid membrane. The positively charged lysine residues (blue) line up and interact with the negatively charged lipid head groups, and the negatively charged glutamic acid residues interact with the cytosol (red), and the hydrophobic residues (black) become imbedded in the fatty acid layer of the lipid tails. Both helices also include some polar residues within the hydrophobic layer (threonine and glutamine), causing the proposed transient relationship of αS binding. Figure taken from (Meade, R. M., Fairlie and Mason, 2019)

As this is an emerging field the full picture is still unclear, but a barrage of evidence is mounting highlighting the importance of the interaction of αS with lipid membranes likely for its native function, and its transition to pathologically relevant forms.

1.6 αS aggregation

αS aggregation progression from soluble random coil monomer to the insoluble β-sheet fibrils, as found in Lewy bodies, is being increasingly understood to exist as a highly dynamic process passing through many stages. These have been simplified into primary nucleation, fibril elongation, secondary nucleation and fibril amplification. Traditionally aggregation has been followed using enhanced Thioflavin T fluorescence upon binding to β-sheet conformations (Fig 1.3) (Khurana et al., 2005). The techniques have required very high concentrations of protein, agitation (shaking or stirring), or preformed fibrils in order for aggregation to occur. The effect on the resulting sigmoidal curves produced have been able to give insights to the mechanism of action of any inhibitors in development (Meisl et al., 2016).
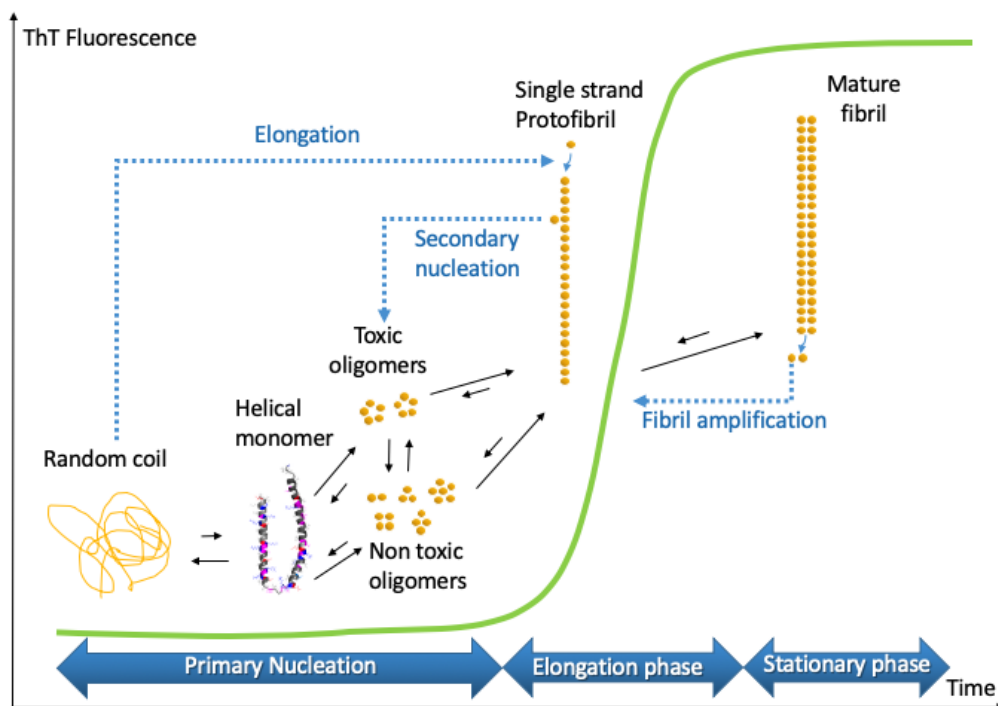
Figure 1.3: Proposed mechanism of αS misfolding from random coil to mature fibril via a population of aggregated oligomers, as followed by Thioflavin T fluorescence (green line). The steps of Primary nucleation, fibril elongation, and secondary nucleation/fibril amplification are highlighted. Primary nucleation is the dynamic equilibrium by which the random coil monomer converts into an α-helical state, which can then assemble into a population of oligomers. One or more of these oligomers may represent the cytotoxic species of αS, and one or more of these can form the kernel to seed fibril growth. Fibril elongation occurs by monomer addition to this fibril 'seed', until all free monomer exists in the energetically favourable fibril state. The fibrils can fragment leading to more nuclei for elongation, causing fibril amplification. Secondary nucleation occurs by monomers associating laterally to form nuclei which can then elongate *in situ* or dissociate to elongate independently, releasing oligomeric species which may or may not be cytotoxic.

Primary nucleation is the process by which random coil αS monomers, either in solution, or on a foreign surface (i.e. phospholipid vesicle membranes, or the air-water interface) (Galvagnion, C. et al., 2015) associate to form a multitude of dynamic oligomers, which convert into β-sheet fibrils (Fig 1.4). This is the main rate limiting step of the aggregation process, and in the absence of lipids leads to the significant lag phase observed in ThT aggregation assays. This is the process which initiates the onset of αS related toxicity.
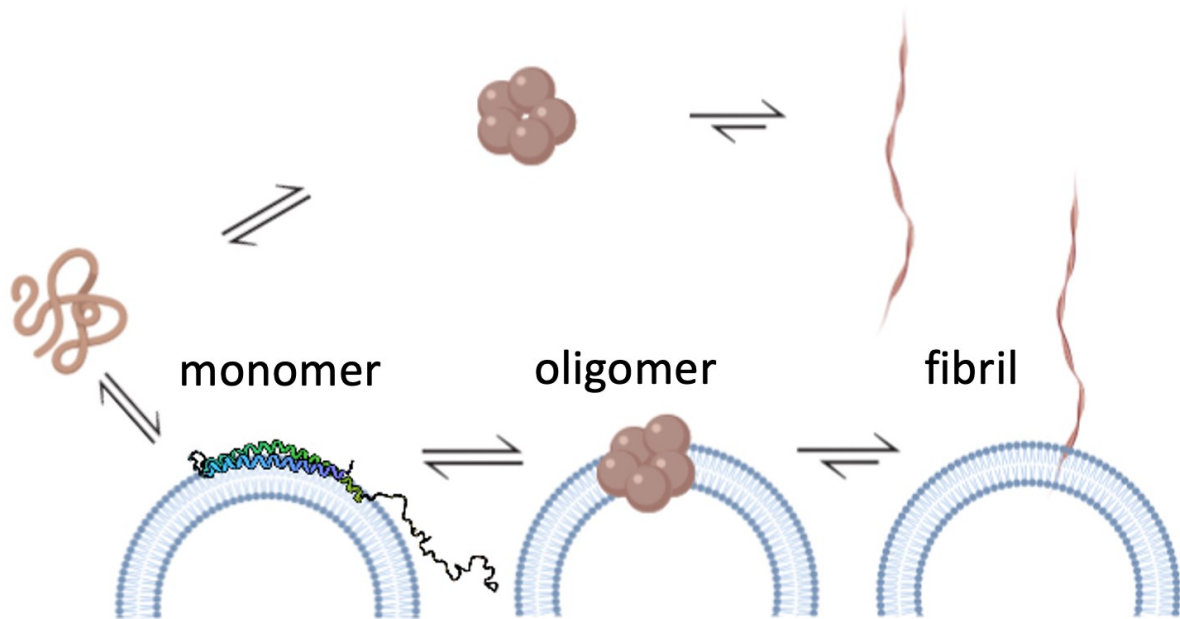
Figure 1.4: Primary nucleation occurs when αS monomers in solution (top) or on a surface such as a phospholipid bilayer (bottom) aggregate to first form oligomeric species which then form β-sheet fibrils.

Fibril elongation is the process where random coil αS monomers are added to the termini of preformed αS fibrils (Buell, A. K., 2019), surpassing the need to misfold through the oligomeric subgroups before reaching the final β-sheet fibril form, leading to a more energetically stable configuration (Fig 1.5).
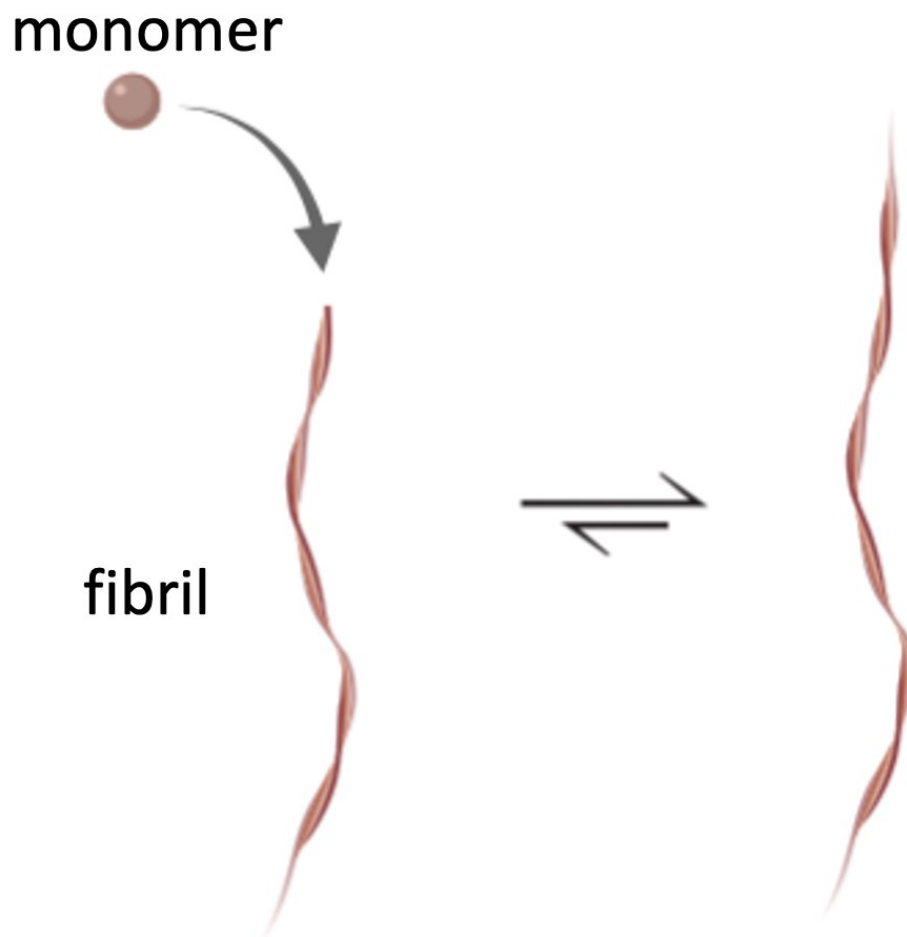
Figure 1.5: Elongation is caused by the addition of soluble random coil aS monomers to the ends of preformed insoluble β-sheet fibrils, a more energetically stable configuration.

Secondary nucleation is a complex process whereby either the amyloid fibrils can shear and fragment, causing fibril amplification, doubling the exposed ends where monomer addition fibril elongation can occur (Knowles et al., 2009), or through a surface catalysed processes (Tornquist et al., 2018), where αS monomers aggregate from the side of preformed fibrils, where further aggregation can then cause the formation and release of toxic oligomers, or can form fibril branch points which can break off leading to fibril amplification (Fig 1.6). Secondary nucleation is believed to be important in the propagation of αS aggregates through the brain, leading to disease progression (Peduzzo, Linse and Buell, 2020).
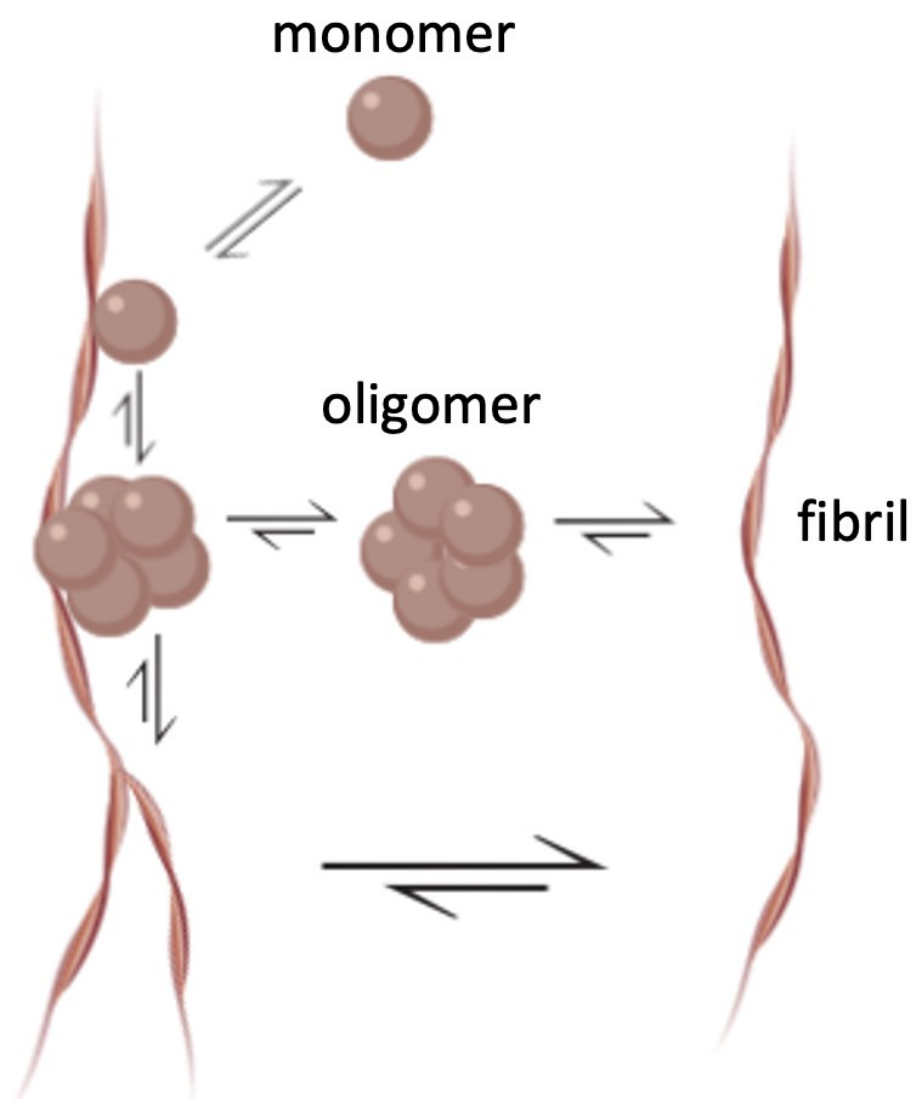
Figure 1.6: Secondary nucleation of amyloid fibrils through surface catalysed nucleation, whereby single monomeric αS aggregates to the side of preformed fibrils which can then cause formation and release of toxic oligomers or branching of the amyloid fibril. Branch points can sheer off leading to fibril amplification.

1.7 αS as an anti-PD target

αS offers a promising drug target for potential anti-PD medication, and there are numerous points in the aggregation cascade which can potentially be targeted to reduce the neuronal cell death caused by αS misfolding into conformations that are cytotoxic.

There are numerous avenues currently being explored in order to do this, including, reducing αS production, inhibiting αS mis-folding and aggregation, degrading intracellular αS aggregates, degrading extracellular αS aggregates and reducing the uptake of extracellular αS 'seeds', which propagate the disease through the brain.

Therapeutic approaches targeting αS

1 – Decrease αS production

2 – Prevent αS aggregation into toxic species

3 – Degrade intracellular αS and aggregates

4 – Degrade extracellular αS and aggregates

5 – Prevent cellular uptake and propagation of αS 'seeds'
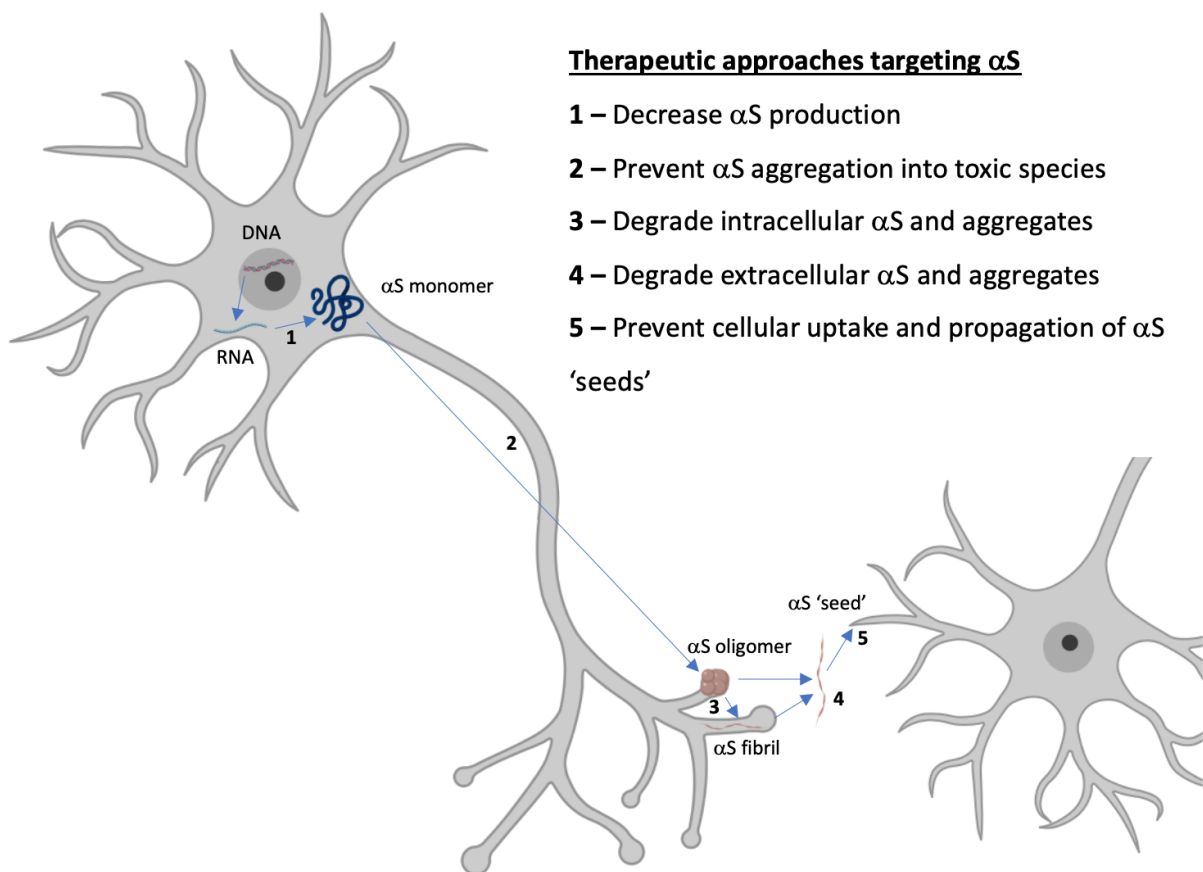
Figure 1.7: Proposed mechanisms for preventing αS related toxicity *in vivo*.

The ability to prevent αS aggregating into toxic conformations, would clearly prevent the damaging reproduction of mis-folding. The advantage of this approach would be that the normal intracellular function of the protein would remain unimpeded.

To date there have been three main approaches to preventing αS misfolding. The first is studying small heat-shock proteins (HSPs) (Klucken et al., 2004), the second with antibodies (Bhatt, Messer and Kordower, 2013), and the third with peptides (Madine, Doig and Middleton, 2008; Cheruvara et al., 2015). Using peptides, following on from the work of Cheruvara *et al.(Cheruvara et al., 2015)*, is the main therapeutic mechanism being explored for this thesis. This method is advantageous over the other methods due to the intracellular method of peptide library screening, selectivity, and smaller molecule size, potentially allowing easier access to the CNS via downstream optimisation.

1.8 Peptides as drugs

In modern medicine a strong emphasis has been put on developing small molecule drugs to target specific sites of action to modulate their effects, typically low molecular weight (less than 500 Da) molecules with a small surface area, which can bind to a specific site of interest, for example a hydrophobic pocket in the active site of an enzyme to prevent functionality. The development and application of these small molecule drugs has proven to be very fruitful and has led to many novel treatments for multiple diseases.

Whilst small molecule drugs present many advantages, like ease of access to site of action, they are not particularly useful at preventing large protein-protein interactions (PPIs) associated with a range of diseases, for example PD and Alzheimer's diseases, and they can cause off target binding, leading to unwanted side effects.

In recent years a shift in emphasis towards synthetic peptide-based therapeutics as drug molecules to modulate protein-protein interactions (PPIs) is showing promise to develop treatment for conditions previously thought to be undruggable (Mason, 2010; Craik et al., 2013; Rastogi et al., 2019). Peptide therapeutics present a number of advantages over that of small molecule in that they are highly selective, therefore will present fewer side effects, have high efficacy, and can present minimal toxicity (Rastogi et al., 2019).

The aim within the peptide community is to fill a niche between small molecule drugs and larger biomolecules, e.g. antibodies, ideally presenting the specificity of the larger

biomolecules and ability to interfere with the large surfaces of PPIs , but with the bioavailability of small molecule drugs (Bruzzoni-Giovanelli et al., 2018).

1.9 Peptide selection

One of the key strengths of peptides as therapeutics is that functionally relevant peptides can be selected from an extremely large parent library relatively quickly, without even complete understanding of the target protein conformation. There are multiple methods which can be used to achieve peptide screening, and new methods are continually under development. To date two of the most popular include phage display (Smith and Petrenko, 1997) and protein complementation assay (PCA) (Pelletier et al., 1999).

Phage display works by presenting the peptides from your library on the coat of a filamentous phage (up to 2700 copies of the peptide on a single phage) (Smith and Petrenko, 1997). These are then flowed over an immobilised target protein. Phages expressing peptides causing them to remain bound to the target after washing can then be recovered, enriched by infection and regrowth in bacteria, and sequenced to elucidate novel functional peptide sequences which bind to your target protein. An example of a peptide based medicine which was discovered by this methodology is Hematide (peginesatide), to treat anaemia (Macdougall et al., 2009). Whilst a very powerful technique it does present a few disadvantages, one of those being that the peptide is presented on the surface of the phage, and therefore may not present in the conformation adopted in an intracellular environment.

Protein complementation assay (PCA) is an intracellular screening technique. It works by selectively inhibiting a crucial respiratory protein in *E.coli* (dihydrofolate reductase; DHFR). A murine version of the same enzyme that is not inhibited is then split, with half of the DHFR attached to a 'bait' protein, and the remaining half to a 'prey' library. For the basis of this thesis the target protein used was aS and the library was based on the 45-54 region of αS (Cheruvara et al., 2015). The bait and prey must associate with each other to create a functional DHFR enzyme to confer cell survival. The library is then incubated through a number of competitive passaging steps to select the strain expressing the library member which gives the greatest survival rate. This is then sequenced to determine the winning

peptide library member. The advantage of PCA over Phage display is that the library selection occurs intracellularly in the host *E. coli*. Therefore a number of traditional hurdles in peptide design are already confronted, in that the selected peptide will bind to the target protein in the presence of a complex protein mixture, be soluble within the cytoplasm, not toxic to the host cell, not targeted for degradation before it is able to bind to the target, not susceptible to proteases, and capable of having a detoxifying effect on the target protein.

The true power of these techniques lies in the size of the libraries which can be created and screened by simple mutation of an amino acid sequence, which can make libraries with hundreds of thousands or even millions of options, dwarfing the high throughput screening methods used for the discovery of small molecule drugs.

1.10 Thesis aims

The overall aim of the thesis is to improve the efficacy of a peptide, 4554W, that was previously selected by PCA assay (Cheruvara et al., 2015). In order to do this further understanding regarding the mechanism of action of the peptide was required, and a suitable cell assay needed to be developed to confirm the activity of the peptide *in vivo*. Following this an alanine scan was performed on the 4554W peptide to elucidate the key residues involved. This information was used to develop *de novo* designed peptides related to these residue changes. These improvements and increased understanding can be used to design a second generation PCA assay with the aim of developing a new drug to be used in the treatment of PD

Chapter 2 presents an in-depth review of emerging principles in the field of αS research, focusing on new fibril structures of αS fibrils, and how these may relate to the early onset mutations.

Chapter 3 focuses on the development of a high throughput cell screening assay which can be used on functionally relevant cells, SH-SY5Y human neuroblastoma cell line, to test the efficacy of peptide inhibitors produced in this thesis within a cellular environment.

Chapter 4 utilised specific conditions in order to deduce where in the aggregation chain of αS the 4554W peptide acted, whether it be primary nucleation, fibril elongation or secondary nucleation. It was determined the 4554W peptide exhibited its effects on primary nucleation. This is consistent with the PCA mode of selection.

Chapter 5 further explored the structure and generation of a novel highly ordered macromolecular fibril polymorph found to be populated with extended incubation period with negatively charged (1,2-Dimyristoyl-sn-glycero-3-phospho-L-serine) DMPS lipid vesicles.

Chapter 6 utilised an alanine scan of 4554W to determine the key residues involved in the inhibition of αS primary nucleation. Contrary to expectation it was found that amino acid substitution to Alanine at positions 1 or 6 of the peptide increased efficacy. These improved peptides were then truncated to ultimately produce a smaller, more effective peptide known as 4654W(N6A).

Using the knowledge of the mechanism of action, and the sequence of the new improved peptide, named 4654W(N6A), a second generation PCA screen can now be performed to produce an increased potency peptide-based drug for the treatment of PD and other related synucleinopathies.

Chapter 2:

Review: Alpha-Synuclein structure and Parkinson's disease - lessons and emerging principles

This declaration concerns the article entitled:

Alpha-Synuclein structure and Parkinson's disease - lessons and emerging principles

Publication status (tick one)									
Draft manuscript		**Submitted**		**In review**		**Accepted**		**Published**	**X**

Publication details (reference)	Meade, R.M., Fairlie, D.P. and Mason, J.M., 2019. Alpha-synuclein structure and Parkinson's disease - lessons and emerging principles. *Molecular Neurodegeneration,* 14, p. 14.

Copyright status (tick the appropriate statement)			
I hold the copyright for this material		Copyright is retained by the publisher, but I have been given permission to replicate the material here	**X**

Candidate's contribution to the paper (provide details, and also indicate as a percentage)	The candidate contributed to / considerably contributed to / **predominantly executed** the… Formulation of ideas: 50% - Contributed to the structure and direction of the review Design of methodology: N/A Experimental work: N/A Presentation of data in journal format: 80% - Contributed to manuscript
Statement from Candidate	This paper reports on original research I conducted during the period of my Higher Degree by Research candidature.
Signed		**Date**	19/09/2020

Alpha-synuclein structure and Parkinson's disease – lessons and emerging principles

Richard M. Meade[1], David P. Fairlie[2] and Jody M. Mason[1,2]*

Abstract

Alpha-synuclein (αS) is the major constituent of Lewy bodies and a pathogenic hallmark of all synucleinopathathies, including Parkinson's disease (PD), dementia with Lewy bodies (DLB), and multiple system atrophy (MSA). All diseases are determined by αS aggregate deposition but can be separated into distinct pathological phenotypes and diagnostic criteria. Here we attempt to reinterpret the literature, particularly in terms of how αS structure may relate to pathology. We do so in the context of a rapidly evolving field, taking into account newly revealed structural information on both native and pathogenic forms of the αS protein, including recent solid state NMR and cryoEM fibril structures. We discuss how these new findings impact on current understanding of αS and PD, and where this information may direct the field.

Keywords: Alpha-synuclein, Amyloid, Oligomers, Parkinson's disease, Protein-protein interactions, CryoEM

Background

Parkinson's Disease (PD) is a progressive neurodegenerative disease, which accounts for approximately 15% of all dementia cases [1], and is the second most common form of neurodegeneration to Alzheimer's disease [2]. The disease has a mean onset of 55 years old and exhibits both physical and neuropsychiatric symptoms. The physical symptoms include slow imprecise movements (bradykinesia), tremors at rest, rigidity, facial paucity (hypomimia), shuffling gait, difficulty walking, freezing and postural instability [2]. The neuropsychiatric symptoms, which occur at later stages of the disease, manifest as cognitive defects, specifically slowness, disrupted sleep, and sensory disturbances, leading to suffers becoming passive and withdrawn [2].

PD is thought to be largely caused by the death of dopaminergic neurons in the *substantia nigra pars compacta*, located in the basal ganglia of the brain. This region of the brain is involved in coordinating movement, sending signals down the spinal cord to control muscle contraction, meaning that damage to this region can compromise signalling, leading to the physical symptoms of PD.

A wide range of both environmental and genetic risk factors have been implicated in the pathogenesis of PD [3]. Environmental risk factors include pesticides (specifically organochlorines) [4] and ambient air pollution [5]. Interestingly, tobacco [6], coffee [7], black tea [8], and a few pharmaceuticals including statins [9], calcium channel blockers [10] and ibuprofen [11], have shown some evidence of neuroprotective properties in a few studies. Autosomal dominant risk factors implicated with PD were first found in the SNCA gene that encodes αS, the primary component of Lewy bodies that are characteristic of all synucleinopathies. This will be discussed in detail and is the main focus of this review. It is worth noting that there are a number of other autosomal dominant and recessive risk factors implicated in PD, some of which occur upstream of the toxicity caused by αS. Other autosomal dominant mutations are found in the Leucine rich repeat Kinase 2 (LRRK2) domain, accounting for 4% of familial PD [12], in the vascular protein sorting 35 (VPS35) gene [13], accounting for 1% of familial PD and in the CHCHD2 [14] and eIF4G1 [15] genes. Recessive genes implicated in familial PD are Parkin [16], PTEN-induced putative kinase 1 (PINK1) [17], and Daisuke-Junko-1 (DJ1) [18] genes. These genes are upstream mutations which appear to increase αS

* Correspondence: j.mason@bath.ac.uk
[1]Department of Biology & Biochemistry, University of Bath, Claverton Down, Bath BA2 7AY, UK
[2]Division of Chemistry and Structural Biology, Australian Research Council Centre of Excellence in Advanced Molecular Imaging, Institute for Molecular Bioscience, The University of Queensland, Brisbane, Queensland 4072, Australia

toxicity, suggesting that further advances in understanding αS structure and function may be crucial to understanding and ultimately treating PD.

PD is strongly associated with the appearance of dopaminergic neuronal cytoplasmic inclusions called Lewy bodies. These are the leading pathogenic hallmarks in brain biopsies of PD patients, and are not present in healthy individuals. In 1997 Lewy body inclusions were shown to contain aggregates of αS [19], a 140 amino acid protein which has consequently been implicated as the likely cause of familial PD [20–22]. Further evidence is provided by the fact that duplication, triplication and autosomal dominant missense mutations in the SNCA gene lead to early onset forms of PD. It is now believed that the misfolding and subsequent aggregation of αS is a primary cause of dopaminergic degradation in PD. This is confounded by a rapidly ageing global population, correlating with an increasing number of sporadic cases of PD. In the United Kingdom alone it is believed that about 0.2% of the population are living with PD, affecting an estimated 127,000 people, and currently costing the NHS approximately £212 million per year [23]. This highlights the importance of discovering new methods to diagnose, treat and especially prevent neurodegeneration associated with PD and related synucleinopathies, and to better understand their pathogenesis. Effective strategies for preventing or reversing αS aggregation and neurotoxicity are urgently needed to avoid an exponential increase in disease with an ageing population. Recent solid state NMR and cryoEM fibril structures have brought new structural insights to the folding and formation of both native and pathogenic conformations of the αS protein [24–27].

α-Synuclein: native structure and function

Despite considerable effort, the precise native structure of αS is still poorly defined. It has been variously described as intrinsically disordered [28, 29], helical [30, 31], or a combination of the two [32]. A helix-rich structure has been shown to be more readily populated in the presence of phospholipid membranes [33, 34] (Fig. 1), offering one possible insight towards the functional role of the protein.

Identifying the precise native state(s) of αS has certainly been hampered by the lack of knowledge of a clear function for the protein, its binding partners, or specific post-translational modifications (see below). The majority of studies have failed to take these variables into account. A wide range of publications have sought to interrogate the structure in a variety of different buffer conditions, including variations in salt, pH and lipid composition [35]. More recently, others have studied different modifications to the protein composition (e.g.
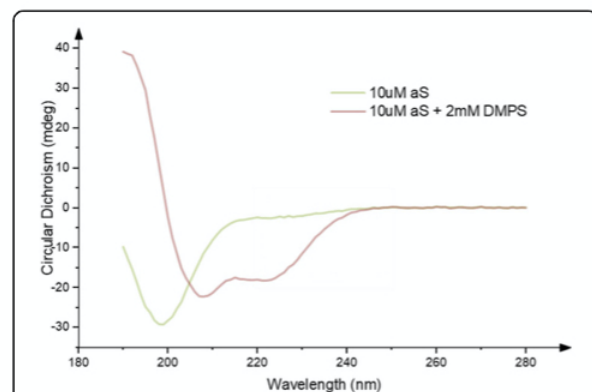
Fig. 1 Change in Circular Dichroism (CD) signal in the far UV caused by the binding of αS to an excess of DMPS vesicles. This demonstrates a shift from a random coil structure in the absence of lipid vesicles (green), towards an alpha-helical secondary structure in the presence of DMPS lipid vesicles (red). Meade *et. al.* unpublished data reproducing data from Galvagnion et al. [34]

phosphorylation, glycation, glycosylation, acetylation) and possible effects on protein structure and function [29, 36, 37]. Some groups have studied protein expression and aggregation in disease-relevant mammalian model systems to identify and understand possible roles for PTMs and the local environment on pathology.

A current consensus is that αS functions to promote membrane curvature, thereby contributing to synaptic trafficking and vesicle budding [38, 39]. This may be important given the association of αS with presynaptic terminal SNARE complexes [40], and suggests a potential role for αS in modulating dopamine release. This in turn has led to a number of studies investigating the transmission of the protein via synaptic terminals. Additional evidence lends support to a 'prion-like' hypothesis, whereby oligomeric αS can migrate between neurons to propagate formation of Lewy bodies throughout the *substantia nigra* and into extranigral regions. In particular, Bartels et al [30] and Wang et al [31] independently provided evidence that αS is able to fold into a stable helical structure by associating to form homotetrameric structures. This result was controversial as it was difficult to reproduce in vitro since multimers can disassemble upon cell lysis to generate aggregation prone monomers [41]. Later, others have reported that the structure could be recapitulated by the addition of lipids [42], providing helical multimers and evidence towards a native role for αS association in membrane interactions and in particular, vesicle budding. A similar effect has been observed either via N-terminal acetylation [43] or by extension of the N-terminus by 10 amino acids [31, 44], leading to formation of a persistent tetramer even in the absence of lipids [30]. Modifications to the N-terminus are known to be particularly important in driving folding towards a

helical form of αS [31], which then impacts upon down-stream aggregation [45].

Interestingly, a similar homotetrameric model for amyloidogenesis as a general principle had been proposed earlier [46, 47] based on the observed properties of a synthetic homotetramer formed from 4 equivalents of a short Glu/Gln rich peptide deliberately assembled in parallel on an artificial scaffold. In these experiments the peptide became significantly more α-helical and indefinitely stable at pH 7 when brought together in a parallel alignment, forming a homotetrameric arrangement. However, acidification transformed the α-helical aggregate, via a more elongated $4(3_{10})$ helix bundle [47] that led to tetramer aggregation, *en-route* to further elongation into four β-strands, seeding β-sheet aggregation and oligomerisation into matted amyloid-like fibrils. The key finding was that the tetrameric α-helix bundle was stabilised in water due to its hydrophobic core and polar hydrophilic exterior, like most proteins. However, the α-helix is in equilibrium with its more elongated 3_{10} helix analogue, and transition to a $4(3_{10})$-helix bundle proceeds under acidosis conditions due to protonation of hydrophilic residues (Glu). Rearrangement of polar Glu/Gln residues to the interior of the helix core and some hydrophobic residues (Leu) to the exterior surface promotes aggregation. This led to core destabilization and an α-helix to $4(3_{10})$-helix transition driven by inter-coil hydrogen bonds formed between facially paired protonated Glu residues (carboxylic acid dimers) and paired Gln residues (hydrogen bonded carboxamides). These interactions provided the catalyst for driving the equilibrium towards thermodynamically more stable strand/sheet formation and aggregation into oligomeric amyloids. For that particular peptide sequence, the process could be completely reversed back to the stable α-helical tetramers by restoring the pH to 7. Interestingly, acidosis has been associated with accumulation of αS oligomers [48, 49]. Local acidosis occurs at sites of inflammation and under conditions of metabolic stress (glycolysis and lactic acidosis), but whether this amyloidogenesis model with partial glutamate protonation or interstrand coupling of polar sidechains is relevant to αS oligomerisation and PD is unknown.

The current paradigm is that αS is likely to exist in vivo as an equilibrium mixture of unstructured monomer and statistically disfavoured helical oligomer(s), perhaps partially folded at membranes through phospholipid interactions. The alpha helical form of the protein may be required for an unknown native function but is not anticipated to be pathogenic, leading to the idea of stabilizing helical αS as a novel intervention strategy for PD. This might be similar to an approach used by Kelly and co-workers in stabilizing the native transthyretin fold, albeit targeting the protein with small molecules [50].

α-Synuclein Misfolding: implications for PD

Following the implication of the SNCA gene, and therefore αS, as a leading cause of pathology in familial forms of PD (see below) [20–22], it was also shown to be the primary protein found within Lewy bodies [19]. In particular, a central hydrophobic region of the protein corresponding to residues 71–82 was found to be essential for the misfolding and aggregation of αS into fibrils. The 71–82 region was also found to be able to aggregate in isolation [51], its deletion (residues 71–82 [51] or 66–74 [52]) preventing aggregation of the protein and implicating these as key regions in misfolding and possibly instigation of amyloidosis. More recently, Tuttle et al. employed ssNMR to demonstrate that the structure of αS in its fibrilar β-sheet arrangement adopts a serpentine Greek key topology [24]. This structure again highlighted the importance of the 71–82 region in stabilizing the pathogenic conformation of αS, but importantly also highlighted a second critical region that is strongly associated with early onset mutations (in particular E46K, H50Q, A53T/E/V and G51D – see below). The region, spanning residues 45–57 is key in mediating β-strand to β-strand interactions in the fibril conformation. This also reflected an exposed surface on fibrils between residues 46–57, suggesting that this region of αS is accessible in the fibril (see below). More recently, a number of cryoEM structures of mature fibrilar forms of the protein has been solved by two independent research groups [25–27, 53] with many similarities to the ssNMR structure. Two structures display a Greek-key topology, with a further two characterised by a hydrophobic cleft stabilised by intermolecular salt bridges and additional interactions between the NAC and the N-terminus [53] (see below). In all cryoEM structures the fibrils form dimeric strands, with rotational symmetry about the axis. In the former two structure is provided by the seemingly exposed 45–57 region of the fibrillised protein. This region may therefore act as a hydrophobic 'steric zipper', as first described in amyloid fibrils by Eisenberg and colleagues [54], between adjacent protofibrils that then serves to facilitate the formation of a more mature double stranded fibril structure [25, 55].

Genetic evidence for αS in PD

A relationship between genetics and PD was first identified in 1990, when members of an Italian-American family (the Contursi Kindred) were found to manifest inherited early onset PD. Studies subsequently found Lewy body pathology after autopsy [21] and the causative mutation leading to familial early on-set PD was located in the αS gene (SNCA) on chromosome four [20]. The specific mutation was an autosomal-dominant single base pair change in SNCA leading to the A53T substitution in αS [20]. Following this discovery, further

autosomal dominant mutations in the SNCA gene have been found to cause familial PD. These include E46K [56–58], H50Q [59–62], G51D [59, 63], A53T [20, 64], A53E [65], A53V [66] and A30P [67–69] (Table 1). The most potent of known mutations, leading to the earliest onsets of the disease, is G51D. Interestingly, despite all of these single amino acid changes leading to early onset of PD, each provides very different effects on the αS aggregation rate and the oligomers that become populated. For instance, the E46K [56–58], H50Q [59–62] and A53T [20, 64] mutations all lead to an increased rate of fibril formation, whereas the G51D [69], A30P [67] and A53E [70] mutations appear to slow the rate of fibril formation. All mutations must therefore lead to either an increase in the aggregation rate, or a change in the oligomeric state or conformation that is populated upon aggregation, as well as a decrease in the normal tetramer: monomer ratios that facilitates these changes. The mutants collectively provide compelling evidence that aggregation of αS directly leads to early onset PD, while others more specifically provide indirect evidence that prefibrilar oligomers are more toxic than mature aggregated fibrils. In addition to changes in aggregation kinetics of mutant αS variants, differences in their association with phospholipid membranes have also been observed. Mutations typically result in reduced phospholipid binding, as for example in G51D, A30P [68, 69] and A53E [70] variants. In contrast E46K and A53T lead to increased phospholipid binding [58]. These observations suggest a functional relationship between αS and lipid binding that can become compromised by changes in interaction and structure in early onset mutants. In addition to missense mutations described above, autosomal dominant familial PD has been observed when the SNCA gene becomes duplicated or triplicated [71, 72]. Consistent with the role of αS in PD, examples where triplication has occurred have led to more severe forms of PD than in instances of gene duplication. This highlights the importance of intracellular concentrations in driving increased likelihood of αS misfolding, seeding,

Table 1 Comparison of the effects of age of onset [106], lipid binding [69, 70, 106] and fibril growth rates [69, 70, 106] of the different early onset mutations in the SNCA gene as compared to the wild-type protein. An additional mutation A53V has also been reported [66]. The mutations listed have additionally been described as leading to different clinical and pathological features [107]

Mutation	Age of Onset	Lipid Binding	Rate of Fibril Growth
A30P	54-76	↓	↓
E46K	50-69	↑	↑
H50Q	60-71	≅	↑
G51D	19-61	↓	↓
A53E	36	↓	↓
A53T	20-85	↑	↑

and ultimately to an early onset of the disease phenotype relative to sporadic cases of PD.

Fibril structure and early onset mutants

Recently, atomic resolution structures of the β-sheet rich fibrilar forms of αS have been elucidated. This was first reported by Tuttle et al [24] using an ssNMR approach to achieve 4.8 Å structural resolution (PDB ID 2n0a), and more recently by Guerrero et al [25] using cryoEM to obtain a 3.4 Å resolution structure (since named polymorph 1a; PDB ID 6h6b), closely followed by Li et al [26] to 3.1 Å resolution (polymorph 1a; PDB ID 6a6b). The deduced 'Greek key' conformation elucidated independently by all three groups is strikingly similar, showing that each αS subunit in the fibril adopts a β-sheet conformation, with hydrogen bonding between adjacent αS subunits, spaced 4.8–4.9 Å apart. The central β-sheet rich core of the structures is located between residues 42–102 and is comprised of an inner hydrophobic region of αS that interlocks into right-angled spirals. N-terminal residues 1–41 and C-terminal residues 103–121 display a flexible random coil arrangement that is consequently poorly resolved within the structure. The outer surface of the fibril is mostly hydrophilic, with the exception of two main regions; L38/V40 and F94/V95, with V82 providing further hydrophobicity [25, 26]. Moreover, the central hydrophobic region is comprised of Ala/Val residues, and one Ile [25]. All structures highlight a potential salt bridge between E46 and K80, which likely serves to stabilize the conformation. An additional protofibril structure known as polymorph 1b (PDB ID 6cu8) shares the kernel structure that comprises the dimeric protofilament, but differs in the interface packing (see section 'Polymorphic amyloids - Rods and Twisters' for more).

Although both polymorph type 1a cryoEM structures exhibit many common features, the most notable is that the fibrils are 10 nm wide and composed of two adjacent protofilaments (Fig. 2). These interact to form a hydrophobic steric zipper, with a potential salt bridge being formed between E57 and H50 of the adjacent subunits. In contrast, the structure determined by ssNMR generated single strand fibrils with a width of 5 nm. It is therefore plausible that native αS can exist either as a single 5 nm protofilament, or as a dimerized 10 nm filament with rotational symmetry about the interface. Indeed, both structures have been observed in PD samples extracted from the *substantia nigra* [73]. The dimeric 10 nm filament is therefore likely to be a more mature fibril than the single 5 nm protofilament. This may also explain other structural discrepancies observed in amino acid orientations, which may be due to a more ordered energetically stable conformation upon dimerization of the protofilament.

30

Fig. 2 Structure of a single layer within a mature αS fibril. Based on the CryoEM structure published by Li et al [26] displaying formation of the 'Greek Key' topology with rotational symmetry about the axis of the fibril. The early onset mutations (E46K, H50Q, G51D/E, A53T) are highlighted (pink) in addition to three key electrostatic interactions that are perturbed in early onset PD (K58-E61, E46-K80 and K45/H50-E57)

There are a number of other differences between the two "polymorph 1a" cryoEM structures. For instance, in the cryoEM structure reported by Li et al [26], there is an additional salt bridge formed between residues E61 and K58 and this was not observed in the structure reported by Guerrero et al [25]. Instead, residue K58 is twisted towards the opposite side of the peptide backbone creating a cluster of positively charged residues (K43, K45, K58, H50) that provide excess electron density in this region. This was also not observed in the Tuttle et al ssNMR structure [24]. These differences could be caused by structural polymorphisms in this region between fibres, as a result of recombinant expression where PTMs are lacking or, as has been suggested [3], by an artefact in the Guerrero-Ferreira et al structure in which the construct used was a C-terminally truncated αS (1–121). However, for both cryoEM structures the fibres otherwise exhibit very similar overall topology and early onset residues display much the same interaction patterns.

The recently elucidated αS fibril structures are shedding new light on the mechanisms through which point mutations lead to early onset PD. A striking feature (Fig. 2) is that the fibril polymorph 1a interface is composed of small shallow hydrophobic residues (G51, A53, V55), that are flanked by strong 'ionic locks' (K45/H50→E57). The β-sheet structure of each subunit is further stabilised by the existence of two further ionic locks, K58→E61 and E46→K80. Importantly, these electrostatic contacts are buried within the fibril core, away from the aqueous environment, potentially enhancing their energetic contribution to overall fibril stability. The individual mutations are discussed in detail below, each appearing to share the fundamental property of destabilizing the formation of mature fibrils (Fig. 2) and potentially increasing the duration that toxic oligomeric species remain stable within the cells.

E46K In the majority of the structures the close proximity of E46 and K80 side chains suggest the formation of a stabilizing salt bridge [27] (Fig. 2). This salt bridge is compromised in the E46K [57] αS mutant, leading to electrostatic repulsion that destabilises the Greek key conformation and likely leads to an increased concentration of smaller oligomers rather than mature fibrils.

H50Q As is the case for E46K, a similar explanation is offered for the mutation H50Q [61]. In both instances the interface between the protofibril dimers is destabilized, leading to a potential shift in the equilibrium towards smaller oligomers. Substituting His with Gln removes the positive charge on the imidazole at physiological pH, preventing formation of a stabilizing salt bridge with E57 on the adjacent filament, and also removes a potential intramolecular salt bridge with K45 that stabilises the Greek key formation. Although not observed in Nature, the E57K mutant [74] generates the same effect by mutagenesis of the partnering side-chain. This perturbation has been shown to lead to the formation of small oligomers that are highly toxic in animal models relative to αS mutants that display significantly enhanced aggregation rates [74].

G51D Similarly, the G51D substitutions [63] on the neighbouring residue may inhibit fibril formation by loss of flexibility and hydrophobicity. It also introduces more steric bulk into the edge of the steric zipper region at the dimeric fibril interface (the G51 sidechain inserts between V55 and E57 on the opposing chain) as well as a potential charge repulsion with E57. This offers a potential explanation as to why this is the most potent of the known early onset mutations. It is also the slowest to aggregate in ThT experiments measuring fibril growth [69], supporting the hypothesis that increased lifetime of smaller oligomers can impart toxic effects. Moreover, the larger D residue is likely to sterically hinder the close interaction of the hydrophobic zipper and decrease local hydrophilicity, potentially inhibiting the formation of the dimeric protofibril. However, the structure from Li and co-workers suggests that a G51D change could impart an intramolecular attraction with K58 (Fig. 2).

A53E/T/V A similar inhibition of the hydrophobic interaction between the two protofibrils can explain the early onset mutations based around A53. The A53T [20] and A53E [65] mutant side-chains are larger and more hydrophilic, and may again inhibit close contact and therefore hydrophobic zipper formation between adjoining protofibrils (A53 inserts between A53 and V55 side chains on the opposing chain). These changes therefore likely weaken hydrophobic packing within the steric zipper. On the contrary, the A53V [66] mutation would increase the hydrophobic interaction, but is a bulkier side chain and so may cause steric hindrance along the tightly intercalated steric zipper, thereby decreasing the contact between the involved residues.

A30P The A30P [67] mutation occurs in the N-terminal random coil region, upstream of the hydrophobic Greek-key region, suggesting an alternative mechanism to

toxicity. For example, the change may result in a compromised role in the native fold, possibly directly affecting interaction with phospholipid membranes.

Summary
To summarize, early onset mutants found at H50, G51 and A53 can be rationalised by the cryoEM structures [25, 26] in a way that is not suggested by the earlier ssNMR structure [24]. In the former they appear to cause steric hindrance of the hydrophobic zipper interface formed between the two protofibrils. In the mature dimeric filaments, the proximity of the H50 and E57 side chains in adjacent protofibrils suggests a stabilizing salt bridge between protofibril subunits.

As for all types of amyloid, the aggregation of αS into mature fibrils may be a neuroprotective measure to shift the equilibrium away from soluble oligomers in a bid to reduce toxicity by lowering the number of exposed β-strands that present and can induce further aggregation. Therefore, when the formation of toxic oligomers is inhibited, this may block the formation of fibrils. On the other hand, if fibril formation is inhibited, this may have the counterproductive effect of serving to breakdown fibrils such that the toxic oligomers have longer lifetimes. One possibility is that the dimeric interface between the two protofibrils might function as a hinge point. Stabilization of the steric zipper leads to more mature fibrils that are less toxic, while mutations that weaken the interface (i.e H50Q, G51D and A53T/V/E, and the artificial mutation E57K) may lead to a population of more toxic smaller and therefore more soluble oligomers. There are most likely additional conformers that are yet to be elucidated, which may play important roles in the neurotoxicity of αS. Further experimentation is required to elucidate: *i)* the identity of oligomers of αS that are soluble and mobile versus insoluble and prone to fibrilisation, *ii)* the types of conformer within each oligomer population and how they are altered by mutations, ***iii)*** structure-function differences between oligomer populations. Addressing these points can distinguish those conformations that are most populated versus those most responsible for αS toxicity.

Polymorphic amyloids - rods and twisters
Following previous work there has very recently been described two additional αS polymorphic structures, named polymorph 2a (PDB ID 6rt0) and polymorph 2b (PDB ID 6rtb), both solved via cryoEM at 3.1 Å and 3.5 Å resolution respectively [53]. As for type 1 polymorphs these are composed of two protofilaments of 10 nm diameter but display very different arrangements (Fig. 3). In particular the steric zipper is missing in the type 2 polymorphs, which instead interact via K45-E57 (polymorph 2a) or K45-E46 (polymorph 2b) intermolecular

Fig. 3 CryoEM structures of four distinct types of full length αS fibril. The four structures are known as type 1a 'rod' [25, 26], type 1b 'twister' [27], type 2a and type 2b polymorphs [53]. Single layer density slices within the rod structure have revealed a Greek Key topology with rotational symmetry about the axis of the fibril. In contrast, single layers within the twister structure reveal a β-arch motif. Both type 1 polymorphs contain two protofilaments composed of stacked β-sheets with rotational symmetry about the fibril axis. In contrast, type 2 polymorphs lack the steric zipper geometry identified in type 1 polymorphs and are instead characterised by a hydrophobic cleft that is stabilised by intermolecular salt bridges and additional interactions between the NAC and the N-terminus. Left Box) Shown is the 3D model of the type 1a (rod) and type 1b (twister) fibril polymorphs, respectively, with their distinctively different helical pitches depicted. Top) Shown are representative regions of density maps of both polymorphs are superimposed with their models showing match of side chains with cryoEM densities. Bottom) How a 5 nm protofilament [24] may represent a shared fibril kernel from which both rod and twister fibrils can develop. In rod fibrils the interface is composed of residues within the preNAC region (blue, residues 47–56), an area in which most of the early onset PD mutations are located (cyan). In the twister fibrils the interface is composed of residues within the NAC core region (red, residues 68–78). This suggests that early onset mutations disfavour the rod like fibrils over the twister structures, offering the possibility for fibril morphogenesis and the potential to shift the aS population towards a more toxic polymorph. The left hand panel has been adapted from Li et al. 2018 [27] (CC-BY 4.0). The right hand panels are adapted from Guerrero-Ferreira et al 2019 [53] (CC-BY-NC-ND 4.0) and show schematic representations of all four currently characterized αS polymorphs with the with the N-terminus in blue, the NAC region in red and the C-terminus in yellow

salt bridges. In both polymorph 2 structures the steric zipper where familial mutation sites are found in polymorphs 1a-b, is replaced by a hydrophobic cleft. Moreover, in both structures the NAC region as before is buried but now additionally interacts with N-terminus of αS (via the C-terminal portion of NAC) that was not observed in polymorphs 1a-b.

Recently Li and co-workers used cryoEM to discern between two distinct types of mature polymorph 1 type fibre arrangements [27]. Both are 10 nm in width and bear many similarities to the earlier structures reported [24–26]. The single protofilament structure of 5 nm [24] resembles the common protofilament kernel of a bent β-arch that is found in both fibrils, suggesting this protofilament could be a precursor structure that gives rise to

other types of polymorph in addition to the two reported. Of the two polymorphs observed, major differences in packing gave rise to structures described as 'rods' (protofilament polymorph type 1a) and 'twisters' (protofilament polymorph type 1b). There are two major differences between these subtypes. The fibre-pitch in the twister structures is 460 Å compared to 920 Å for the rods. The second key difference is the structure of each αS molecule within a given polymorph. In the twister structure each molecule forms a bent β-arch with a NACore interface (residues 68–78), whereas for the rod structure the bent β-arch contains additional ordered residues that lead to the formation of a 'Greek-key' fold as reported by others [24–26] with a preNAC interface (residues 47–56). In this work, of particular

Meade *et al. Molecular Neurodegeneration*   (2019) 14:29

Page 8 of 14

note is that fact that mutations associated with early-onset PD are located in the preNAC region. These would appear to disrupt the intermolecular interface of the rod structures, but not the interface of of the twister structures (see Fig. 3). This suggests that in cases of early onset PD the equilibrium might shift towards a higher amount of twister-like structures. This in turn implies that twister polymorphs, rather than rod polymorphs, may be the more disease-relevant of the two type 1 polymorphic species in contributing to PD pathology. Consistent with this recent structural evidence is the fact that others have also described distinct polymoph subtypes, including αS fibrils isolated from PD patient brains with distinct polymorphic structures with fibril widths of 5 and 10 nm respectively [73]. The increasing number of different strains identified may also account for distinct clinico-pathological characteristics within different synucleinopathies [75].

Toxic versus non-toxic oligomeric conformations

The misfolding of soluble monomeric αS into insoluble fibrils observed in Lewy bodies requires the protein to exit from the usual folding trajectory. As molecules pass through a number of different transiently stable intermediate structures, there is the possibility for them to self-associate into oligomers via formation of β-strand to β-strand intermediates. It is gradually being accepted in the field that one or more specific, likely smaller, water soluble oligomers and their conformers are likely to represent the toxic species leading to disease [76, 77], directing research into identifying and characterizing these different oligomeric states and their relative toxicities. However, since these systems are metastable they are in constant flux and the oligomers are only transiently populated. Experiments that can delineate the precise states, structures and relative toxicities are therefore extremely challenging. However, in the last few years some inroads are finally beginning to be made.

Chen et al recently described a method for isolating stable toxic αS oligomers that have accumulated during amyloid formation, then characterized their structures [77]. They found two distinct subgroups of large stable oligomers, which they termed 10S and 15S oligomers, corresponding to an average of 18 and 29 monomer units per oligomer respectively. They were shown to be able to induce a toxic response at concentrations as low as 40 nM [77]. Atomic force microscopy (AFM) demonstrated that the oligomeric species were spherical in nature and contained ~ 35% β-sheet structure content with an antiparallel arrangement [77, 78], whereas more mature fibrils contained ~ 65% β-sheet structure [77] and are typically packed in a parallel arrangement [24, 25]. Further analysis by cryoEM demonstrated that both subgroups exist as either doughnut-like or cylindrical

conformers, and in similar proportions. They displayed a hollow core with an increased solvent-exposed hydrophobic surface, suggesting that they may interact favourably with hydrophobic membranes. The pore-like structure has previously been proposed as an important feature for amyloid oligomers in general to impart their toxicity [79]. It is worth noting that they found that αS oligomers smaller than 14 αS molecules were unstable and dissociated into monomers. There is a strong possibility that some smaller, less stable, oligomers could represent the more toxic species, and further approaches are required to identify these and to discern their unique structural and biochemical properties.

Later, Fusco et al formed two distinct groups of αS oligomers, described as type-A and type-B [80]. Type-A were prepared in the presence of (-)-epigallocatechin-3-gallate (EGCG) and were deemed non-toxic species, while type-B were found to be similar to those observed by Chen et al [77] and conferred cytotoxicity. The main difference between the two subspecies was their ability to disrupt lipid bilayers, with type-B conferring > 10 times the amount of disruption of type A, monomeric αS or even mature fibrils. One possibility is that type-B oligomers function by reducing mitochondrial activity in susceptible neurons [80]. This result has been further advanced by Ludtmann et al, who have demonstrated that αS oligomers can induce mitochondrial dysfunction by binding to the outer membrane and inhibiting ATP synthase by oxidation of the β-subunit [81]. Further aggregation of the oligomers can lead to increased ROS-induced opening of the mitochondrial permeability transition pore (PTP), leading to release of NADH into the cytosol [81], and depolarization of the mitochondrial membrane. These findings are supported by rat models in which the A30P mutation was also observed to cause mitochondrial impairment [82].

Klenerman and colleagues have been investigating the nature of different oligomeric species using Single-Molecule Förster Resonance Energy Transfer (FRET) Measurements. They have determined two distinct subpopulations of oligomers, termed Low-FRET and High-FRET [83], which appear to correlate with the Type-A and Type-B oligomers prepared by Fusco et al [80]. Their experiments suggest that formation of fibrils from monomeric αS follow a structured funnelling down the energy landscape, whereby monomeric αS first forms low-FRET, proteinase K sensitive, ThT inactive [84] oligomers with a diverse range of surface hydrophobicity [84] averaging 60 ± 2.6 nm in size. They then undergo a conversion step to a more compact, High-FRET, proteinase K resistant, cytotoxic, β-sheet rich, ThT active oligomer with a highly hydrophobic surface [84], averaging 80 ± 5.5 nm. These in turn form into the β-sheet rich, ThT active, less hydrophobic fibrils [83]. The High-FRET

34

oligomers were found to be composed of 6–150 subunits, although the majority of species in the reaction were smaller than 10-mers [83], and found to be cytotoxic to primary neuronal cultures, by promoting ROS production [85]. Indeed ROS production was measured in cells exposed to concentrations of the high-FRET oligomers as low as 50 pM [83], a result that highlights the probability that this is the pathogenic form of αS.

Further delineating the pathogenic species, or alternatively better defining the native role and structure of αS, may provide *bone fide* targets or a viable approach for the rational design of drugs to prevent the death of susceptible neurons. Once the precise toxic species are determined, the design of drug candidates will become more rational and accelerated. Moreover, the experimental tools used to gain these insights may enable characterization of drug targets for other amyloidogeneic proteins involved in related age-related diseases, for which a similar amyloid assembly mechanism might prevail.

Post-translational modifications

αS has been found to undergo a variety of post translational modifications (PTMs) in vivo, suggesting their importance in PD pathology. To date these have mainly included acetylation, phosphorylation and nitration which have been observed to affect the formation of different oligomers and fibril growth rates. N-terminal acetylation is a general post-translational modification of αS in mammalian cells [29]. It has been shown to cause increased helicity in the N-terminal region of the protein and decreased aggregation rates [86], as well as a 2-fold increase in affinity for lipid vesicles [87]. This PTM was included in the protein used by Li et al to identify the cryoEM structure of mature fibrils [26].

Phosphorylation has been identified on residues S87, Y125, Y133 and Y136 [37], but the most prominent pathologically relevant phosphorylation site appears to be on residue S129 [88]. This PTM has been found on more than 90% of the αS in Lewy bodies, but only 4% of the soluble αS, extracted from brain tissues of PD sufferers [89], and it has been shown to increase the rate of αS fibrilisation in vitro [88]. The specific function of this PTM remains unclear, with both toxic and protective effects reported in different animal and cell models, confounding the issue. Toxicity was accelerated in αS-overexpressing SH-SY5Y cells when phosphorylation of S129 was increased [90], and neuronal loss was observed to decrease in *Drosophila melanogaster* when S129 phosphorylation was inhibited [91]. The opposite has been found in yeast and rat studies where knockouts preventing S129 phosphorylation were observed to increase αS toxicity [92, 93], and formation of beta-sheet rich aggregates [93]. It therefore seems likely
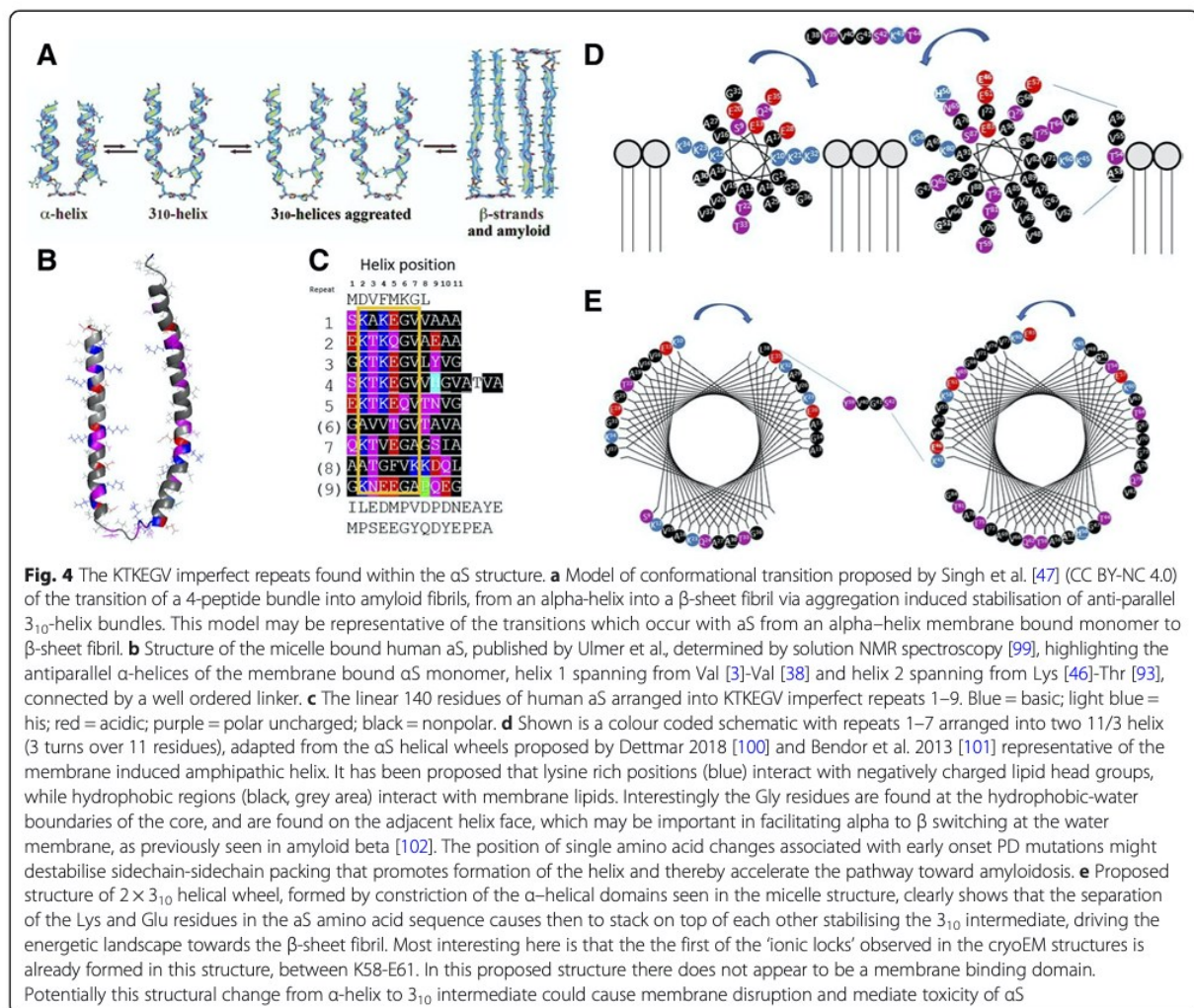
that this PTM plays a role in αS toxicity, but the nature of that role so far remains unclear and seems model dependent.

Nitration, caused by increasing levels of oxidative stress within neurons, is another commonly seen PTM of αS that has been detected on tyrosine residues Y39, Y125, Y133 and Y136 [36]. It is unclear whether this is caused by early stage pathogenesis of PD, or is a mitigating factor leading to PD. The most interesting, physiologically relevant, nitration appears to be at Y39, which has been observed to inhibit fibril formation and stabilize oligomeric species via dityrosine crosslinking [94]. It has been shown to inhibit αS association to synthetic vesicles [95], potentially mirroring the effects of the A30P [67] early onset mutation, adding further credibility to the idea of the toxic form of αS being an oligomer species rather than fibril. Dopaminergic neurons in the *substantia nigra* likely have a considerable energetic demand to support their unmyelinated axonal arbor [96] which results in the production of, and susceptibility to, reactive oxygen species [97], possibly explaining why these neurons are the first to become susceptible to αS toxicity.

Oxidative stress is seen to play a very important role in αS aggregation by affecting PTMs in the molecule, but it remains unclear whether they are a causative effect, which would open new targets for the treatment of PD, or a by-product further propagating a cascade effect of PD progression, explaining why the disease progresses so rapidly after its initial onset.

Misfolding via a 3_{10} intermediate?

Could the same KTKEGV repeat sequences that are thought to stabilize the tetramer be involved in amyloid formation, or possibly act as a nucleation sequence via a 3_{10} intermediate? In the helical model shown [98] (Fig. 4d), there is evidence that specific amino acid types can become periodic within helical structures. This could explain interaction with lipids, multimerization into a tetrameric structure, and have implications for a functional role in vesicle budding and neurotransmitter release. Some early onset mutants may also shift equilibria and lead to loss of interactions within helical multimers and/or with the membrane leading to increased likelihood of aggregation. Indeed, KTKEGV repeat motifs have been speculated to be key mediators of normal αS tetramerization. Their mutation has been hypothesized to lead to formation of monomers as well as neurotoxicity [98]. Moreover, it has been shown that abrogating native αS tetramers in mice can lead to an L-DOPA-Responsive motor syndrome that closely resembles PD [103]. By introducing a series of E➔K mutations into several of the KTKEGV repeats it was shown that tetrameric αS formation could be abrogated therefore leading to an increased likelihood of misfolding [100].

35

Fig. 4 The KTKEGV imperfect repeats found within the αS structure. **a** Model of conformational transition proposed by Singh et al. [47] (CC BY-NC 4.0) of the transition of a 4-peptide bundle into amyloid fibrils, from an alpha-helix into a β-sheet fibril via aggregation induced stabilisation of anti-parallel 3_{10}-helix bundles. This model may be representative of the transitions which occur with aS from an alpha–helix membrane bound monomer to β-sheet fibril. **b** Structure of the micelle bound human aS, published by Ulmer et al., determined by solution NMR spectroscopy [99], highlighting the antiparallel α-helices of the membrane bound αS monomer, helix 1 spanning from Val [3]-Val [38] and helix 2 spanning from Lys [46]-Thr [93], connected by a well ordered linker. **c** The linear 140 residues of human aS arranged into KTKEGV imperfect repeats 1–9. Blue = basic; light blue = his; red = acidic; purple = polar uncharged; black = nonpolar. **d** Shown is a colour coded schematic with repeats 1–7 arranged into two 11/3 helix (3 turns over 11 residues), adapted from the αS helical wheels proposed by Dettmar 2018 [100] and Bendor et al. 2013 [101] representative of the membrane induced amphipathic helix. It has been proposed that lysine rich positions (blue) interact with negatively charged lipid head groups, while hydrophobic regions (black, grey area) interact with membrane lipids. Interestingly the Gly residues are found at the hydrophobic-water boundaries of the core, and are found on the adjacent helix face, which may be important in facilitating alpha to β switching at the water membrane, as previously seen in amyloid beta [102]. The position of single amino acid changes associated with early onset PD mutations might destabilise sidechain-sidechain packing that promotes formation of the helix and thereby accelerate the pathway toward amyloidosis. **e** Proposed structure of $2 \times 3_{10}$ helical wheel, formed by constriction of the α–helical domains seen in the micelle structure, clearly shows that the separation of the Lys and Glu residues in the aS amino acid sequence causes then to stack on top of each other stabilising the 3_{10} intermediate, driving the energetic landscape towards the β-sheet fibril. Most interesting here is that the the first of the 'ionic locks' observed in the cryoEM structures is already formed in this structure, between K58-E61. In this proposed structure there does not appear to be a membrane binding domain. Potentially this structural change from α-helix to 3_{10} intermediate could cause membrane disruption and mediate toxicity of αS

An 11/3 helical wheel projection (Fig. 4d) implies an amphipathic helix with a hydrophobic face that can conceivably interact with lipids and a polar face that might interact with the solute. The two faces can be separated by a Lys rich seam that can potentially interact with negative charged head groups within the lipid [100]. There is likely to be an equilibrium between multimers and lipid binding in addition to changes in folded state structure. In addition, early onset mutations may play a dual playing in both destabilising the helical structures and their ability to interact with lipids, while destabilising rod polymorphs in favour of twisters.

Conformational transformation of natively folded αS into a partially folded intermediate (Fig. 4e) might account for aggregation and fibrillation. Given the potential helical structure of the native protein, particularly upon exposure to lipids or a membrane environment, one possibility is that the interactions which natively stabilise this structure are lost in aqueous environments. This might lead to destabilisation in favour of a β-sheet rich structure that is ultimately prone to aggregation and fibrilisation. One possibility is that a 3_{10} helix becomes populated en route from a compact α-helical structure stabilised by $i{\rightarrow}i+4$ contacts to a more stretched helix stabilised by $i{\rightarrow}i+2$ contacts. The latter 3_{10} helical structure might act as the first scaffold responsible for initiating further elongation to strands and sheets involved in early amyloid assembly events. In a 3_{10} helix model, the spacing of Lys and Glu residues in KTEGV repeats enables these residues to stack on top of one another (Fig. 4e), which we predict could stabilise such a misfolded intermediate structure over an α-helix, with this shift in equilibrium potentially leading to further elongation to β-strands that pair in β-sheets. Notably, the K58-E61 'ionic lock' observed in the CryoEM 'Greek-key' structure is already in position in this model. This conformational change may

36

tighten membrane bound helices and lead to disruption of lipid bilayers believed to be key for toxicity of toxic type-B oligomers [80].

Diagnostics, therapies and Theranostics

Recent advances in our understanding of how αS confers its cytotoxic effects in susceptible neurons will invariably direct future avenues of study to the prevention and diagnosis of synucleinopathies. The focus in the field has previously been directed towards preventing the formation of fibrils, when in fact the toxic effects of the protein may occur much earlier at the soluble oligomer stage and be independent of fibril formation. The primary focus should be to understand the specific prefibril, soluble oligomer(s) of αS and their specific conformations, so that future treatments can be designed to prevent their formation or inhibit their interactions that mediate toxicity. This may represent a more promising approach to drug discovery. Such protein-protein interactions (PPIs) are often difficult to target with small molecule drugs, owing to the many points of contact needed over large, solvent-exposed, polar and shallow, surface areas in order to drive both affinity and selectivity of interaction. Consequently, larger biologics and brain-permeable peptidomimetics are increasingly becoming of interest for modulating polar PPIs as they are large enough to make multiple interactions, distinguish between conformations, or stabilize non-toxic oligomers. If the equilibrium could be shifted away from the toxic oligomers, this may permit the native functionality of αS to remain unaltered by treatment. A promising peptide is currently in development based on the region relating to the early onset mutations, between residues 45–54 [104].

Understanding the identity and properties of early stage soluble oligomers that enable identification of toxic oligomers could also enable the development of a diagnostic for early identification of risk of PD, allowing treatment to begin early to prevent disease. A molecule with high affinity and selectivity for the toxic conformation of αS could be used to show the extent of the disease progression also acting as a valuable biomarker to support drug discovery. Such approaches clearly need to be coupled with the added challenge of improved diagnostics that are able to detect dopaminergic loss and Lewy body accumulation in the years and decades before symptoms present. Drugs that are applied at such a later stage are unlikely to be able to reverse symptoms. They may also be too late to prevent further pathologies resulting from affected pathways downstream of neuronal damage and loss that has already been incurred.

Future directions

As has been the case for other amyloidogenic proteins, a major advance in the field is likely to come from further structural studies from human brain samples [105]. This also needs to be coupled with more techniques that can interrogate transiently formed metastable species (ideally in conditions resembling the chemical complexity faced in neurons), and not only easily isolated endpoint products. As we have discussed, inroads towards these objectives are being made. Other questions remain and will surely be addressed over time. For example, which populations of αS have statistical weight? How can we best judge which strains are relevant? Which forms interact with lipids, and which (if any) with other compartments? Which αS strains can form such interactions and what are their affinities? Do different forms of αS co-assemble with other αS forms, or in time with other proteins? What are the relative stabilities of different αS assemblies and co-assemblies? Experiments aimed at addressing some of the above questions will help the community to embed and judge structural polymorphisms in a disease relevant context.

Conclusions

Gaining a better understanding of αS structure, folding and function is complicated by the dynamic nature of the protein, which can form a range of monomeric and oligomeric species, different conformers that may be dependent upon the environment, different definitions of the native structure, posttranslational modifications and interactions with lipids or other agents in the neuronal environment. Moreover, fibrils grown under controlled experimental laboratory conditions understandably cannot mimic all (unknown) physiological conditions that may influence fibril development in the brain, where there may be important differences, including competing and dynamic events that may produce different oligomeric structures. All of these variables currently make the understanding of αS properties difficult to interpret both in its native and in diseased states. However, recent structural insights have begun to progress the understanding of structure, folding and function suggesting that rational approaches to a designed treatment for PD and other synucleinopathies are now closer than ever before.

Authors' contributions
JMM and RM conceived and wrote most of the manuscript. JMM, DPF and RM contributed to writing and revising the manuscript. All authors read and approved the final manuscript.

Meade *et al. Molecular Neurodegeneration*   (2019) 14:29

Page 12 of 14

References
1. Cookson MR. Alpha-Synuclein and neuronal cell death. Mol Neurodegener. 2009;4:14. https://doi.org/10.1186/1750-1326-4-9.
2. Dauer W, Przedborski S. Parkinson's disease: mechanisms and models. Neuron. 2003;39:889–909. https://doi.org/10.1016/s0896-6273(03)00568-3.
3. Delamarre A, Meissner WG. Epidemiology, environmental risk factors and genetics of Parkinson's disease. Presse Med. 2017;46:175–81. https://doi.org/10.1016/j.lpm.2017.01.001.
4. Dutheil F, Beaune P, Tzourio C, Loriot MA, Elbaz A. Interaction between ABCB1 and professional exposure to organochlorine insecticides in Parkinson disease. Arch Neurol. 2010;67:739–45. https://doi.org/10.1001/archneurol.2010.101.
5. Hu CY, et al. Association between ambient air pollution and Parkinson's disease: systematic review and meta-analysis. Environ Res. 2019;168:448–59. https://doi.org/10.1016/j.envres.2018.10.008.
6. Ritz B, et al. Pooled analysis of tobacco use and risk of Parkinson disease. Arch Neurol. 2007;64:990–7. https://doi.org/10.1001/archneur.64.7.990.
7. Costa J, Lunet N, Santos C, Santos J, Vaz-Carneiro A. Caffeine exposure and the risk of Parkinson's disease: a systematic review and meta-analysis of observational Studiess. Journal of Alzheimers Disease. 2010;20:S221–38. https://doi.org/10.3233/jad-2010-091525.
8. Tan LC, et al. Differential effects of black versus green tea on risk of Parkinson's disease in the Singapore Chinese health study. Am J Epidemiol. 2008;167:553–60. https://doi.org/10.1093/aje/kwm338.
9. Wolozin B, et al. Simvastatin is associated with a reduced incidence of dementia and Parkinson's disease. BMC Med. 2007;5:11. https://doi.org/10.1186/1741-7015-5-20.
10. Pasternak B, et al. Use of Calcium Channel blockers and Parkinson's disease. Am J Epidemiol. 2012;175:627–35. https://doi.org/10.1093/aje/kwr362.
11. Samii A, Etminan M, Wiens MO, Jafari SNSAID. Use and the risk of Parkinson's disease systematic review and meta-analysis of observational studies. Drugs Aging. 2009;26:769–79. https://doi.org/10.2165/11316780-000000000-00000.
12. Zimprich A, et al. Mutations in LRRK2 cause autosomal-dominant parkinsonism with pleomorphic pathology. Neuron. 2004;44:601–7. https://doi.org/10.1016/j.neuron.2004.11.005.
13. Zavodszky E, et al. Mutation in VPS35 associated with Parkinson's disease impairs WASH complex association and inhibits autophagy. Nat Commun. 2014;5:16. https://doi.org/10.1038/ncomms4828.
14. Funayama M, et al. CHCHD2 mutations in autosomal dominant late-onset Parkinson's disease: a genome-wide linkage and sequencing study. Lancet Neurol. 2015;14:274–82. https://doi.org/10.1016/s1474-4422(14)70266-2.
15. Chartier-Harlin MC, et al. Translation initiator EIF4G1 mutations in familial Parkinson disease. Am J Hum Genet. 2011;89:398–406. https://doi.org/10.1016/j.ajhg.2011.08.009.
16. Kitada T, et al. Mutations in the parkin gene cause autosomal recessive juvenile parkinsonism. Nature. 1998;392:605–8.
17. Valente EM, et al. Hereditary early-onset Parkinson's disease caused by mutations in PINK1. Science. 2004;304:1158–60. https://doi.org/10.1126/science.1096284.
18. Benitez BA, et al. Resequencing analysis of five Mendelian genes and the top genes from genome-wide association studies in Parkinson's disease. Mol Neurodegener. 2016;11:12. https://doi.org/10.1186/s13024-016-0097-0.
19. Goedert M, Jakes R, Spillantini MG. The Synucleinopathies: twenty years on. Journal of Parkinsons Disease. 2017;7:S53–71. https://doi.org/10.3233/jpd-179005.
20. Polymeropoulos MH, et al. Mutation in the alpha-synuclein gene identified in families with Parkinson's disease. Science. 1997;276:2045–7. https://doi.org/10.1126/science.276.5321.2045.
21. Golbe LI, Diiorio G, Bonavita V, Miller DC, Duvoisin RC. A large kindred with autosomal dominant parkinsons-disease. Ann Neurol. 1990;27:276–82. https://doi.org/10.1002/ana.410270309.
22. Polymeropoulos, M. H. et al. Mapping of a gene for Parkinson's disease to chromosome 4q21-q23. Science 274, 1197–1199, doi: https://doi.org/10.1126/science.274.5290.1197 (1996).
23. Morgan J. A seat at the table for people with Parkinson's disease. The Lancet Neurology. 2015;14:1077–8. https://doi.org/10.1016/s1474-4422(15)00246-x.
24. Tuttle MD, et al. Solid-state NMR structure of a pathogenic fibril of full-length human alpha-synuclein. Nat Struct Mol Biol. 2016;23:409–15. https://doi.org/10.1038/nsmb.3194.
25. Guerrero-Ferreira R, et al. Cryo-EM structure of alpha-synuclein fibrils. eLife. 2018;7. https://doi.org/10.7554/eLife.36402.
26. Li YW, et al. Amyloid fibril structure of alpha-synuclein determined by cryoelectron microscopy. Cell Res. 2018;28:897–903. https://doi.org/10.1038/s41422-018-0075-x.
27. Li BS, et al. Cryo-EM of full-length alpha-synuclein reveals fibril polymorphs with a common structural kernel. Nat Commun. 2018;9:10. https://doi.org/10.1038/s41467-018-05971-2.
28. Breydo L, Wu JW, Uversky VN. Alpha-Synuclein misfolding and Parkinson's disease. Biochimica Et Biophysica Acta-Molecular Basis of Disease. 2012;1822:261–85. https://doi.org/10.1016/j.bbadis.2011.10.002.
29. Theillet FX, et al. Structural disorder of monomeric alpha-synuclein persists in mammalian cells. Nature. 2016;530:45–+. https://doi.org/10.1038/nature16531.
30. Bartels T, Choi JG, Selkoe DJ. Alpha-Synuclein occurs physiologically as a helically folded tetramer that resists aggregation. Nature. 2011;477:107–U123. https://doi.org/10.1038/nature10324.
31. Wang W, et al. A soluble alpha-synuclein construct forms a dynamic tetramer. Proc Natl Acad Sci U S A. 2011;108:17797–802. https://doi.org/10.1073/pnas.1113260108.
32. Burre J, et al. Properties of native brain alpha-synuclein. Nature. 2013;498:E4–6. https://doi.org/10.1038/nature12125.
33. Rovere M, Sanderson JB, Fonseca-Ornelas L, Patel DS, Bartels T. Refolding of helical soluble alpha-synuclein through transient interaction with lipid interfaces. FEBS Lett. 2018;592:1464–72. https://doi.org/10.1002/1873-3468.13047.
34. Galvagnion C, et al. Lipid vesicles trigger alpha-synuclein aggregation by stimulating primary nucleation. Nat Chem Biol. 2015;11:229–U101. https://doi.org/10.1038/nchembio.1750.
35. Buell AK, et al. Solution conditions determine the relative importance of nucleation and growth processes in alpha-synuclein aggregation. Proc Natl Acad Sci U S A. 2014;111:7671–6. https://doi.org/10.1073/pnas.1315346111.
36. Giasson BI, et al. Oxidative damage linked to neurodegeneration by selective alpha-synuclein nitration in synucleinopathy lesions. Science. 2000;290:985–9. https://doi.org/10.1126/science.290.5493.985.
37. Oueslati, A., Fournier, M. & Lashuel, H. A. in Recent Advances in Parkinsons Disease: Basic Research Vol. 183 Progress in Brain Research (eds A. Bjorklund & M. A. Cenci) 115–145 (Elsevier Science Bv, 2010).
38. Chandra S, Chen XC, Rizo J, Jahn R, Sudhof TC. A broken alpha-helix in folded alpha-synuclein. J Biol Chem. 2003;278:15313–8. https://doi.org/10.1074/jbc.M213128200.
39. Varkey J, et al. Membrane curvature induction and Tubulation are common features of Synucleins and apolipoproteins. J Biol Chem. 2010;285:32486–93. https://doi.org/10.1074/jbc.M110.139576.
40. Burre J, et al. Alpha-Synuclein promotes SNARE-complex assembly in vivo and in vitro. Science. 2010;329:1663–7. https://doi.org/10.1126/science.1195227.
41. Fauvet B, et al. Alpha-Synuclein in central nervous system and from erythrocytes, mammalian cells, and Escherichia coli exists predominantly as disordered monomer. J Biol Chem. 2012;287:15345–64. https://doi.org/10.1074/jbc.M111.318949.

42. Dong CH, et al. Structural characteristics and membrane interactions of tandem alpha-synuclein oligomers. Sci Rep. 2018;8:11. https://doi.org/10.1038/s41598-018-25133-0.

43. Trexler AJ, Rhoades E. N-terminal acetylation is critical for forming a-helical oligomer of a-synuclein. Protein Sci. 2012;21:601–5. https://doi.org/10.1002/pro.2056.

44. Gurry T, et al. The dynamic structure of alpha-Synuclein Multimers. J Am Chem Soc. 2013;135:3865–72. https://doi.org/10.1021/ja310518p.

45. Iyer A, et al. The impact of N-terminal acetylation of alpha-Synuclein on phospholipid membrane binding and fibril structure. J Biol Chem. 2016;291:21110–22. https://doi.org/10.1074/jbc.M116.726612.

46. Harrison, R. S., Sharpe, P. C., Singh, Y. & Fairlie, D. P. in Reviews of Physiology, Biochemistry and Pharmacology, Vol 159 Vol. 159 Reviews of Physiology Biochemistry and Pharmacology (eds S. G. Amara et al.) 1–77 (springer-Verlag Berlin, 2007).

47. Singh Y, et al. Amyloid formation from an alpha-Helix peptide bundle is seeded by 3(10)-Helix aggregates. Chem Eur J. 2011;17:151–60. https://doi.org/10.1002/chem.201002500.

48. Jiang P, et al. AMPK over-activation leads to accumulation of alpha-synuclein oligomers and decrease of neurites. Society for Neuroscience Abstract Viewer and Itinerary Planner. 2012;42.

49. Stephens AD, Zacharopoulou M, Kaminski Schierle GS. The cellular environment affects monomeric alpha-Synuclein structure. Trends Biochem Sci. 2018. https://doi.org/10.1016/j.tibs.2018.11.005.

50. Johnson SM, et al. Native state kinetic stabilization as a strategy to ameliorate protein misfolding diseases: a focus on the transthyretin amyloidoses. Acc Chem Res. 2005;38:911–21. https://doi.org/10.1021/ar020073i.

51. Giasson BI, Murray IVJ, Trojanowski JQ, Lee VMY. A hydrophobic stretch of 12 amino acid residues in the middle of alpha-synuclein is essential for filament assembly. J Biol Chem. 2001;276:2380–6. https://doi.org/10.1074/jbc.M008919200.

52. Du HN, et al. A peptide motif consisting of glycine, alanine, and valine is required for the fibrillization and cytotoxicity of human alpha-synuclein. Biochemistry. 2003;42:8870–8. https://doi.org/10.1021/bi034028+.

53. Guerrero-Ferreira R, et al. Two new polymorphic structures of alpha-synuclein solved by cryo-electron microscopy. bioRxiv. 2019. https://doi.org/10.1101/654582.

54. Sawaya MR, et al. Atomic structures of amyloid cross-beta spines reveal varied steric zippers. Nature. 2007;447:453–7. https://doi.org/10.1038/nature05695.

55. Peelaerts W. Baekelandt, V. alpha-synuclein folds: the cards are on the table. Nat Struct Mol Biol. 2016;23:359–60.

56. Greenbaum EA, et al. The E46K mutation in alpha-synuclein increases amyloid fibril formation. J Biol Chem. 2005;280:7800–7. https://doi.org/10.1074/jbc.M411638200.

57. Zarranz JJ, et al. The new mutation, E46K, of alpha-synuclein causes Parkinson and Lewy body dementia. Ann Neurol. 2004;55:164–73. https://doi.org/10.1002/ana.10795.

58. Choi W, et al. Mutation E46K increases phospholipid binding and assembly into filaments of human alpha-synuclein. FEBS Lett. 2004;576:363–8. https://doi.org/10.1016/j.febslet.2004.09.038.

59. Rutherford NJ, Moore BD, Golde TE, Giasson BI. Divergent effects of the H50Q and G51D SNCA mutations on the aggregation of alpha-synuclein. J Neurochem. 2014;131:859–67. https://doi.org/10.1111/jnc.12806.

60. Ghosh D, et al. The Parkinson's disease-associated H50Q mutation accelerates alpha-Synuclein aggregation in vitro. Biochemistry. 2013;52:6925–7. https://doi.org/10.1021/bi400999d.

61. Appel-Cresswell S, et al. Alpha-synuclein p.H50Q, a novel pathogenic mutation for Parkinson's disease. Mov Disord. 2013;28:811–3. https://doi.org/10.1002/mds.25421.

62. Khalaf O, et al. The H50Q mutation enhances alpha-Synuclein aggregation, secretion, and toxicity. J Biol Chem. 2014;289:21856–76. https://doi.org/10.1074/jbc.M114.553297.

63. Lesage S, et al. G51D alpha-Synuclein mutation causes a novel parkinsonian-pyramidal syndrome. Ann Neurol. 2013;73:459–71. https://doi.org/10.1002/ana.23894.

64. Serpell LC, Berriman J, Jakes R, Goedert M, Crowther RA. Fiber diffraction of synthetic alpha-synuclein filaments shows amyloid-like cross-beta conformation. Proc Natl Acad Sci U S A. 2000;97:4897–902. https://doi.org/10.1073/pnas.97.9.4897.

65. Pasanen P, et al. A novel alpha-synuclein mutation A53E associated with atypical multiple system atrophy and Parkinson's disease-type pathology. Neurobiol Aging. 2014;35:5. https://doi.org/10.1016/j.neurobiolaging.2014.03.024.

66. Yoshino H, et al. Homozygous alpha-synuclein p.A53V in familial Parkinson's disease. Neurobiol Aging. 2017;57:6. https://doi.org/10.1016/j.neurobiolaging.2017.05.022.

67. Kruger R, et al. Ala30Pro mutation in the gene encoding alpha-synuclein in Parkinson's disease. Nat Genet. 1998;18:106–8. https://doi.org/10.1038/ng0298-106.

68. Jo EJ, Fuller N, Rand RP, St George-Hyslop P, Fraser PE. Defective membrane interactions of familial Parkinson's disease mutant A30P alpha-synuclein. J Mol Biol. 2002;315:799–807. https://doi.org/10.1006/jmbi.2001.5269.

69. Fares MB, et al. The novel Parkinson's disease linked mutation G51D attenuates in vitro aggregation and membrane binding of alpha-synuclein, and enhances its secretion and nuclear localization in cells. Hum Mol Genet. 2014;23:4491–509. https://doi.org/10.1093/hmg/ddu165.

70. Ghosh D, et al. The newly discovered Parkinson's disease associated Finnish mutation (A53E) attenuates alpha-Synuclein aggregation and membrane binding. Biochemistry. 2014;53:6419–21. https://doi.org/10.1021/bi5010365.

71. Singleton, A. B. et al. Alpha-synuclein locus triplication causes Parkinson's disease. Science 302, 841–841, doi:https://doi.org/10.1126/science.1090278 (2003).

72. Chartier-Harlin MC, et al. Alpha-synuclein locus duplication as a cause of familial Parkinson's disease. Lancet. 2004;364:1167–9. https://doi.org/10.1016/s0140-6736(04)17103-1.

73. Crowther RA, Daniel SE, Goedert M. Characterisation of isolated alpha-synuclein filaments from substantia nigra of Parkinson's disease brain. Neurosci Lett. 2000;292:128–30. https://doi.org/10.1016/s0304-3940(00)01440-3.

74. Winner B, et al. In vivo demonstration that alpha-synuclein oligomers are toxic. Proc Natl Acad Sci U S A. 2011;108:4194–9. https://doi.org/10.1073/pnas.1100976108.

75. Peelaerts W, et al. Alpha-Synuclein strains cause distinct synucleinopathies after local and systemic administration. Nature. 2015;522:340–+. https://doi.org/10.1038/nature14547.

76. Chiti, F. & Dobson, C. M. in Annual Review of Biochemistry Vol. 75 Annual Review of Biochemistry 333–366 (annual reviews, 2006).

77. Chen SW, et al. Structural characterization of toxic oligomers that are kinetically trapped during alpha-synuclein fibril formation. Proc Natl Acad Sci U S A. 2015;112:E1994–2003. https://doi.org/10.1073/pnas.1421204112.

78. Celej MS, et al. Toxic prefibrillar alpha-synuclein amyloid oligomers adopt a distinctive antiparallel beta-sheet structure. Biochem J. 2012;443:719–26. https://doi.org/10.1042/bj20111924.

79. Kayed R, et al. Common structure of soluble amyloid oligomers implies common mechanism of pathogenesis. Science. 2003;300:486–9. https://doi.org/10.1126/science.1079469.

80. Fusco G, et al. Structural basis of membrane disruption and cellular toxicity by alpha-synuclein oligomers. Science. 2017;358:1440–+. https://doi.org/10.1126/science.aan6160.

81. Ludtmann MHR, et al. Alpha-synuclein oligomers interact with ATP synthase and open the permeability transition pore in Parkinson's disease. Nat Commun. 2018;9:16. https://doi.org/10.1038/s41467-018-04422-2.

82. Robson E, et al. Impaired fast network oscillations and mitochondrial dysfunction in a mouse model of alpha-synucleinopathy (A30P). Neuroscience. 2018;377:161–73. https://doi.org/10.1016/j.neuroscience.2018.02.032.

83. Iljina M, et al. Kinetic model of the aggregation of alpha-synuclein provides insights into prion-like spreading. Proc Natl Acad Sci U S A. 2016;113:E1206–15. https://doi.org/10.1073/pnas.1524128113.

84. Lee J-E, et al. Mapping surface hydrophobicity of alpha-Synuclein oligomers at the nanoscale. Nano Lett. 2018. https://doi.org/10.1021/acs.nanolett.8b02916.

85. Cremades N, et al. Direct observation of the interconversion of Normal and toxic forms of alpha-Synuclein. Cell. 2012;149:1048–59. https://doi.org/10.1016/j.cell.2012.03.037.

86. Kang LJ, et al. N-terminal acetylation of alpha-synuclein induces increased transient helical propensity and decreased aggregation rates in the intrinsically disordered monomer. Protein Sci. 2012;21:911–7. https://doi.org/10.1002/pro.2088.

87. Maltsev AS, Ying JF, Bax A. Impact of N-terminal acetylation of alpha-Synuclein on its random coil and lipid binding properties. Biochemistry. 2012;51:5004–13. https://doi.org/10.1021/bi300642h.

88. Fujiwara H, et al. Alpha-Synuclein is phosphorylated in synucleinopathy lesions. Nat Cell Biol. 2002;4:160–4. https://doi.org/10.1038/ncb748.

89. Anderson JP, et al. Phosphorylation of Ser-129 is the dominant pathological modification of alpha-synuclein in familial and sporadic Lewy body disease. J Biol Chem. 2006;281:29739–52. https://doi.org/10.1074/jbc.M600933200.

39

90. Sugeno N, et al. Serine 129 phosphorylation of alpha-synuclein induces unfolded protein response-mediated cell death. J Biol Chem. 2008;283: 23179–88. https://doi.org/10.1074/jbc.M802223200.

91. Chen L, Feany MB. Alpha-Synuclein phosphorylation controls neurotoxicity and inclusion formation in a Drosophila model of Parkinson disease. Nat Neurosci. 2005;8:657–63. https://doi.org/10.1038/nn1443.

92. Mbefo MK, et al. Phosphorylation of Synucleins by members of the polo-like kinase family. J Biol Chem. 2010;285:2807–22. https://doi.org/10.1074/jbc.M109.081950.

93. da Silveira SA, et al. Phosphorylation does not prompt, nor prevent, the formation of alpha-synuclein toxic species in a rat model of Parkinson's disease. Hum Mol Genet. 2009;18:872–87. https://doi.org/10.1093/hmg/ddn417.

94. Souza JM, Giasson BI, Chen QP, Lee VMY, Ischiropoulos H. Dityrosine cross-linking promotes formation of stable alpha-synuclein polymers - implication of nitrative and oxidative stress in the pathogenesis of neurodegenerative synucleinopathies. J Biol Chem. 2000;275:18344–9. https://doi.org/10.1074/jbc.M000206200.

95. Hodara R, et al. Functional consequences of alpha-synuclein tyrosine nitration - diminished binding to lipid vesicles and increased fibril formation. J Biol Chem. 2004;279:47746–53. https://doi.org/10.1074/jbc.M408906200.

96. Pissadaki EK, Bolam JP. The energy cost of action potential propagation in dopamine neurons: clues to susceptibility in Parkinson's disease. Front Comput Neurosci. 2013;7:17. https://doi.org/10.3389/fncom.2013.00013.

97. Sanders LH, et al. Mitochondrial DNA damage: molecular marker of vulnerable nigral neurons in Parkinson's disease. Neurobiol Dis. 2014;70:214–23. https://doi.org/10.1016/j.nbd.2014.06.014.

98. Dettmer U, Newman AJ, von Saucken VE, Bartels T, Selkoe D. KTKEGV repeat motifs are key mediators of normal alpha-synuclein tetramerization: their mutation causes excess monomers and neurotoxicity. Proc Natl Acad Sci U S A. 2015;112:9596–601. https://doi.org/10.1073/pnas.1505953112.

99. Ulmer TS, Bax A, Cole NB, Nussbaum RL. Structure and dynamics of micelle-bound human alpha-synuclein. J Biol Chem. 2005;280:9595–603. https://doi.org/10.1074/jbc.M411805200.

100. Dettmer U. Rationally designed variants of alpha-Synuclein illuminate its in vivo structural properties in health and disease. Front Neurosci. 2018;12: 14. https://doi.org/10.3389/fnins.2018.00623.

101. Bendor JT, Logan TP, Edwards RH. The function of alpha-Synuclein. Neuron. 2013;79:1044–66. https://doi.org/10.1016/j.neuron.2013.09.004.

102. Coles M, Bicknell W, Watson AA, Fairlie DP, Craik DJ. Solution structure of amyloid beta-peptide (1-40) in a water-micelle environment. Is the membrane-spanning domain where we think it is? Biochemistry. 1998;37: 11064–77. https://doi.org/10.1021/bi972979f.

103. Nuber S, et al. Abrogating native alpha-Synuclein tetramers in mice causes a L-DOPA-responsive motor syndrome closely resembling Parkinson's disease. Neuron. 2018;100:75–+. https://doi.org/10.1016/j.neuron.2018.09.014.

104. Cheruvara H, Allen-Baume VL, Kad NM, Mason JM. Intracellular screening of a peptide library to derive a potent peptide inhibitor of alpha-Synuclein aggregation. J Biol Chem. 2015;290:7426–35. https://doi.org/10.1074/jbc.M114.620484.

105. Fitzpatrick AWP, et al. Cryo-EM structures of tau filaments from Alzheimer's disease. Nature. 2017;547:185–+. https://doi.org/10.1038/nature23002.

106. Flagmeier P, et al. Mutations associated with familial Parkinson's disease alter the initiation and amplification steps of alpha-synuclein aggregation. Proc Natl Acad Sci U S A. 2016;113:10328–33. https://doi.org/10.1073/pnas.1604645113.

107. Rosborough K, Patel N, Kalia LV. Alpha-Synuclein and parkinsonism: updates and future perspectives. Current Neurology and Neuroscience Reports. 2017;17:11. https://doi.org/10.1007/s11910-017-0737-y.

Publisher's Note

40

Chapter 3:

Optimising Methods for Alpha-Synuclein Production and Cultured Neuronal Cell Assays

3.1 Introduction

The main aim of the thesis was to develop a peptide inhibitor of alpha-synuclein (αS) aggregation and related toxicity. The planned experiments therefore required a consistent supply of high purity αS, in relatively large amounts. Due to the cost implications and quality concerns in buying this protein, all αS used for the experiments performed in this thesis was expressed and purified in our laboratory. A variety of method are used to produce αS in the literature, therefore three alternative methods of αS production were undertaken and compared to determine the most appropriate production method for the experiments.

In order to determine the efficacy of inhibitory peptides produced in this project, within living cells, an effective, consistent and representative cell-based assay had to be developed and utilized. The SH-SY5Y human derived neuroblastoma cell was used for this, because of their ease of production, the fact they express dopaminergic neuronal markers (Kovalevich and Langford, 2013), and their success in previous αS related assays (Fusco et al., 2017; Perni et al., 2018; Cascella et al., 2019). A range of different conditions were explored to determine a reproducible, and accurate method of determining αS mediated toxicity, which could then be utilized to measure a peptides ability to inhibit the formation of toxic αS oligomeric species.

αS is expressed as a random coil monomer and is known to polymerize into extended amyloid β-sheet fibrils, via populations of soluble oligomers. The current consensus is that αS mediated cytotoxicity is driven by the formation of these oligomers, leading to membrane disruption within the cell (Fusco et al., 2017), impairing cellular function. Originally αS oligomers were found to be compact β-sheet enriched globular species, as observed by Circular dichroism (CD), X-ray scattering and atomic force microscopy (AFM) (Hong, Fink and Uversky, 2008). More recent isolation and analysis by CryoEM image reconstruction has shown the presence of two distinct subgroups of stable toxic oligomers, produced during amyloid formation (Chen, S.W. et al., 2015). Both oligomeric subgroups have a hollow 'doughnut-like' architecture (Figure 3.1), and these structures would need to be present in any cellular assay used to determine αS toxicity
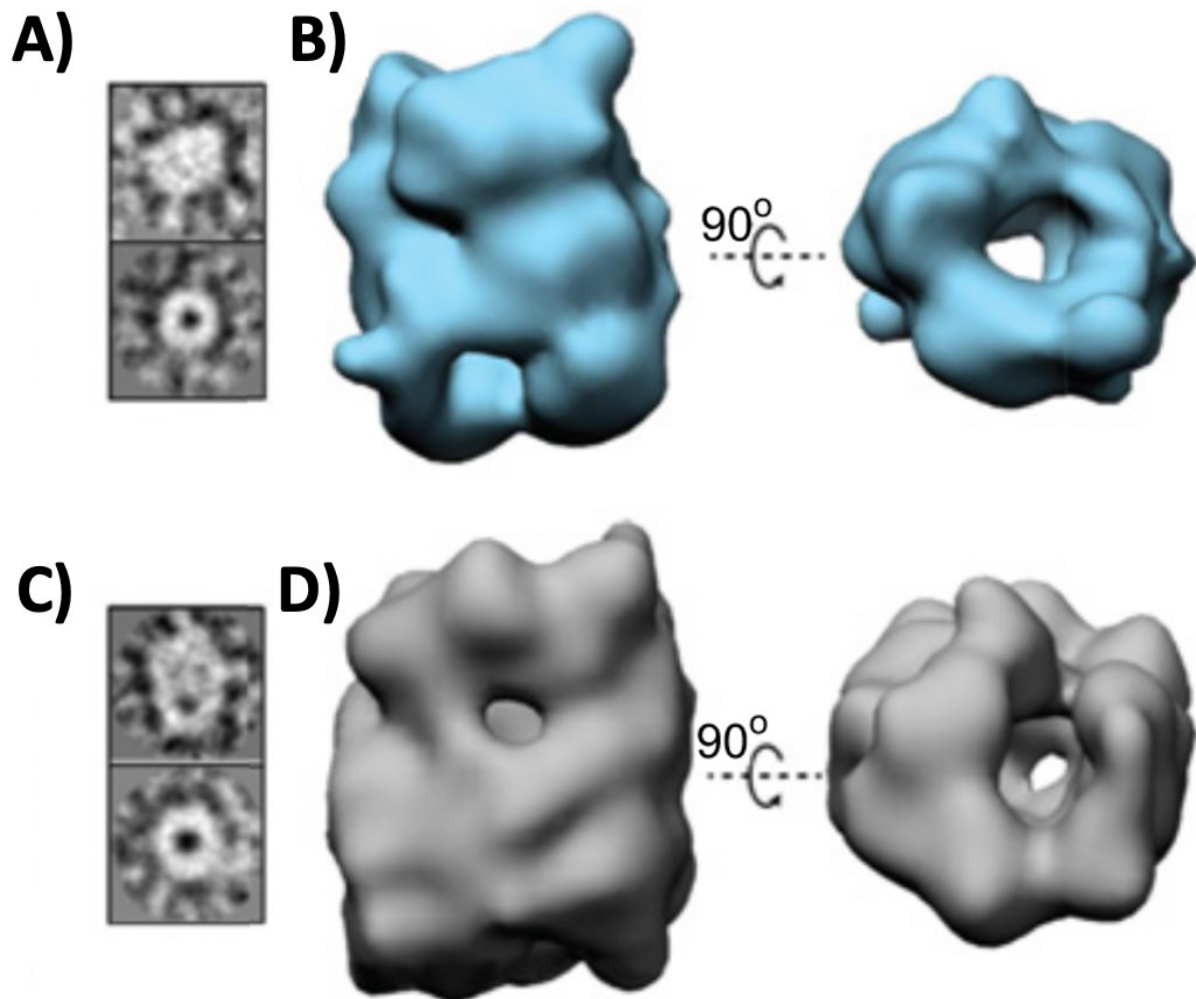
Figure 3.1: Taken from Chen *et al.* (2015) (Chen, S.W. et al., 2015) showing the toxic aS oligomer species. **A)** CryoEM image of the 10S oligomer **B)** 3D reconstruction of the 10 S oligomer **C)** CryoEM image of the 15S oligomer **D)** 3D reconstruction of the 15S oligomer.

αS oligomers have proven difficult to consistently produce, and purify, as they only exist for a very short time at the early stages of the αS aggregation process, and even at this stage they are only found to comprise ~1% of the aggregation solution (Ludtmann et al., 2018). Albeit, numerous groups have managed to purify, characterize, and induce cell toxicity with solution of these oligomers in SH-SY5Y (Fusco et al., 2017; Perni et al., 2018; Cascella et al., 2019) neuroblastoma cell culture, rat primary cortical neurons (Fusco et al., 2017; Perni et al., 2018; Cascella et al., 2019) and pyramidal cells (Kaufmann et al., 2016). Oligomer formation was achieved by a range of different methods, including agitation (Kaufmann et al., 2016; Ludtmann et al., 2018), lyophilisation and incubation at high concentration (Fusco et al., 2017; Perni et al., 2018), and fragmentation from pre-formed fibrils (Kaufmann et al., 2016).

The difficulty in developing an assay to determine the effectiveness of a peptide treatment is that previously utilized cell toxicity assays with oligomers require the oligomer to be pre-formed in solution. If the peptide acts at an earlier stage of the aggregation process, inhibiting the formation of these oligomers, then the addition of preformed oligomers to the experiment will not measure this inhibitory activity. Therefore, a method was developed to 'age' αS which produced the toxic oligomeric species, with the intention that ultimately inhibitory peptides can be added to the solution during the 'aging' process, and the inhibition of the formation of cytotoxic species can be measured by cell viability assay.

The main aims of this chapter are as follows: -

1 – Optimize an efficient, high yielding method of αS production.

2 – Develop an αS toxicity assay on a functionally relevant cell line.

3.2 Methods

Protein Purification

Purified αS was expressed and purified from *E. coli* using 3 different methods, these were:

i) αS-SUMO-Histag fusion method (expressed in p300d);

ii) αS-Thrombin-Histag fusion method (expressed in the pET15b plasmid);

iii) αS-alone method (expressed in the pET21a plasmid).

The first method utilizing the αS-SUMO-Histag fusion was used because sumoylation has been found to increase the solubility of aggregation-prone proteins, and inhibit the aggregation of αS (Krumova et al., 2011), and was also the method originally used to characterize the inhibition of αS aggregation by the 4554W peptide (Cheruvara et al., 2015), which is the basis of this PhD thesis. The second method utilizing the αS-Thrombin-Histag fusion, aimed to improve on the first method as fewer steps were required. The first two methods had added complexity as the cleavage enzymes and cleaved tails needed to be separated from the pure αS. Finally, the third method expressing αS alone was utilized modified from a previous purification method (Pujols et al., 2017). The three methods were compared and contrasted, ultimately highlighting that the optimal method to produce a large quantity of pure

monomeric αS was the αS alone method, and aggregation of the protein during purification was not an issue.

Approach 1: Producing αS: αS-SUMO-Histag fusion Method

The αS-SUMO-Histag fusion method was utilized by Cheruvara *et al*.(Cheruvara et al., 2015) for the initial production of the 4554W peptide, and used to show its inhibit of αS aggregation in kinetic and cell toxicity assays. Therefore, this method was initially utilized for αS production.

Protein	Amino Acid Sequence	MW (Da) (Av) (Da)	MW (Da) (mono-isotopic)	Absorption coefficient at 280 nm
αS-SUMO-His	MGHHHHHHGSDSEVNQEAKPEVKPEVK PETHINLKVSDGSSEIFFKIKKTTPLRRLME AFAKRQGKEMDSLRFLYDGIRIQADQTPE DLDMEDNDIIEAHREQIGGASMDVFMK GLSKAKEGVVAAAEKTKQGVAEAAGKTK EGVLYVGSKTKEGVVHGVATVAEKTKEQ VTNVGGAVVTGVTAVAQKTVEGAGSIAA ATGFVKKDQLGKNEEGAPQEGILEDMPV DPDNEAYEMPSEEGYQDYEPEACAP	27023.114	27006.446	8,463
ULP-1 Protease	LVPELNEKDDDQVQKALASRENTQLMN RDNIEITVRDFKTLAPRRWLNDTIIEFFMK YIEKSTPNTVAFNSFFYTNLSERGYQGVRR WMKRKKTQIDKLDKIFTPINLNQSHWAL GIIDLKKKTIGYVDSLSNGPNAMSFAILTD LQKYVMEESKHTIGEDFDLIHLDCPQQPN GYDCGIYVCMNTLYGSADAPLDFDYKDAI RMRRFIAHLILTDALK	25472.135	25455.918	31,008
αS from αS-SUMO-His	**AS**MDVFMKGLSKAKEGVVAAAEKTKQG VAEAAGKTKEGVLYVGSKTKEGVVHGVA TVAEKTKEQVTNVGGAVVTGVTAVAQKT VEGAGSIAAATGFVKKDQLGKNEEGAPQ EGILEDMPVDPDNEAYEMPSEEGYQDYE PEA**GAP**	14842.542	14833.406	4,836

Table 3.1: The sequence of proteins grown in *E.coli* recombinant cells from the Alpha-Synuclein-SUMO-His / ULP1 Protease Method and the resulting αS purified. Additional amino acids as compared to wt αS are highlighted in red.
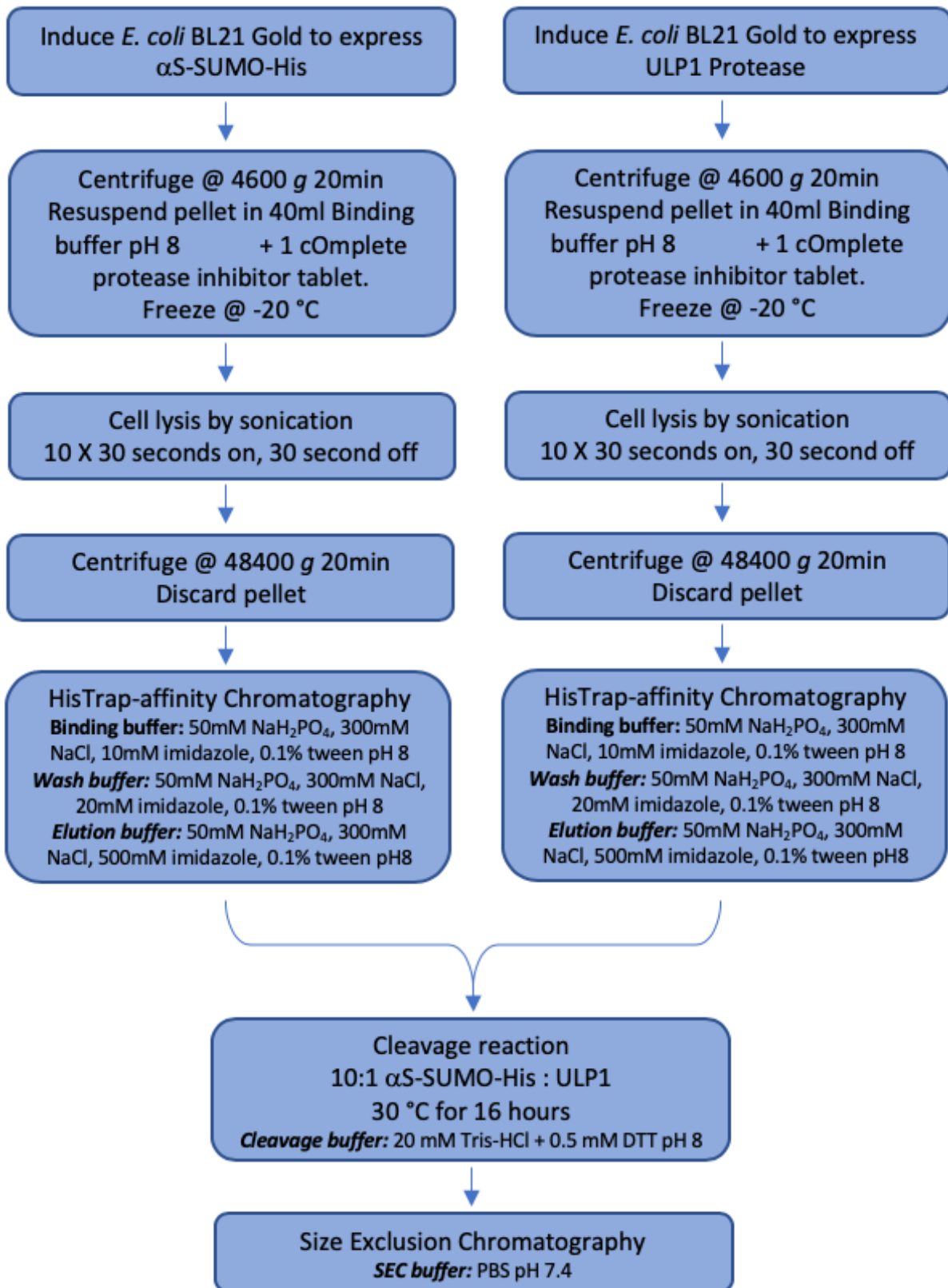
Figure 3.2: General strategy for the purification of αS using the αS-SUMO-His method.

ULP 1 protease expression in bacterial culture, and purification

Glycerol stocks of *E.coli* (BL21-Gold) containing the p300d expression plasmid containing the ULP-1 protease gene were used to inoculate 10ml 2XYT nutrient broth containing ampicillin (100 μg/ml). The cells were grown overnight at 37 ˚C, and shaken at 200rpm, in an Innova-44 incubator shaker. This overnight culture was then used to inoculate 1l of 2XYT nutrient broth containing ampicillin (100 μg/ml) until the cells reached optimal mid-log growth phase (Od_{600} = 0.6 - 0.8). At this point the cells were induced by 1 mM IPTG and grown overnight at 21 ˚C. The protein was then harvested from the cell culture and purified from the cell lysate by His-tag affinity chromatography.

αS-SUMO-Histag fusion expression in bacterial culture

Glycerol stocks of *E.coli* (BL21-Gold) containing the p300d expression plasmid containing the alpha synuclein-SUMO-His gene were used to inoculate 10ml 2XYT nutrient broth containing ampicillin (100 μg/ml). The cells were grown overnight at 37 ˚C, and shaken at 200rpm, in an Innova-44 incubator shaker. This overnight culture was then used to inoculate 1l of 2XYT nutrient broth containing ampicillin (100 μg/ml) until the cells reached optimal mid-log growth phase (Od_{600} = 0.6 - 0.8). At this point the cells were induced by 1mM IPTG and grown overnight at 21 ˚C. The protein was then harvested from the cell culture and purified from the cell lysate by His-tag affinity chromatography.

Alpha Synuclein-SUMO-His / ULP1 cleavage reaction

Protein purification buffers	
Buffer	**Composition**
Cleavage buffer pH 8.0	20 mM Tris HCl, 0.5 mM DTT

Table 3.2: Composition of buffers used for sumo/ULP1 cleavage reaction

Buffer exchange of the elution fractions was required because imidazole inhibits the ULP1 protease cleavage reaction. To do this, elution fractions containing the αS-SUMO-Histag fusion protein, collected from the His-column affinity purification were buffer exchanged

from elution buffer to cleavage buffer using an Amicon ultra centrifugal filter, with 3 kDa cut-off (Merck Millipore). The solution was centrifuged at 4000rcf, 4 °C, using a bench top centrifuge (Eppendorf 5430 R), until only 500 µl remained in the column, this was then filled with the standard buffer, and repeated once.

Purified ULP1 protease was mixed with the αS-SUMO-Histag fusion protein solution at a ratio of 10:1, at a concentration of 1 mg ULP1 Protease per ml. This cleavage solution was left at 30 °C for 16 hours in a temperature-controlled water bath.

The collected protein was then concentrated to 2 ml using an Amicon ultra centrifugal filter, with 3kDa cut-off (Merck Millipore), and further purified, and buffer exchanged by size exclusion chromatography (SEC).

Approach 2: Producing αS: αS-Thrombin-His Method

This method purified αS from *E. coli*, using a pET15b vector, by first expressing αS-Thrombin-His to enable purification by HisTrap chromatography, followed by a thrombin cleavage step to remove the His-tag.

Protein	Amino Acid Sequence	MW (Ave) (Da)	MW (Da) (mono-isotopic)	Absorption coefficient at 280 nm
αS-Thrombin-His	MGSSHHHHHHSSGLVPRGSHMDVFMKGLSKAKEGVVAAAEKTKQGVAEAAGKTKEGVLYVGSKTKEGVVHGVATVAEKTKEQVTNVGGAVVTGVTAVAQKTVEGAGSIAAATGFVKKDQLGKNEEGAPQEGILEDMPVDPDNEAYEMPSEEGYQDYEPEA	16622.460	16612.209	4,836
αS from αS-Thrombin-His	**SH**MDVFMKGLSKAKEGVVAAAEKTKQGVAEAAGKTKEGVLYVGSKTKEGVVHGVATVAEKTKEQVTNVGGAVVTGVTAVAQKTVEGAGSIAAATGFVKKDQLGKNEEGAPQEGILEDMPVDPDNEAYEMPSEEGYQDYEPEA	14683.357	14674.316	4,836

Table 3.3: The sequence of proteins grown in *E.coli* recombinant cells from the αS-Thrombin-His / Thrombin Method, and the resulting αS purified at the end. Additional amino acids as compared to wt αS are highlighted in red. Absorbance coefficient at 280 nm calculated using the molar extinction coefficient of tyrosine as 1209 M^{-1} cm^{-1}.
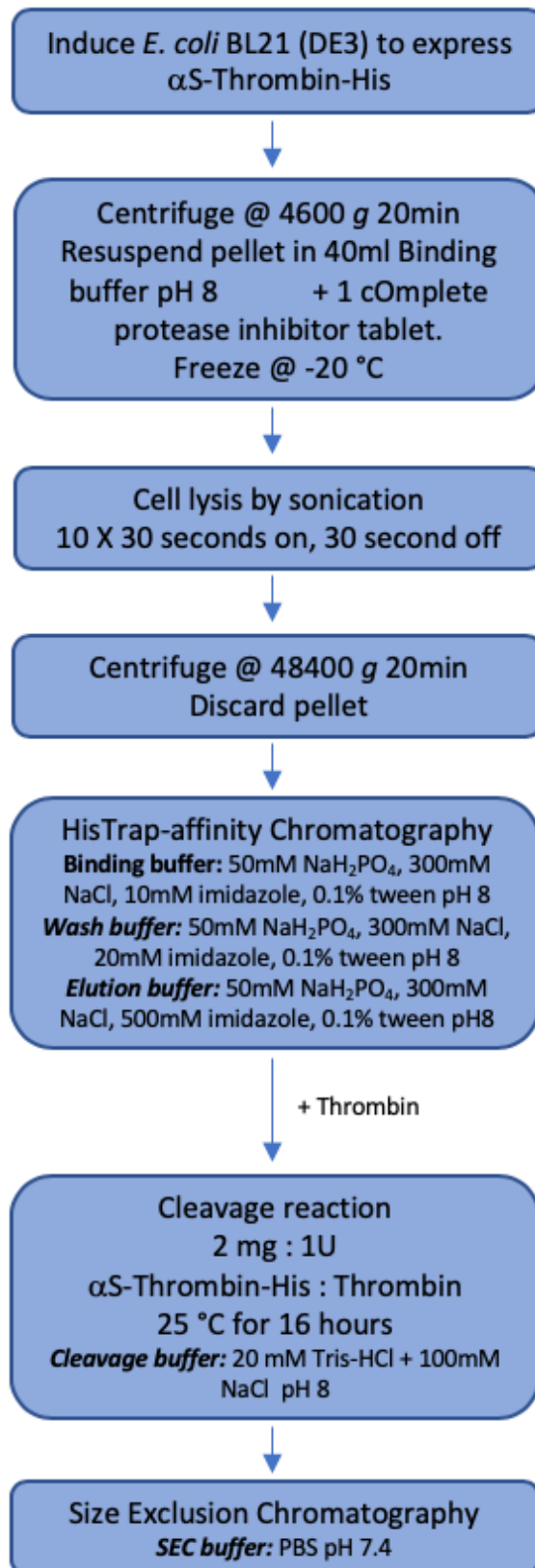
Figure 3.3: General strategy for the purification of αS using the αS-Thrombin-His method.

αS-Thrombin-Histag fusion protein expression in bacterial culture

Glycerol stocks of *E.coli* (BL21 (DE3) containing the pET15b expression plasmid with the alpha synuclein-SUMO-His gene were used to inoculate 10ml 2XYT nutrient broth containing ampicillin (100 μg/ml). The cells were grown overnight at 37 ˚C, and shaken at 200rpm, in an Innova-44 incubator shaker. This overnight culture was then used to inoculate 1l of 2XYT nutrient broth containing ampicillin (100 μg/ml) until the cells reached optimal mid-log growth phase (OD_{600} = 0.6 - 0.8). At this point the cells were induced by 1mM IPTG and grown overnight at 25 ˚C. The protein was then harvested from the cell culture and purified from the cell lysate by His-tag affinity chromatography.

αS-Thrombin-Histag fusion cleavage reaction

Protein purification buffers	
Buffer	**Composition**
Thrombin cleavage buffer pH 8.0	20mM Tris-HCl, 100mM NaCl

Table 3.4: Composition of buffers used for thrombin cleavage reaction

Buffer exchange of the elution fractions is required because imidazole inhibits the thrombin cleavage reaction. To do this, elution fractions containing the αS-Thrombin-Histag fusion protein, collected from His-column affinity purification were buffer exchanged from elution buffer to thrombin cleavage buffer using an Amicon ultra centrifugal filter, with 3KDa cut-off (Merck Millipore). The solution was centrifuged at 4000rcf, 4 °C, using a bench top centrifuge (Eppendorf 5430 R), until only 500 μl remained in the column, this was then filled with the cleavage buffer, and repeated once.

Lyophilised thrombin powder containing ≥2,000 NIH units/mg (SIGMA) was dissolved to a concentration of 1U / 100 μl. This thrombin solution was added to the alpha synuclein-Thrombin-His protein solution at a ratio of 0.5 U thrombin: 1mg alpha synuclein-Thrombin-His protein. This cleavage solution was left at room temperature with gentle agitation for 16 hours.

Following incubation, the cleavage solution was passed through a 1ml Ni-NTA column calibrated with binding buffer. The cleaved protein was collected in the flow through, and any uncleaved protein, and the cleaved thrombin-His tag remained bound to the column. The flow through (containing the cleaved αS, and thrombin) was then further purified and buffer exchanged by size exclusion chromatography (SEC).

Approach 3: Producing αS: Human wild-type αS pET21a Method

This method purifies unmodified human wild-type αS from *E. coli*, based on and modified from previously published methods (Pujols et al., 2017).

Protein	Amino Acid Sequence	MW (Da) (Ave)	MW (Da) (mono-isotopic)	Absorption coefficient at 280 nm
Human wt αS (1-40)	MDVFMKGLSKAKEGVVAAAEKTKQGVA EAAGKTKEGVLYVGSKTKEGVVHGVATV AEKTKEQVTNVGGAVVTGVTAVAQKTVE GAGSIAAATGFVKKDQLGKNEEGAPQEG ILEDMPVDPDNEAYEMPSEEGYQDYEPE A	14,460	14451.209	4,836

Table 3.5: The sequence of proteins grown in *E.coli* recombinant cells from the Human wild-type αS pET21a Method, and the resulting αS purified.
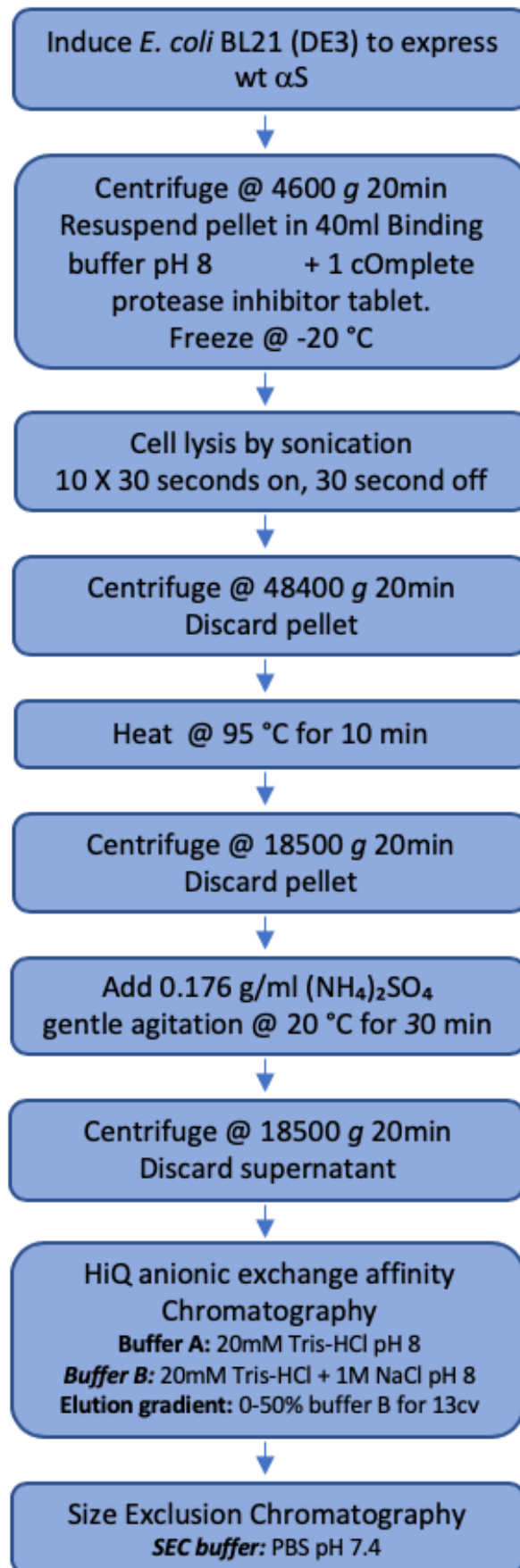
Figure 3.4: General strategy for the purification of αS using the Human wild-type αS pET21a Method.

wt Alpha Synuclein expression in bacterial culture

Wild type human αS was recombinantly expressed in *E. coli* containing the pET21a plasmid with the human wt αS (1-140) gene, purchased from Addgene (deposited by the Michal J Fox Foundation MJFF), and transformed into *E. coli* expression cell line BL21 (DE3). 10ml 2XYT media, containing 100 mg/l Ampicillin, in a 50 ml falcon tube was inoculated with human wt αS (1-140) pET21a BL21 (DE3) from glycerol stock, and incubated overnight at 37°C with 200 rpm shaking in an Innova 44 Incubator shaker (New Brunswick Scientific). The 10 ml overnight cultures were used to inoculate 1 l 2XYT cultures, containing 100 mg/lt Ampicillin, grown at 37°C, 200rpm shaking, to OD_{600} = 0.6 - 0.8 and induced by 1 mM isopropyl-1-thio-D-galactopyranoside (IPTG) at 37 °C, 200 rpm shaking, for 3-4 hours in an Innova 44 Incubator shaker (New Brunswick Scientific). The protein was then harvested from the cell culture and purified from the cell lysate by heating and ammonium sulphate crash, followed by ionic exchange affinity chromatography, and SEC.

Crude purification by heating, and ammonium sulphate crash

Cell lysate was boiled at 95 °C for 10 minutes in a heated circulating bath (Grant, TX15). The precipitated protein removed by centrifugation in a 50ml falcon tube, at 18500 × *g* for 20 min at 4 °C in a 5810 R Centrifuge (Eppendorf), using a F-34-6-38 (Eppendorf) fixed-angle rotor. The supernatant was collected, and ammonium sulphate added to 30% saturation (0.176 g / ml), left shaking at 20 °C for 30 min, and the precipitated protein removed by centrifugation at 18500 × *g* for 20 min at 20°C in a 5810 R Centrifuge (Eppendorf), using a F-34-6-38 (Eppendorf) fixed-angle rotor. The precipitated protein pellet was resuspended in 50 ml 20 mM Tris buffer pH8 by gentle agitation at 4 °C. The αS was further purified by anionic exchange affinity chromatography, and monomerised by size exclusion chromatography (SEC).

General Protein Purification Methods

Protein harvesting from cell culture

The bacteria were harvested by centrifugation at $4600 \times g$ for 20 minutes at 4 ˚C, in an Avanti J-25 centrifuge (Beckman Coulter), using a JLA-10.500 rotor (Beckman Coulter). The supernatant was discarded and the resulting cell pellet was resuspended in 40ml 20 mM Tris buffer pH8 containing 1 cOmplete protease inhibitor tablet (Roche) and freeze-thawed at -20°C before lysis, by sonication, using a Soniprep 150 plus sonicator, set to an amplitude of 14, for 20 cycles of 30 seconds on and 30 seconds off. The sonicated lysate was centrifuged at $48400 \times g$ for 20 minutes, in an Avanti J-25 centrifuge (Beckman Coulter), using a JA-25.50 rotor (Beckman Coulter). The supernatant was collected for further purification.

Anionic exchange affinity chromatography

His-tag affinity chromatography buffers	
Buffers	**Composition**
Buffer A pH 8.0	20mM Tris-HCl
Buffer B pH 8.0	20mM Tris-HCl, 1M NaCl

Table 3.6: Composition of buffers used for anionic exchange affinity chromatography

Cell lysate was purified by anion exchange chromatography on an AKTA pure purification system (GE Healthcare) with a 5ml HiTrap Q HP (GE Healthcare) pre-packed column. The HiTrap Q column was washed with 2 column volumes (cv) MilliQ H_2O at a flow rate of 5 ml/min, then equilibrated with 2 cv of Buffer A (20 mM Tris buffer pH 8) at a flow rate of 5 ml/min. The 50 ml sample was then loaded onto the column using a 50 ml superloop at a flow rate of 2 ml/min, followed by 5 cv wash with buffer A to remove any unbound protein from the column. An elution gradient was run at 3 ml/min for 13 cv from 0 - 50 % Buffer B (20 mM Tris buffer + 1 M NaCl pH 8), collecting 2 ml fractions. The column was then washed by 5 cv of 100% buffer B, 5 cv MilliQ H_2O and 5 cv 20% ethanol, for storage and reuse. The peak fractions were collected, and analysed by SDS-page gel electrophoresis, the fractions containing purified αS were pooled.

His-tag Affinity chromatography

His-tag affinity chromatography buffers	
Buffers	**Composition**
Binding buffer pH 8.0	50mM NaH_2PO_4, 300mM NaCl, 10mM imidazole, 0.1% tween
Wash buffer pH 8.0	50mM NaH_2PO_4, 300mM NaCl, 20mM imidazole, 0.1% tween
Elution buffer pH 8.0	50mM NaH_2PO_4, 300mM NaCl, 500mM imidazole, 0.1% tween

Table 3.7: Composition of buffers used for His-tag affinity chromatography

An AKTA prime purification system (Amersham Biosciences), with a 5ml Ni-NTA superflow cartridge (Qiagen) was used to perform the His-affinity chromatography. The column was first calibrated with 30 ml water followed by 30 ml 0.2 M EDTA (pH 8.0) at a flow rate of 5ml/min. This was washed through with 30 ml H_2O. The white, nickel free column was then reloaded with approximately 15 ml of 100 mM $NiSO_4$. The Excess Ni^{2+} ions were washed off with 30 ml ddH_2O and the calibrated with 30 ml binding buffer at a flow rate of 5 ml/min.

The extracted cell lysate, made up to 50ml with binding buffer, was loaded into the column using a superloop at a flow rate of 1ml/min. The column was then washed with Wash buffer at a rate of 5 ml/min until no further drop was seen in the absorbance, measured at 280 nm. After washing, the bound proteins were eluted using a gradient between the wash buffer and the elution buffer, at 1ml/min, reaching 100% elution buffer after 60 minutes. 2ml Fractions were collected, and analysed by SDS-page gel electrophoresis, and fractions containing purified protein were pooled.

Size Exclusion chromatography buffers	
Buffer	**Composition**
Phosphate buffered saline (PBS)	PBS, 10x solution (Melford). 10x solution components (Sodium chloride 1.37 M, Potassium chloride 27mM, Phosphate Buffer 119mM) 100ml, diluted in 900ml, pH 7.4

Table 3.8: Composition of size exclusion chromatography buffers.

Further purification by size exclusion chromatography (SEC) was used to buffer exchange the α-synuclein into PBS (pH 7.4) and to ensure that only unaggregated monomers were collected.

SEC was performed on an AKTA pure (GE Healthcare) purification system, using a HiLoad 16/60 Superdex 75 pg (GE Healthcare) prepacked purification column. The column was initially cleaned with 1 cv MilliQ H_2O, 1 cv 1M NaOH, 1cv MilliQ H_2O, and equilibrated with 1.5cv PBS pH 7.4. 2ml of the αS solution from the previous step was loaded onto the column using a 2ml loop and a flow rate of 0.5 ml/min. 1.5 cv of PBS pH 7.4 was passed through the column at 1 ml/min, and samples collected by fractionation. The elution profile was followed by absorbance at 280 nm. The pure monomeric αS eluted between 54 - 60ml. The purity of αS was confirmed by SDS-Page gel electrophoresis and fractions containing pure monomeric αS were pooled.

High Pressure Liquid Chromatography (HPLC) purification and desalting of αS for cell toxicity assay

HPLC Solution	**Composition**
Solution A	0.1 % TFA in HPLC grade H_2O
Solution B	0.1 % TFA in Acetonitrile (MeCN)

Table 3.9: Solutions used for the HPLC purification of peptides.

The purified αS was purified and de-salted for lyophilisation by reverse phase High Pressure Liquid Chromatography (HPLC) on an AKTA pure protein purification system (GE lifesciences) with a Jupiter 4 μm Proteo C-18 90 Å reverse phase prep column. The column was first equilibrated with 1 cv (column volume) 5% solution B at 15 ml/min. 5 ml of the purified αS solution was added to the column using 5% solution B at a 2 ml/min. This was washed with 1 cv of 5% solution B, and a pre-gradient performed to 35% solution B over 0.5 cv at 15 ml/min. The αS was eluted by linear gradient, at 15 ml/min, from 35% solution B to 50% solution B over 150 ml at 15 ml/min, and the elution collected in 3 ml fractions. The column was then cleared of any remain residues by ramping to 95% solution B. The purified peak was confirmed by mass spectrometry and lyophilised in 2ml aliquots. The dry weight lyophilised αS was quantified to 0.1 μg accuracy using a Sartorius SE2 Ultra Micro Balance and stored as a dry pellet at -80 °C until required. For the cell toxicity assays this was resuspended in PBS (pH7.4) to the required concentration.

Protein Characterisation

Determination of Protein Concentration

The concentration of the αS collected after purification was determined in a 2mm path length quartz cuvette in a Cary 50 Conc UV-visible Spectrophotometer (Varian), using an extinction coefficient of 4836 $M^{-1}cm^{-1}$ at 280 nm. Samples were separated into 2ml aliquots, snap frozen in liquid N_2, and stored at -80°C until required.

SDS-PAGE Electrophoresis

SDS-Page gel electrophoresis was performed using RunBlue SDS 12% gels (Expedeon), in RunBlue SDS Run Buffer (Expedeon) at 150 V for 45 min. The Gel was stained overnight, with gentle agitation, using InstantBlue (Expedeon).

Mass Spectrometry of Purified Alpha Synuclein

The correct mass was confirmed by mass spectrometry on a Dionex Acclaim RSLC Polar Advantage II (PA2), 2.2 μm, 120 Å, 2.1 x 50 mm (Thermo Fisher Scientific, California, USA) with a flow rate of 0.4 mL/min, and an injection volume of 5 μL. Mobile phases A and B consisted of 0.1% v/v formic acid in water, and 0.1% v/v formic acid in acetonitrile.

Circular Dichroism (CD) assay

CD buffers	
Buffers	**Composition**
CD buffer (Phosphate buffer)	20 mM Phosphate Buffer (Na_2HPO_4 / NaH_2PO_4), pH8.0

Table 3.10: Composition of the buffer used to dilute CD samples.

A CD spectra scan was performed, to confirm the random coil conformation of the monomeric αS stock, and the β-sheet content of fully aggregated aS fibrils, on a Chirascan V100 (Applied Photophysics) in a 1mm quartz cuvette, scanning from 300 – 190 nm with a 1 nm bandwidth, averaged over 3 scans, blanked against the buffer and performed using a 10 μM dilution of αS (monomeric equivalents).

Quantification/Purification of Oligomers in αS solutions by SEC

To purify, or quantify the concentration, of oligomeric species in 'aged' αS solutions SEC was utilized. The αS samples were first ultracentrifuged using an Optima MAX Ultracentrifuge (Beckman Coulter) for 10 minutes at 100,000g in a TL-100 rotor (Beckman), to remove any insoluble fibrillary species which may be present. 100 μl of the supernatant (containing soluble monomer and oligomeric species) was loaded onto a Superdex 200 Increase 10300/GL size exclusion chromatography column (GE Life Sciences) equilibrated in PBS buffer pH 7.4, and run with a flow rate of 0.5 ml/min. Monomer peak eluted at about 15 ml flow volume and an oligomeric peak eluted at about 9 ml total flow volume, and could be quantified by integration under the curve.

Transmission Electron Microscopy (TEM)

αS Samples were viewed by TEM. 5 μL of the sample solution was put onto on glow discharged Formvar/carbon-coated, 200 mesh, copper grids for 1 minute. The samples were dried with filter paper and washed twice with MilliQ water for 1 second, each time removed with filter paper. The sample was stained by incubating the grids with 5 μL Uranyl Acetate Zero (Agar Scientific) for 30 seconds, followed by removal of the excess stain with filter paper. The grids were left to air-dry for 2 hours and imaged using a Transmission Electron Microscopy Jeol

2100 Plus (JEOL), operating at an accelerating voltage of 200 kV. Multiple grids were screened in order to obtain representative images of the samples.

Molecular biology protocols

Production of E.coli glycerol stocks

Solution	Composition
Glycerol stock	60% Glycerol in MilliQ H_2O

Table 3.11: Composition of the glycerol stock solution.

10 ml overnight cultures for the *E.coli* strains were grown in 2XYT media, containing 10 µl of the required antibiotic stocks, at 37 °C and 200 rpm in an Innova 44 shaking incubator. The overnight cell cultures were mixed 1:2 with 30% glycerol solution (1ml overnight culture with 500 µl glycerol stock), mixed, flash frozen in liquid nitrogen and stored at -80 °C.

Miniprep plasmid DNA extraction and Purification

Glycerol stocks were used to inoculate 5ml 2XYT media containing the appropriate antibiotics, and grown overnight, at 37 °C and 200 rpm, in an Innova 44 shaking incubator. The was centrifuged, at 5000g in a desktop centrifuge (Eppendorf 5430 R) and the supernatant discarded.

The plasmid DNA was extracted from the cell pellet using a Thermo Scientific GeneJET Plasmid Miniprep Kit. The cell pellet was resuspended in 250 µl of the Resuspension solution (with RNase A added), followed by addition of 250 µl lysis solution, and mixed by inversion. A further 350 µl of neutralization solution was then added, and again mixed by gentle inversion. This solution was the centrifuged for 5 minutes at 13,000g in a VWR Micro Star 17 desktop centrifuge, and the supernatant was transferred to a GeneJET spin column and centrifuged for a further 1 minute, discarding the flowthrough. The GeneJET spin column was washed twice with 500 µl of wash solution (diluted with ethanol), and the flow through discarded. The empty spin column was then subjected to a final 1min centrifuge spin to ensure that the wash

solution was completely removed. The column was transferred to a sterile 1.5 ml Eppendorf tube, and 50 µl of the elution buffer was added, and left to incubate at room temperature for 2 minutes. The plasmid DNA was eluted by spinning at 5000g in a desktop centrifuge (Eppendorf 5430 R) for 2 minutes. The DNA concentration was determined using a Nanodrop 2000 Spectrophotometer (ThermoScientific) and stored at -20 °C until required

Plasmid DNA sequencing

All plasmid DNA sequencing was performed by GATC-Biotech (Germany). To prepare the samples for sequencing 5 µl of the purified plasmid DNA at a concentration of 80-100 ng/µl was mixed, in a 1.5 ml Eppendorf, with 5 µl of primer DNA at a concentration of 5 µM.

Cellular biology protocols

Developing a cell-based assay to determine αS toxicity

In order to ultimately determine the efficacy of any inhibitory peptides produced in this project within living cells an effective and consistent cell-based assay had to be developed and utilized. The SH-SY5Y human derived neuroblastoma cell was ultimately selected for use, because of the ease of production, the fact they express dopaminergic markers, and their success in previous αS related assays.

SH-SY5Y cell culture protocol

SH-SY5Y cell culture media	
Media	**Composition**
Basic growth media (500ml)	DMEM/F12 (435ml) supplemented with Foetal bovine serum (10 %) Penicillin (100 IU), streptomycin (100 µg/ml), L-Glutamine (2 mM), Non-essential amino acids (5 %)

Table 3.12: Composition of the media used to culture SH-SY5Y cells.

The basic growth media (Dulbecco's modified Eagle's medium) was prepared and warmed to 37 °C. Human neuroblastoma cell line SH-SY5Y (ECACC 94030304) was purchased from Public Health England's European Collection of Authenticated Cell Cultures (ECACC). The cryovial of SH-SY5Y cells was rapidly thawed in a water bath at 37 °C, ensuring that some ice remained. 9ml of pre-warmed media was dispensed into a 15ml falcon tube, along with the contents of the cryotube, which were resuspended in the media. The falcon tube was centrifuged at 1,000g for 2 minutes. The supernatant was discarded, and the cells resuspended in 10 ml basic growth medium and plated into a T-25 flask. This was incubated in sterile conditions at 37 °C, 5% CO_2, and saturated humidity. The cells were maintained in 1 T-75 flask in 15ml Basic growth media and split every 3-5 when they reached 70-80% confluency.

For toxicity assays the stock culture was seeded in 96 well plates. To seed the 96 well plates for assay 500 µl of cell suspension was diluted with 500 µl PBS in in a 1.5 ml Eppendorf tube. A manual cell count was performed, and the cells were seeded at 0.6 x 10^5 in 100 µl volume in 96 well plates and grown for 24 hours to reach 60-80% confluency at 37 °C, 5% CO_2, and saturated humidity.

SH-SY5Y cell culture differentiation protocol

SH-SY5Y cultured neuroblastoma cells were differentiated to a neuronal phenotype using a modified protocol from Forester et al. (Forster et al., 2016) The modified method extended Phase 1 of the differentiation, after addition of the Retinoic acid (10 µM), to 5 days, and no FBS was added in the media at this stage. Differentiation of the cell culture was confirmed by visual inspection (see Figure 3.19).
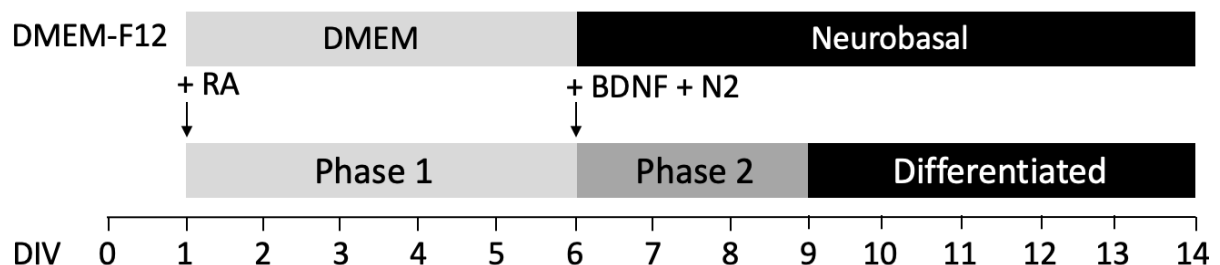

Figure 3.5: Modified protocol for the differentiation of SH-SY5Y cells. X-axis showing Days In Vitro (DIV), and the addition of 10 µM Retinoic acid (RA) on day 1, and 1% (50 ng/ml) brain-derived neurotrophic factor (BDNF) with 1% (v/v) N-2 100x supplement on day 6.

Preparation of fOligomers

Toxic oligomers were produced by fragmentation of larger pre-formed αS fibrils, termed fOligomers, based on a previously published methodology (Kaufmann et al., 2016).

Mature fibrils were first produced in a 10 mm Quartz cuvette by incubating 1.5 ml of 400 μM αS monomers in 20mM sodium phosphate buffer (pH 6.5) for 48 hours at 40°C maximal stirring (1500rpm), using a PTFE magnetic stirrer, on an RCT Basic Heat Plate (IKA, Staufen, Germany). The mature fibrils mixture was then sonicated using a Soniprep 150 plus sonicator, set to an amplitude of 14, for 20 seconds. The sonicated αS solution was ultracentrifuged using an Optima MAX Ultracentrifuge (Beckman Coulter) for 10 minutes at 100,000g, in a TL-100 rotor (Beckman), to remove any insoluble fibrillary species. Following this 100 μl of the supernatant (containing soluble monomer and oligomeric species) was then loaded onto a Superdex 200 Increase 10300/GL size exclusion chromatography column (GE Life Sciences) equilibrated in PBS buffer pH 7.4, and run with a flow rate of 0.5 ml/min. Monomer peak eluted at about 15 ml flow volume and an oligomeric peak eluted at about 9 ml total flow volume. The oligomer peak was collected, and the monomeric equivalent concentration was measured by absorbance at 280 nm.

Multiple runs were performed, the oligomer fractions pooled, and concentrated using an Amicon ultra centrifugal filter, with 100KDa cut-off (Merck Millipore).

Preparation of Oligomers by Agitation

Oligomer production buffers	
Buffers/gels	**Composition**
Phosphate buffered saline (PBS), pH 7.4	PBS, 10x solution (Melford). 10x solution components (NaCl 1.37 M, KCl 27mM, Phosphate Buffer 119mM) 100ml, diluted in 900ml, pH 7.4
αS solution	400 or 200 μM αS in PBS buffer

Table 3.13: Composition of the buffers and stocks used for cell toxicity assays.

Solutions of αS containing the toxic oligomeric species were produced by incubating 400 μl αS stock solution of either 400 or 200 μM in PBS buffer in a 1.5 ml Eppendorf tube on a Thermomixer comfort (Eppendorf) at 37 °C, agitated at either 900rpm for 6 hours, or 300 rpm for 24 hours respectively. The resulting 'aged' solution was passed through a 0.2 μm SPARTAN Filter unit (Whatman, GE Healthcare Life Sciences) and was used for the cell toxicity assays.

Preparation of Oligomers by Lyophilisation and incubation at High concentration

Oligomer production buffers	
Buffers/gels	**Composition**
Phosphate buffered saline (PBS), pH 7.4	PBS, 10x solution (Melford). 10x solution components (Sodium chloride 1.37 M, Potassium chloride 27mM, Phosphate Buffer 119mM) 100ml, diluted in 900ml, pH 7.4
αS solution	800 μM αS in PBS buffer

Table 3.14: Composition of the buffers and stocks used for cell toxicity assays.

Solutions of αS containing the toxic oligomeric species were produced by resuspending lyophilised dry αS powder to make an 800 μM stock solution in PBS buffer. 500 μl of the αS stock solution was aged in a 1.5 ml Eppendorf tube on a Thermomixer comfort (Eppendorf) at 37 °C, under quiescence for 24 hours. The resulting 'aged' solution was passed through a 0.2 μm SPARTAN Filter unit (Whatman, GE Healthcare Life Sciences) and used for the cell toxicity assays.

αS cell toxicity MTT reduction assay

Varying volumes of either the 'aged' αS solutions, or PBS volume equivalent, were added to a 96 well plate, in triplicate, to wells containing SH-SY5Y cells at 80% confluency in 100 μl basic growth media to give a range of final αS concentrations (0 – 300 μM). The plates were incubated at 37 °C, 5% CO_2, and saturated humidity for either 24 hours or 48 hours.

Following incubation, cell viability was determined using the 3-(4-5-dimethylthiazol-2-yl)-2,5-diphenyltetrazolium bromide) MTT reduction assay. For this the basic cell growth media was

removed by aspiration and replaced with 100 µl fresh basic growth media containing 1 mg/ml MTT (solubilized by vortexing) and incubated at 37 °C, 5% CO_2, and saturated humidity for 1 hour.
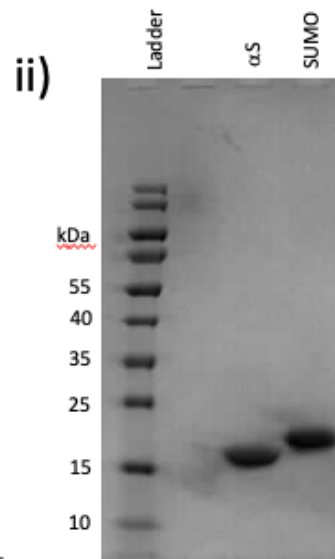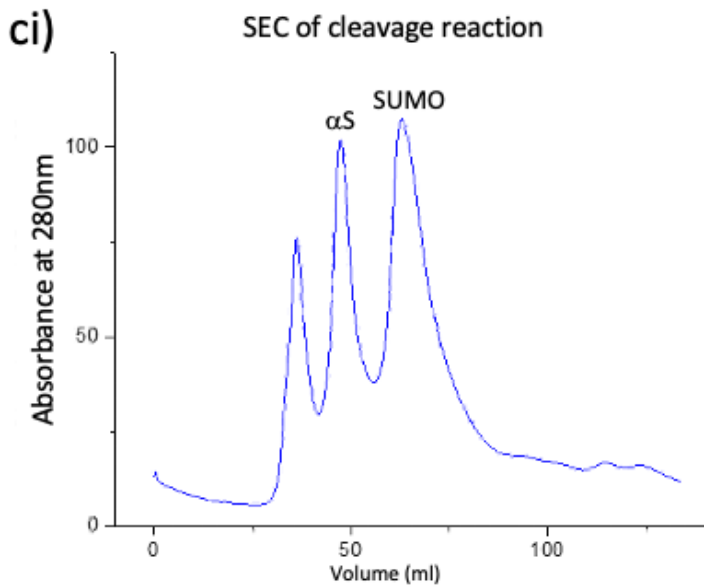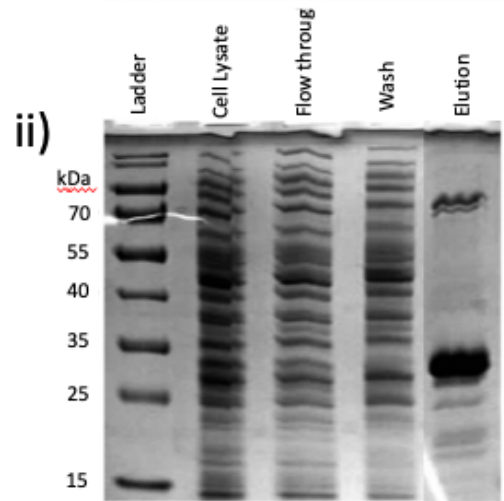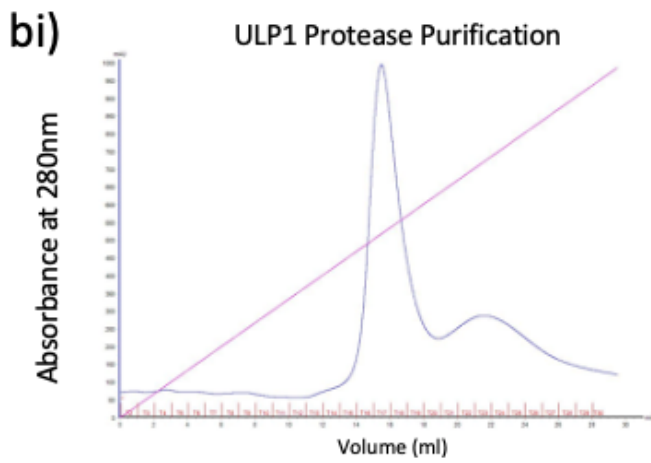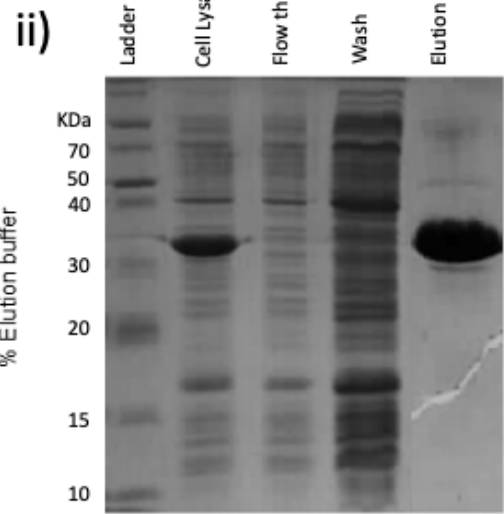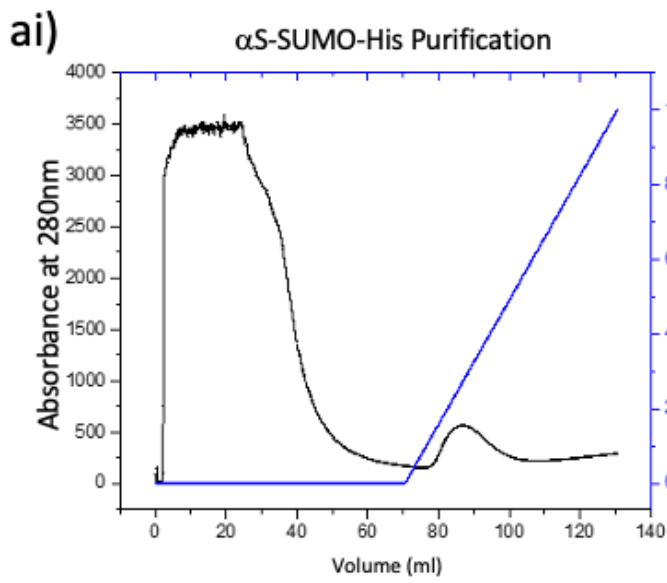
Absorbance of the reduced formazan was measured at 590 nm using an absorbance plate reader (BioRad) and cell viability was expressed as the percentage of MTT absorbance relative to equivalent volume of PBS buffer control. For the % toxicity readings, 0% toxicity referred to the MTT absorbance for the PBS control.

3.3 Results and Discussion

Alpha-Synuclein Production and Purification

Purification by αS-SUMO-His / ULP1 Protease Method

αS was purified using the Alpha-Synuclein-SUMO-His / ULP1 Protease Method, although the yield per litre was low ($\approx$ 2 mg / lt), and the protocol required the purification from two separate protein grows, and therefore took a considerable amount of time. Overall, this protocol was not very efficient. The αS produced using this method contained additional amino acids on the N-terminus (AS), and on the C-terminus (GAP) (See table 18). Therefore, the behaviour of this protein may be abnormally affected, and not accurately represent the true misfolding of wt αS.
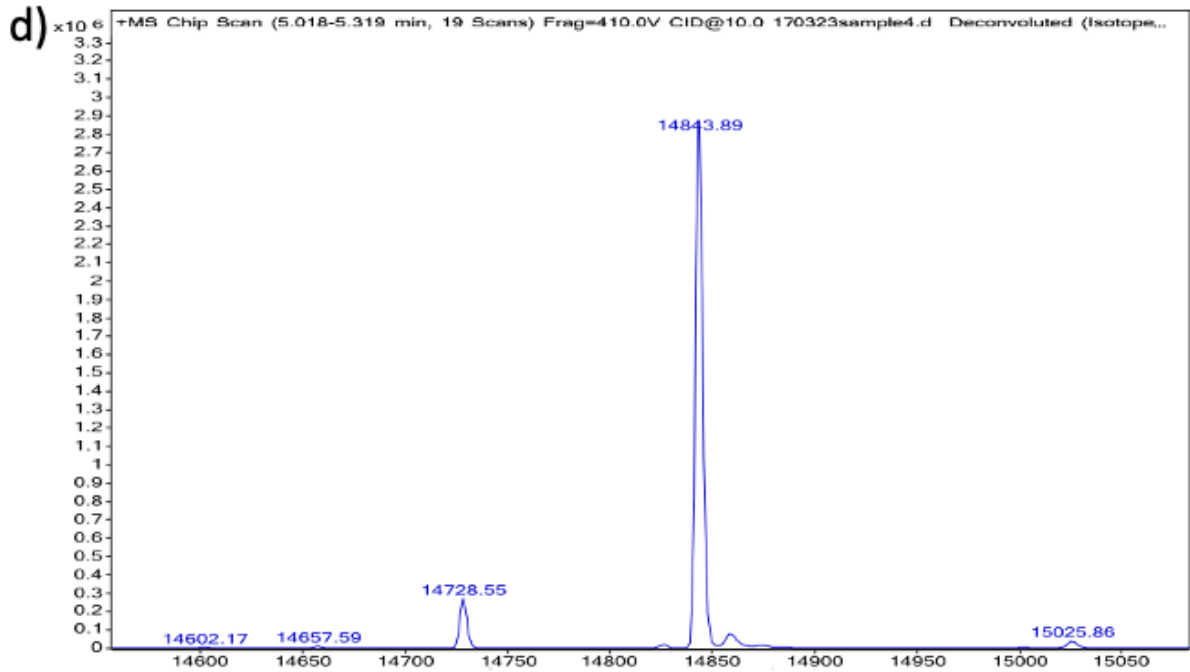
ai) αS-SUMO-His Purification

ii) [gel image: Ladder, Cell Lysate, Flow through, Wash, Elution]

bi) ULP1 Protease Purification

ii) [gel image: Ladder, Cell Lysate, Flow throug, Wash, Elution]

ci) SEC of cleavage reaction

ii) [gel image: Ladder, αS, SUMO]

65

Figure 3.6: αS-SUMO-His / ULP1 Protease Method a) i) Elution Profile and **ii)** SDS-PAGE gel showing the purification of Alpha-Synuclein-SUMO-His. **b) i)** Elution Profile and **ii)** SDS-PAGE gel showing the purification of ULP1 protease. **c) i)** SEC chromatogram of cleavage reaction mixture separating Alpha synuclein-SUMO-His (peak1), cleaved alpha synuclein (peak 2), SUMO-His (peak 3) and ULP1 Protease following cleavage reaction with ULP1 ii) SDS-PAGE gel showing corresponding bands to SEC peaks **d)** De-convoluted Mass spectrum of purified Alpha-Synuclein from the Alpha-synuclein-SUMO-His/ULP1 Protease method, using Q-TOF mass spectrometer. A peak at 14843.89 can be seen corresponding to the [αS + H]⁺ daughter ion of the purified alpha-synuclein (average mass 14842.542)

Purification by αS-Thrombin-His / Thrombin Method

Pure αS was produced using the αS-Thrombin-His / Thrombin Method and gave a reasonable yield per litre (≈ 10 mg/l). The protocol was relatively simple and straight forward, and the αS could be purified from the cell lysate in a couple of days. This was aided by the fact that purified Thrombin could be procured relatively cheaply (SIGMA), therefore did not need to be grown and purified separately. The slow step was the required overnight cleavage of the thrombin-His tail. The αS produced using this method contained additional amino acids on the N-terminus (SH), but no additions to the C-terminus (See table 19). This may abnormally affected behaviour of this protein, and not truly represent the true misfolding of wt αS.
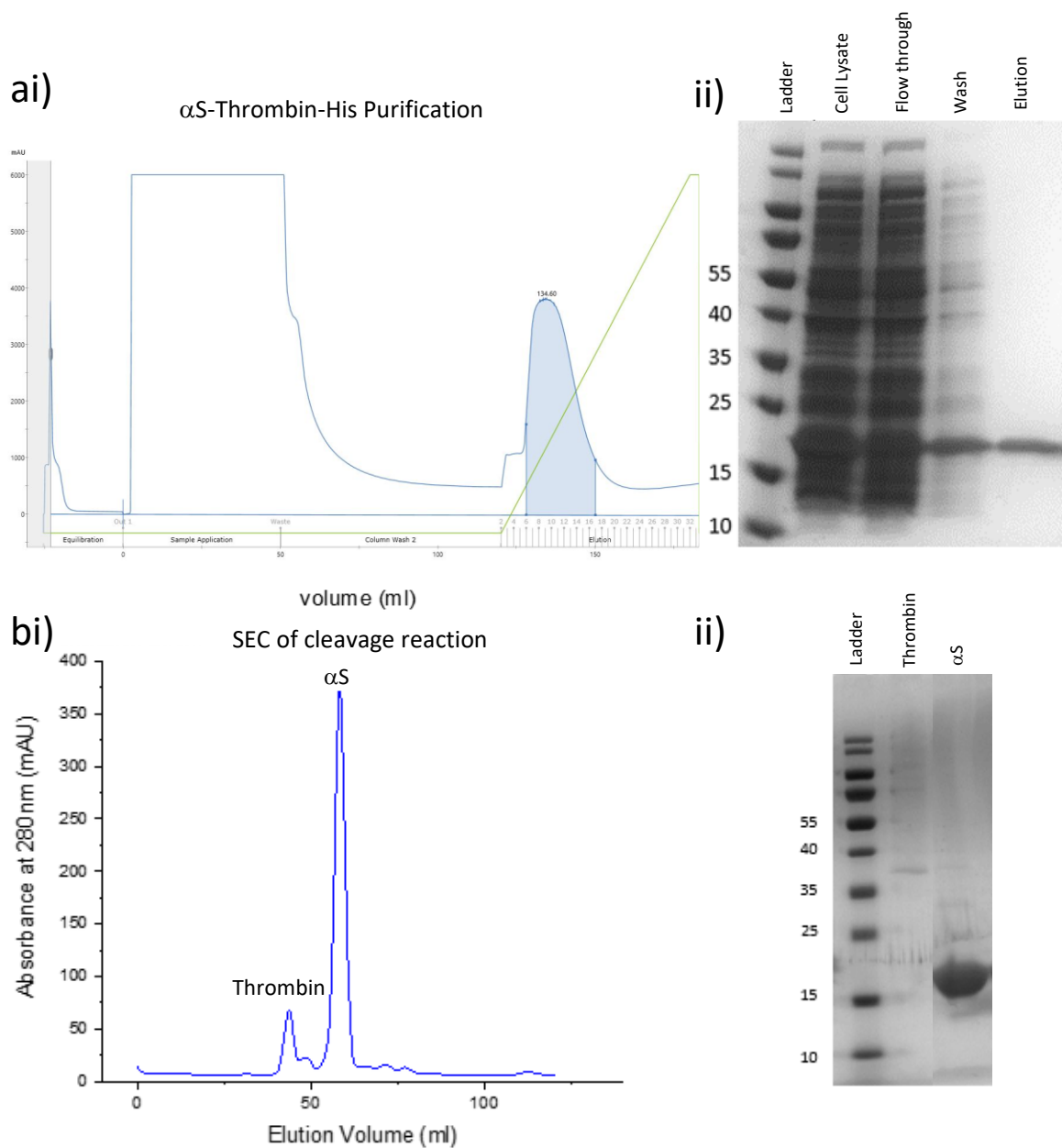
Figure 3.7: αS-Thrombin-His / Thrombin Method a) i) Elution Profile and **ii)** SDS-PAGE gel showing the purification of αS-Thrombin-His **b) i)** SEC chromatogram following the cleavage reaction, separating thrombin (peak 1) from the cleaved αS (peak 2). **ii)** SDS-PAGE gel showing the separated thrombin and the final purified αS.

Human wild-type αS pET21a Method

Pure αS was produced using the wild type αS pET21a Method and gave a high yield per litre (≈ 20 mg / l). The protocol was simple and straight forward, and the αS could be purified from the cell lysate on the same day. The αS produced using this method contained no additional amino acids on the N-terminus, or on the C-terminus (See table 19). Therefore, the behaviour of this protein should accurately report the true misfolding of wt αS.
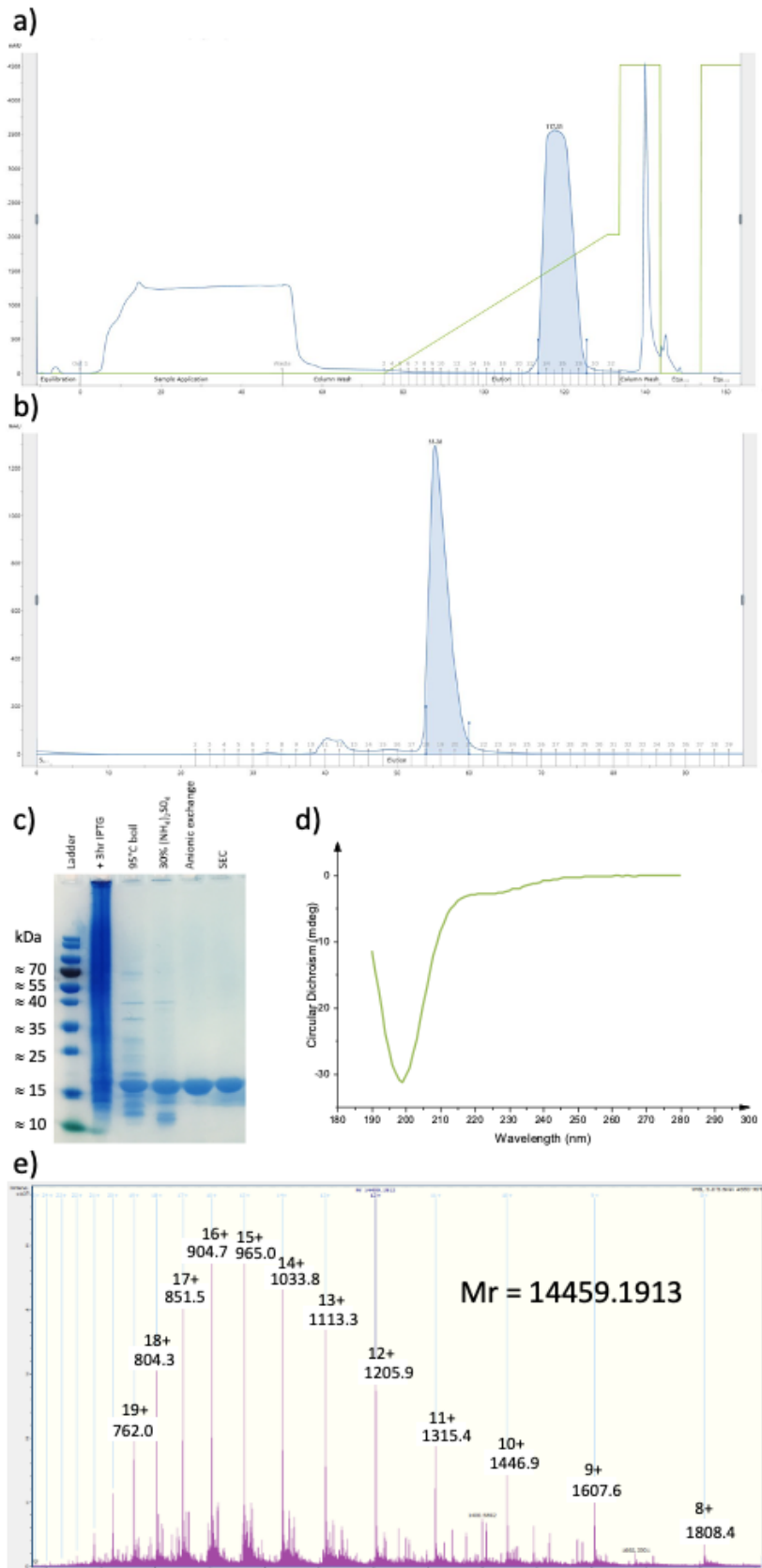
Figure 3.8: wt αS pET21a Method a) Hi-Q anionic exchange elution profile. b) SEC monomerization and buffer exchange chromatogram **c)** SDS-PAGE gel showing an overview of the entire purification protocol. **d)** Far-UV circular dichroism spectra of the purified αS showing that the monomeric αS is in a random coil conformation. **e)** De-convoluted mass spectrum, showing a mass of the protein of 14459 m/z, representing the mass of wt Human αS (1-140).

Comparing αS production methods

Of the three methods explored for αS production, the Human wild type αS pET21a method was by far the most superior for several reasons. This method was the quickest of the three methods, as the purification protocol could be performed in a single day. The yield was also much higher in comparison to the two alternative methods, and the final purified αS did not contain any addition amino acids on the C, or N-Terminus, therefore more representative of the protein found in the brain.

Method	αS-SUMO-Histag fusion	αS-Thrombin-Histag fusion	αS alone
Yield	≈ 2 mg/lt	≈ 10 mg/lt	≈ 20 mg/lt
Extra N-terminal amino acids	AS	SH	N/A
Extra C-terminal amino acids	GAP	N/A	N/A
Days to Purify	2	2	1

Table 3.15: Overview of the three aS production methods used.

For the experiments performed within this PhD only αS purified from the Human wild type αS pET21a method was utilized.

Optimising αS Cell Toxicity Assays

Varying PBS volumes for different time points

The effect of PBS volumes added to undifferentiated SH-SY5Y human neuroblastoma cells grown in a 96 well plate, in 100 μL culture volumes, was investigated, as a control, to determine how much sample volume could be added to the cell cultures, in PBS buffer (pH7.4), without influencing the viability of the cultured cells for the duration of the assay.

It was determined that up to 45 µl of PBS (pH 7.4) could be added to the cultured cells for 24 hours without having a negative effect on their viability, as measured by MTT reduction. Therefore, αS in solution in PBS up to a volume of 45 µl (pH 7.4) can be added to the wells to determine the optimal conditions for the viability assays.
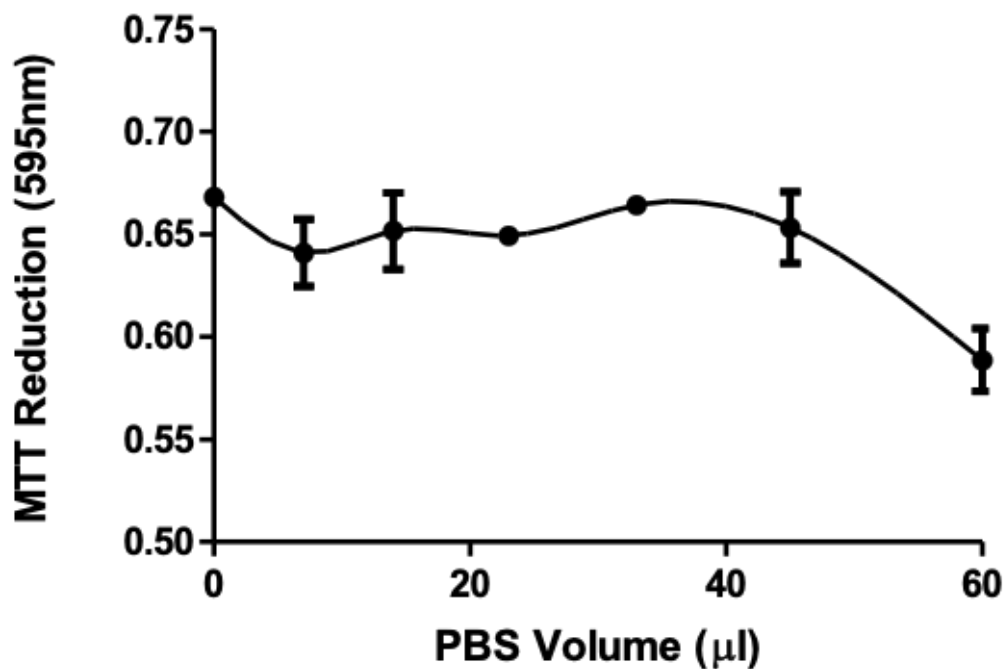

Figure 3.9: Different volumes of PBS buffer (pH 7.4) were added to cultured SH-SY5Y cells in a 96 well plate with initial well volume of 100 µl to determine the volume of PBS buffer can be added to the cells without having a negative impact on viability. Results are a combination of different experiment controls, with up to 3 repeats per well, and show that up to 45 µl of PBS (pH 6.4) can be added to the wells without affecting viability as measured by MTT assay up to 24 hours. The y-axis represents the absorbance reading at 595 nm, measuring the conversion of MTT into purple formazan.

Inducing Cell toxicity with fOligomers

To produce oligomers from fibrils, fOligomers, monomeric αS was first matured into fibrillar aggregates using a Teflon stirring bar as per previously published methods (Kaufmann et al., 2016). Far-UV circular dichroism was performed on the aggregated fibril mixture to confirm that complete conversion of random coil monomeric αS had converted into β-sheet αS fibrils.
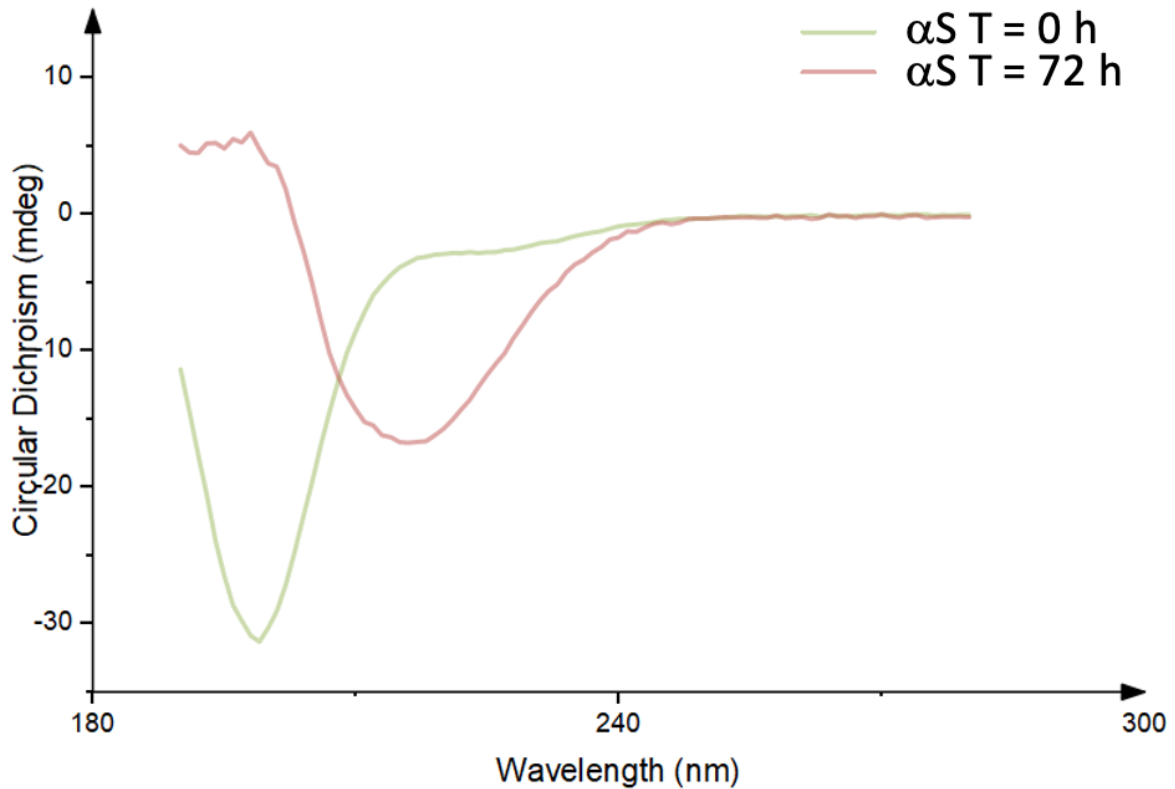
Figure 3.10: The αS monomer before aggregation shows a random coil spectra (green). The αS is seen to be fully converted to beta-sheet fibril seeds (red) after 400 μM αS was stirring at 40°C with a teflon bar at 1500rpm for 72 hours.

The aggregated αS fibril mixture was then subjected to sonication to fragment the fibrils and lead to the formation of some oligomeric species, termed fOligomers (oligomers produced from fibrils). The insoluble fibril aggregates were then removed from the solution by ultra-centrifugation, leaving behind a solution of soluble oligomers and monomers. These were separated by SEC to collect a solution of pure oligomers.
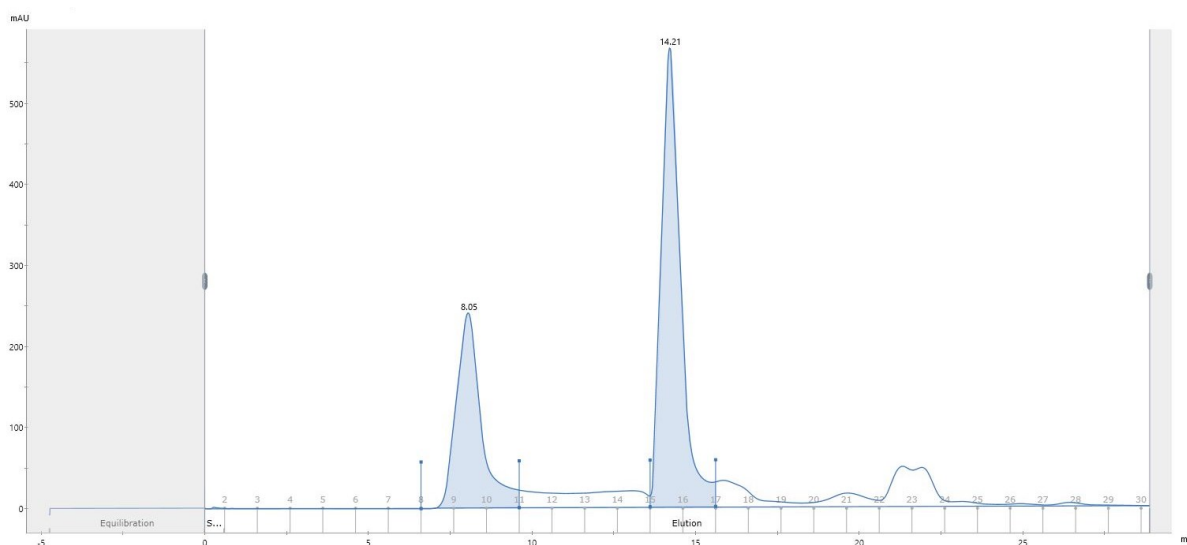
Figure 3.11: SEC chromatogram of the solution containing αS fOligomers and αS monomers. The fOligomers can be seen to elute at about 8 ml elution volume, and the monomer peak is seen to elute at about 14.2ml elution volume. The oligomer fraction was collected.

Multiple runs collecting the oligomer peak were combined and concentrated. The resulting concentration of the fOligomer solution was measured by absorbance at 280 nm to be 14.3 μM.

The fOligomer solution was added to cultured SH-SY5Y cells, of 80% confluency, in triplicate to give a final fOligomer concentration of 0, 0.4, 2 and 4 μM. Equivalent volumes of PBS solution was added to separate wells in triplicate as a control. The fOligomers were left to incubate on the cells for 48hrs, at 37 °C, 5% CO_2, and saturated humidity. The resulting cell toxicity was measured by MTT reduction. The fOligomers were found to be toxic to the cells in a dose dependent manner. About 20% cell death was reported with only 400 nM fOligomer concentration, similar to previously reported toxicity of oligomers on SH-SY5Y cells at this concentration (Fusco et al., 2017; Cascella et al., 2019). The maximal death measured was 32% at 4 μM fOligomer concentration. The curve appeared to flatten at 2 μM, suggesting that this may be the maximum level of toxicity achievable with αS on this cell line over this timescale, and therefore would be a good target % toxicity to achieve for the development of future cell toxicity assays.

[αS oligomers] (μM)	% toxicity compared to PBS control
0.4	20 ± 11
2	34 ± 2
4	38 ± 4

Table 3.16: % toxicity of fOligomers incubated for 48 hours on SH-SY5Y neuroblastoma cells grown on a 96 well plate at 37 °C, 5% CO_2, and saturated humidity. Cell viability was measured by MTT reduction, in triplicate, as compared to PBS control of equal volume. Error bars show standard error between the replicates.

Inducing cell toxicity with monomeric αS

The effect of incubation time on cell toxicity was investigated over a range of monomeric αS concentrations [0-300 μM], applied to cultured SH-SY5Y cells for either 24 or 48 hours. Over a 24-hour incubation period negligible cell death was recorded for any of the concentrations tested, suggesting that the monomeric αS had not aggregated into cytotoxic conformations over this time period. In contrast, at 48-hour incubation cell death, as measured by MTT reduction, was seen to increase in a dose-dependent manner, with maximum cell death of about 20% observed. This suggests that during the 48-hour incubation period some of the monomeric αS had indeed aggregated into cytotoxic oligomeric conformations, resulting in cell death. Toxicity appeared to reach a maximum and plateau at concentrations of 200 μM and above.

Previously published research has suggested that at best the αS solution will only form ~1% toxic oligomers (Ludtmann et al., 2018). Therefore, even at the highest concentration used for this experiment [300 μM], it is unlikely that the oligomeric concentration of toxic oligomers in the solution will be above 3 μM (monomeric equivalent).
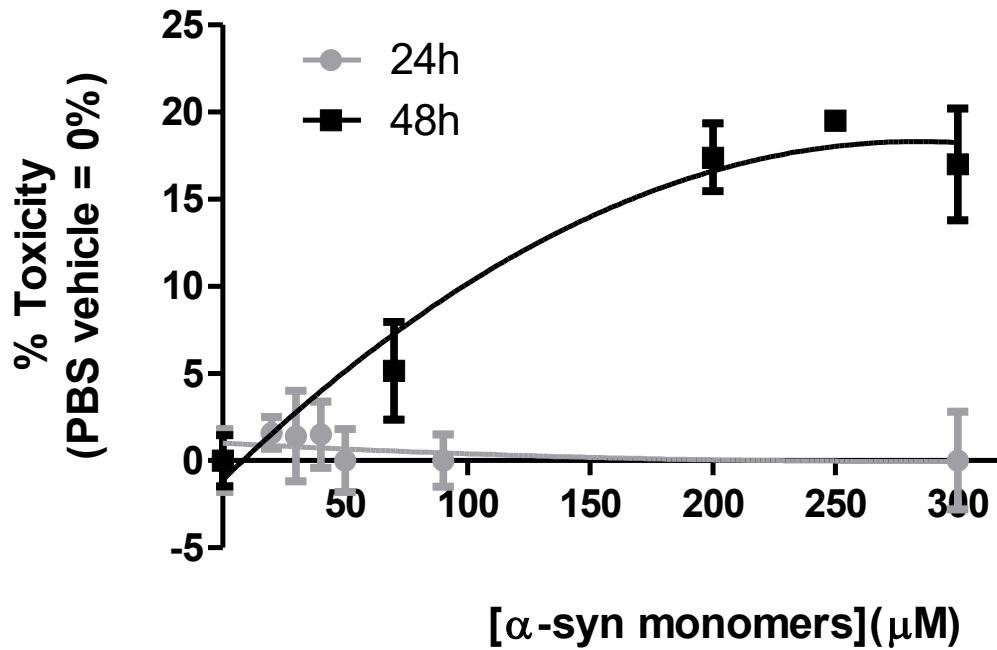
Figure 3.12: % toxicity of monomeric αS in PBS buffer pH 7.4 added to SH-SY5Y cells grown in a 96 well plate at 37 °C, 5% CO_2, and saturated humidity, and incubated for either 24 hours or 48 hours. Cell viability was measured by MTT reduction, in triplicate, as compared to PBS control of equal volume. Error bars show standard error between the replicates.

'aged' αS cell toxicity assay

Aging αS by agitation to produce oligomers for cell toxicity assays

Previously published research has shown the possibility of creating toxic αS oligomers by agitating solutions of monomeric αS (Lorenzen et al., 2014; Kaufmann et al., 2016). Therefore, a range of stock concentrations, shaking durations and times of exposure on cells were tested to determine the optimum conditions for producing αS mediated toxicity by this method.

	Condition a	Condition b	Condition c
Cell line	Undifferentiated SH-SY5Y	Undifferentiated SH-SY5Y	Undifferentiated SH-SY5Y
Culture Plate	96 well	96 well	96 well
Replicates	3	3	3
αS stock	400 μM	400 μM	200 μM
Shake speed	900 rpm	900 rpm	300 rpm
Shake time	6 hours	6 hours	24 hours
Time on cells	24 hours	48 hours	24 hours
Temperature	37 °C	37 °C	37 °C
Lyophilised αS	No	No	No

Table 3.17: Different conditions utilized to produce toxic oligomers by 'aging' αS using agitation on an Eppendorf thermomixer compact.
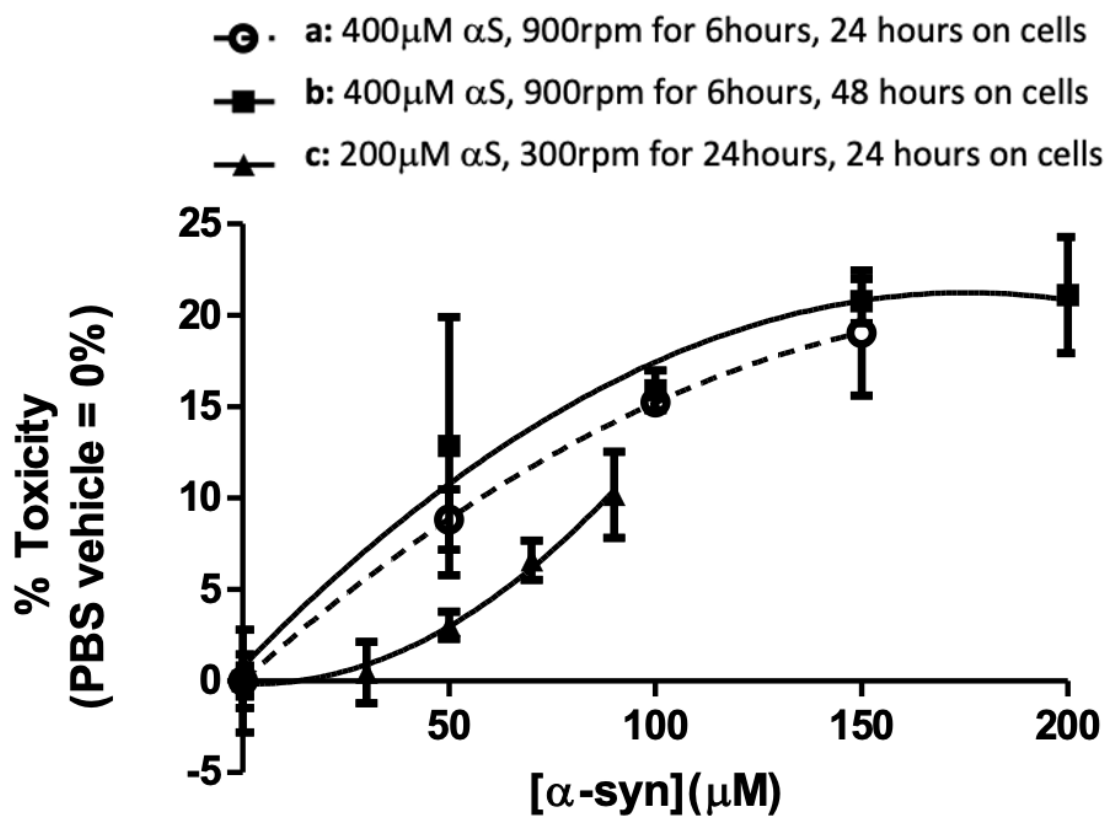
Figure 3.13: Solutions of αS 'aged' by agitation in PBS (pH 7.4) were added to 100 μl wells containing 80 % confluent SH-SY5Y cells to give final concentrations ranging from 0 – 200 μM monomeric equivalents. The plates were left incubating at 37 °C, 5% CO_2, and saturated humidity for 24 and 48 hours the test the effect on cell viability, as measured by MTT reduction, in triplicate, compared to PBS control of equal volume. Error bars show standard error between the replicates.

A toxicity dose response was seen with the 3 different shaking protocols used, with a maximum toxicity of 20% achieved (figure 3.13). The optimal methodology was to shake 400 µM αS at 900 rpm for 6 hours and incubated on the cells for 48 hours. It should be noted here that additional conditions were also explored, with varying concentrations of αS, shake speeds, and shake times, but failed to produce reliable αS toxicity, and therefore have been omitted for clarity.

Although the shaking methodology has been shown to be suitable to age αS into cytotoxic conformations, it presents some experimental limitations. Aggregating αS by shaking is very dependent on the volume used in the Eppendorf tubes, as this affects the fluid dynamics within the tube. It is also highly dependent on the specific equipment used to shake the tube at the desired settings. It would therefore be advantageous to use a more universal methodology, less reliant on a single piece of lab equipment, and with flexibility in the volume of solution to be 'aged'.

Preparing 'aged' αS Oligomers from Lyophilised Samples for Cell Toxicity Assays

Previously published research has successfully used lyophilized αS to produce oligomeric species for cell toxicity assays (Perni et al., 2017; Ludtmann et al., 2018; Perni et al., 2018; Cascella et al., 2019). The lyophilisation process has been shown to catalyse the formation of αS oligomers (Stephens, A. D. et al., 2018). Therefore, purified αS stocks were passed through HPLC (figure 3.14) to ensure purity, and to buffer exchange the protein into a solution which could be removed by lyophilization.
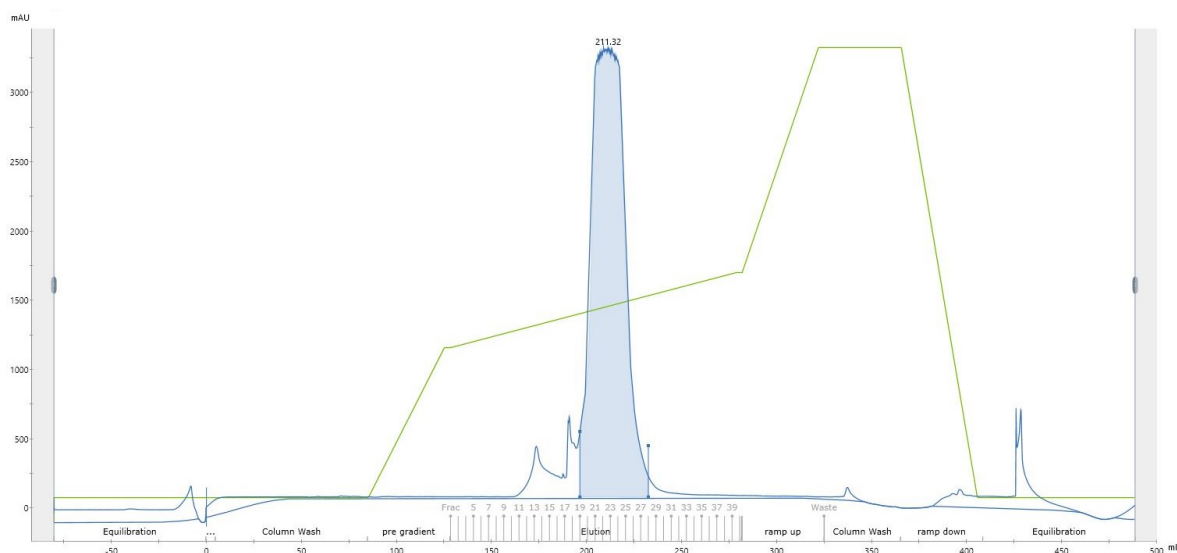
Figure 3.14: HPLC purification of Pre-purified αS by affinity to C18 column to remove buffer prior to lyophilisation for cell toxicity assays. Absorption at 280 nm used to follow the elution of aS from the c18 column (blue), by increasing concentrations of acetonitrile + 0.1% TFA (green).

SEC experiments on the pre-lyophilized αS, post-lyophilised αS and post-lyophilised αS 'aged' at 800 μM at 37 °C under quiescent conditions, demonstrated the formation of an oligomer peak following lyophilization, and an increasing of this oligomer peak, and an apparent shift towards a higher molecular weight following 'aging' (figure 3.15). The total proportion of oligomer present in the lyophilised and 'aged' αS solution was 14.6% monomeric equivalent, measured by curve integration. The oligomer peak of the lyophilised and aged sample was collected and viewed using negative stain TEM. Many different conformations of αS were present, and strikingly 'doughnut-like' oligomer structures, similar to previously reported toxic oligomeric species (Chen, S.W. et al., 2015), were observed (figure 3.15e).
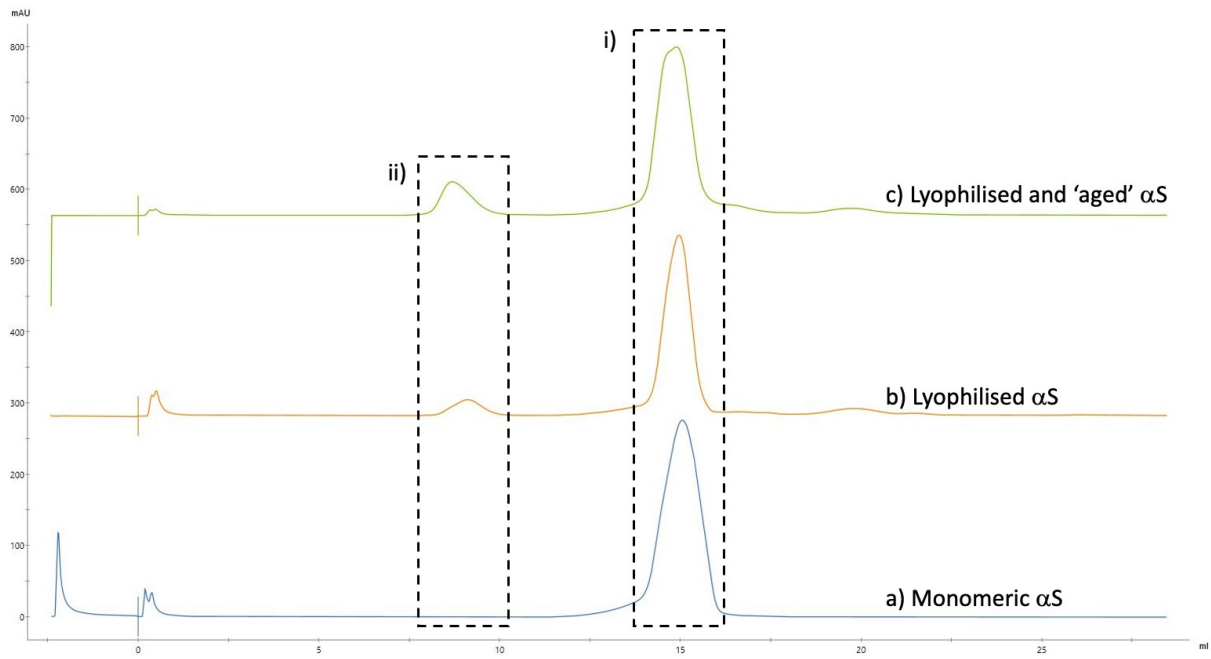
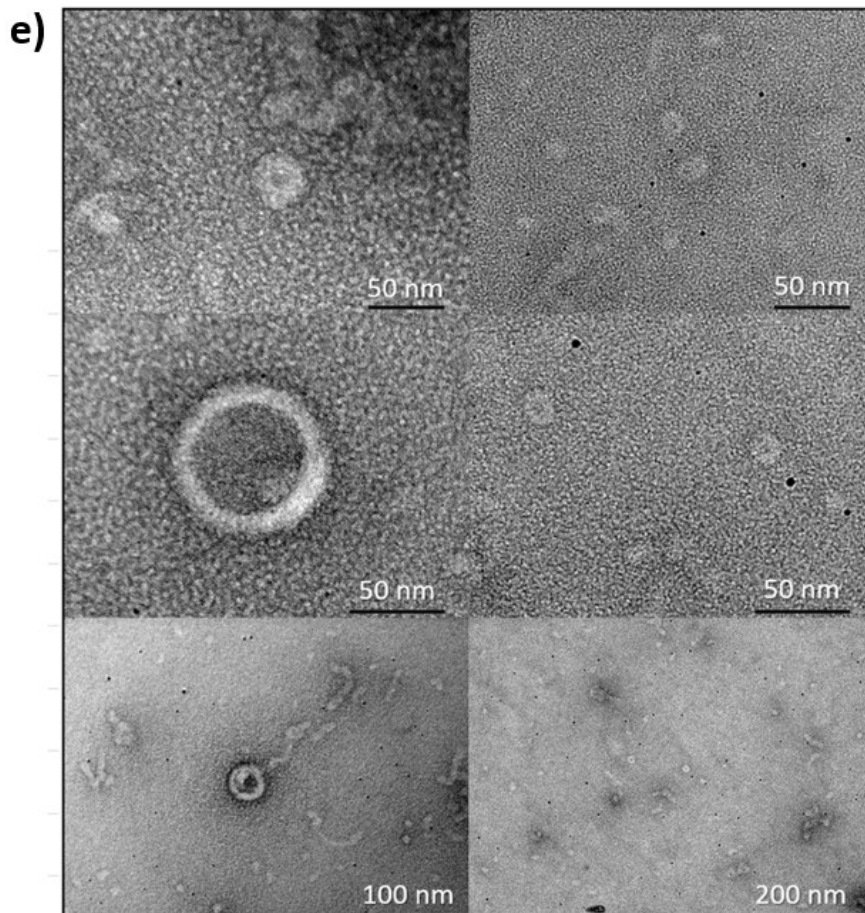| d)	Oligomer	Monomer
Monomeric αS	0.0%	100.0%
Lyophilised αS	8.7%	91.3%
Lyophilised and 'aged' αS	14.6%	85.4%

Figure 3.15: SEC elution chromatogram when 100 µl of 800 µM αS sample is loaded onto a Superdex 200 Increase 10/300 column (GE lifesciences) and run at 0.5 ml/min in PBS buffer pH 7.4, showing absorbance at 280 nm. **a) Monomeric αS** (blue) showing a clean monomer peak (i) at 15ml elution volume. **b) Lyophilised αS** (orange) resuspended in PBS pH 7.4 and incubated at 37 °C and filtered through a 0.22 µM filter showing a monomer peak (i) at 15ml elution volume, and an additional oligomer peak (ii) eluted at 9ml run volume. **c) Lyophilised and 'aged' αS** (green) resuspended in PBS pH 7.4 and incubated at 37 °C for 24hrs and filtered through a 0.22 µM filter showing a monomer peak (i) at 15ml elution volume, and an additional oligomer peak (ii) eluted at 9ml run volume. **d)** Comparison of total oligomer to monomer percentage in the protein solution, showing final oligomeric percentage of 14.6% after lyophilization and 'aging' for 24 hours in PBS pH 7.4 at 37 °C. **e)** Negative stain TEM images taken from the oligomer SEC Peak of the lyophilized and 'aged' αS (green), that appear to show doughnut like oligomer structures similar to those previously reported (Chen, S.W. et al., 2015) (see figure 3.1).

The lyophilised and 'aged' (24 hours, under quiescence, at 37 °C) αS solution was added to SH-SY5Y cells grown in a 96-well plate to 80% confluency and left to incubate for 24 hours. Cell toxicity was measure by MTT reduction and showed a dose dependent toxicity. The maximum death rate achieved was 19.5% at 120 µM αS, monomeric equivalent.
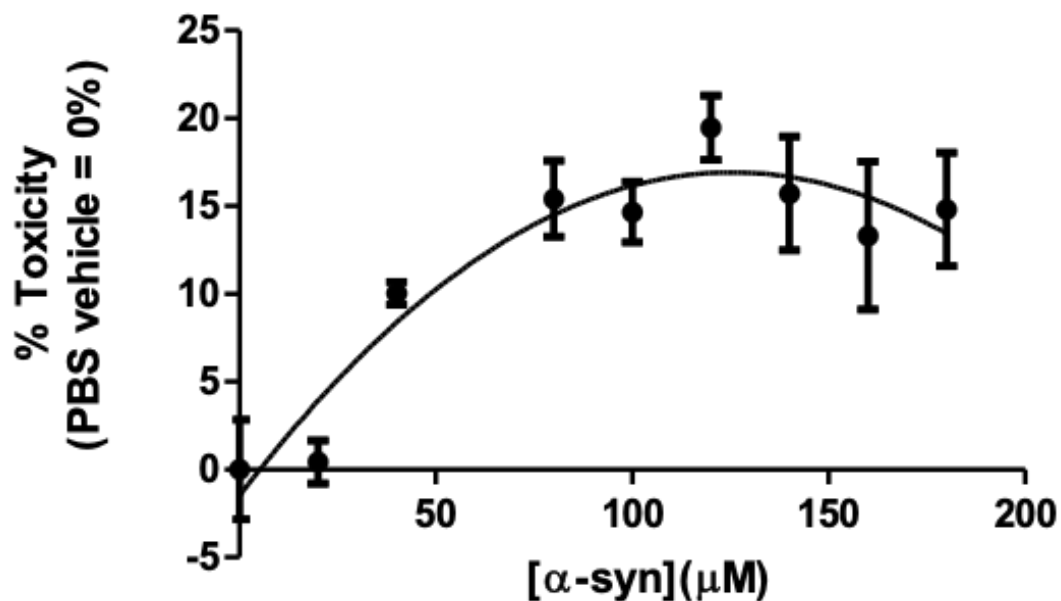

Figure 3.16: % toxicity measured by MTT reduction when 800µM stock of lyophilised αS was 'aged' for 24 hours at 37 °C, filtered using a 0.2 µm SPARTAN Filter unit (Whatman, GE Healthcare Life Sciences), and added to 100 µl wells containing 80 % confluent SH-SY5Y to give final concentrations ranging from 0 – 180 µM monomeric equivalents. The plates were left incubating at 37 °C, 5% CO_2, and saturated humidity for 24 hours before performing cell viability assay, as measured by MTT reduction, in triplicate, as compared to PBS control of equal volume. Error bars show standard error between the replicates.

Comparing this data to when the αS is aged by agitation it can be seen that a similar dose response is achieved suggesting that both methods can produce toxic αS oligomeric species capable of causing equivalent levels of cell death in undifferentiated SH-SY5Y cells.
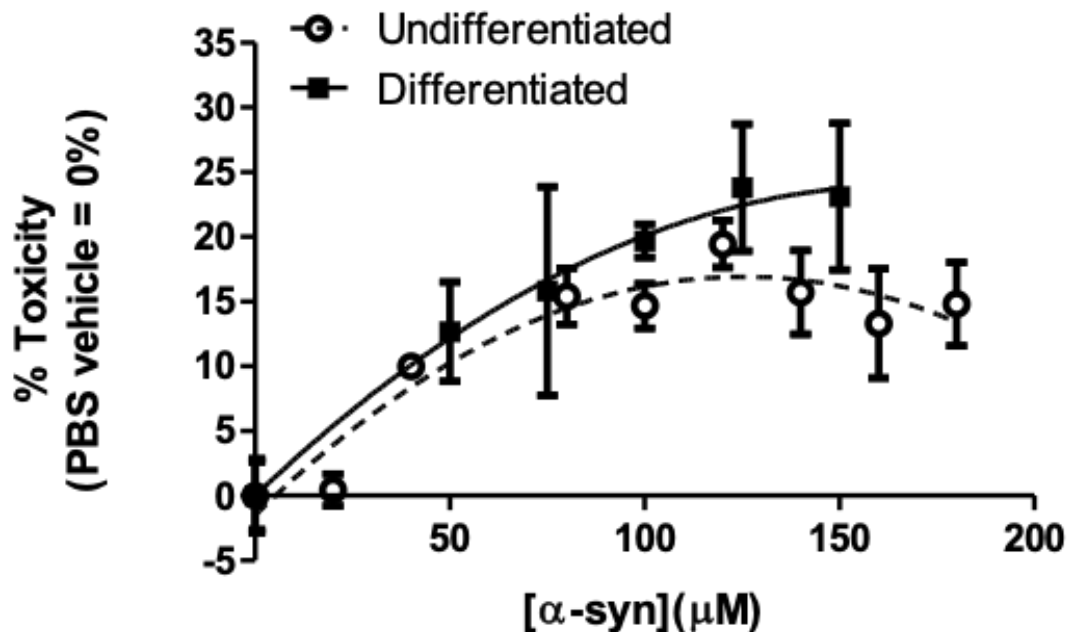

Figure 3.17: % toxicity measured by MTT reduction comparing when αS solutions are 'aged' by agitation of 400 μM solution at 900 rpm and 37 °C for 6 hours vs 'aging' by lyophilisation and incubation at 800 μM under quiescence for 24 hours at 37 °C. Following addition of the aged αS the plates were left incubating at 37 °C, 5% CO_2, and saturated humidity for 24 hours before performing the MTT viability test.

Comparing the Sensitivity of Undifferentiated and Differentiated SH-SY5Y Cells to αS-Mediated Toxicity

Previous reports investigating amyloid-β toxicity on cultured SH-SY5Y human neuroblastoma cells have shown that these cells show a higher degree of toxicity when they have been differentiated to a phenotype more resembling that of mature neurons (Krishtal et al., 2017). We therefore investigated the effect of adding increasing concentrations of lyophilized 'aged' αS to both undifferentiated and differentiated cell cultures to determine if differentiation increased the cellular susceptibility to αS mediated toxicity.
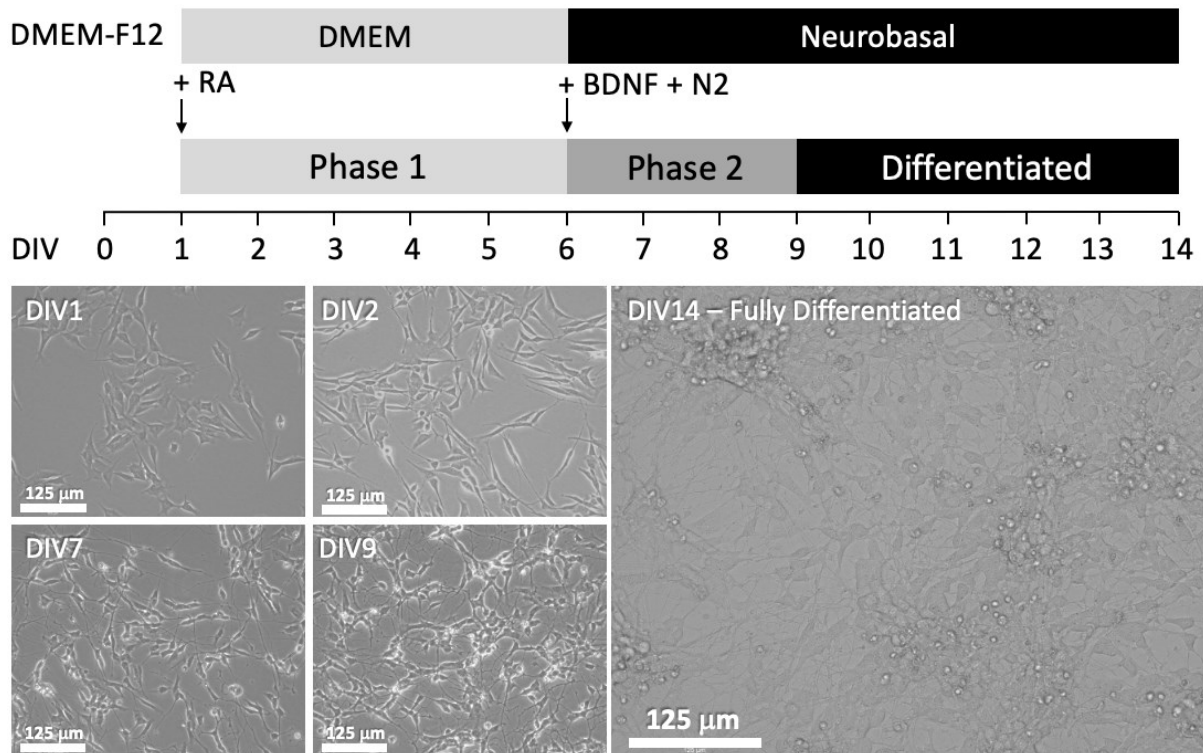
Figure 3.18: Light microscopy images of the SH-SY5Y cells taken at different stages throughout the differentiation protocol. Time measured as Days In Vitro (DIV).

Throughout the differentiation protocol the cells were monitored by light microscopy looking for the formation of dendrites, axons and connections between adjacent cells to ensure that differentiation had occurred by DIV14 as compared to the undifferentiated cells at DIV1 (figure 3.19). The differentiated SH-SY5Y cells showed no significant difference to αS toxicity, reaching a maximum of about 24 % toxicity at an αS concentration of 125 μM, as compared to the undifferentiated SH-SY5Y which reached a maximum of about 20 % at 120 μM. The toxicity appears to plateau at around 100-120 μM. This could be because at higher concentrations the αS is more rapidly converted from toxic oligomers to less toxic fibrils, therefore the toxic oligomers may not persist in the solution for as long before conversion to fibrils. The slight increase in susceptibility between differentiated and undifferentiated neurons may be accounted for by the fact that the undifferentiated neurons are still dividing in the culture, due to the presence of the F-12 supplement in the media, which was not included in the differentiated media. Undifferentiated cells do not have mature synapses and therefore are much less dependent on physiological processes involving αS. The differences only become apparent at concentrations of about 100 μM and above.
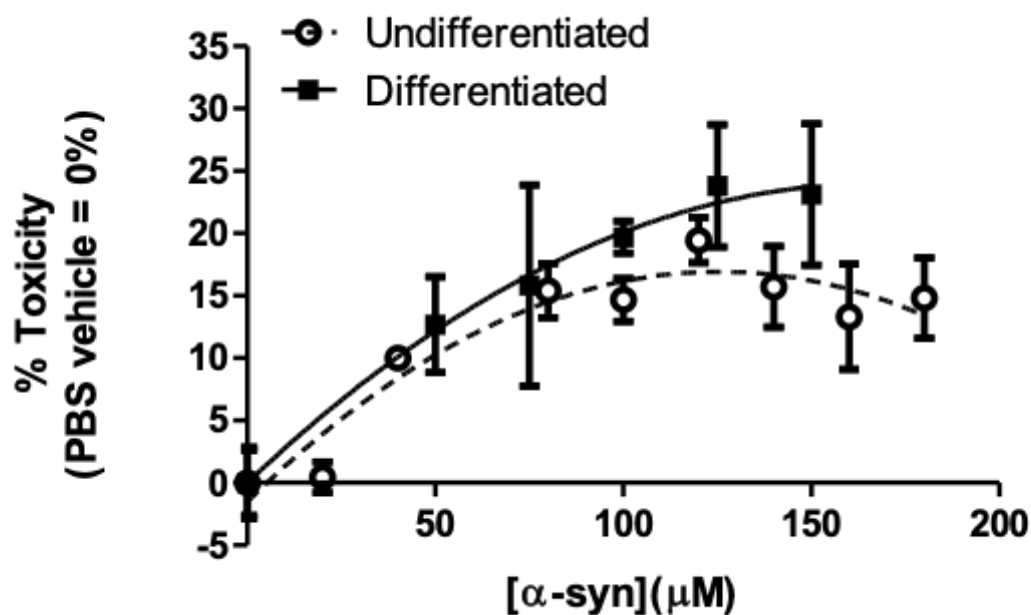
Figure 3.19: % toxicity comparing undifferentiated and differentiated SH-SY5Y cells following the addition of αS 'aged' by lyophilisation and incubation at 800 μM under quiescence for 24 hours at 37 °C. Cell viability was measured by MTT reduction, in triplicate, as compared to PBS control of equal volume. Error bars show standard error between the replicates.

Although the differentiated neurons show a slightly increased susceptibility to αS, at higher concentrations, the process of differentiation is complex and more time consuming compared to using undifferentiated cells. In addition, SH-SY5Y cells need to be differentiated in 24 well plates, as opposed to 96 well plates, and therefore much larger amounts of αS starting material is required, and less conditions can be performed simultaneously. Considering the above, the undifferentiated cells represent a simpler and more cost-effective screening platform for studying αS toxicity.

3.4 Conclusion

Of the three different methods for producing αS explored here, it is clear that the best for the production of αS was the method producing wild type αS, with no additional amino acids on the N, or C-terminus, utilizing the pET21a plasmid. Not only did this produce the most accurate representation of αS for *in vitro* experiments, it was also the fastest of the methods, and gave the highest yield. Therefore, this is the αS production method that will be utilized for the experiments presented within this PhD thesis.

As previously reported, purified oligomers induced cell toxicity at low concentration (table 3.16), confirming the basic suitability of the SH-SY5Y cells to measure αS mediated cytotoxicity. Variations of previously reported protocols to produce toxic oligomeric species did so in a dose-dependent manner, and using lyophilised αS, aggregated at high concentration under quiescent conditions, gave the most reproducible results, with increased flexibility on equipment required and aggregation volume (figure 3.16). With this method the addition of 100 μM αS induced the maximum levels of cytotoxicity, corresponding with the concentration of αS reported in dopaminergic neurons in the brain (70-140 μM) (van Raaij et al., 2008). From previously published research it is likely that only about 1% of this aged αS solution will be in the form of toxic oligomers (Ludtmann et al., 2018), in the region of 1 μM toxic oligomeric species, consistent with the toxicity resulting from the addition of low micromolar concentrations of preformed fOligomers (table 3.16).

Although differentiated SH-SY5Y cells did show some increase in sensitivity to aged αS, the method of differentiation was complicated and time consuming, compared to using undifferentiated cells. The limited increase in toxicity therefore did not warrant the routine use of differentiated SH-SY5Y cells for measuring αS toxicity. Therefore, the cell toxicity assays in this thesis utilised undifferentiated SH-SY5Y cells treated with lyophilised αS 'aged' at 800 μM for 24 hours under quiescent conditions and at 37 °C

Chapter 4:

A PCA Derived Peptide (4554W) Inhibits Primary Nucleation of α-Synuclein in the Presence of Lipid Vesicles

4. 1 Abstract

Aggregation of α-Synuclein (αS) is widely regarded as a key factor in neuronal cell death, leading to a wide range of synucleinopathies that includes Parkinson's Disease. Development of therapeutics has therefore focused on inhibiting aggregation of αS into toxic forms. One such inhibitor, based on the preNAC region αS$_{45-54}$ (4554W), was identified using an intracellular peptide library screen, and subsequently shown to both inhibit formation of αS aggregates while simultaneously lowering toxicity. Subsequent efforts have sought to determine the mode of 4554W action. In particular, and consistent with the fact that target and peptide are co-produced during screening, we find that the peptide inhibits primary nucleation of αS but does not modulate downstream secondary nucleation or elongation events. These findings hold significant promise towards mechanistic understanding and development of molecules that can module the first steps in aggregation towards novel treatments for Parkinson's disease and related synucleinopathies.

4.2 Introduction

Synucleinopathies are caused by the misfolding and subsequent aggregation of the protein α-Synuclein (αS), a 140- residue protein, highly expressed in neuronal synapses (Takeda et al., 1998), and the main protein constituent found in Lewy bodies (Goedert, Jakes and Spillantini, 2017); the pathogenic hallmark of PD. The pathway of αS misfolding is highly complex, and not entirely understood. However in synucleinopathies, αS is seen to ultimately aggregate into extended β-sheet amyloid fibrils with the potential for a number of different polymorphisms (Li, B.S. et al., 2018; Meade, R. M., Fairlie and Mason, 2019). Moreover, during the course of amyloidogenesis αS is able to form a variety of pre fibrillary oligomers, which can be on or off the pathway to fibrils (Lorenzen et al., 2014; Chen, S.W. et al., 2015; Pieri, Madiona and Melki, 2016; Fusco et al., 2017; Cascella et al., 2019). Some of these oligomers and their conformers may be functionally relevant to the disease, with some appearing to be highly toxic to cells (Fusco et al., 2017). Whilst there is increasing evidence regarding precisely which molecular species might be critical for inducing αS toxicity, a number of unanswered questions remain. Pinpointing the precise molecular species responsible for αS driven toxicity

and either inhibiting their formation or sequestering them represents a promising mechanism towards the treatment of PD and synucleinopathies in general.

Due to the complex nature of the protein-protein interactions (PPIs) formed during αS aggregation, ranging from monomeric to a wide variety of conformers and oligomers, it has proven extremely difficult to rationally design effective small molecule inhibitors to modulate the process, leading many to determine this condition as undruggable (Rastogi et al., 2019). Identification of small molecules is difficult for amyloids owing to the requisite number of interactions needed to block these shallow and broad PPIs and therefore to efficiently inhibit the aggregation process. Larger biotherapeutics, such as antibodies, also pose limitations due to their difficulty in traversing the blood-brain barrier (BBB) and other cell membranes to locate at required site of action within neurons. An area of emerging interest therefore has been the development of short peptide based molecules that are able to occupy the niche between small molecules and biotherapeutics (Mason, 2010; Helmer and Schmitz, 2016); being large enough to form structures that can specifically modulate PPIs by making multiple interactions that can generate the requisite affinity and selectively, and hence distinguish between conformations, or stabilize non-toxic oligomers, while being small enough to be readily modified to cross biological membranes. Peptide-based therapeutics present a number of advantages over that of small molecules in that they can *i)* make more interactions over larger surface areas and shallow binding pockets in PPIs, *ii)* avoid immunogenicity when short since they fall below the immunogenic threshold, *iv)* be more target-specific, due to more interactions, and therefore less toxic, *v)* be quickly synthesized to high purity, *vi)* be readily modified to prevent the formation of extended strand motifs that are most susceptible to protease degradation, and *vii)* be optimized to impart membrane permeability. Limitations such as low cell permeability, loss of affinity due to flexibility, high clearance rates and low oral bioavailability are now being addressed, for example via non-peptidic or cyclic modifications, cell-penetrating peptides (CPP), or lipidic appendages (Rastogi et al., 2019).

Using an in-cell derived peptide (4554W) capable of inhibiting αS toxicity by modulating aggregation (Cheruvara et al., 2015), we sought to gain further mechanistic insight by establishing where within the amyloidogenic pathway the peptide functions (Fig 4.1). To do so, aggregation experiments were performed under carefully designed experimental

conditions that sought to individually probe each of the three key processes within the aggregation pathway. In particular, the effect of the peptide was deconvoluted into *i)* changes in heterogeneous primary nucleation (Buell, Alexander K. et al., 2014; Galvagnion, C. et al., 2015; Perni et al., 2017), *ii)* changes to fibril elongation (Buell, Alexander K. et al., 2014; Perni et al., 2018), and *iii)* changes to fibril amplification/secondary nucleation (Buell, Alexander K. et al., 2014; Agerschou et al., 2019). 4554W was generated from a library based on preNAC αS_{45-54}; a region within which most early onset SNCA mutations are located, and one that has subsequently been found to feature prominently at the dimeric fibril interface for the majority of αS polymorphs identified (Meade, R. M., Fairlie and Mason, 2019; Zhao et al., 2020). Therefore, an improved understanding of the mechanism of action for 4554W could lead towards increased efficacy of treatments for αS driven pathologies, as well as other age-related diseases in which amyloids present.
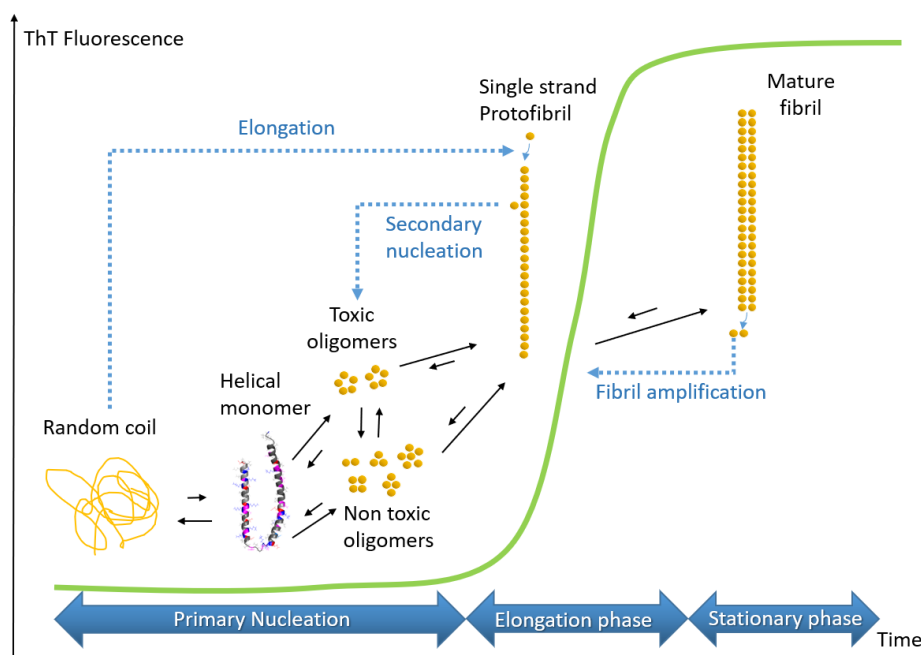

Figure 4.1: Proposed mechanism of αS misfolding from random coil to mature fibril via a population of aggregated oligomers, as followed by Thioflavin T fluorescence (green line). The steps of Primary nucleation, fibril elongation, and secondary nucleation/fibril amplification are highlighted. Primary nucleation is the dynamic equilibrium by which the random coil monomer converts into an α-helical state, which can then assemble into a population of oligomers. One or more of these oligomers may represent the cytotoxic species of αS, and one or more of these can form the kernel to seed fibril growth. Fibril elongation occurs by monomer addition to this fibril 'seed', until all free monomer exists in the energetically favourable fibril state. The fibrils can fragment leading to more nuclei for elongation, causing fibril amplification. Secondary nucleation occurs by monomers associating laterally to form nuclei which can then elongate *in situ* or dissociate to elongate independently, releasing oligomeric species which may or may not be cytotoxic.

4.3 Results and Discussion

Derivation of peptide 4554W

An intracellular Protein-fragment Complementation Screening Assay (PCA) (Pelletier et al., 1999) was previously utilised to generate the peptide inhibitor, 4554W, based on an analogue of αS_{45-54} (Cheruvara et al., 2015). This 10 residue region within αS was selected owing to the fact that it contained all but one (A30P (Kruger et al., 1998)) of the then known early onset mutations (E46K (Zarranz et al., 2004), H50Q (Appel-Cresswell et al., 2013), A53T (Polymeropoulos et al., 1997) and A53E (Pasanen et al., 2014)). An additional G51D/E (Lesage et al., 2013) mutant was discovered later, hence D/E residues were not included as options at this position within the library. The 4554W peptide was identified from 209,952 members (Fig 4.2) and demonstrated to be effective using MTT cytotoxicity assays, Thioflavin T (ThT), circular dichroism (CD) and atomic force microscopy (AFM). In particular 4554W was found to be capable of inhibiting αS fibril formation in a dose dependent manner when mixed with monomeric αS and stirred in a fluorescence cuvette, and was able to rescue PC12 cells from αS related toxicity in a dose dependent manner (Cheruvara et al., 2015).
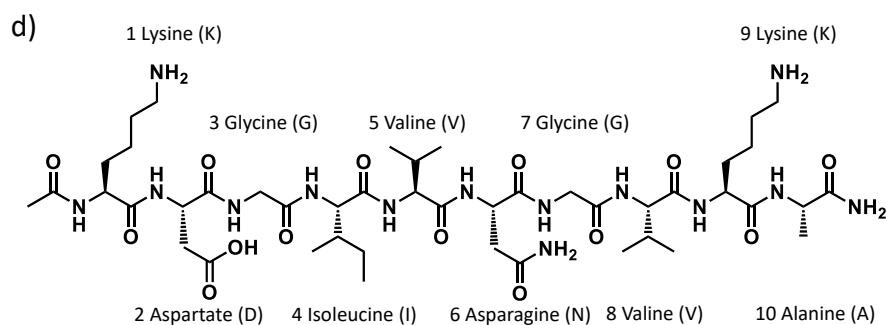
Figure 4.2: Reproduced from Cheruvara *et al.* (Cheruvara et al., 2015) showing *a)* the template region of αS consisting of residues 45 to 54 of the wild type protein. *b)* A 209,952-member library was screened using a protein-fragment complementation approach, in which those that bind to and detoxify αS result in the recombination of an essential enzyme required for cell survival. *c)* The sequence of the 4554W peptide selected at the end of the PCA assay. *d)* Chemical structure of the winning peptide showing the structural orientation of the residues.

Although encouraging, the precise point at which 4554W exerted its action upon αS aggregation remained unclear. By using specific experimental conditions to probe the aggregation pathway we have now separated this for αS into its three distinct *in vitro* processes – *i)* primary nucleation (Galvagnion, C. et al., 2015; Brown et al., 2016; Perni et al., 2017; Perni et al., 2018), *ii)* fibril elongation (Buell, Alexander K. et al., 2014) and *iii)* secondary nucleation (Buell, Alexander K. et al., 2014; Brown et al., 2016; Perni et al., 2018) (Fig 4.1). These three steps are common to all amyloidogenic pathways (Chatani and Yamamoto, 2018) and identifying which are specifically modulated by the 4554W sequence holds significant promise towards 4554W optimisation and for future rational design of aS toxicity modulators.

4554W inhibits ThT monitored αS aggregation at neutral pH with agitation

The effect of 4554W on αS aggregation was first determined by following ThT fluorescence to report fibril growth at physiological pH and temperature (pH 7.4, 37 °C). Agitation of the sample in a 96 well plate was used to promote aggregation, based on previous high throughput screening methods (Pujols et al., 2017) . In this experiment 450 μM monomeric αS was aggregated in the absence or presence of equimolar 4554W peptide, consistent with the mode of production during PCA (i.e. both αS and 4554W are co-expressed from monomer via IPTG induction and therefore prior to aggregation). This experiment was undertaken to mimic previous ThT experiments undertaken by Cheruvara *et al*. during the initial validation of the 4554W peptide (Cheruvara et al., 2015). To demonstrate robust reproducibility under modified conditions, the experiment was repeated in microtiter plate format (to reduce the amount of αS required), using shaking rather than stirring to facilitate parallel replicates, thereby increasing reproducibility across different samples.

As previously reported the 4554W peptide inhibited aggregation of αS (Cheruvara et al., 2015). In the conditions described above, monomeric αS was found to produce the expected

sigmoidal aggregation profile with the elongation phase reached at ~18 hours, and the stationary phase reached after ~30 hours (Fig 4.3a). In contrast, in the presence of 4554W at a stoichiometry of 1:1 the lag phase significantly increased, and the time taken to reach the elongation phase was delayed to ~50 hours. The time taken to reach stationary phase was increased to ~65 hours. In the presence of 4554W a small rise in ThT fluorescence was observed between ~15–50 hours, suggesting that the peptide may act to inhibit the progression of a partially aggregated αS species. Once the exponential phase was reached however, the rate of aggregation was similar to that of αS alone (i.e. gradient is unchanged). Based on previous aggregation models monitored using this method (Cohen et al., 2015), an increased lag phase, but identical exponential growth rate would suggest that the inhibitor suppresses primary nucleation at the earliest stages of the aggregation process, but does not inform upon additional potential points of inhibition (Cohen et al., 2015).

CD spectra taken at the start and end of the experiment (Fig 4.3b) show complete conversion from random coil to β-sheet in the absence of 4554W. In the presence of 4554W, the β-sheet signal is less intense, and a significant amount of signal associated with a random coil is still visible.
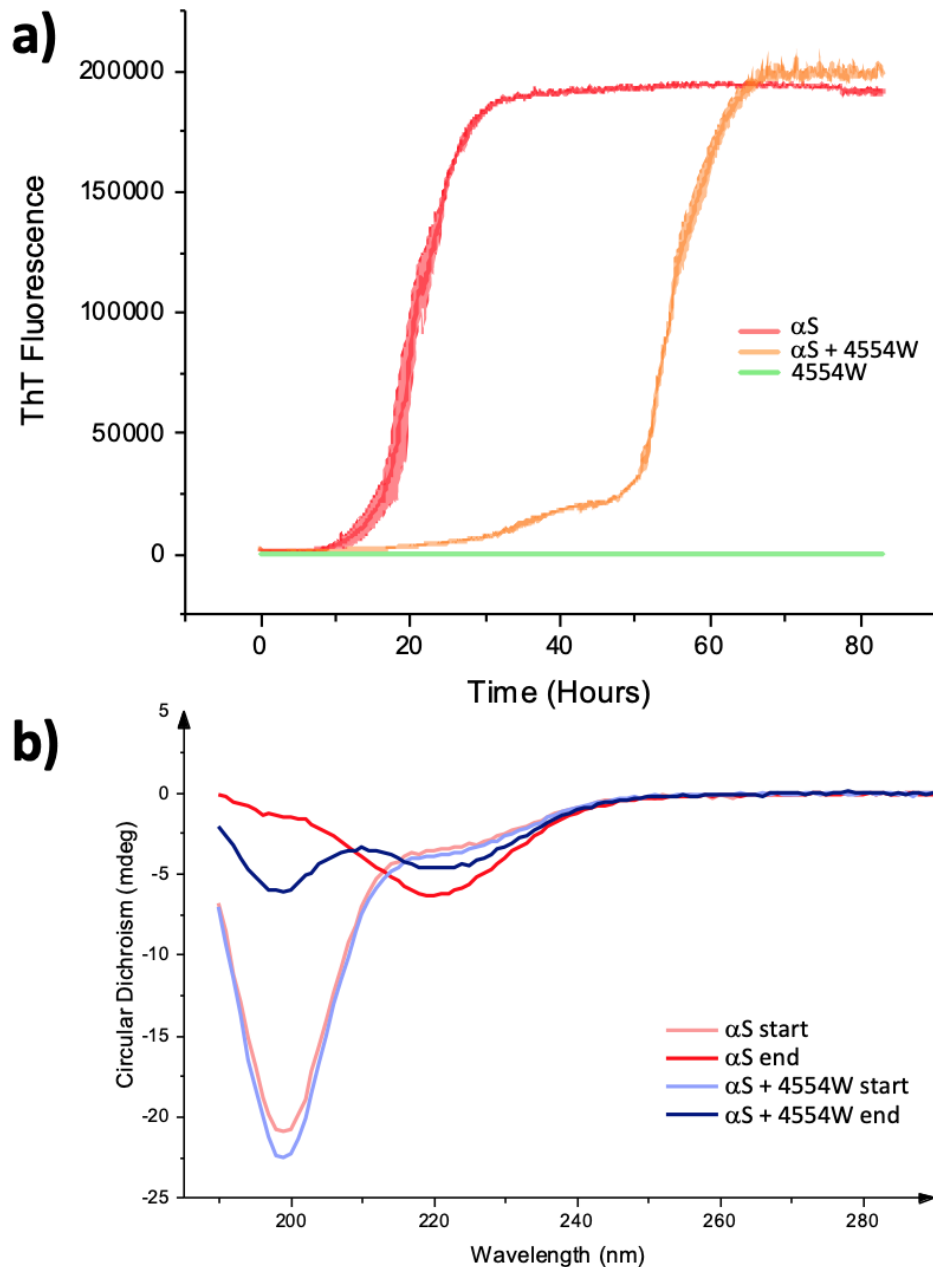
Figure 4.3: a) Effect of 4554W on continuous growth aggregation assay with shaking. Inhibition of αS aggregation with 4554W peptide was measured by monitoring the change in ThT fluorescence intensity when monomeric αS (450 μM) was incubated in the presence and absence of equimolar 4554W, and agitated (700rpm double orbital shaking) at 37°C, pH 7.4. αS alone (red) can be seen to aggregate in the standard sigmoidal pattern, whereas αS in the presence of 1:1 4554W (yellow) shows a reduced aggregation in the primary nucleation section of the graph, pushing the elongation phase to the right. 4554W alone (green) shows no aggregation in isolation. These kinetic curves are shown as an average of three repeats, showing standard error. **b)** Circular dichroism spectra scans of aS in the presence/absence of 4554W. At 0 hours the CD spectra displays a spectrum associated with a random coil conformation in the presence and absence of 4554W. However, at the stationary phase of aggregation (80 hours) aS alone display a spectrum of complete conversion to a b-sheet conformation (red). In contrast, the CD spectra at the end (80 hours) in the presence of 4554W shows a less prominent conversion to β-sheet, with presence of a random coil component remaining (blue). Samples were sonicated for 10 seconds in a sonicating water bath to ensure that sample was homogenised and would remain in the beam.

4554W Peptide Inhibits the Lipid Induced Primary Nucleation step of αS Aggregation

To probe the effect of the 4554W peptide on only the primary nucleation step, monomeric αS was aggregated in the presence of 1,2-Dimyristoyl-sn-glycero-3-phospho-L-serine (DMPS) small unilamellar vesicles (SUVs), at neutral pH (pH 6.5, 30 °C; Fig 4.4a). Under these conditions, primary nucleation has been shown to be the predominant mechanism of aggregation (Buell, Alexander K. et al., 2014; Galvagnion, C. et al., 2015; Perni et al., 2017; Perni et al., 2018). In this experiment aggregation was promoted directly from the surface of DMPS vesicles, leading to an accelerated lag phase. DMPS vesicles were chosen as a model phospholipid since they are a key component of dopaminergic synaptic vesicles, display a negatively charged headgroup, promote αS membrane binding (Meade, R. M., Fairlie and Mason, 2019), and lead to an increased local concentration of αS that accelerates primary nucleation (Galvagnion, C. et al., 2015; Galvagnion, C., 2017; Killinger et al., 2019; Fanning, Selkoe and Dettmer, 2020). Soluble αS is able to bind to DMPS lipid bilayers, leading it to adopt a distinct α-helical conformation (Fig. 4.5a), which may produce a nucleation point for aggregation. This specific αS -lipid interaction could play a key role *in vivo* by triggering the conversion of soluble αS into more toxic aggregated forms of the molecule that are associated with disease. For these experiments the concentration of monomeric αS was reduced to 100 μM, which has been proposed to represent a physiologically relevant concentration (αS is abundant in brain and estimated to exist at 70-140 μM in healthy neural cells (van Raaij et al., 2008)). Briefly, αS was mixed with 200 μM DMPS SUVs, of 30-40 nm diameter (consistent with those found in dopaminergic vesicles (Sulzer, Cragg and Rice, 2016)), and incubated under quiescent conditions. The aggregation kinetics (undertaken in triplicate) were followed by measuring ThT florescence in the presence of increasing concentrations of 4554W [0 – 1000 μM]. Under these conditions a dose-dependent inhibition of αS primary nucleation was observed (Fig 4.4a). This result is consistent with the shaking aggregation assay in the absence of lipid, again demonstrating that 4554W acts at the earliest stages of aggregation, but it does preclude additional inhibitory activity on downstream processes. Moreover, the mechanism is consistent with the mode of selection, where αS and 4554W are concomitantly expressed, potentially facilitating binding upstream of aggregation events.

The αS aggregates formed with DMPS SUVs (to probe primary nucleation) in the presence and absence of a tenfold molar excess of 4554W were next analysed by transmission electron microscopy (TEM). In the absence of 4554W the aggregates were observed to form two distinct fibril types. The most prevalent type (Fig 4.4bi) were narrow aggregates, similar to those previously described by others using AFM (Galvagnion, C. et al., 2015) and TEM (Galvagnion, Celine et al., 2019) approaches. These aggregates can be seen to emanate from the lipid vesicles, and it appears that on average two independent fibrils can grow from one vesicle of the size used for this experiment (30 - 40nm diameter). The width of these fibrils measured either ~5 nm or ~10 nm, implying that both αS protofibrils and mature fibrils are formed respectively from the lipid vesicles. A novel series of helical fibril polymorphs were also discovered in the samples viewed by TEM, in the absence of the 4554W peptide (Fig 4.4bii). These morphologies were found to be much larger than has been previously documented in mature fibril imaging and were observed in three independent aggregation experiments (as well as fresh DMPS and αS preparations) under these conditions, and have been described in detail elsewhere (Meade, Richard M., Williams and Mason, 2020). Briefly, the morphology is that of a tightly coiled helix, presumably made from β-sheet fibril aggregates. This structure appears to have grown from an initial ribbon-like structure, with a width of approximately 30-40 nm, and a repeating pitch twist of about 300-400 nm. This is in contrast to recent structures derived from ssNMR and CryoEM experiments, which typically describe a width of 5 nm or 10 nm, and a pitch of 460 Å (twister polymorph) or 920 Å (rod polymorph). The unique αS morphologies are presumably built from a fundamental fibril structure that is also produced in the presence of the DMPS SUVs (Meade, Richard M., Williams and Mason, 2020).

In the presence of 4554W there were significant changes to both the observed morphologies and the prevalence of the aggregates produced (Fig 4.4c), providing further evidence that αS aggregation had been inhibited by the presence of 4554W. The structures observed show a flexible and meandering amyloid that emanated from the lipid vesicles (Fig 4.4c). Some of these structures presented with a width of ~5 nm, suggestive of a single protofibrillar structure as described previously. (Tuttle et al., 2016). Other aggregates within the same samples, emanating from the vesicles, showed a more weaving morphology, and displayed a width of 10 nm consistent with the more mature dimeric fibril structures described by others

(Li, B.S. et al., 2018; Meade, R. M., Fairlie and Mason, 2019), but with a much reduced pitch of about 90 nm. ThT data, and corresponding TEM images taken together show that 4554W inhibits aS aggregation at the point of primary nucleation.
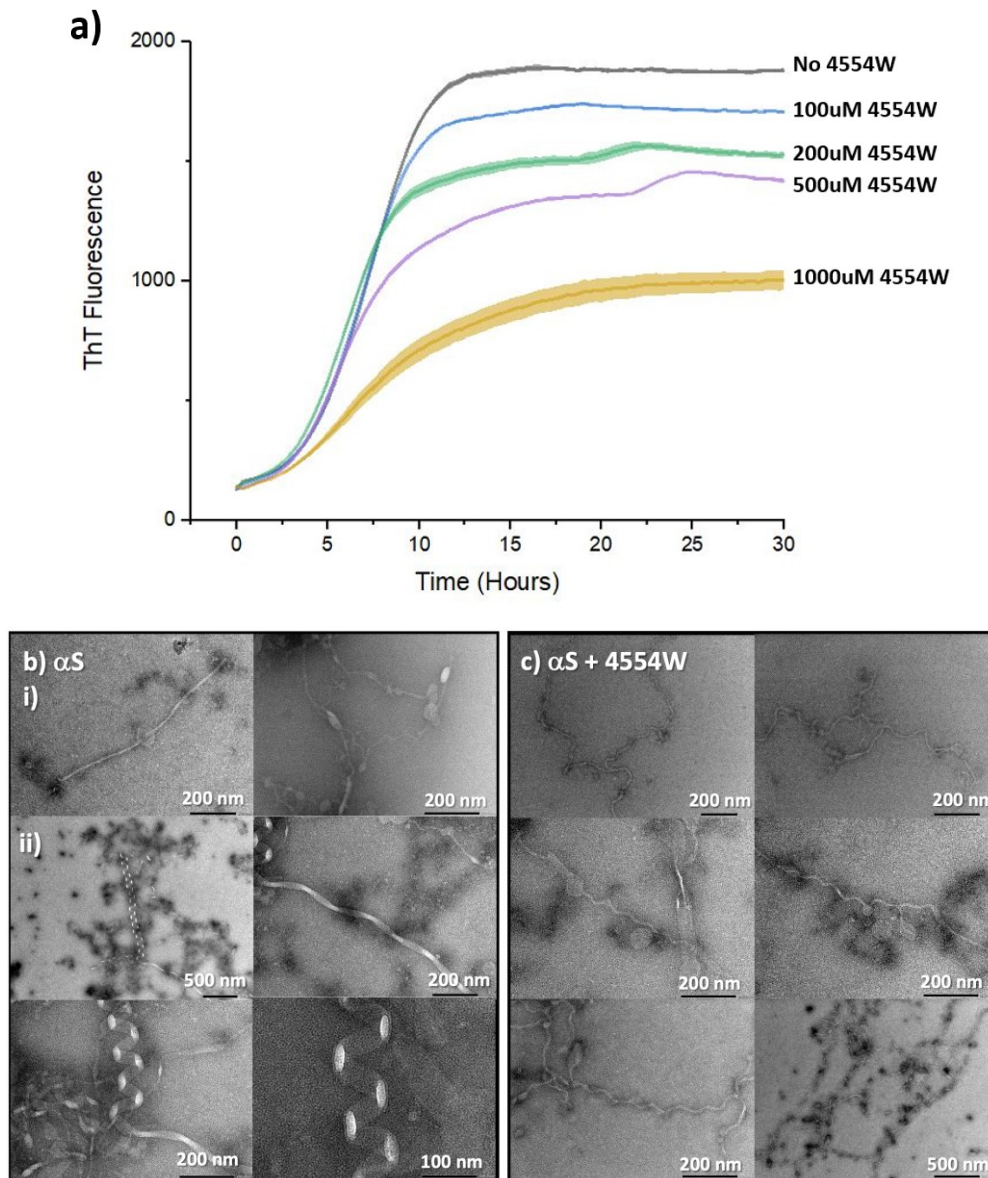

Figure 4.4: Effect of 4554W on primary nucleation. *a)* Dose dependent inhibition of lipid induced primary nucleation of αS with 4554W peptide measured by change in ThT fluorescence intensity when 100 μM monomeric αS was incubated in the presence of 200 μM DMPS SUVs and 50 μM ThT in 20 mM sodium phosphate buffer pH 6.5 under quiescent conditions at 30 °C. Average of three repeats showing standard error. *b)* Negative stain TEM images of the aggregated αS at t = 30hrs showing that aggregation into fibril like structures had occurred. *bi)* fibril like structures can be seen growing from the surface of the DMPS SUVs *bii)* much larger fibril polymorphs. The larger structures were observed separately on three different aggregations. *c)* Negative stain TEM images of the aggregated αS in the presence of a tenfold excess of 4554W peptide at t = 30hrs*.* As in the absence of peptide, fibril like structures can be seen emanating from the DMPS SUVs, but in reduced prevalence, which appear to adopt a meandering morphology, but lack the larger assemblies observed in the absence of peptide.

4554W does not reduce binding of αS to lipid vesicles

To further deduce mechanism of action on the primary nucleation stage, lipid binding properties of αS in the presence of increasing concentrations of 4554W was investigated using a modified version of a previously described far-UV circular dichroism (CD) spectroscopy methodology (Perni et al., 2018). This involved incubating 0.75 mM DMPS SUVs with increasing concentrations of 4554W (0 - 100 μM) before addition of αS to a concentration of 5 μM. In the presence of increased concentrations of DMPS αS displayed an increasingly α-helical signature, suggesting that it interacts with the lipids to adopt this conformation (Fig 4.5a). In the presence of increasing concentrations of 4554W no effect was observed on the binding of αS to the DMPS vesicles after incubation, suggesting that 4554W does not function by modulating the binding of αS to the vesicles (Fig 4.5b). Moreover, no difference in the CD spectrum was observed for 4554W in the presence of DMPS SUVs (supp. Fig. 4.6). This suggests that 4554W is likely to exert its inhibitory effect downstream of lipid binding, i.e. after αS monomers have become bound to the surface of the vesicles.
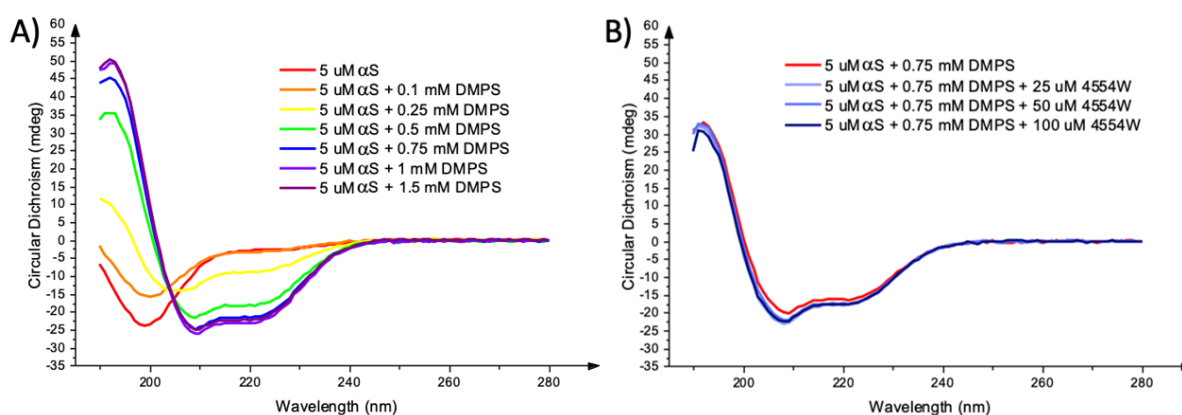

Figure 4.5: Circular Dichroism studies in the presence of lipid vesicles *a)* Circular dichroism of αS with increasing concentrations of DMPS SUVs. In isolation αS (5 μM) exists as a random coil. The conformation of αS shifts towards an α-helical structure with increasing concentration of DMPS SUVs (0.1 to 1.5 mM). The αS is seen to reach maximal α-helical conformation at a ratio of 200:1 DMPS:αS. Average of three repeats. *b)* Increasing concentration of 4554W when incubated with DMPS SUVs shows no discernible effect on the binding of ΦS to the vesicles. Average of three repeats. All samples in a) and b) were blanked against identical samples that lacked the aS component. Spectra of peptide alone with DMPS SUV can be found in supplementary figure 4.6.

We next placed αS in conditions that strongly favoured elongation as the dominant mode of aggregation and probed the effect of 4554W (Fig 4.6a). This was undertaken by the addition of preformed fibril seeds at neutral pH and under quiescent conditions, as previously described (Buell, Alexander K. et al., 2014; Perni et al., 2018). Briefly, 100μM monomeric αS was mixed with 15 μM preformed fibril seeds (monomeric equivalents – see methods section for protocol), under quiescent conditions, at neutral pH (pH 6.5, 37 °C), with aggregation followed by monitoring ThT florescence. The aggregation kinetics were undertaken in triplicate, with increasing concentrations of 4554W peptide [0 – 1000 μM]. These experiments established that 4554W had no effect upon the elongation rate of the fibrils as detected by ThT, even up to a molar ratio of 10:1.

Using TEM, we next sought to probe fibril morphology arising from elongation phase (after 30 hours) in the absence and presence of a tenfold molar excess of 4554W. The initial preformed fibrils used to seed the elongation process were also viewed by TEM (Fig 4.6b). These seeds were found to be of a consistent length, between 150 -250 nm in length and of types displaying both 5 nm and 10 nm in width. After 30 hours of incubation in the presence of seeds the fibrils were found to be elongated, rather uniformly, with very few branches to lengths of about 5 μm; this representing a 25-fold increase in length relative to the seeds introduced. The structures observed were identical in the presence and absence of 4554W peptide; both samples contained single stranded protofibrils, and more mature double stranded fibrils, with a pitch length appearing to represent that of the 'rod' polymorph (Li, B.S. et al., 2018; Li, Y.W. et al., 2018). This is consistent with the elongation ThT fluorescence assay, and the aggregation assay (Fig 4.6a) with shaking, providing evidence that the 4554W peptide has no effect on the elongation of preformed amyloid fibrils.
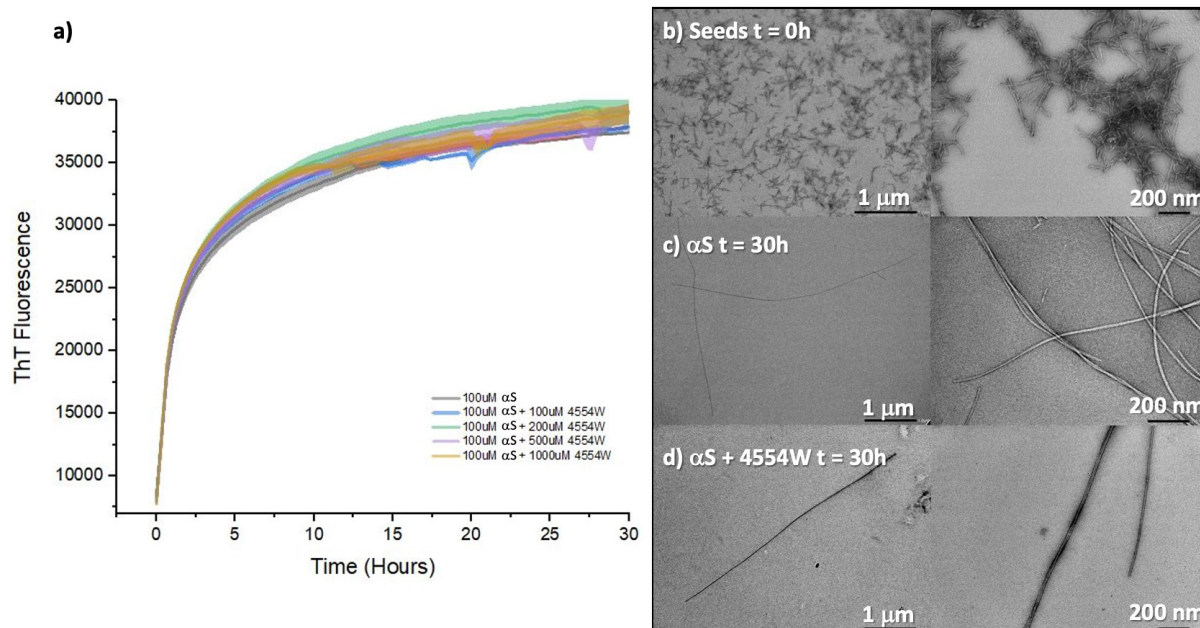
Figure 4.6: Effect of 4554W on fibril elongation. *a)* Change in ThT fluorescence intensity when 100 μM monomeric αS was incubated in the presence of 15 μM preformed fibril seeds and 50 μM ThT in 20 mM sodium phosphate buffer pH 6.5 under quiescent conditions at 37 °C, with increasing concentrations of 4554W peptide (100 – 1000 μM). No effect on ThT fluorescence was observed by addition of 4554W peptide. Each trace is the average of three repeats showing standard error. *b)* Negative stain TEM images of 15 μM preformed seeds at t = 0h before addition of 100 μM monomeric αS. *c)* Negative stain TEM images of the aggregated αS at t = 30hrs shows that fibril elongation had occurred, with seeds observed at t=0 no longer present. *d)* Negative stain TEM images of aggregated ⏃S in the presence of 10:1 4554W peptide at t = 30hrs showing that fibril elongation was unaffected by 4554W.

Secondary Nucleation/ Fibril Amplification is not inhibited by 4554W

Conditions that strongly favoured secondary nucleation/ fibril amplification were next examined by incubating 100 μM monomeric αS with 1 μM preformed fibril seeds (monomeric equivalents – see methods section for protocol), in a slight acidic environment (pH 5), under quiescent conditions. These conditions have been shown by others to accelerate secondary nucleation, such that it is the dominant aggregation mechanism (Buell, Alexander K. et al., 2014; Agerschou et al., 2019). Under these conditions, it was found that 4554W does not detectably influence secondary nucleation as measured by ThT fluorescence (Fig 4.7a), or by fibril morphology observed in TEM after 80 hrs (Fig 4.7b and 4.7c). In these experiment in the presence and absence of a tenfold molar excess of 4554W the fibrils formed presented a different morphology to those observed with elongation; they were seen either to form larger irregular interconnected shapes, likely due to fibril branching, consistent with secondary nucleation and with those observed by others (Yedlapudi et al., 2016). This suggests that

4554W has no effect on the secondary nucleation/ fibril amplification of preformed amyloid fibrils. Although section of unbranched fibrils was observed in the presence of 4554W (figure 4.7c bottom right), it is unclear if this is an actual effect of the peptide, or if just unobserved in the αS sample in the absence of peptide. Suggesting that there may be still a possibility of 4554W effecting secondary nucleation, but inconclusive at this time.
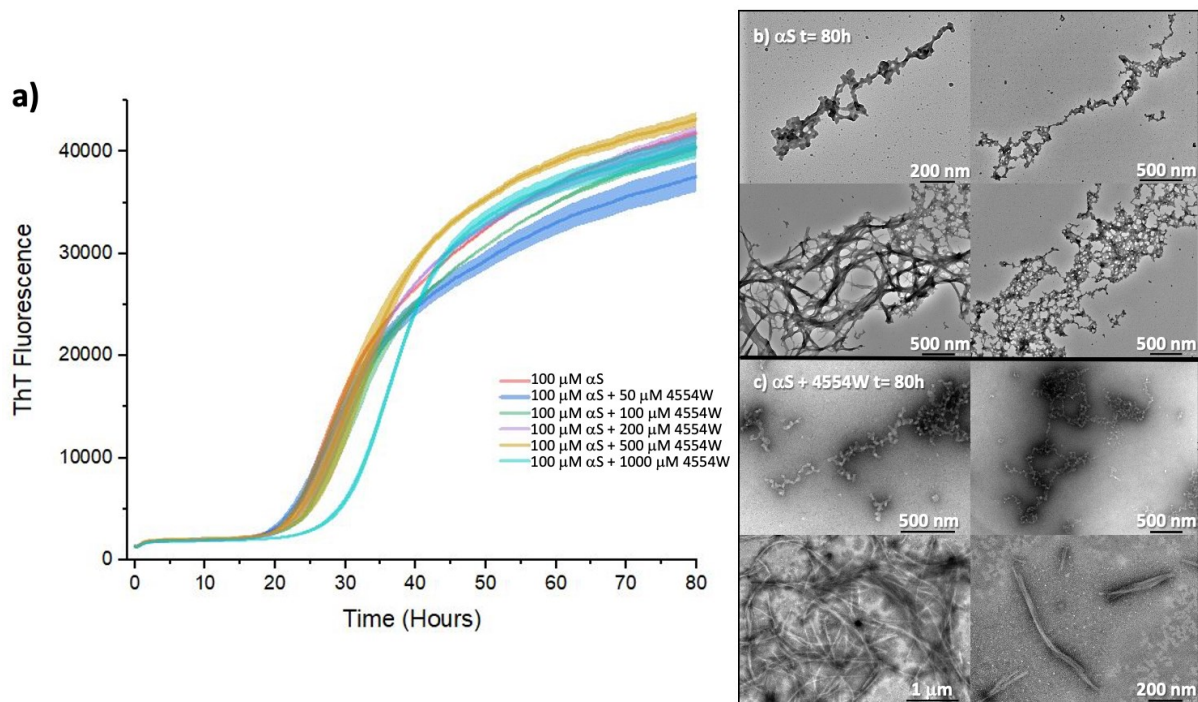

Figure 4.7: Effect of 4554W on fibril amplification/secondary nucleation. *a)* Change in ThT fluorescence intensity when 100 μM monomeric αS was incubated in the presence of 1 μM preformed fibril seeds and 50 μM ThT in 20 mM sodium acetate buffer pH 5 under quiescent conditions at 37 °C, with increasing concentrations of 4554W peptide. No effect on ThT fluorescence was observed by addition 4554W. Each trace is the average of three repeats showing standard error. *b)* Negative stain TEM images of the aggregated αS at t = 80hrs showing that secondary nucleation had occurred. *c)* Negative stain TEM images of the aggregated αS in the presence of 10:1 4554W at t = 80hrs show that secondary nucleation had unlikely been affected by the 4554W peptide.

αS mediated toxicity is suppressed by 4554W in human neuroblastoma SH-SY5Y cells

An assay to measure the effect on αS mediated cytotoxicity on cultured human neuroblastoma SH-SY5Y cells was developed, based on previously published research (Chen, S.W. et al., 2015; Fusco et al., 2017; Perni et al., 2018). Briefly, samples of lyophilised monomeric αS were resuspended in PBS pH 7.4 and aged at 37 °C for 24 hours at 800 μM, under quiescent conditions with variable concentrations of 4554W. These conditions have previously been shown to produce toxic oligomeric species that are responsible for inducing

αS toxicity (Chen, S.W. et al., 2015). 100 μM monomeric equivalents of the aged αS solutions was added to the cell cultures, equivalent to the estimated *in vivo* concentration of αS in healthy neurons (70-140 μM) (van Raaij et al., 2008). At this concentration of aged αS sample, only a very small percentage of the solution exists in oligomeric state (e.g. see supp. Fig 4.11). It has previously been suggested that at their most abundant the toxic oligomers only populate ~1% of the aggregation mixture (Ludtmann et al., 2018), equating to the addition of a concentration of 1 μM monomeric equivalent of the toxic oligomer to the cells. Oligomers in these samples show a similar structure to previously reported toxic oligomers as viewed by negative stain TEM (Supp Fig 4.12).

The human neuroblastoma SH-SY5Y cell line displayed recovery from αS mediated toxicity by 4554W in a dose dependent manner. In particular a ~58% and ~71% recovery from αS mediated toxicity was observed at 1:1 and 5:1 ratio of 4554W: αS respectively. This result is consistent with the lipid induced ThT aggregation assays, suggesting that 4554W acts to prevent monomeric αS aggregating into the disease-relevant toxic oligomeric forms which lead to neuronal cell death.
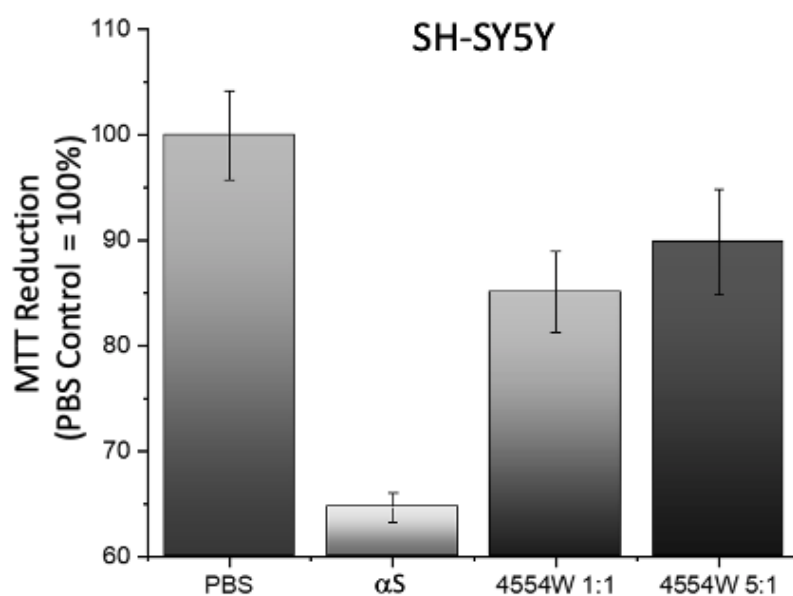

Figure 4.8: 4554W rescues human neuroblastoma SH-SY5Y from αS toxicity in a dose dependent manner. 100 μM αS aged in the presence of 1:0, 1:1 and 1:5 4554W was incubated with the human neuroblastoma SH-SY5Y cell culture for 48 hours, and the cell viability measured by MTT reduction assay. The presence of 4554W rescued the SH-SY5Y cells from the toxic effects of αS in a dose dependent manner. Results are represented as a mean average of 6 wells (technical replicates), showing standard error.

4.4 Conclusions

Primary nucleation represents the first step of the aggregation process, where soluble, and monomeric αS is converted to an aggregated state. This first step is believed to be highly important for the neurotoxicity associated with αS and is a desired point of inhibitor function. We observe that 4554W inhibits lipid induced primary nucleation of αS *in vitro*, but has no discernible effect, on the downstream rate of elongation or the secondary nucleation and amplification of αS fibrils. This is consistent with experiments presented here, using agitation to aggregate the αS, and with previously published research using stirring (Cheruvara et al., 2015).

One potential mechanism of 4554W is that it binds to a very early non-toxic low-*n* oligomer, possibly even the monomer, stabilising it and preventing its conversion into a higher molecular weight toxic oligomeric species. This is consistent with the mode of production as well as the high molar ratio required for efficacy. 4554W holds promise as a scaffold in the development of new therapeutics against α-synucleinopathies, to prevent the initial stages of αS aggregation into toxic oligomeric forms, potentially preventing neurodegeneration associated with this family of diseases.

4.5 Methods

Protein Expression and Purification of Human wt αS (140)

Wild type human α-synuclein was recombinantly expressed and purified, based on, and modified from, a previously published method (Volles and Lansbury, 2007; Pujols et al., 2017). Briefly, the pET21a plasmid containing the human wt αS (1-140), purchased from Addgene (deposited by the Michal J Fox Foundation MJFF) was transformed into *E. coli* expression cell line BL21 (DE3). 2XYT overnight cultures containing ampicillin of this human wt αS (1-140) pET21a BL21 (DE3) *E.coli* strain were used to inoculate 1lt 2XYT cultures, containing 100 mg/l Ampicillin, and grown at 37°C, 200rpm shaking, to OD_{600} = 0.6 - 0.8 and induced with 1mM isopropyl-1-thio-D-galactopyranoside (IPTG) at 37°C, 200rpm shaking, for 4 hours in an Innova 44 Incubator shaker (New Brunswick Scientific). The bacteria were harvested by centrifugation at 4600*g*, and resuspended in 40ml of 20 mM Tris buffer pH8 containing 1 cOmplete protease inhibitor tablet (Roche) and freeze-thawed at -20°C before lysis, by

sonication. The cell debris was discarded by centrifugation at 48400g, and the supernatant was collected and boiled at 95 °C for 10 minutes. The precipitated protein removed by centrifugation at 18500g. The supernatant was collected, and ammonium sulphate added to 30% saturation (0.176 g / ml), left shaking at 20 °C for 1 hour. The precipitated protein, containing the αS, was harvested by centrifugation at 18500g, and resuspended in 50 ml 20 mM Tris buffer pH8 by gentle agitation at 4 °C. This was purified by anion exchange chromatography on an AKTA pure purification system (GE Healthcare) with a 5ml HiTrap Q HP (GE Healthcare) pre-packed column, to remove protein impurities and protein bound nucleic acids. The purified fractions were combined and further purified by size exclusion chromatography (SEC) , using a HiLoad 16/60 Superdex 75 pg (GE Healthcare) prepacked purification column, to buffer exchange the αS into the relevant reaction buffer (20 mM sodium phosphate buffer pH 6.5/ 20mM sodium acetate pH 5) and ensure that only monomers were collected. Pure monomeric αS eluted between 54 - 60ml.

The concentration of the purified αS was determined in a 2mm path length quartz cuvette, using an extinction coefficient of 4836 M^{-1}cm^{-1} at 280 nm, separated into 1ml aliquots, snap frozen in liquid N$_2$, and stored at -80°C until required.

The purity of αS following SEC was confirmed by SDS-Page gel electrophoresis, and the correct mass was confirmed by mass spectrometry on a Dionex Acclaim RSLC Polar Advantage II (PA2), 2.2 μm, 120 Å, 2.1 x 50 mm (Thermo Fisher Scientific, California, USA). The deconvoluted average mass of the protein was confirmed as 14459.749 m/z, representing the mass of wt Human αS (1-140). A CD spectra scan was performed, to confirm the random coil conformation of the monomeric αS stock.

Production and purification of 4554W peptide

The 4554W peptide was synthesized in the laboratory using a Liberty Blue microwave peptide synthesizer (CEM).

The liberty blue peptide synthesizer produced the peptides on a Rink amide ChemMatrix resin (PCAS BioMatrix) employing Fmoc solid-phase technique, with repeated steps of coupling-

deprotection-washing for each amino acid. The activator solution consisted of 26g PyBOP in 100ml DMF, and the de-protection solution was 20% Piperidine in DMF with the addition of 5% Formic acid to prevent aspartamide formation of the peptide.

The peptide was removed from the matrix by incubating in cleavage solution (95% Trifluoroacetic acid (TFA), 2.5% Triisopropylsilane, and 2.5% water), on a shaker at 25 °C, for 4 hours. The resin was removed by filtration, and the peptide precipitated using ice cold ether, with vortexing and centrifugation at 7000g for 3 rounds. The pellet was left overnight at room temperature to completely dry, and purified by HPLC with a Jupiter 4 μm Proteo C-18 90 Å reverse phase prep column.

The fractions of the HPLC peaks were examined by mass spectroscopy, using a microTOF (Bruker Daltonics) to confirm which fractions contained the purified peptide. Fractions, containing the peptide were pooled, and lyophilised. The dry weight of the purified peptides was measured to 0.1 μg accuracy using a Sartorius SE2 Ultra Micro Balance and stored at -80°C.

Circular Dichroism (CD) Spectroscopy

Concentrations of 4554W ranging from 0-50 μM, were incubated with 750 μM DMPS SUVs in 20 mM phosphate buffer (pH 6.5) at 30 °C for 1 hour. 5 mM αS was added to the mixture and again left to incubate at 30 °C for 1 hour. Far UV CD spectra scans were then recorded of the solutions on a Chirascan V100 (Applied Photophysics), at 30 °C, in a 1 mm path length quarts cuvette, scanning from 300 – 190 nm with a 1 nm bandwidth, averaged over 3 scans, blanked against the DMPS vesicles with the relevant concentrations of 4554W in 20 mM phosphate buffer (pH 6.5)

Microplate ThT fluorescence Kinetic Assays with shaking

For continuous growth ThT assay with shaking 100 μl of reaction mixture, containing 450 μM αS, 450 μM 4554W peptide, 90 μM ThT in 10mM potassium phosphate buffer and 100mM KF (pH 7.5) was transferred, in triplicate, to wells in in a black, clear bottomed 96 well half area polystyrene plate with Non-bonding surface (Corning #3881) covered with Aluminium

Thermowell Sealing Tape (Corning #6570). Fluorescence was monitored using a CLARIOstar fluorescence microplate reader (BMG Labtech), maintaining a constant internal temperature of 37 °C, and constant shaking at 700rpm in double orbital mode. The focal height was set to 4.2 mm, and gain to 752, with an excitation filter of 450-15 nm and emission filter of 495-20nm and a dichroic cut-off of 469.8 nm. Well measurements were taken using the bottom optic, with 20 flashes per well and a cycle time of 500 seconds. The outer wells of the plate were not used.

Microplate ThT Kinetic Assays Without Shaking to Determine Mechanism of Action

ThT kinetic assays to determine the effect of inhibitors on the lipid induced primary nucleation, fibril elongation and secondary nucleation of αS were performed in a CLARIOstar fluorescence microplate reader (BMG Labtech), under quiescent conditions (without shaking), at 37 °C (or 30 °C for lipid induced primary nucleation) in black, clear bottomed 96 well half area polystyrene plates with Non-bonding surface (Corning #3881) covered with Aluminium Thermowell Sealing Tape (Corning #6570). The focal height was set to 4.9 mm, and gain to 800, with an excitation filter of 440-15 nm and emission filter of 480-15nm and a Dichroic cut-off of 460 nm. Well measurements were taken by spiral average of 4 mm using the bottom optic, with 50 flashes per well and a cycle time of 1200 seconds. The outer wells of the plate were not used.

Lipid preparation for induced Primary Nucleation Method

The mass of dry DMPS lipid powder was determined using an ultra-micro balance (Sartorius), and dissolved in 20mM sodium phosphate buffer pH 6.5 to a concentration of 2 mM. This was dissolved by shaking, in a 2ml Eppendorf tube, on a Thermomixer compact (Eppendorf), at 45°C, 1400 rpm for 3 hours. The solution was then freeze thawed five times using dry ice and the thermomixer compact (Eppendorf) at 45 °C and 500rpm. The preparation of the vesicles was carried out by sonication, using a Soniprep 150 plus sonicator, set to an amplitude of 10.0, for 5 cycles of 30 seconds on and 30 seconds off.

Dynamic Light Scattering (DLS) Measurements

A sample of the vesicles produced at each step were diluted to 100 μM in 20mM phosphate buffer pH 6.5. Their size distribution was measured by DLS, using a Zetasizer Nano ZSP (Malvern Instruments), to ensure a final consistent size of between 20-30 nm was obtained.

Lipid induced Aggregation Kinetic Assay to Primary nucleation

Lipid induced primary nucleation experiments were performed in a CLARIOstar fluorescence microplate reader (BMG Labtech), under quiescent conditions (without shaking), at 30 °C in black, clear bottomed 96 well half area polystyrene plates with Non-bonding surface (Corning #3881) covered with Aluminium Thermowell Sealing Tape (Corning #6570). The experiments were performed in 100 μl aliquots, in triplicate, each containing 100 μM αS, 50 μM ThT, 100 μM DMPS and varying concentrations of 4554W peptide (0 μM, 100 μM and 1mM) in 20mM phosphate buffer pH 6.5.

Seed Fibril Formation for Elongation method

Mature fibrils were produced in a 10 mm Quartz cuvette by incubating 1.5 ml of 400 μM αS monomers in 20mM sodium phosphate buffer (pH 6.5) for 48 hours at 40°C maximal stirring (1500rpm), using a PTFE magnetic stirrer, on an RCT Basic Heat Plate (IKA, Staufen, Germany). The mature fibrils were diluted to 200 μM monomer equivalents using 20mM sodium phosphate buffer (pH6.5) (1.5ml) and broken into seeds by 3 rounds of freeze-thawing with liquid N_2 followed by 55°C water bath. The mixture was then sonicated using a Soniprep 150 plus sonicator, set to an amplitude of 10, for 3 cycles of 10 seconds on and 10 seconds off. The final seed fibrils were measured by circular dichroism (10 μM monomer equivalent αS in 20 μM sodium phosphate buffer pH 6.5) to ensure complete conversion to β-sheet and confirmed by TEM. The seed stock was divided into 500 μl aliquots, frozen in liquid N_2, and stored at -80°C until required.

Seeded Aggregation Kinetic Assay to Measure Elongation

Seeded elongation experiments were performed in a CLARIOstar fluorescence microplate reader (BMG Labtech), under quiescent conditions (without shaking), at 37 °C in black, clear

bottomed 96 well half area polystyrene plates with Non-bonding surface (Corning 3881) covered with Aluminium Thermowell Sealing Tape (Corning 6570). The experiments were performed in 100 μl aliquots, in triplicate, each containing 100 μM αS, 50 μM ThT, 15μM (monomer equivalents) preformed fibril 'seeds' and varying concentrations of 4554W peptide (0 μM, 100 μM and 1mM) in 20mM phosphate buffer pH 6.5.

Formation of Seeds for Secondary Nucleation

Seed fibrils for inducing secondary nucleation were produced by incubating 25 μM αS monomer in 20 mM sodium acetate, 50 μM ThT and 0.01% sodium azide, split into 100 μl aliquots in a black, clear bottomed 96 well half area polystyrene plates with Non-bonding surface (Corning 3881), with each well containing a single 4 mm glass bead (Hecht Karl ref. 41401004), covered with Aluminium Thermowell Sealing Tape (Corning 6570). The plate was incubated at 37 °C in a CLARIOstar fluorescence microplate reader (BMG Labtech) at 500rpm for 96 hrs. The aliquots were pooled into a 2 ml Eppendorf tube and sonicated using a Soniprep 150 plus, set to an amplitude of 10, for 5 cycles of 1 seconds on and 5 seconds off. The seeds were flash frozen in liquid N_2 and stored at -80 °C until required.

Seeded Aggregation Kinetic Assay to Measure Secondary Nucleation/ Fibril Amplification

Seeded elongation experiments were performed in a CLARIOstar fluorescence microplate reader (BMG Labtech), under quiescent conditions (without shaking), at 37 °C in black, clear bottomed 96 well half area polystyrene plates with Non-bonding surface (Corning 3881) covered with Aluminium Thermowell Sealing Tape (Corning 6570). The experiments were performed in 100 μl aliquots, in triplicate, each containing 100 μM αS, 50 μM ThT, 1 μM (monomer equivalents) preformed fibril 'seeds' and varying concentrations of 4554W peptide (0 μM, 100 μM and 1mM) in 20mM sodium acetate buffer pH 5.

Transmission Electron Microscopy (TEM)

αS samples from the end point of the aggregation kinetics were collected. 5 μL of these samples were put onto on glow discharged Formvar/carbon-coated, 200 mesh, copper grids for 1 minute. The samples were dried with filter paper and washed twice with MilliQ water for 1 second, each time removed with filter paper. The sample was stained by incubating the

grids with 5 µL Uranyl Acetate Zero (Agar Scientific) for 30 seconds, followed by removal of the excess stain with filter paper. The grids were left to air-dry for 2 hours. The samples were imaged using a Transmission Electron Microscopy Jeol 2100 Plus (JEOL), operating at an accelerating voltage of 200 kV. Multiple grids were screened in order to obtain representative images of the samples.

Neuroblastoma Cell Culture

Human neuroblastoma cell line SH-SY5Y (ECACC 94030304) was purchased from Public Health England's European Collection of Authenticated Cell Cultures (ECACC). Unless otherwise stated, all cell culture consumables were purchased from ThermoFisher. Cells were cultured in Dulbecco's modified Eagle's medium (DMEM)/F-12 media with Phenol red and without HEPES and L-glutamine. DMEM/F12 was supplemented with 10% Foetal Bovine Serum, 2mM L- glutamine and 5% Non-essential Amino Acids; with 100IU penicillin and 100µg/ml streptomycin (Corning). The culture was maintained in an incubator at 37 °C, 5% CO_2, and saturated humidity until about 80 % confluency was reached, for a maximum of 20 passages. For toxicity assays the stock culture was seeded in 96 well plates and grown for 24 hours to reach 60-80% confluency at 37 °C, 5% CO_2, and saturated humidity.

Preparation of αS for cell toxicity experiments

Pre-purified αS was further purified by HPLC with a Jupiter 4 µm Proteo C-18 90 Å reverse phase prep column, using an acetonitrile gradient containing TFA. The eluted αS peak was pooled, flash frozen in liquid N_2, and lyophilized. The dried pellet was resuspended at 800 µM in PBS pH7.4 with increasing concentrations of 4554W (0, 800 and 4000 µM), incubated at 37 °C under quiescent conditions for 24 hours. Following incubation these samples were passed through a spartan 0.2 µm SPARTAN filter unit (Whatman).

MTT cell viability assay

Aliquots of the pre-incubated αS with the varying concentrations of 4554W (1:1 an 1:5 stoichiometry) were added to the media of the primary cortical neurons and the SH-SY5Y neuroblastoma cell cultures to a final concentration of 100 µM αS monomer equivalents, in

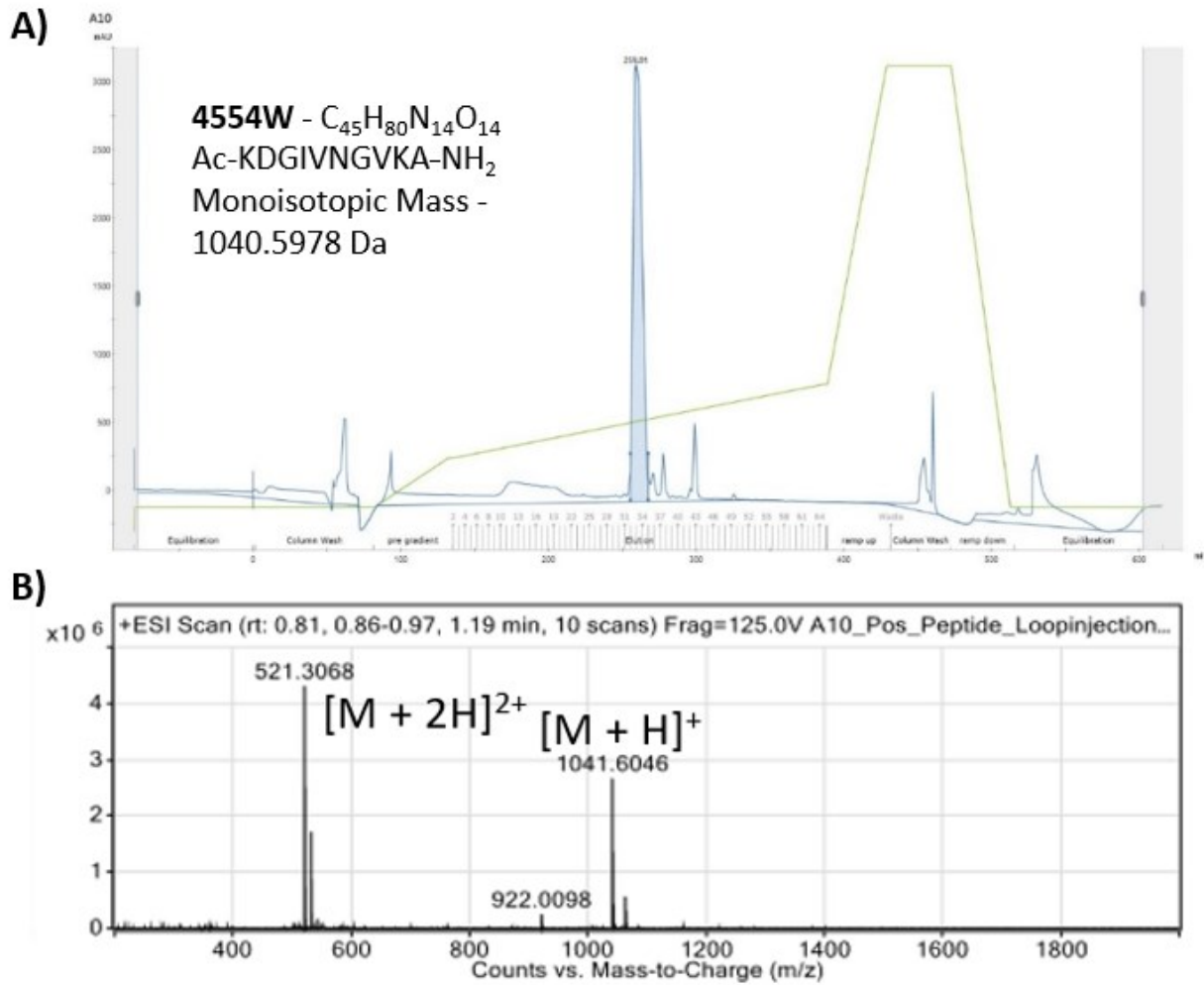replicates of 6, and incubated for 48 hours at 37 °C, 5% CO_2, and saturated humidity. Cell viability was assessed by 3-(4,5-dimethylthiazol-2-yl)-2,5-diphenyltetrazolium bromide (MTT) reduction assay. Briefly, the cell growth media was removed, and replaced with equivalent volume of growth media containing 1 mg/ml MTT solution at 37 °C, 5% CO_2, and saturated humidity for 1 hour. The MTT solution was then removed and the resulting blue formazan was resuspended in 150 µl 2-Propanol. The absorbance of the blue formazan solution was measured at 595 nm and presented as an average of the 6 wells for each condition.
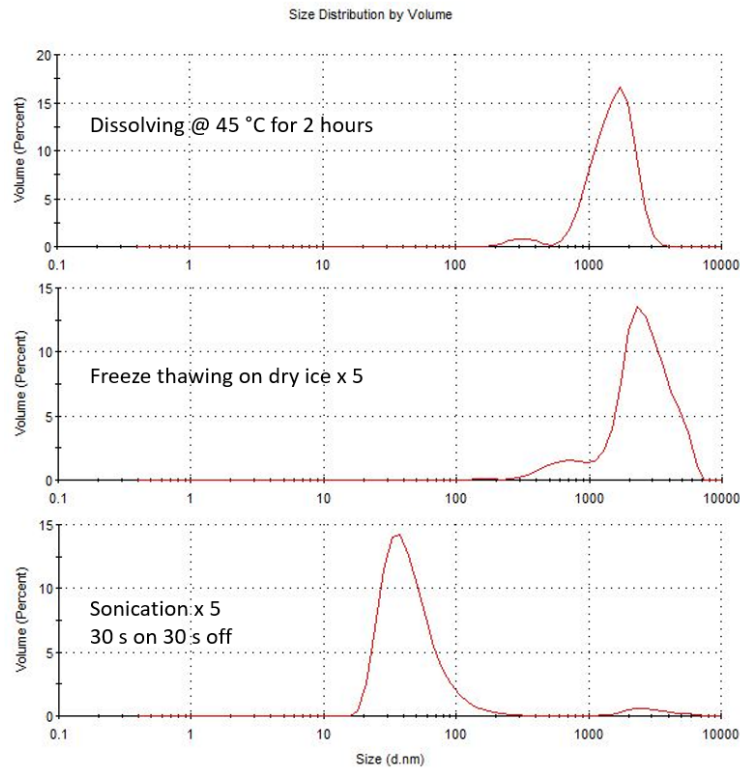
Chapter 4:

Supporting information
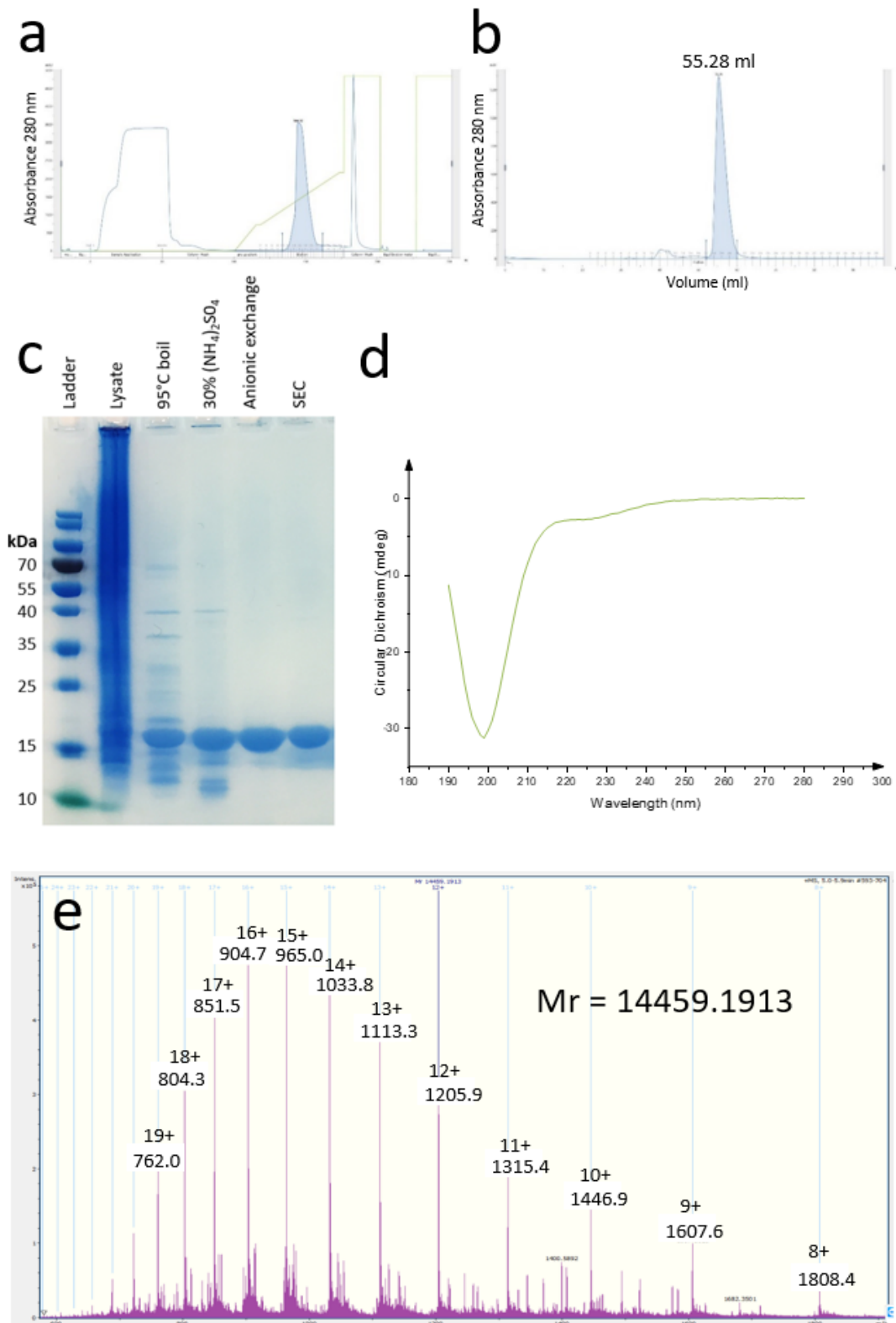
Supplementary Figure 4.1: Overview of the purification of αS used for the experiments. a) Chromatograph of the Hi-Q anionic exchange purification. b) Chromatograph of the Size exclusion chromatography and buffer exchange. c) SDS page gel showing an overview of the entire purification protocol. d) Far-UV circular dichroism spectra of the purified αS showing that the monomeric αS is in a random coil conformation. e) De-convoluted mass spectrum, showing a mass of the protein of 14459 m/z, representing the mass of wt Human αS (1-140).
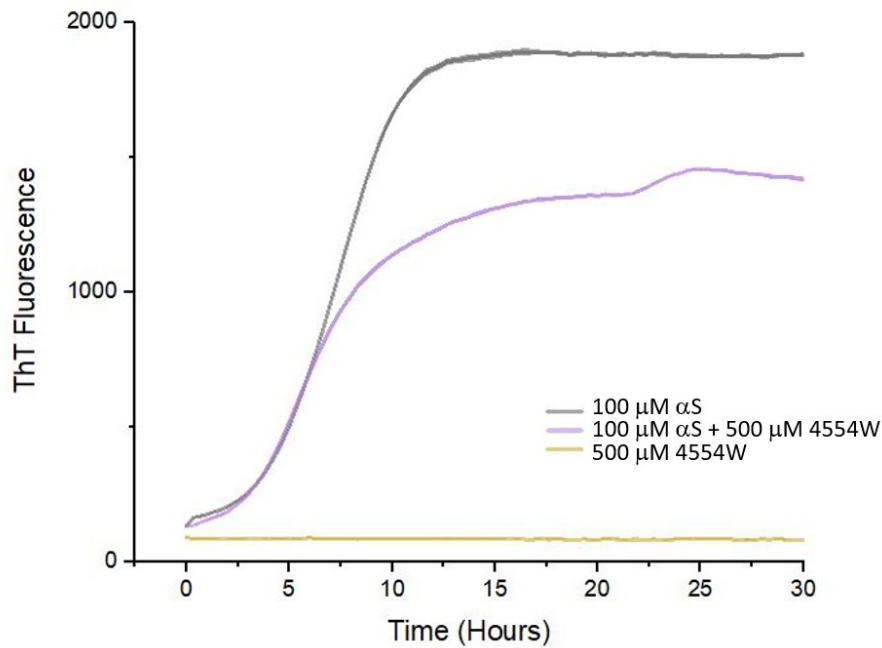
A)

4554W - $C_{45}H_{80}N_{14}O_{14}$
Ac-KDGIVNGVKA–NH$_2$
Monoisotopic Mass –
1040.5978 Da

B)

+ESI Scan (rt: 0.81, 0.86-0.97, 1.19 min, 10 scans) Frag=125.0V A10_Pos_Peptide_Loopinjection...

521.3068

[M + 2H]$^{2+}$ [M + H]$^+$

1041.6046

922.0098

Counts vs. Mass-to-Charge (m/z)

Supplementary Figure 4.2: Production and purification of the 4554W peptide. A) HPLC purification trace measured at 215 nm for 4554W. B) Mass spectrometry profile measured by time of flight spectroscopy confirming 4554W mass to be 1040.6 Da, as expected.

Supplementary Figure 4.3: Dynamic light scattering size distribution of the DMPS small unilamellar vesicles (SUVs) used for lipid induced nucleation assays, showing a size distribution centred around 30nm post sonication. Data presented as 'size distribution by volume' to reduce the impact of the signal being swamped by large particles if presented as 'size distribution by intensity' because the larger particles would disproportionately scatter the light beam.
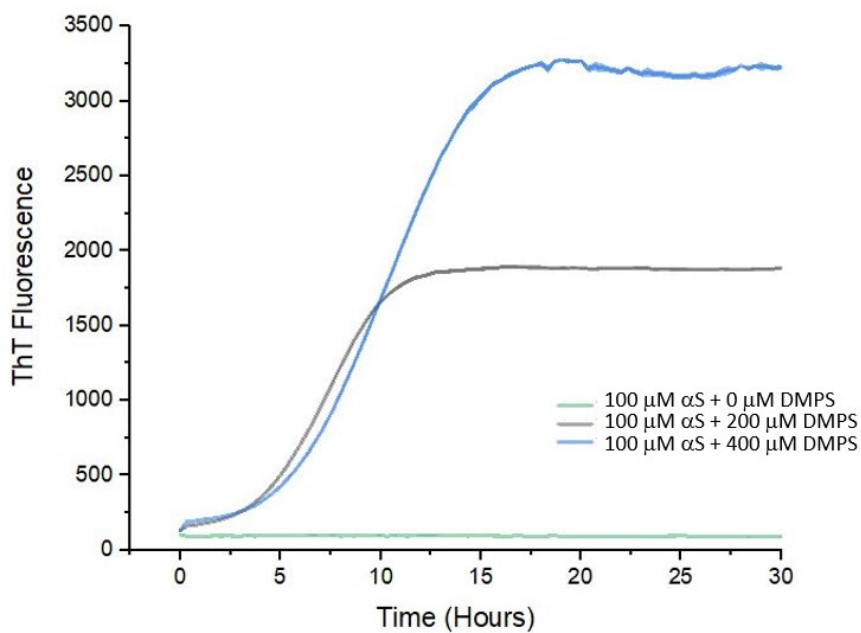

Supplementary Figure 4.4: ThT fluorescence intensity when 100 μM αS is incubated with 0 μM, 200 μM , or 400 μM DMPS vesicles and 50 μM Thioflavin T in 20 mM phosphate buffer (pH 6.5) under quiescent conditions at 30 °C.
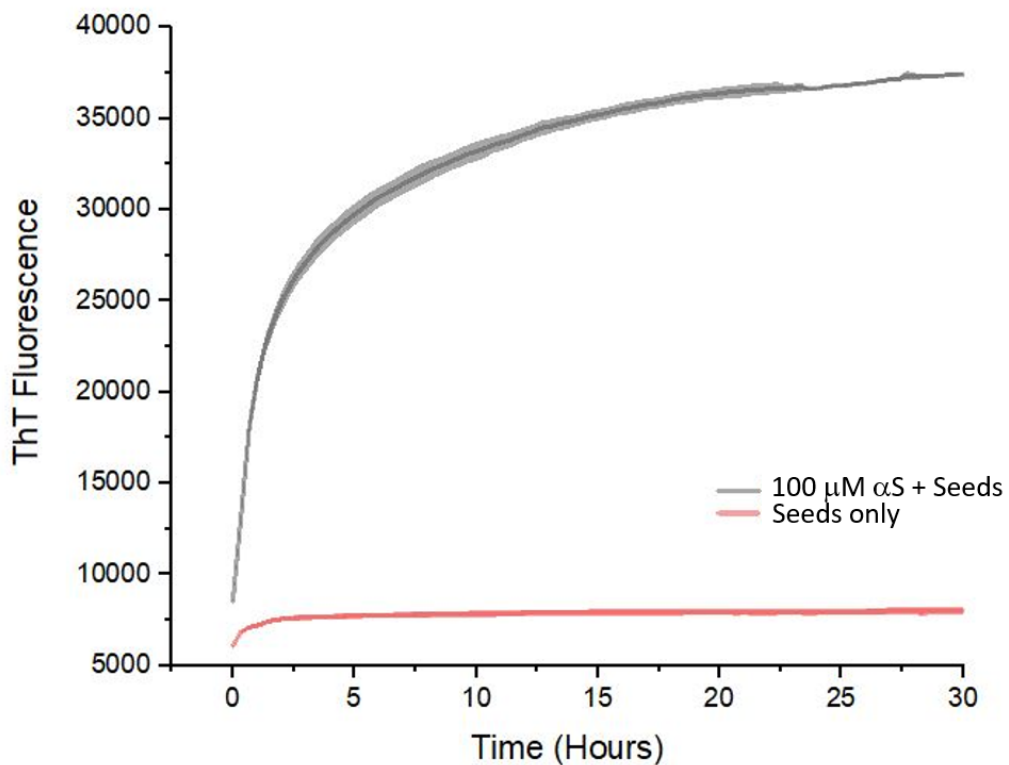
Supplementary Figure 4.5: ThT fluorescence intensity when 100 μM αS is incubated with 200 μM DMPS vesicles and 50 ⬜M Thioflavin T in 20 mM phosphate buffer (pH 6.5) under quiescent conditions at 30 °C. It can be seen that the 4554W peptide has an inhibitory effect on lipid induced primary nucleation, and no aggregation is observed for 4554W peptide in the absence of αS.
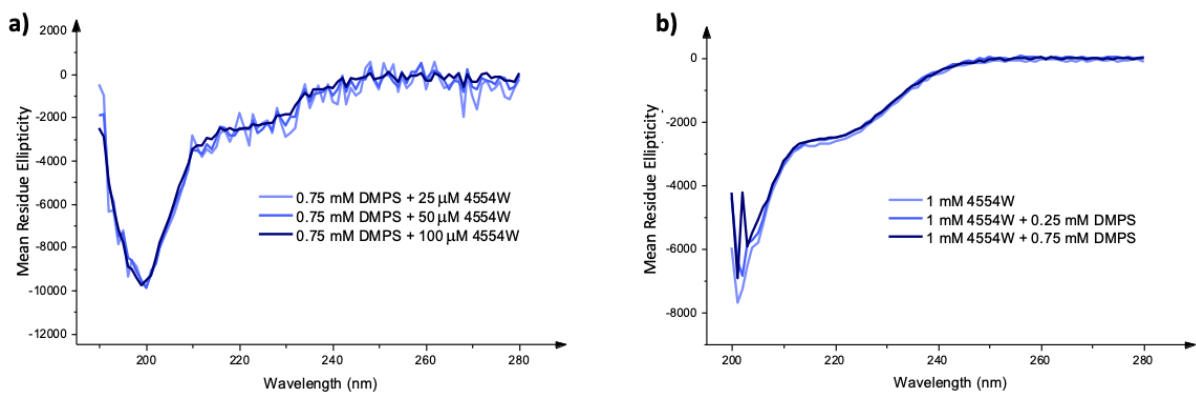

Supplementary Figure 4.6: Circular dichroism spectra of a) increasing concentrations (25-100 μM) of 4554W incubated at 30 °C with 0.75 mM DMPS vesicles, and b) increasing concentrations (0 - 0.75 mM) of DMPS SUVs incubated at 30 °C with 1 mM 4554W, showing that the peptide retains a random coil structure in the presence of lipid vesicles, suggesting that the peptide does not bind independently to lipid vesicles. All spectra were recorded as an average of 3 scans, blanked against corresponding DMPS concentration in 20mM sodium phosphate buffer (pH 6.5), and presented as mean residue ellipticity.
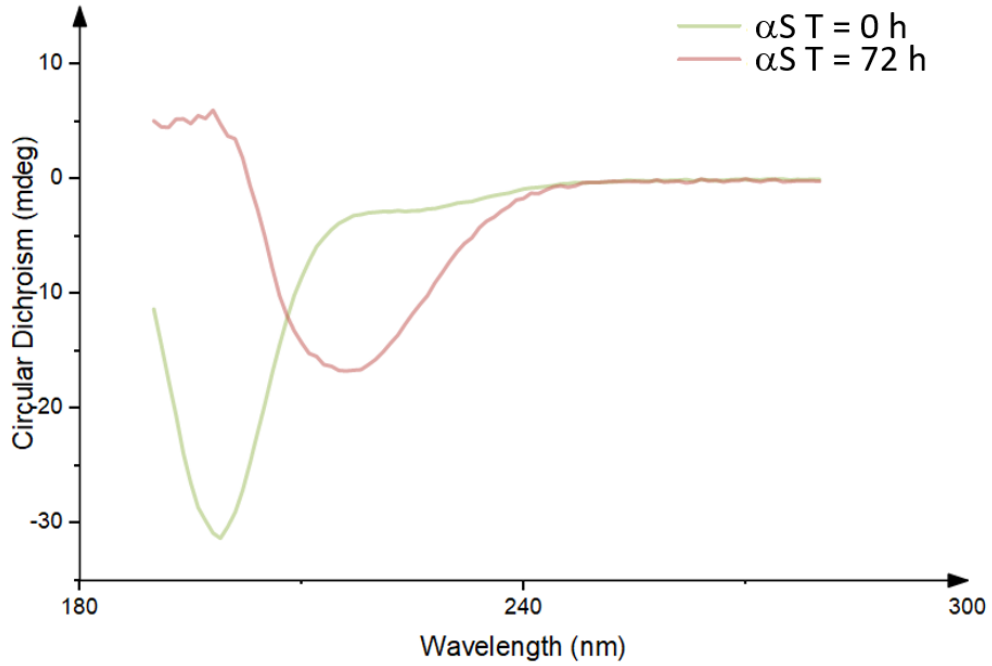
Supplementary Figure 4.7: Circular dichroism spectra of 10 μM seeds formed for ThT assay to probe fibril elongation rates. The αS monomer before aggregation shows a random coil spectra (green). The αS is seen to be fully converted to β-sheet fibril seeds (red) after 400 μM αS was stirring at 40°C with a teflon bar at 1500rpm for 48 hours, followed by 3 rounds of freeze-thawing in liquid N_2 and 3 rounds of sonication for 10 seconds on 10 seconds off.


Supplementary Figure 4.8: ThT fluorescence experiment measuring seeds only vs seeds and monomer to show seed stability. 100 μM in the presence of 15μM seeds (grey) vs 15 μM seeds without addition of monomer (red), showing that the seeds remained stable.
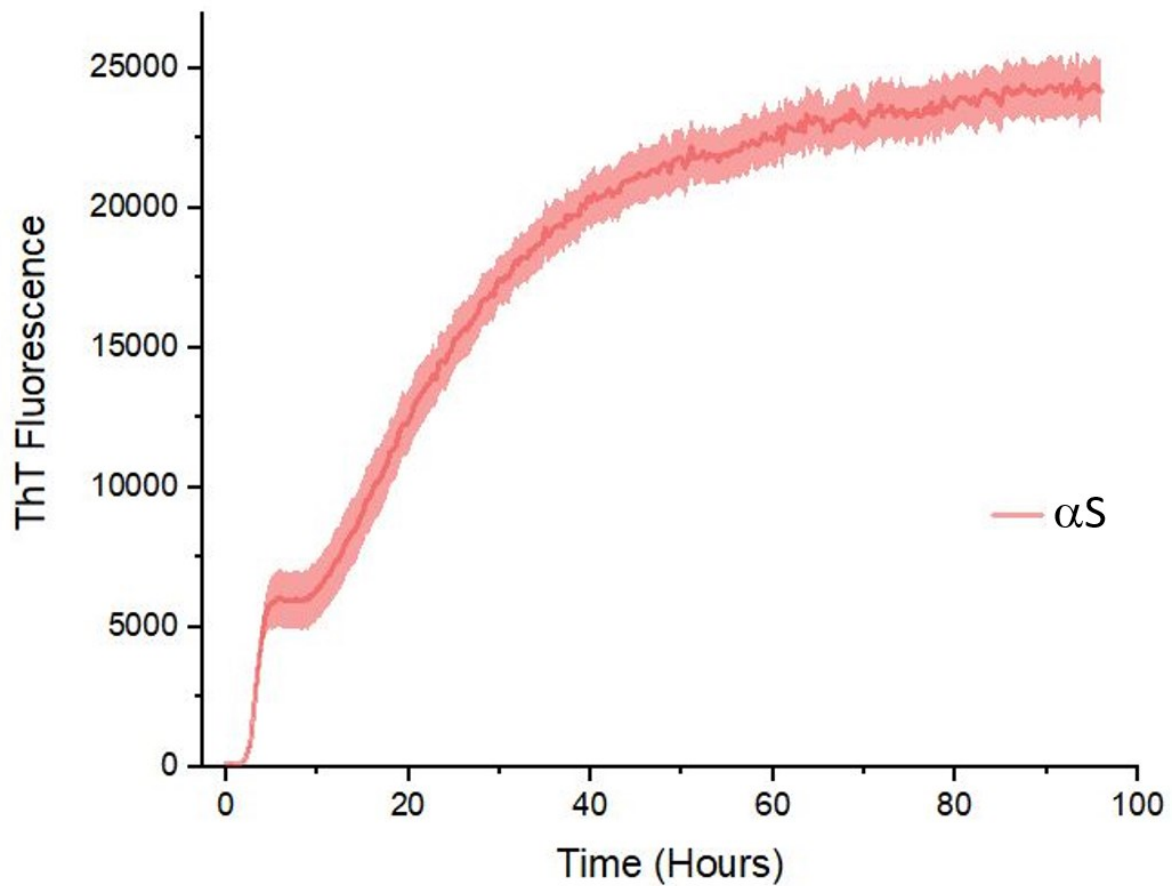
Supplementary Figure 4.9: ThT curve following seed creation for secondary nucleation studies, created in 96 well plates containing glass beads in the wells, with shaking at 500 rpm at a constant temperature of 37 °C. Interestingly the αS aggregated with a glass bead in this way greatly minimises the lag times, and produces an abnormal bump in the sigmoidal curve in the first 5 hours.
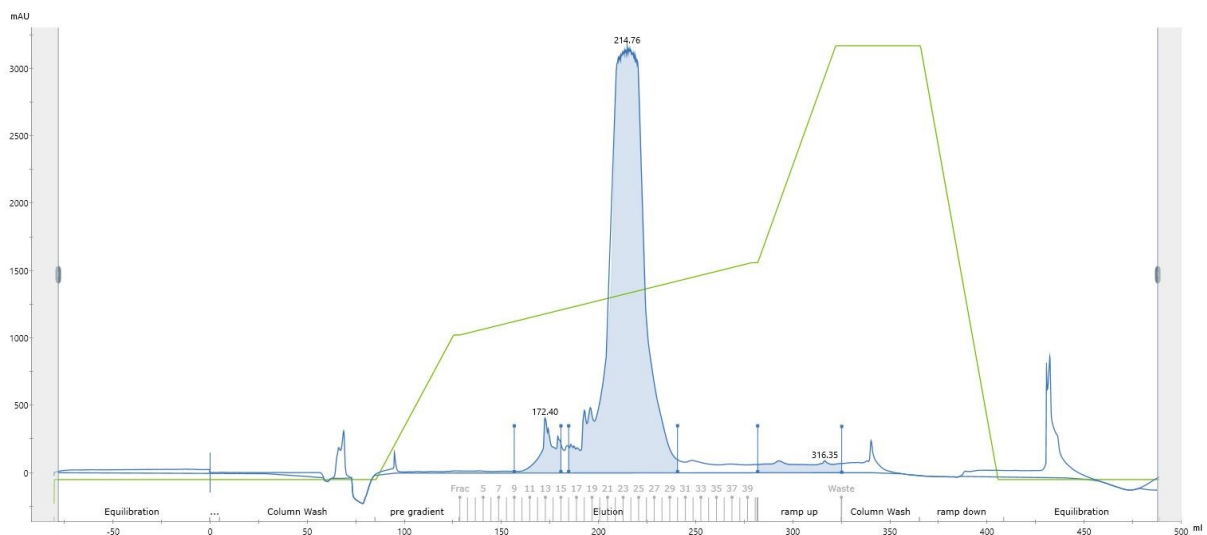
Supplementary Figure 4.10: HPLC purification of Pre-purified αS by affinity to C18 column to remove buffer prior to lyophilisation for cell toxicity assays. Absorption at 280 nm used to follow the elution of aS from the c18 column (blue), by increasing concentrations of acetonitrile + 0.1% TFA (green).
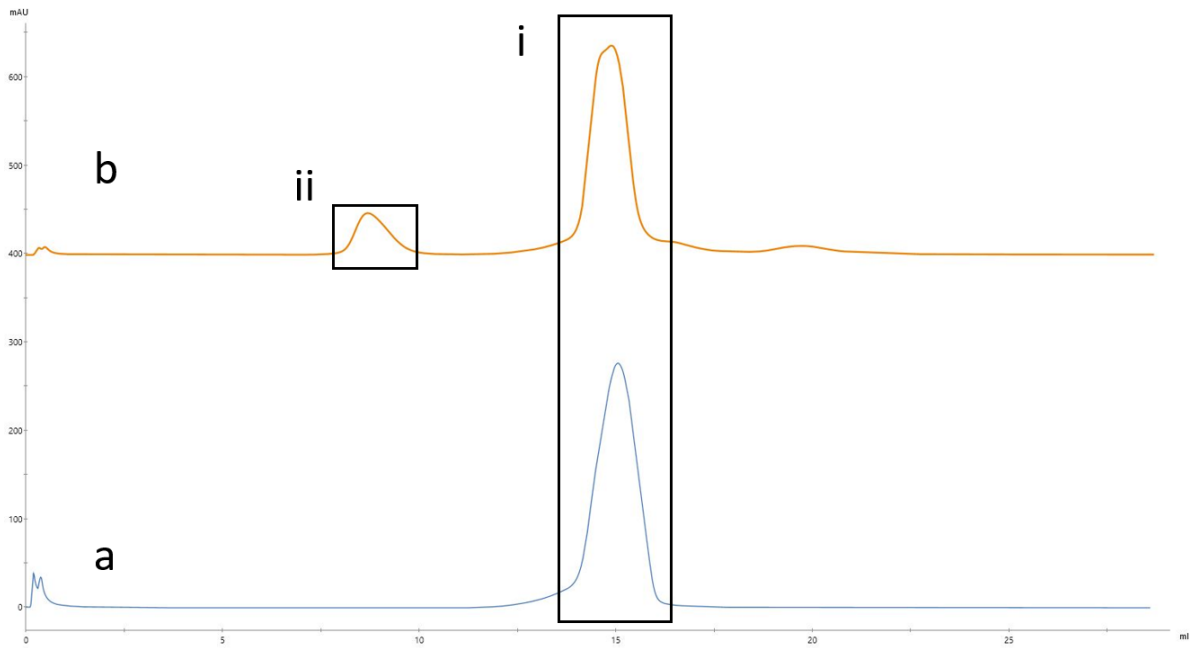
Supplementary Figure 4.11: SEC elution chromatogram when 100 μl of 800 μM αS sample is loaded onto a Superdex 200 Increase 10/300 column (GE lifesciences) and run at 0.5 ml/min in PBS buffer pH 7.4, showing absorbance at 280 nm. **a)** Monomeric αS showing a clean monomer peak (i) at 15ml elution volume. **b)** Lyophilised αS resuspended in PBS pH 7.4 and incubated at 37 °C for 24hrs and filtered through a 0.22 μM filter showing a monomer peak (i) at 15ml elution volume, and an additional oligomer peak (ii) eluted at 9ml run volume.
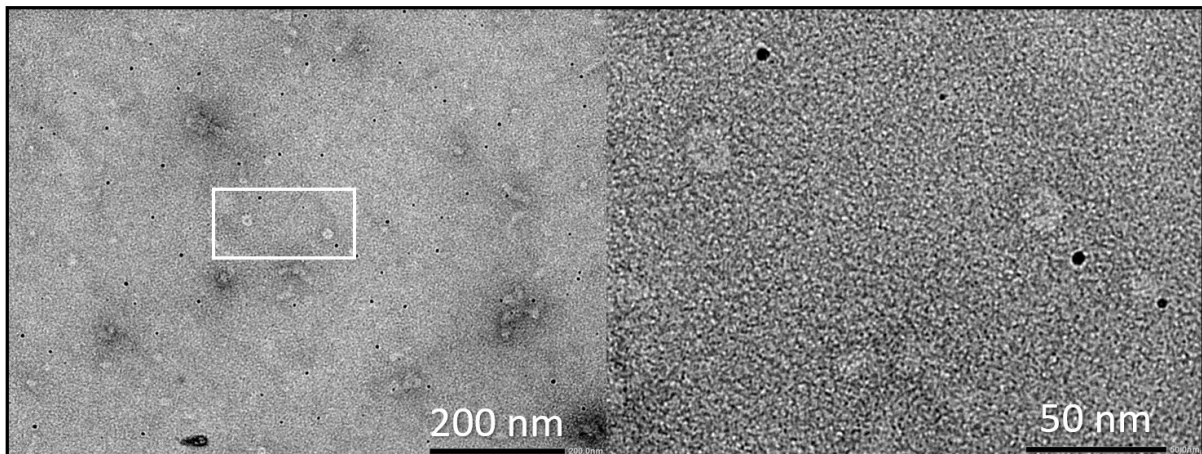
Supplementary Figure 4.12: Negative stain TEM images taken from the oligomer SEC Peak (supplementary figure 11ii), that appear to show doughnut like oligomer structures similar in shape and diameter to those previously reported.

Chapter 5:

A Series of Helical α-synuclein Fibril Polymorphs Are Populated in the Presence of Lipid Vesicles

This declaration concerns the article entitled:		
A Series of Helical α-synuclein Fibril Polymorphs Are Populated in the Presence of Lipid Vesicles		

Publication status (tick one)

Draft manuscript		Submitted		In review		Accepted		Published	X

Publication details (reference)	Meade, R.M., Williams, R.J. & Mason, J.M. (2020). A series of helical α-synuclein fibril polymorphs are populated in the presence of lipid vesicles. *npj Parkinsons Dis.* **6,** 17.

Copyright status (tick the appropriate statement)

I hold the copyright for this material		Copyright is retained by the publisher, but I have been given permission to replicate the material here	X

Candidate's contribution to the paper (provide details, and also indicate as a percentage)	The candidate contributed to / considerably contributed to / **predominantly executed** the… Formulation of ideas: 80% - Modified existing protocols, and discovered the novel polymorphs Design of methodology: 80% - Designed the experiment Experimental work: 100% - Performed all included experimental work Presentation of data in journal format: 50% - Contributed to manuscript
Statement from Candidate	This paper reports on original research I conducted during the period of my Higher Degree by Research candidature.
Signed		**Date**	19/09/2020

BRIEF COMMUNICATION   OPEN

Check for updates

A series of helical α-synuclein fibril polymorphs are populated in the presence of lipid vesicles

Richard M. Meade[1], Robert J. Williams [ID][1] and Jody M. Mason [ID][1] ✉

α-Synuclein (αS) deposition is a defining characteristic of Parkinson's disease (PD) pathology, and other synucleinopathies. αS aggregates in disease, leading to the generation of neuronal inclusions known as Lewy bodies. These accumulate in the cytoplasmic space of dopaminergic neurons in the *substantia nigra pars compacta* region of the brain, causing cell death, resulting in decreased dopamine levels, and ultimately PD symptoms. To date, a significant proportion of structural information has arisen from in vitro studies using recombinantly purified forms of the protein, often failing to acknowledge that αS is natively located in the presence of phospholipids, where it likely plays a direct role in regulating synaptic vesicle function and neurotransmission. Here we present a series of macromolecular αS assemblies not previously described that form in the presence of lipid vesicles. These fibrillar structures are striking in both their large size relative to those previously reported and by their varying helical content, from ribbons to wave-like helices of long pitch shortening to those more compact and bulkier. These studies provide the foundation for more detailed structural analysis, and may offer new possibilities to further define disease-relevant versions of the protein that are accessible to pharmacological intervention.

INTRODUCTION

α-Synuclein (αS), which has been described as intrinsically disordered or helical, is capable, under certain conditions, of aggregating into a range of different amyloid fibril morphologies[1]. These structures are typically probed via imaging techniques that include electron microscopy (EM) and atomic force microscopy, and more recently at the atomic level using solid-state nuclear magnetic resonance[2], and increasingly, cryoEM[3-8]. Many approaches describe structures gained via recombinant means under in vitro conditions[2-5,7,9,10]. Others have employed the use of lipids during in vitro experiments, since this is critical to αS function in situ[6,11-17]. More recent studies are emerging in which aggregates of αS from specific neurodegenerative diseases and key regions of the brain are isolated in small quantities[8,18]. The latter have then been used to seed recombinant forms of αS produced in bacteria or cell culture, with the assumption that seed conformation is maintained in mature fibres, without polymorphic shift, and thus those observed within imaging is of the disease-relevant type. To date, all but one of the structures are defined by a double protofilament. Most, but not all, display rotational symmetry about the axis of the fibril.

In particular, the bacterial approach has been used to describe an increasing number of fibril morphologies. Using this approach the first morphologies were described—type 1a ('rods'[3,5]) and 1b ('twisters'[5]), as well as types 2a and 2b[9]. This approach has also extended to structures of early-onset αS mutants, including E46K[5,19] and H50Q[19]. Studying αS using seeds isolated from brain samples and growing mature fibres from them using additional protein produced by bacterial/mammalian cells is also beginning to yield new structures[18]. For example, in multiple system atrophy (MSA) two further unique morphologies (named Type I and Type II) have been described; these contain non-proteinaceous, potentially negatively charged molecules, at the protofilament interface. Interestingly, in both structures each protofibril within the mature fibril adopts a different morphology, rendering the

fibrils asymmetric[8]. In contrast to MSA-derived filaments, those seeded from αS isolated from individuals with dementia with Lewy bodies were reported to lack any twist and were reported to be thinner than those from the brains of individuals with MSA, suggested another currently uncharacterised morphological fibril type.

All structures identified to date display a mature fibril width of ~10 nm and a typical helical pitch in the Angstrom range (e.g. ~460 Å for twisters, or ~920 Å for rods). Here we describe very different and much larger assemblies that have not been previously reported, and which form specifically in the presence of lipid vesicles. This is particularly interesting given the emerging discussion over whether Parkinson's disease (PD) is a proteinopathy or lipidopathy[20]. These newly reported structures are able to be readily viewed using transmission EM (TEM) and range in polymorph from structures that are ribbon like to those that are highly helical and compact, with a range of observed helical assemblies in between. Interestingly, the addition of lipid vesicles to the monomeric αS sample appears to be an absolute requirement for the morphological shift to such larger assemblies. We believe, given the role that αS plays within the cell, that these structures could have biological or pathological relevance and therefore far-reaching implications in defining a disease-relevant conformation towards identification of a druggable target.

RESULTS AND DISCUSSION

Lipid vesicle-induced fibril polymorphs

The addition of lipids to αS has been reported to modulate misfolding and toxicity[21], causing the protein to form an extended helical structure on small unilamellar vesicles (SUVs). The binding of αS to lipid membranes has complex effects on the latter[13], altering the curvature of the bilayer structure and leading to the formation of small vesicles[14]. αS has been shown to be capable of
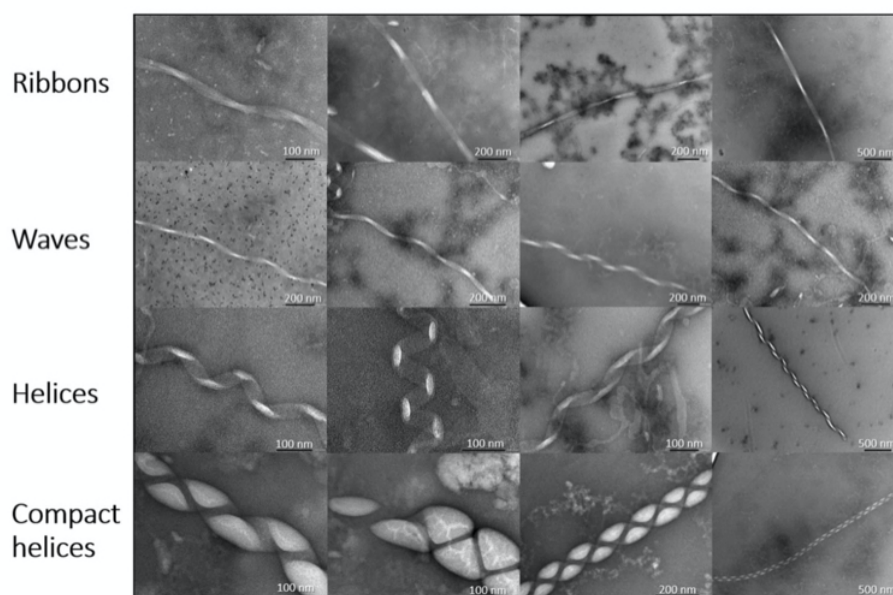
Fig. 1 A variety of large fibril polymorphs are formed upon incubation of αS with DMPS lipid vesicles. These structures were formed by aggregating 100 µM αS in the presence of 200 µM DMPS lipid vesicles at 30 °C for 190 h. The structures have initially been divided into four subtypes with varying degrees of helicity named ribbons, waves, helices and compact helices.

bending membranes consisting of negatively charged phospholipid vesicles and forming tubules from large lipid vesicles[22].

Using TEM we report for the first time the formation of a range of large macromolecular structures that vary widely in their morphology (Fig. 1). In particular, we describe the formation of a much larger type of macro-assembly that can form in the presence of lipid vesicles. Specifically, 1,2-dimyristoyl-sn-glycero-3-phospho-L-serine (DMPS) was used, at neutral pH (pH 6.5, 30 °C), as previously described[15,23,24]. DMPS vesicles were chosen as a model phospholipid system since they are a key component within dopaminergic synaptic vesicles, and the negative charge on their surface has been shown to be capable of significantly promoting αS primary nucleation[15,16]. Interestingly, DMPS lipid vesicles have been previously shown to act by forming kinetically trapped αS protofibrils[25]. Moreover, lipid-induced fibril production has been shown to be strongly affected by early-onset mutations, which can induce dramatic changes in such crucial processes thought to be associated with the initiation and spreading of αS aggregation[26]. Phospholipid biosynthetic enzymes have also been seen to be elevated in the substantia nigra of PD patients[27]. Specific membrane interactions can therefore play a key role in triggering a conversion of αS from a soluble to aggregated form that is associated with disease.

To induce the formation of the macromolecular structures, briefly, 100 µM monomeric αS (Supplementary Fig. 1) was mixed with 200 µM DMPS SUVs, of ~30–40 nm diameter (as measured by dynamic light scattering (DLS); Supplementary Fig. 2), under quiescent conditions (Fig. 2). The solution was left to aggregate, as monitored by ThT fluorescence, for a period of 48 h, allowing the fluorescence to progress through the lag and exponential phases of aggregation before plateauing at this time at the stationary phase. A sample was collected from this phase and analysed by TEM (Fig. 2a). During this time distinctive fibril-like structures were observed to emerge from the surface of the SUVs that are similar to those reported by others in the presence of DMPS[6,15]. In particular, these meandering fibril-like structures, were ~5 nm in diameter, suggesting that they are protofibrils of the single-stranded variety[2]. Also observed were wider fibrillar structures, measuring 10 nm in diameter (Supplementary Fig. 3), suggestive
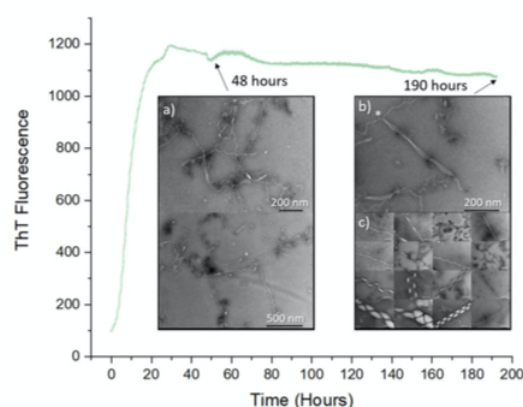

Fig. 2 Lipid-induced αS aggregation followed by ThT fluorescence. Aggregation of 100 µM αS in the presence of 200 µM DMPS lipid vesicles at 30 °C, followed by ThT fluorescence and TEM. **a** TEM samples taken at 48 h show the formation of meandering fibril-like structures growing from the surface of punctate lipid vesicles. These are observed to be ~5 nm in width and straight, or ~10 nm in width (Supplementary Fig. 3). **b** TEM samples taken at ≈190 h show two meandering 10 nm fibrils fusing to form a 40-nm-wide ribbon-like structure*. **c** TEM samples observed at ≈190 h display a range of macromolecular polymorphs (image is shown in more detail in Fig. 1).

of a more mature double strand fibril structure that is consistent with previously reported dimensions[3–5]. The samples were next left to further incubate at 30 °C until 190 h had passed, upon which the helical assemblies reported were observed. Since lipid-induced meandering protofibrils may represent kinetically trapped intermediates[6,25], extended incubation times may be required for conversion to the much larger helical assemblies reported here. Of note during this period is the fact that no detectable change in ThT fluorescence was observed (Fig. 2; Supplementary Fig. 4). This may explain why these structures have not been previously reported, since it also suggests that no additional ThT becomes
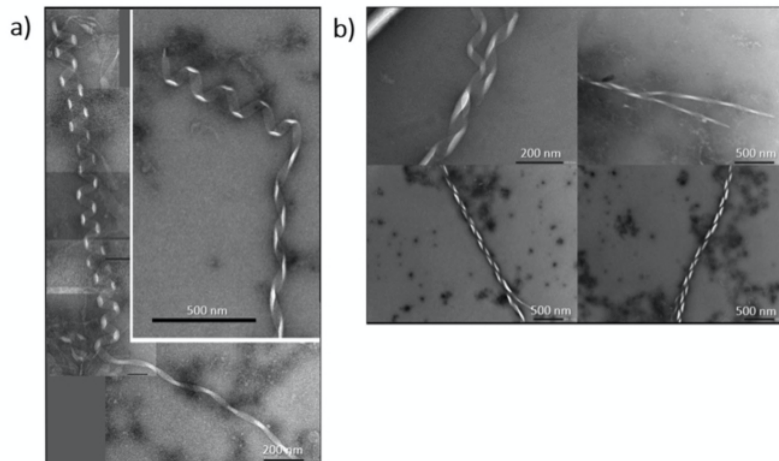
Fig. 3 Polymorph unwinding. a αS polymorph 'helices' are observed to unwind into 'ribbons' and 'waves'. **b** The αS macromolecular assemblies have been observed to have frayed ends, suggesting a common building block between the different polymorphs.

bound during the formation of these structures. At 190 h the sample was again analysed by TEM, with fibril-like structures appearing to aggregate into much larger macromolecular assemblies (Fig. 2b). Within the sample a range of macromolecular polymorphs not previously described can be seen ranging in width and helicity (Figs. 1, 2b).

The width of the assemblies are up to ten times larger than αS structures reported previously; up to 100 nm, with helical pitches of ~40–100 nm (Fig. 1). Observed helicity is also wide ranging; in the most elongated assemblies (Fig. 1), we observe ribbon-like structures ('ribbons') with a pitch ~200 nm, increasing to low helicity structures ('waves') with a similar pitch of ~200 nm. Next, we observe structures that resemble a classic helical signature ('helices') with a pitch of ~100 nm. Finally, very electron-dense compact helical structures ('compact helices') are formed. 'Ribbons', 'waves' and 'helices' are all ~40–50 nm wide, but as would be expected, 'compact helices' by contrast are much larger at ~100 nm in width. All structures are capable of reaching many microns in length with some variations in width and helicity. Interestingly, we also observe changes in helical type within the same fibril, suggesting that 'helices', 'waves' and 'ribbons' are interconvertible (Fig. 3a). Finally, we also report upon branched fibril termini, which may represent the formation of the larger assemblies from smaller structures (Fig. 3b). This also suggests that these macromolecular assemblies may be formed by the same common αS fibril building blocks that then cluster adjacently along the vertical axis. Reassuringly, the same structures were observed upon three separate repetitions of the experiment. These were undertaken weeks apart and in each case were prepared using both fresh αS and DMPS vesicle preparations (Supplementary Fig. 5), demonstrating both the reproducibility of our findings and similar morphologies of the αS aggregates observed (Supplementary Fig. 6).

Regarding molecular determinants of αS–lipid interaction that may predetermine the formation of the structures we report, it has been proposed that lysine-rich positions within αS may interact with negatively charged lipid head groups, while hydrophobic regions may interact with membrane lipids, leading to an initial helical conformation[1,28,29]. Specifically, the central region of the protein (residues 26–97) has been shown to bind to lipid membranes and positive charge within the N-terminal region may also play a key role in mediating binding to anionic lipids[30,31]. A high local concentration of αS at the membrane could potentially lead to primary nucleation and a conversion to β-sheet formation. The position of single amino acid changes associated

with early-onset PD mutations is likely to alter sidechain–sidechain or sidechain–lipid interactions that modulate helix formation, thereby accelerating the pathway toward amyloidosis[26].

Given the proposed native role of αS in synaptic transmission and signalling, and the clear interaction of αS with dopaminergic neuronal membranes, the discovery of these structures in the presence of phospholipid vesicles is likely to have far-reaching implications towards defining a pathogenic αS conformation that has significant potential to open up new routes towards new conformations and drug targets for diseases in which αS aggregates present.

METHODS

Protein expression and purification of human wild-type αS
Wild-type (wt) human αS was recombinantly expressed and purified based on, and modified from, a previously published method (Supplementary Fig. 1)[32,33]. Briefly, the pET21a plasmid containing the human wt αS (1–140), purchased from Addgene (deposited by the Michal J. Fox Foundation (MJFF), Plasmid #51486), was transformed into *Escherichia coli* expression cell line BL21 (DE3). 2xYT overnight cultures containing ampicillin of this human wt αS (1–140) pET21a BL21 (DE3) *E. coli* strain were used to inoculate 1 l 2xYT cultures, containing 100 mg l^{-1} ampicillin, and grown at 37 °C, 200 r.p.m. shaking, to $OD_{600} = 0.6$–0.8 and induced with 1 mM isopropyl-1-thio-D-galactopyranoside at 37 °C, 200 r.p.m. shaking, for 4 h in an Innova 44 Incubator shaker (New Brunswick Scientific). The bacteria were harvested by centrifugation at 4600 × g, and resuspended in 40 ml of 20 mM Tris buffer pH 8 containing 1 complete protease inhibitor tablet (Roche) and freeze-thawed at −20 °C before lysis, by sonication. The cell debris was discarded by centrifugation at 48,400 × g, and the supernatant was collected and boiled at 95 °C for 10 min. The precipitated protein was removed by centrifugation at 18,500 × g. The supernatant was collected, and ammonium sulfate was added to 30% saturation (0.176 g ml^{-1}), and left shaking at 20 °C for 1 h. The precipitated protein, containing the αS, was harvested by centrifugation at 18,500 × g, and then resuspended in 50 ml of 20 mM Tris buffer pH 8 by gentle agitation at 4 °C. The proteins were purified by anion exchange chromatography on an AKTA pure purification system (GE Healthcare) with a 5 ml HiTrap Q HP (GE Healthcare) pre-packed column, to remove protein impurities and protein-bound nucleic acids. The purified fractions were combined and further purified by size-exclusion chromatography (SEC), using a HiLoad 16/60 Superdex 75 pg (GE Healthcare) pre-packed purification column, to buffer exchange the αS into the relevant reaction buffer (20 mM sodium phosphate buffer pH 6.5/20 mM sodium acetate pH 5.0) and ensure that only monomers were collected. Pure monomeric αS was eluted between 54 and 60 ml.

The concentration of the purified αS was determined in a 2-mm path length quarts cuvette, using an extinction coefficient of 4836 M^{-1} cm^{-1} at

280 nm, separated into 1 ml aliquots, snap frozen in liquid N_2, and stored at −80 °C until required.

The purity of αS following SEC was confirmed by sodium dodecyl sulfate-polyacrylamide gel electrophoresis, and the correct mass was confirmed by mass spectrometry on a Dionex Acclaim RSLC Polar Advantage II (PA2), 2.2 μm, 120 Å, 2.1 × 50 mm^2 (Thermo Fisher Scientific, California, USA). The deconvoluted average mass of the protein was confirmed as 14,459.749m/z, representing the mass of wt human αS (1–140). A circular dichroism spectra scan was performed, to confirm the random coil conformation of the monomeric αS stock (Supplementary Fig. 5).

Microplate ThT kinetic assays without shaking to measure lipid-induced aggregation

ThT kinetic assays for lipid induced primary nucleation of αS were performed in a CLARIOstar fluorescence microplate reader (BMG Labtech), under quiescent conditions (without shaking), 30 °C in black, clear-bottomed 96-well half area polystyrene plates with non-bonding surface (Corning #3881) covered with Aluminium Thermowell Sealing Tape (Corning #6570). The focal height was set to 4.9 mm, and gain to 800, with an excitation filter of 440–15 nm and emission filter of 480–15 nm and a dichroic cut-off of 460 nm. Well measurements were taken by spiral average of 4 mm using the bottom optic, with 50 flashes per well and a cycle time of 1200 s. The outer wells of the plate were not used. The experiments were performed in 100 μl aliquots, in triplicate, each containing 100 μM αS, 50 μM ThT, 200 μM DMPS, and 0.01% sodium azide in 20 mM phosphate buffer pH 6.5.

Lipid preparation for induced primary nucleation method

The mass of dry DMPS lipid powder was determined using an ultra-micro balance (Sartorius), and dissolved in 20 mM sodium phosphate buffer pH 6.5 to a concentration of 2 mM. This was dissolved by shaking, in a 2 ml Eppendorf tube, on a Thermomixer compact (Eppendorf), at 45 °C, 1400 r.p.m. for 3 h. The solution was then freeze-thawed five times using dry ice and the thermomixer compact (Eppendorf) at 45 °C and 500 r.p.m. The preparation of the vesicles was carried out by sonication, using a Soniprep 150 plus sonicator, set to an amplitude of 10.0, for five cycles of 30 s on and 30 s off.

DLS measurements

A sample of the vesicles produced at each step was diluted to 100 μM in 20 mM phosphate buffer pH 6.5. Their size distribution was measured by DLS, using a Zetasizer Nano ZSP (Malvern Instruments), to ensure a final consistent size of between 20 and 30 nm was obtained (Supplementary Fig. 2).

Transmission electron microscopy

αS samples from the end point of the aggregation kinetics were collected. Five microlitres of these samples were put onto glow-discharged Formvar/carbon-coated, 200-mesh, copper grids for 1 min. The samples were dried with a filter paper, and then washed twice with Milli-Q water for 1 s, and removed each time with filter paper. The sample was stained by incubating the grids with 5 μl Uranyl Acetate Zero (Agar Scientific) for 30 s, followed by removal of the excess stain with a filter paper. The grids were left to air dry for 2 h. The samples were imaged using a Transmission Electron Microscopy Jeol 2100 Plus (JEOL), operating at an accelerating voltage of 200 kV. Multiple grids were screened in order to obtain representative images of the samples.

Reporting summary

Further information on experimental design is available in the Nature Research Reporting Summary linked to this article.

DATA AVAILABILITY

The datasets generated during and/or analysed during the current study are available from the corresponding author on reasonable request.

REFERENCES

1. Meade, R. M., Fairlie, D. P. & Mason, J. M. Alpha-synuclein structure and Parkinson's disease—lessons and emerging principles. *Mol. Neurodegen.* **14**, 14 (2019).
2. Tuttle, M. D. et al. Solid-state NMR structure of a pathogenic fibril of full-length human alpha-synuclein. *Nat. Struct. Mol. Biol.* **23**, 409–415 (2016).
3. Guerrero-Ferreira, R. et al. Cryo-EM structure of alpha-synuclein fibrils. *eLife* **7**. https://doi.org/10.7554/eLife.36402 (2018).
4. Li, Y. W. et al. Amyloid fibril structure of alpha-synuclein determined by cryoe-lectron microscopy. *Cell Res.* **28**, 897–903 (2018).
5. Li, B. S. et al. Cryo-EM of full-length alpha-synuclein reveals fibril polymorphs with a common structural kernel. *Nat. Commun.* **9**, 10 (2018).
6. Galvagnion, C. et al. Lipid dynamics and phase transition within alpha-synuclein amyloid fibrils. *J. Phys. Chem. Lett.* https://doi.org/10.1021/acs.jpclett.9b03005, 7872–7877 (2019).
7. Zhao, K. et al. Parkinson's disease associated mutation E46K of alpha-synuclein triggers the formation of a distinct fibril structure. *Nat. Commun.* **11**, 2643 (2020).
8. Schweighauser, M. et al. Structures of alpha-synuclein filaments from multiple system atrophy. *Nature.* https://doi.org/10.1038/s41586-020-2317-6 (2020).
9. Guerrero-Ferreira, R. et al. Two new polymorphic structures of human full-length alpha-synuclein fibrils solved by cryo-electron microscopy. *Elife* **8**. https://doi.org/10.7554/eLife.48907 (2019).
10. Stephens, A. D. et al. Extent of N-terminus exposure of monomeric alpha-synuclein determines its aggregation propensity. *Nat. Commun.* **11**, 2820 (2020).
11. Viennet, T. et al. Structural insights from lipid-bilayer nanodiscs link alpha-synuclein membrane-binding modes to amyloid fibril formation. *Commun. Biol.* **1**, 12 (2018).
12. Boyer, D. R. et al. The alpha-synuclein hereditary mutation E46K unlocks a more stable, pathogenic fibril structure. *Proc. Natl Acad. Sci. USA.* https://doi.org/10.1073/pnas.1917914117 (2020).
13. Jao, C. C., Hegde, B. G., Chen, J., Haworth, I. S. & Langen, R. Structure of membrane-bound alpha-synuclein from site-directed spin labeling and computational refinement. *Proc. Natl Acad. Sci. USA* **105**, 19666–19671 (2008).
14. Madine, J., Doig, A. J. & Middleton, D. A. A study of the regional effects of alpha-synuclein on the organization and stability of phospholipid bilayers. *Biochemistry* **45**, 5783–5792 (2006).
15. Galvagnion, C. et al. Lipid vesicles trigger alpha-synuclein aggregation by stimulating primary nucleation. *Nat. Chem. Biol.* **11**, 229–U101 (2015).
16. Galvagnion, C. The Role of Lipids Interacting with alpha-synuclein in the pathogenesis of Parkinson's disease. *J. Parkinsons Dis.* **7**, 433–450 (2017).
17. Agerschou, E. D. et al. An engineered monomer binding-protein for alpha-synuclein efficiently inhibits the proliferation of amyloid fibrils. *Elife* **8**, 31 (2019).
18. Strohaker, T. et al. Structural heterogeneity of alpha-synuclein fibrils amplified from patient brain extracts. *Nat. Commun.* **10**, 12 (2019).
19. Boyer, D. R. et al. Structures of fibrils formed by alpha-synuclein hereditary disease mutant H50Q reveal new polymorphs. *Nat. Struct. Mol. Biol.* **26**, 1044–1052 (2019).
20. Fanning, S., Selkoe, D. & Dettmer, U. Parkinson's disease: proteinopathy or lipidopathy? *NPJ Parkinsons Dis.* **6**, 3 (2020).
21. Rawat, A., Langen, R. & Varkey, J. Membranes as modulators of amyloid protein misfolding and target of toxicity. *Biochimica Et. Biophysica Acta-Biomembranes* **1860**, 1863–1875. https://doi.org/10.1016/j.bbamem.2018.04.011 (2018).
22. Varkey, J. et al. Membrane curvature induction and tubulation are common features of synucleins and apolipoproteins. *J. Biol. Chem.* **285**, 32486–32493 (2010).
23. Perni, M. et al. Multistep inhibition of alpha-synuclein aggregation and toxicity in vitro and in vivo by trodusquemine. *ACS Chem. Biol.* **13**, 2308–2319 (2018).
24. Buell, A. K. et al. Solution conditions determine the relative importance of nucleation and growth processes in alpha-synuclein aggregation. *Proc. Natl Acad. Sci. USA* **111**, 7671–7676 (2014).
25. Brown, J. W. P. et al. Kinetic barriers to alpha-synuclein protofilament formation and conversion into mature fibrils. *Chem. Commun.* **54**, 7854–7857 (2018).
26. Flagmeier, P. et al. Mutations associated with familial Parkinson's disease alter the initiation and amplification steps of alpha-synuclein aggregation. *Proc. Natl Acad. Sci. USA* **113**, 10328–10333 (2016).

27. Ross, B. M., Mamalias, N., Moszczynska, A., Rajput, A. H. & Kish, S. J. Elevated activity of phospholipid biosynthetic enzymes in substantia nigra of patients with Parkinson's disease. *Neuroscience* **102**, 899–904 (2001).

28. Dettmer, U. Rationally designed variants of alpha-synuclein illuminate its in vivo structural properties in health and disease. *Front. Neurosci.* **12**, 14 (2018).

29. Bendor, J. T., Logan, T. P. & Edwards, R. H. The function of alpha-synuclein. *Neuron* **79**, 1044–1066 (2013).

30. Fusco, G. et al. Structural basis of membrane disruption and cellular toxicity by alpha-synuclein oligomers. *Science* **358**, 1440–+ (2017).

31. Fusco, G. et al. Direct observation of the three regions in alpha-synuclein that determine its membrane-bound behaviour. *Nat. Commun.* **5**, 8 (2014).

32. Pujols, J. et al. High-throughput screening methodology to identify alpha-synuclein aggregation inhibitors. *Int. J. Mol. Sci.* **18**. https://doi.org/10.3390/ijms18030478 (2017).

33. Volles, M. J. & Lansbury, P. T. Jr. Relationships between the sequence of alpha-synuclein and its membrane affinity, fibrillization propensity, and yeast toxicity. *J. Mol. Biol.* **366**, 1510–1522 (2007).

ACKNOWLEDGEMENTS

AUTHOR CONTRIBUTIONS

J.M.M. directed the research. R.M.M. conducted the experiments, and expressed, purified and characterised the protein. R.M.M., R.J.W. and J.M.M. participated in experimental design, analysis of the data and writing the paper.

COMPETING INTERESTS

J.M.M. is an advisor to Sapience Therapeutics. The authors declare no other competing interests.

ADDITIONAL INFORMATION

Supplementary information is available for this paper at https://doi.org/10.1038/s41531-020-00122-1.

Correspondence and requests for materials should be addressed to J.M.M.

Reprints and permission information is available at http://www.nature.com/reprints

Publisher's note Springer Nature remains neutral with regard to jurisdictional claims in published maps and institutional affiliations.

122

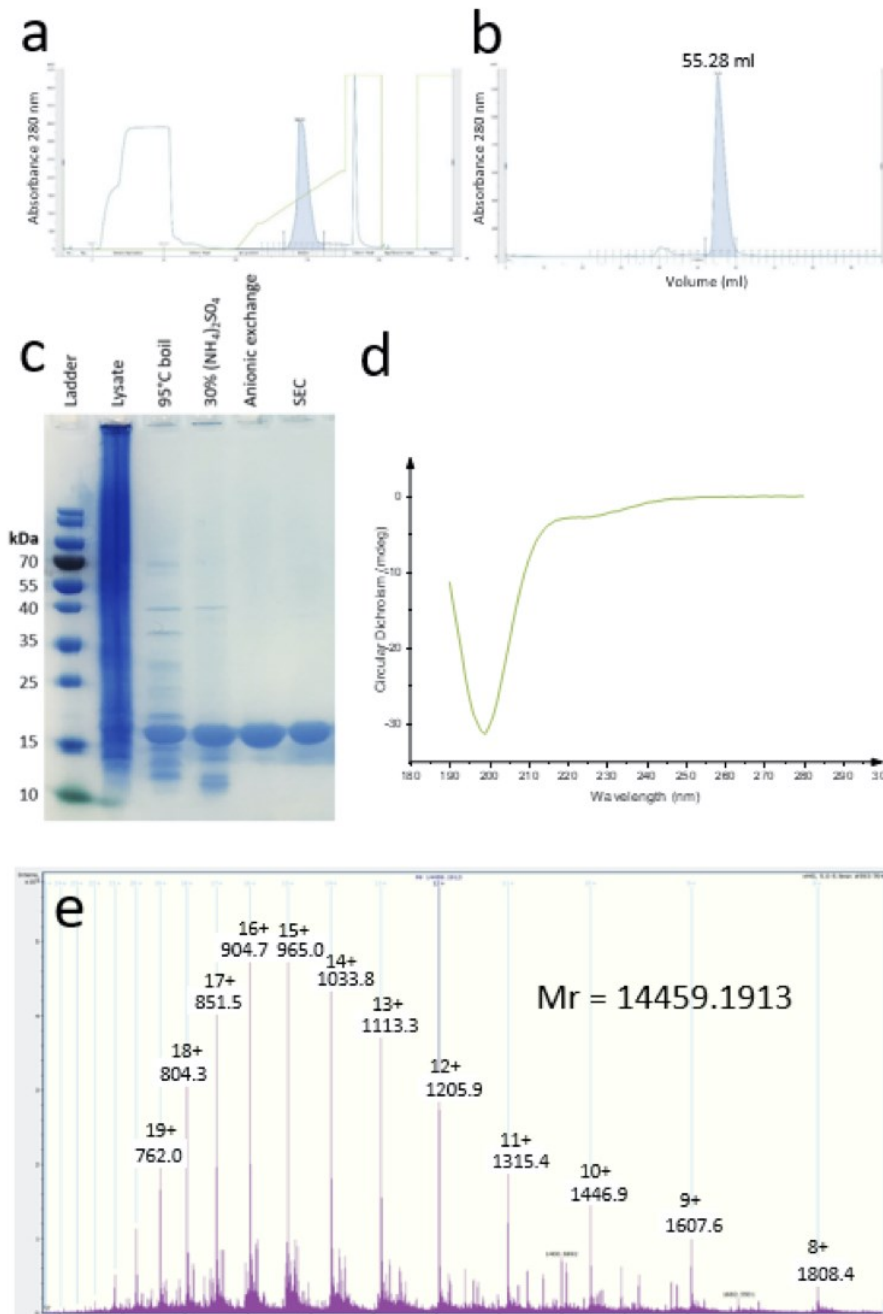# Chapter 5:
Supporting Information

Supporting Information

Production and of Purification of Human wt αS

Supplementary Figure 1: Overview of the purification of αS used for the experiments. a) Chromatograph of the Hi-Q anionic exchange purification. b) Chromatograph of the Size exclusion chromatography and buffer exchange. c) SDS page gel showing an overview of the entire purification protocol. d) Far-UV circular dichroism spectra of the purified αS showing that the monomeric αS is in a random coil conformation. e) De-convoluted mass spectrum, showing a mass of the protein of 14459 m/z, representing the mass of wt Human αS (1-140).

Production and of DMPS SUVs
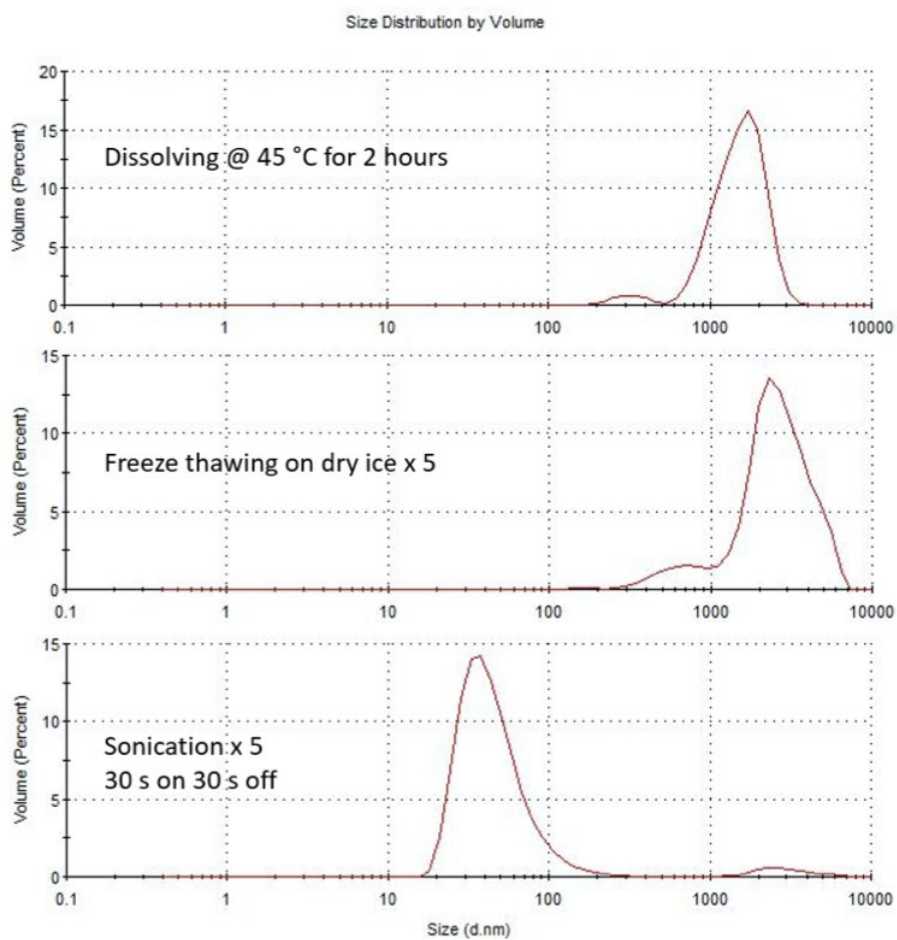
Supplementary Figure 2: Dynamic light scattering size distribution of the DMPS small unilamellar vesicles (SUVs) used for lipid induced nucleation assays, showing a size distribution centred around 30 nm post sonication.

Production and of DMPS SUVs
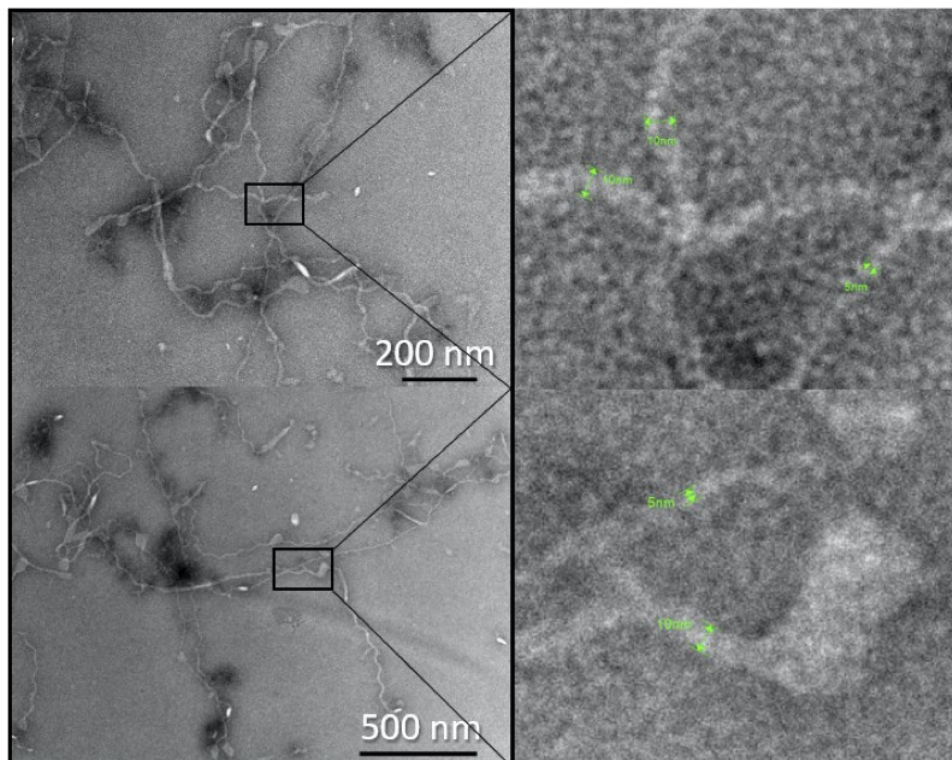
Supplementary Figure 3: TEM images of fibril like structures from 48 hours incubation with lipids, displaying fibril widths of 5 and 10 nm width wavy fibrils.
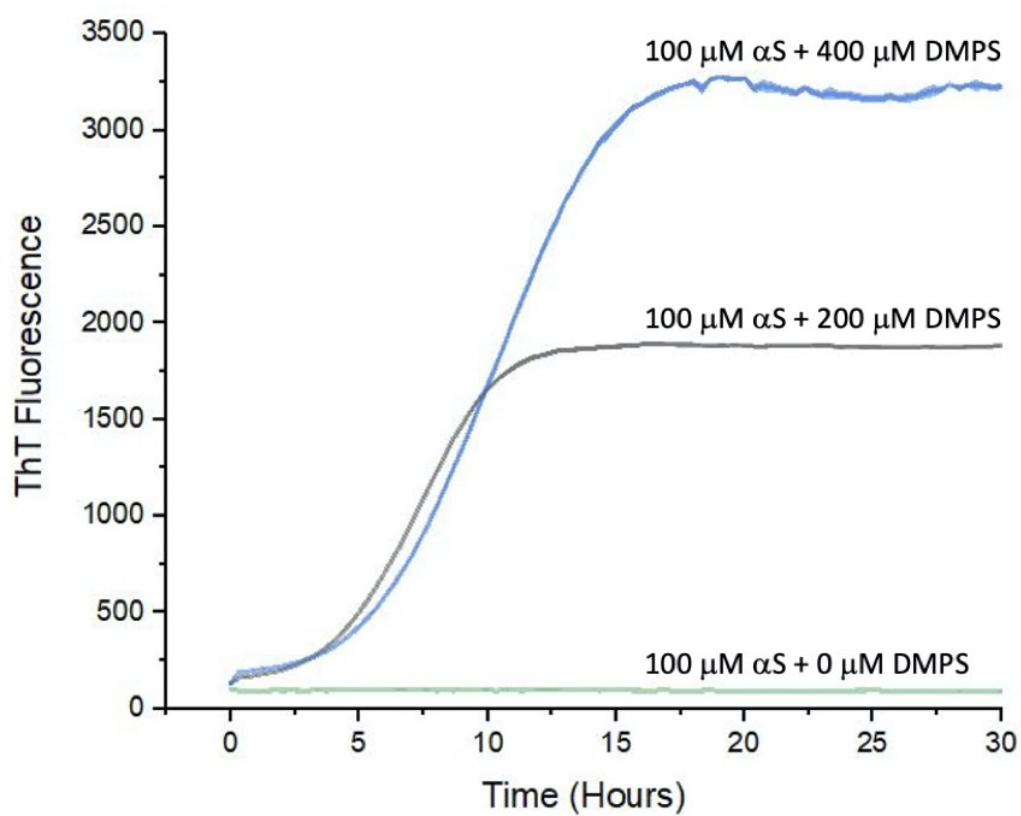
Supplementary Figure 4: αS incubation in the presence and absence of DMPS SUVs. αS (100 μM) in 20 mM sodium phosphate buffer (pH 6.5), with ThT (50 μM), incubated with DMPS (200 μM – grey; 400 μM - blue), or in the absence of DMPS (green) at 30 °C under quiescent conditions Each trace is the average of three repeats showing standard error.
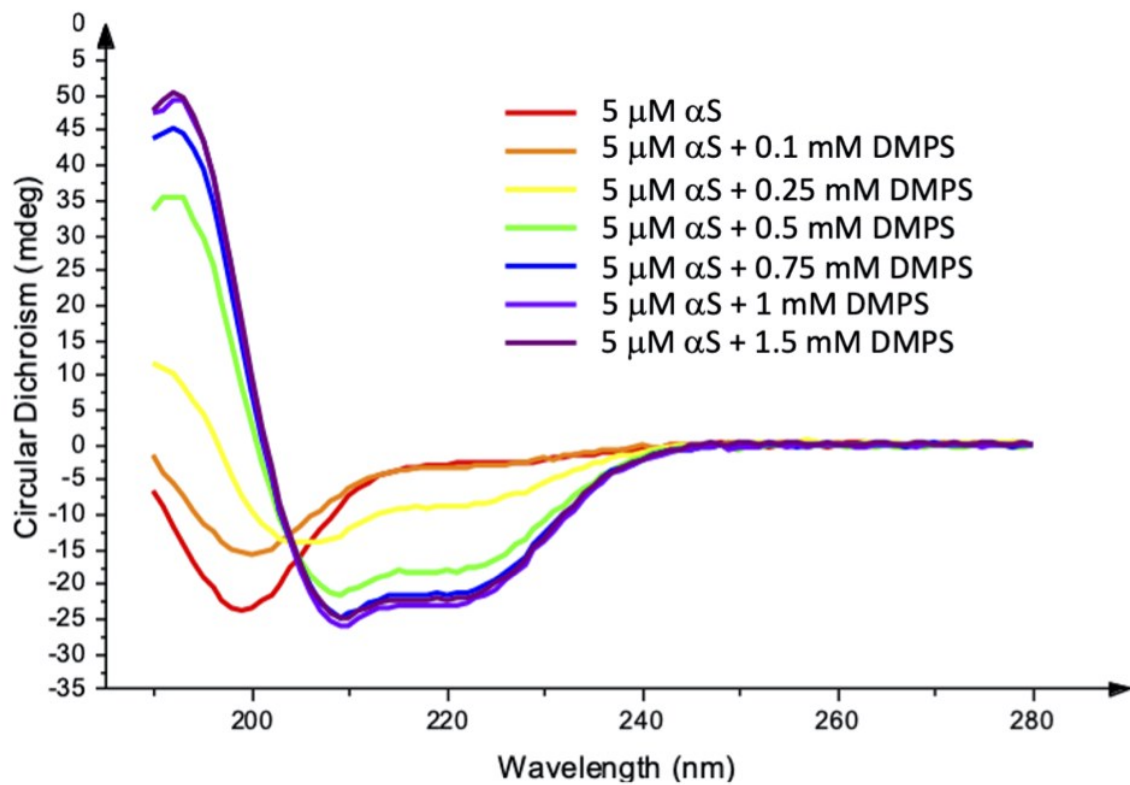
Supplementary Figure 5: Circular Dichroism studies in the presence of lipid vesicles *a)* Circular dichroism of αS with increasing concentrations of DMPS SUVs. In isolation αS exists as a random coil. The conformation of αS shifts towards an α-helical structure with increasing concentration of DMPS SUVs. Data presented represent an average of three repeats.
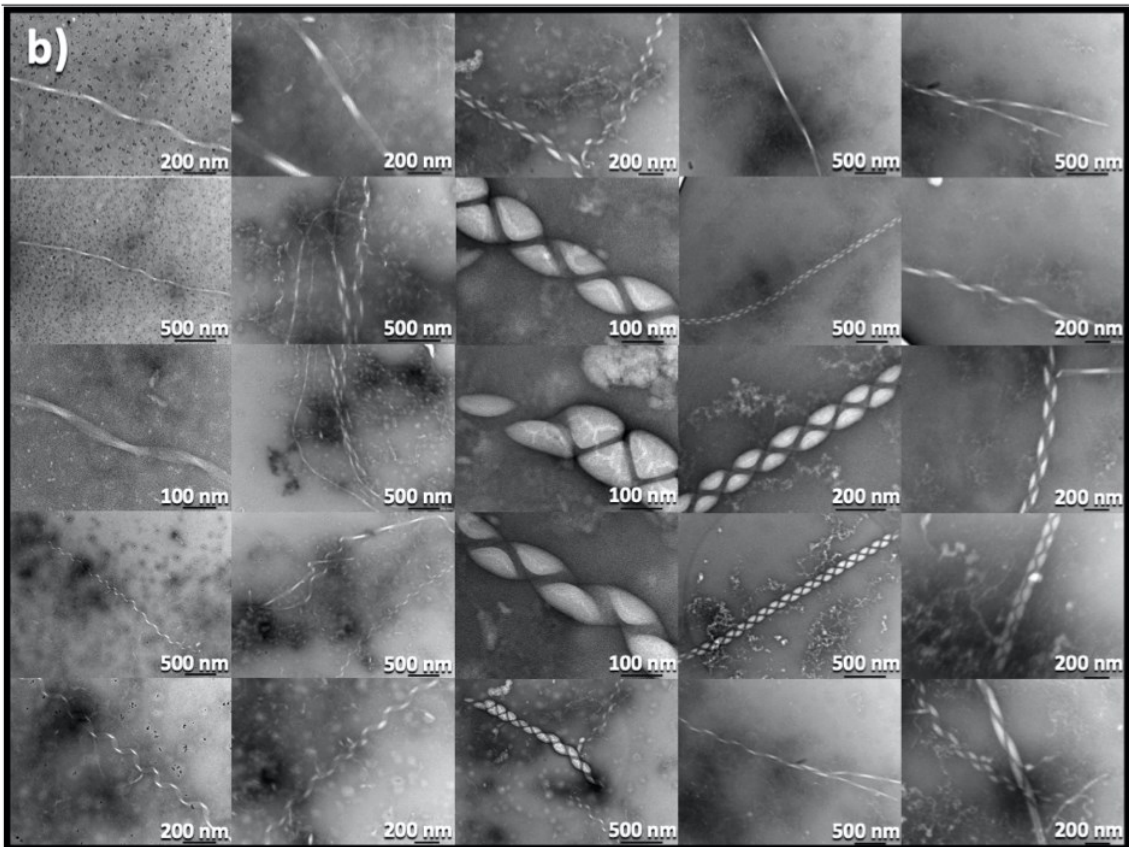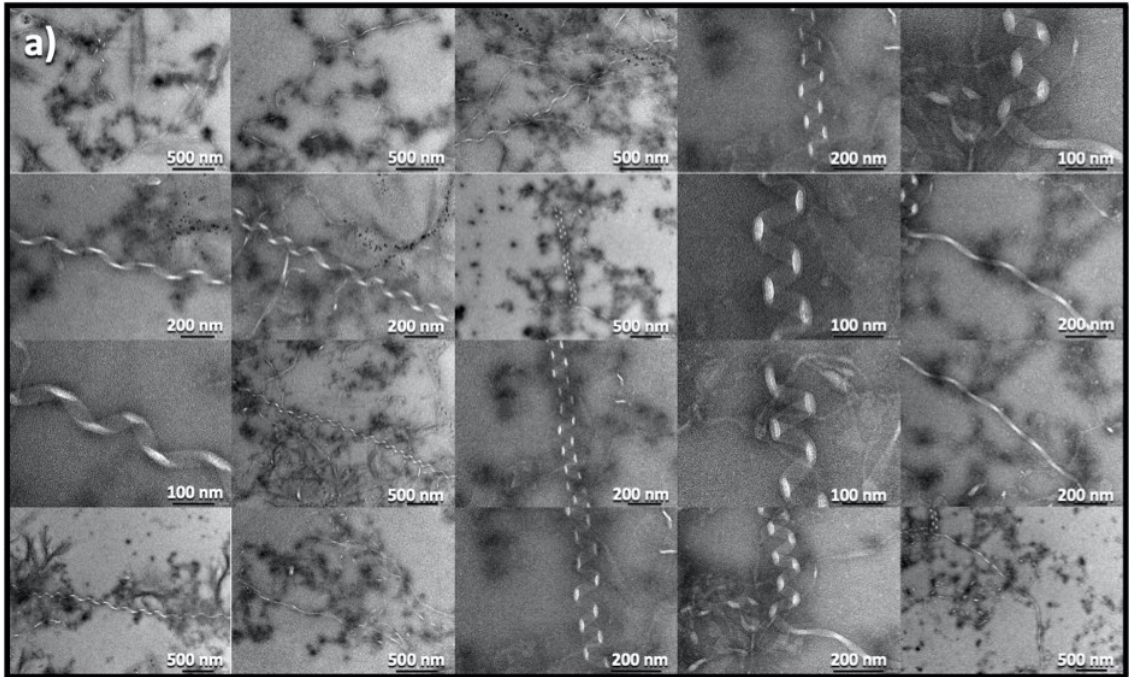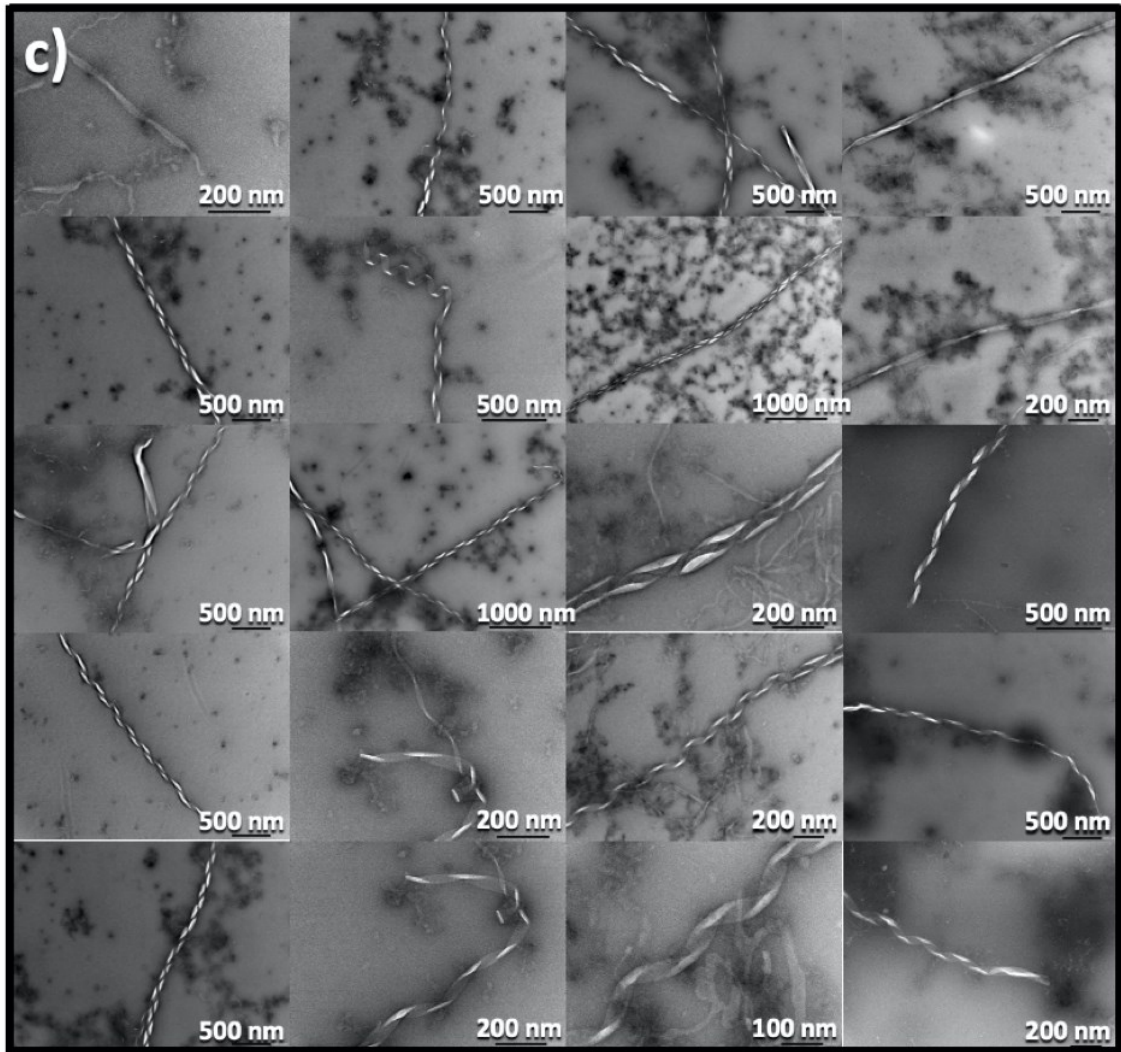
Supplementary Figure 6: TEM images taken from three separate repetitions of the experiment using fresh αS and DMPS SUV preparations. The fibrils were created by aggregating 100 μM αS in the presence of 200 μM DMPS lipid vesicles at 30 °C for 190 hrs. The structures have initially been divided into four subtypes with varying degrees of helicity named ribbons, waves, helices and compact helices (see Fig 1). This work highlights both the reproducibility of the findings and confirms the variability in morphologies of the αS aggregates produced. Shown are fibrils images in *a)* November 2019 *b)* January 2020 *c)* February 2020

Chapter 6:

Refinement of an intracellular library-derived peptide inhibitor of alpha-synuclein aggregation

6.1 Abstract

The misfolding and aggregation of alpha-synuclein (αS) within dopaminergic neurons are key factors in the development and progression of a group of age-related synucleinopathies, that includes Parkinson's disease. A previously described peptide was derived from a 209,952-member intracellular library screen, and employed the 45-54 'preNAC' region of αS as a design template. Key early-onset mutants (E46K, H50Q, A53T, G51D) are located in this region, strongly implicating it in the modulation of protein-protein interactions that lead to increased aggregation and cytotoxicity. The selected peptide, 4554W, has been shown to inhibit lipid-induced primary nucleation of αS into cytotoxic conformations. Here we perform a full alanine scan upon the 4554W peptide, followed by analysis of the aggregation pathway, to elucidate if inhibitory function is maintained, and to reveal the precise residues involved in inhibitory interaction and function. In particular, we find that a truncated and modified peptide derivative, 4654W(N6A), displays increased efficacy over 4554W, paving the way towards the major aim of deriving an increased potency peptide antagonist of αS pathogenicity.

6.2 Introduction

The misfolding and aggregation of Alpha-synuclein (αS), a 140-residue membrane associated neuronal protein, is believed to be the leading cause of a number of neurodegenerative diseases, referred to collectively as synucleinopathies. This includes Parkinson's disease (PD), multiple system atrophy (MSA), and Dementia with Lewy Bodies (DLB), and accounts for approximately 15% of all known dementia cases (Cookson, 2009). Previous research seeking to target and detoxify aggregation induced cytotoxicity of αS employed an intracellular Protein-fragment Complementation Assay (PCA) (Pelletier et al., 1999) . The 209,952 member library, based on preNAC residues 45-54 of αS was screened resulting in the derivation and development of 4554W (Cheruvara et al., 2015), a peptide which has been shown to function by inhibiting the primary nucleation step of the αS aggregation pathway (see chapter 4). Moreover the peptide was found to be capable of rescuing αS mediated cytotoxicity in PC-12 cells(Cheruvara et al., 2015), as well as SH-SY5Y human neuroblastoma cells (see chapter 4). The 45-54 region of αS is a particularly compelling antagonist design template, (Fig 6.1a)

and was chosen since it is the sequence where most early onset familial mutations are located (E46K (Choi et al., 2004; Zarranz et al., 2004; Greenbaum et al., 2005), H50Q (Appel-Cresswell et al., 2013; Ghosh et al., 2013; Khalaf et al., 2014; Rutherford et al., 2014), G51D(Lesage et al., 2013; Rutherford et al., 2014), A53T(Polymeropoulos et al., 1997), A53E(Ghosh et al., 2014; Pasanen et al., 2014), A53V(Yoshino et al., 2017)), demonstrating the importance of this region in modulating both intra- and intermolecular protein-protein interactions (PPIs) that subsequently lead to the accelerated development of αS aggregates, and ultimately the symptoms of PD. The known mutations at that time, (E46K, H50Q and A53T), along with residues presenting similar properties to those within the scaffold region, were included in the library design (Fig. 6.1b) and resulted in the selection of 4554W (Cheruvara et al., 2015) (Fig. 6.1c).

Subsequently 4554W was shown to function by inhibiting the primary nucleation of αS into fibril like structures in the presence of small unilamellar vesicles (SUVs) composed of the anionic lipid 1,2-Dimyristoyl-sn-glycero-3-phospho-L-serine (DMPS), which is able to interact at least in part via positively charged residues within αS (Meade, R. M., Fairlie and Mason, 2019) (see chapter 4). The role of DMPS is not fully understood, but levels of phosphotidylserine have been found to increase by about 36%, in brains of patients showing Lewy body pathology but devoid of motor symptoms (Fabelo et al., 2011), and DMPS has been suggested to play a role in regulating αS-facilitated synaptic vesicle docking, linked to SNARE complex formation (Lou et al., 2017; Fanning, Selkoe and Dettmer, 2020). The use of vesicles composed of this phospholipid have proven to be a useful tool in probing the effectiveness of molecules to inhibit primary nucleation (Galvagnion, C. et al., 2015; Galvagnion, C., 2017; Perni et al., 2017; Perni et al., 2018; Galvagnion, Celine et al., 2019).

Here we perform a full alanine scan on 4554W (Fig 6.1d), followed by inspection of the principle steps within the aggregation pathway to elucidate which residues are key for 4554W interacting with αS, which are required for inhibiting αS aggregation into toxic conformations, and to establish for each construct if efficacy is maintained via modulation at same point of aggregation as the 4554W parent peptide. Understanding the contribution of each side chain upon the primary nucleation, elongation and secondary nucleation of αS aggregation will facilitate the design of more potent peptides, with increased αS affinity and efficacy.

6.3 Results and discussion

Probing Inhibition of Lipid Induced Primary Nucleation of αS Aggregation Using Alanine Scanning.

To establish the effect of the 4554W alanine scan variants on lipid induced primary nucleation of monomeric αS, aggregation experiments were performed in the presence of DMPS vesicles, at neutral pH (pH 6.5) and 30 °C, as per previously developed methods (Buell, Alexander K. et al., 2014; Galvagnion, C. et al., 2015; Perni et al., 2018; Meade, Richard M., Williams and Mason, 2020) (see chapter 4) (Fig. 6.2). Briefly, monomeric αS (100μM), and peptide (1000 μM) were mixed with DMPS SUVs (200 μM), of approximately 30-40 nm diameter (i.e. of similar size to vesicles found at the synaptic terminal of dopaminergic neurons (Sulzer, Cragg and Rice, 2016)), under quiescent conditions. A 10:1 excess of peptide:αS was utilized to ensure that inhibitory activity was not overlooked, even at a low level. The aggregation kinetics were followed by monitoring the increase in ThT florescence. Experiments were carried out in triplicate in a 96 well plate. Under these conditions' inhibition of αS aggregation was found to differ widely between peptide variants (Fig 6.1 and 6.2), highlighting key residues within 4554W that impact upon this initial stage of the aggregation pathway.

.	Residue	1	2	3	4	5	6	7	8	9	10
a)	αS45-54	K	E	G	V	V	H	G	V	A	T
b)	Library	K	E	G	V	V	H	G	I	A	T
		E	Q	A	I	I	Q	A	L	V	A
			N	V	L	L	N	V		T	
			K				K			I	
			D				D			K	
			H				E			E	
c)	Winner	K	D	G	I	V	N	G	V	K	A
d)	4554W(K1A)	A	D	G	I	V	N	G	V	K	A
	4554W(D2A)	K	A	G	I	V	N	G	V	K	A
	4554W(G3A)	K	D	A	I	V	N	G	V	K	A
	4554W(I4A)	K	D	G	A	V	N	G	V	K	A
	4554W(V5A)	K	D	G	I	A	N	G	V	K	A
	4554W(N6A)	K	D	G	I	V	A	G	V	K	A
	4554W(G7A)	K	D	G	I	V	N	A	V	K	A
	4554W(V8A)	K	D	G	I	V	N	G	A	K	A
	4554W(K9A)	K	D	G	I	V	N	G	V	A	A
	4554W	K	D	G	I	V	N	G	V	K	A
e)	4553W(N6A)	K	D	G	I	V	A	G	V	K	
	4654W(N6A)		D	G	I	V	A	G	V	K	A
	4754W(N6A)			G	I	V	A	G	V	K	A
	4552W(N6A)	K	D	G	I	V	A	G	V		
	4653W(N6A)		D	G	I	V	A	G	V	K	

Figure 6.1: 4554 region library design, winner, and alanine scan sequence variants: a) the template region of αS consisting of residues 45 to 54 of the wild type protein. **b)** PCA library members used to create a 209,952-member library. Early onset mutant residue options are shown (orange) **c)** The sequence of the 4554W peptide selected via the PCA assay. **d)** Alanine scan variants of 4554W. Variant alanine position shown (red) **e)** Truncated peptide variants based on active sequence 4554W(N6A).

During lipid induced primary nucleation experiments, it was observed that all substitutions except K1A and N6A disrupted the inhibitory effect of 4554W. This suggests that all other residues, (D2, G3, I4, V5, G7, V8, K9 and possibly A10) play important roles in the inhibitory effect of 4554W upon this part of the aggregation pathway. Of particular note, both 4554W(K1A) and 4554W(N6A) exhibited an increase in efficacy of the peptide. At the concentration measured, 4554W represented a 36% reduction in aggregation as measured by ThT fluorescence relative to αS alone, 4554W(K1A) represented a 90% reduction, and 4554W(N6A) represented a 100% reduction over the 20-hour timescale of the experiment. Since Alanine was not presented as an option in these positions in the original library (Fig 6.1b), this suggests an improvement to the original 4554W template, and that sidechain

truncation and loss of charge/polarity at positions 1 and 6 is potentially of benefit. Of these two alanine scan peptides, 4554W(N6A) was the most potent, as it represents a more favourable inhibitory effect. In addition, 4554W(K1A) presented issues with solubility at higher stock concentrations, with 4554W(N6A) soluble at 5 mM, compared to 4554W(K1A), which was only soluble up to 2 mM), and therefore only 2 mM stocks were used for all the peptides. This can be attributed to the loss of a positive charge for the K1A substitution, which is more dramatic than N6A.

Additional it should be noted that the G3A, G7A and K9A substitutions all rendered the peptide inactive. In each of these positions' alanine was an option in the original library screen suggesting that the original residues in these positions are important. The glycine residues in position 3 and 7 may confer an element of rotational flexibility to the peptides, and the lysine residue in position 9 may be crucial to peptide docking via an 'ionic lock'.
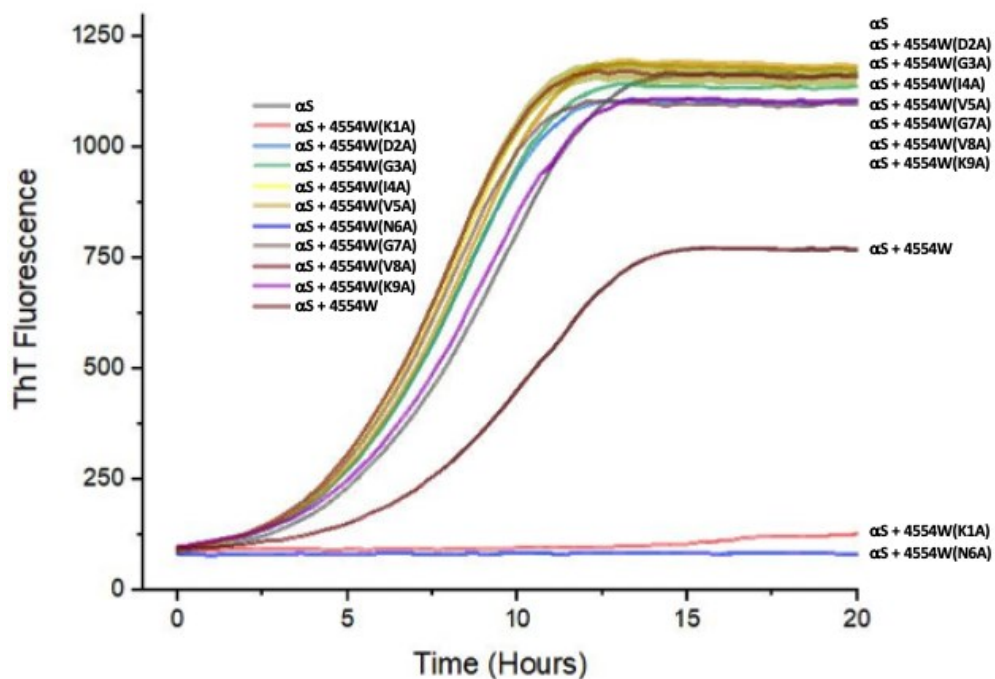
Figure 6.2: Effect of 4554W alanine scan variants on lipid induced primary nucleation. Inhibition of lipid induced primary nucleation of αS with the 4554W alanine scan variant peptides measured by change in ThT fluorescence intensity when 100 μM monomeric αS was incubated with 1000 μM peptide in the presence of 200 μM DMPS SUVs and 50 μM ThT in 20 mM sodium phosphate buffer pH 6.5 under quiescent conditions at 30 °C. The inhibitory effect is lost with D2A, G3A, I4A, V5A, G7A, V8A and K9A variants, suggesting that these residues are required for the peptide to induce primary nucleation. Inhibitory activity is improved for K1A and N6A relative to the parental protein (A10), suggesting that these substitutions are important for binding and can be improved (Ala was not a library option in either position). All profiles show the averages of assays undertaken in triplicate showing standard error.

It was previously determined that the parental 4554W peptide acts upon lipid-induced primary nucleation, with no effect reported on fibril elongation rates, or secondary nucleation/fibril amplification (see chapter 4), under conditions that favoured these pathways as the prominent mechanism of aggregation (Buell, Alexander K. et al., 2014; Agerschou et al., 2019). Here we report that consistent with 4554W, all alanine scan peptide variants exhibited no antagonistic effects on αS fibril elongation or secondary nucleation/fibril amplification (supp. Fig 6.8 and 6.10), and that rather the effects were only observed upon primary nucleation (Fig 6.2). Therefore, the effect of further peptide modifications were only explored on primary nucleation.

4554W(N6A) Inhibits the Lipid Induced Primary Nucleation Step of αS Aggregation in a Dose Dependant Manner to Prevent the Formation of Fibril-like Structures.

The effect of 4554W(N6A) on lipid induced primary nucleation of monomeric αS was found to be more potent than 4554W, and the most potent peptide overall. At the concentration used (a 1:10 molar excess) no aggregation was measured when monitored by ThT fluorescence over 20 hours (Fig. 6.2). To probe this further, aggregation kinetics of lipid induced nucleation were followed and again repeated in triplicate, with increasing concentrations of 4554W(N6A) (0 – 1000 μM – from 10-fold sub-stoichiometric to 10 fold super-stoichiometric). Under these conditions a dose dependent inhibition of αS aggregation was observed. At the highest dose of 10-fold excess (1000 μM) 4554W(N6A), the aggregation of αS was seen to be completely prevented.

To further interrogate this finding, end point samples from the ThT assay were imaged using negative staining TEM to determine the effects of 4554W(N6A) concentration on the formation of fibril like aggregates. In the absence of 4554W(N6A), αS was seen to form thin and curly fibril like structures growing from the DMPS SUVs of varying length, with a width of ~5 or ~10 nm, potentially representing either single protofibrils or more mature double stranded fibrils, similar to those previously viewed by Cryo-EM (Galvagnion, Celine et al., 2019). With the addition of 500 mM 4554W(N6A), (a 5x molar excess), the prevalence of these aggregates was greatly reduced. Those aggregates which were observed were of the ~5 nm

width variety, suggesting that further maturation towards more mature double stranded fibrils had been inhibited. At the highest stoichiometry of 1:10, addition of 1000 μM 4554W(N6A) appeared to completely inhibit growth of fibril like aggregates from the SUVs. In the TEM images the SUVs are clearly observed, however in contrast no fibril like structures are observed to protrude, suggesting that the fibrillation process has been completely abolished at this concentration.
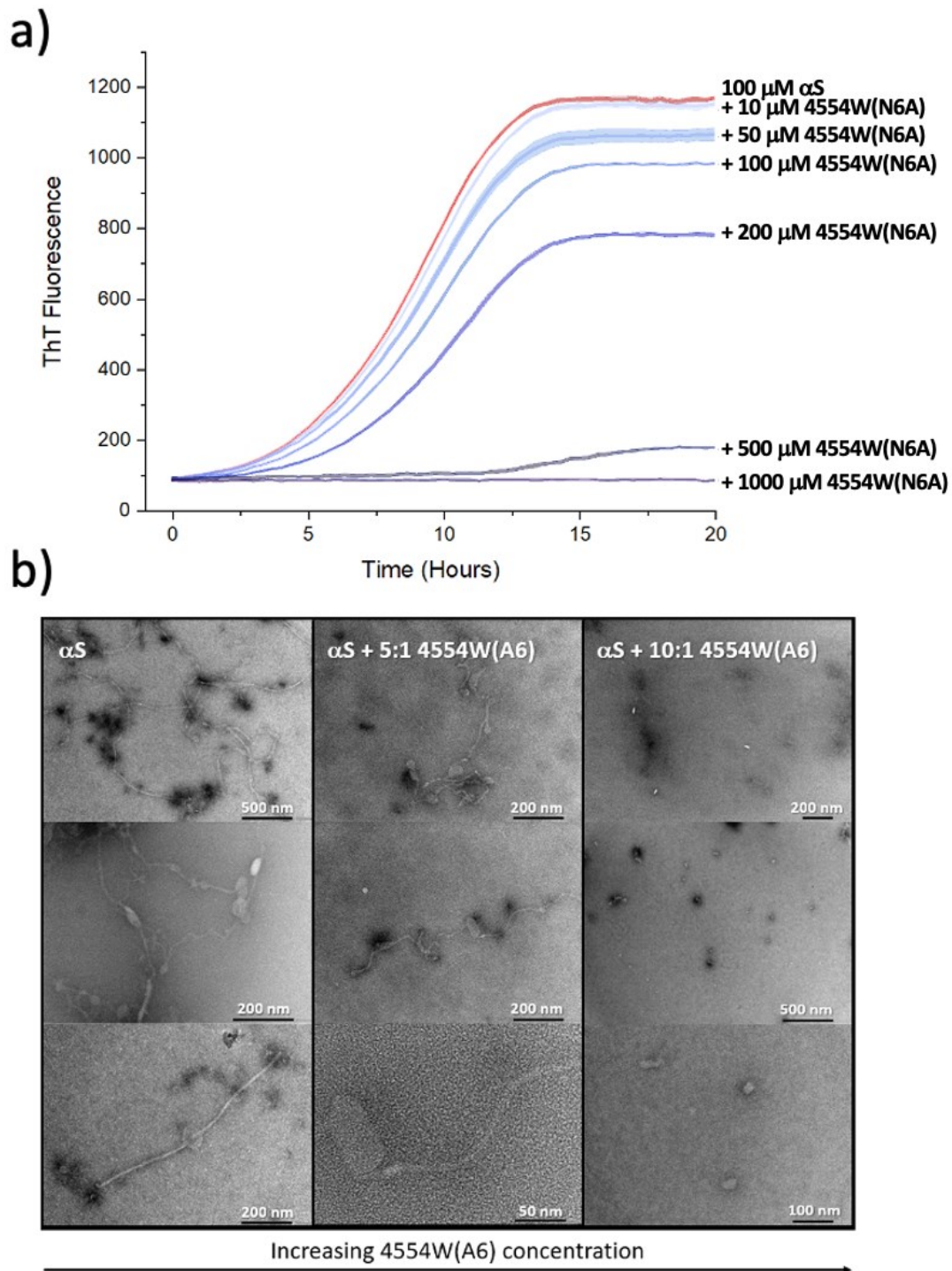
Figure 6.3: Dose response effect of 4554W(N6A) on lipid induced primary nucleation of αS. *a)* Dose dependent inhibition of lipid induced primary nucleation of αS with 4554W(A6) measured by change in ThT fluorescence intensity when 100 μM monomeric αS was incubated in the presence of 200 μM DMPS SUVs and 50 μM ThT in 20 mM sodium phosphate buffer pH 6.5 under quiescent conditions at 30 °C alone (red) or with increasing concentration of 4554W(A6) (0-1000 μM) (light blue 10 fold αS excess - dark blue 10 fold peptide excess). ***b)*** Negative stain TEM images of aggregated αS at t = 30hrs show that lipid induced aggregation into fibril like structures has occurred. The prevalence of the fibril like structures decreased with the addition of 4554W(N6A), and at a 10 old excess of peptide. In contrast to αS and SUVs alone, in the presence of the peptide SUVs are observed but no fibril like structures are either observed or associated with the SUVs.

Photo-crosslinking of 4554W(N6A) Inhibition Highlights a Decrease in Oligomer Formation

The end point samples of the ThT assay (t = 20 hr) were collected and analysed using Photo-Induced Cross-linking of Unmodified Proteins (PICUP) (Rahimi, Maiti and Bitan, 2009) to investigate the differences in the oligomer populations present. The PICUP method works by covalently cross-linking oligomers together via the aromatic groups, allowing quantitative analysis of metastable oligomeric population, and has previously been used with αS to determine oligomeric distributions (Acharya et al., 2014). The technique serves as a useful indicator of the ability of inhibitors to modulate oligomeric distribution patterns. Although care must be taken not to over-interpret data collected by PICUP crosslinking, as some of the oligomers presented may be artefacts of the method itself forming artificial oligomeric species, and some oligomeric species may not be crosslinked at all if the aromatic sidechains are not in a suitable conformation. Therefore PICUP must only be used as a guide. That said SDS-PAGE analysis of the cross-linked samples (Fig 6.4a) shows the appearance of a faint band appearing at $\approx$ 30 kDa (band b), which becomes more prominent as the concentration of 4554W(N6A) increases, suggesting that a dimeric species becomes stabilized upon introduction of the peptide. There are also multiple higher-n oligomeric bands (bands c-f) which are observed to decrease in intensity as the concentration of 4554W(N6A) increases (Fig 6.4b). This loss of these oligomers provides evidence that the peptide is functioning to stabilize low-n oligomeric species while preventing progression towards higher-n species that are more toxic.
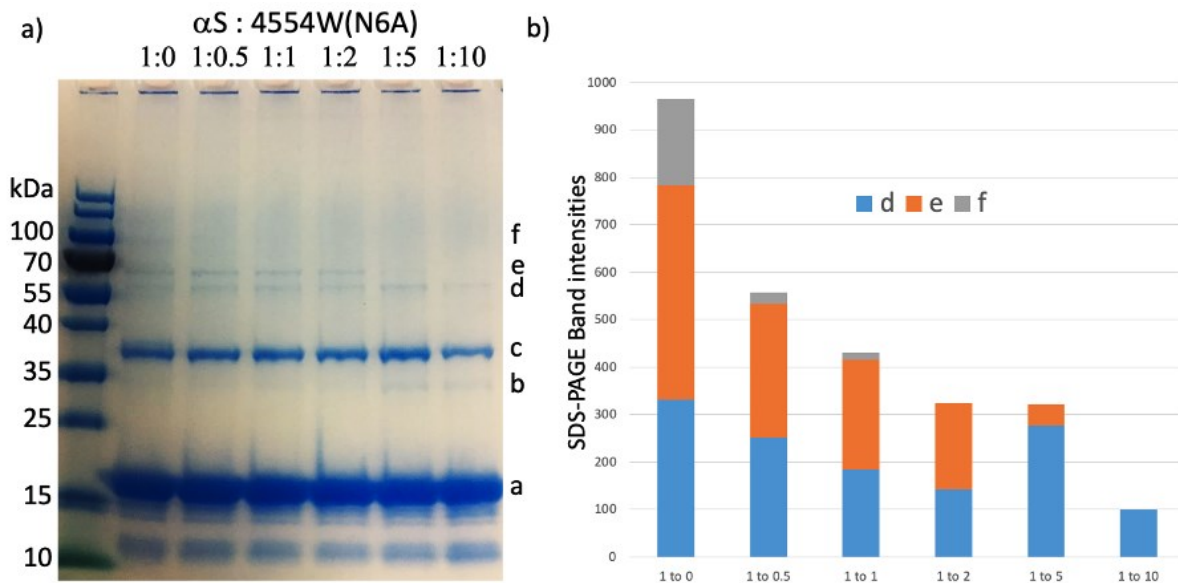
Figure 6.4: Oligomer formation analysed by Photo-Induced Cross-linking of Unmodified Proteins (PICUP) and SDS-PAGE analysis a) SDS-PAGE gel analysis of the end point samples subjected to PICUP showing a monomeric band (a) as well as formation of a range of higher order oligomers (b-f) **b)** Band intensities of the SDS-PAGE gel of the higher order oligomers (d-f), band intensity analysed in ImageJ (Fiji).

Effect of Truncated Peptides upon Lipid Induced Primary Nucleation

As discussed, the original library contained four alanine options at positions 3, 7, 9 and 10, although these were searched concomitantly with all other semi-randomised positions. However, one might expect that modification of these residues to Alanine might weaken the ability of 4554W modulate αS aggregation, as was observed experimentally with the alanine scan (Fig 6.2). Starting from the 4554W(NA6) peptide we therefore sought to probe the importance of the terminal residues with a view to further downsizing the peptide. In particular K1, and A10 deletion constructs were created. Since A10 was selected during PCA screening, no change was implemented during the alanine scan. The K1A substitution enhanced inhibition of primary nucleation (Fig 6.2). Therefore, to determine if either of these residues were important for 4554W(A6) function, as well as two further deletions, five additional truncated variants were probed to elucidate their functionally importance upon lipid induced primary nucleation (Fig 6.5a).

All five truncated peptides tested showed some inhibition of αS aggregation (Fig. 6.5), although in every case deletion of A10 reduced inhibitory function, highlighting that this

residue is an absolute requirement for peptide efficacy. In contrast, deletion of K1 had no effect upon efficacy, suggesting that this residue is expendable for inhibitory function. We next sought to remove the next residue, D2, which in accordance with the alanine scan result, was expected to decrease peptide efficacy (Fig. 6.2). To first confirm that K1 is expendable, a dose response ThT assay was undertaken using 4654W(N6A) and was compared with 4554W(A6), which was found to deliver and equal inhibitory response (Fig. 6.5c).
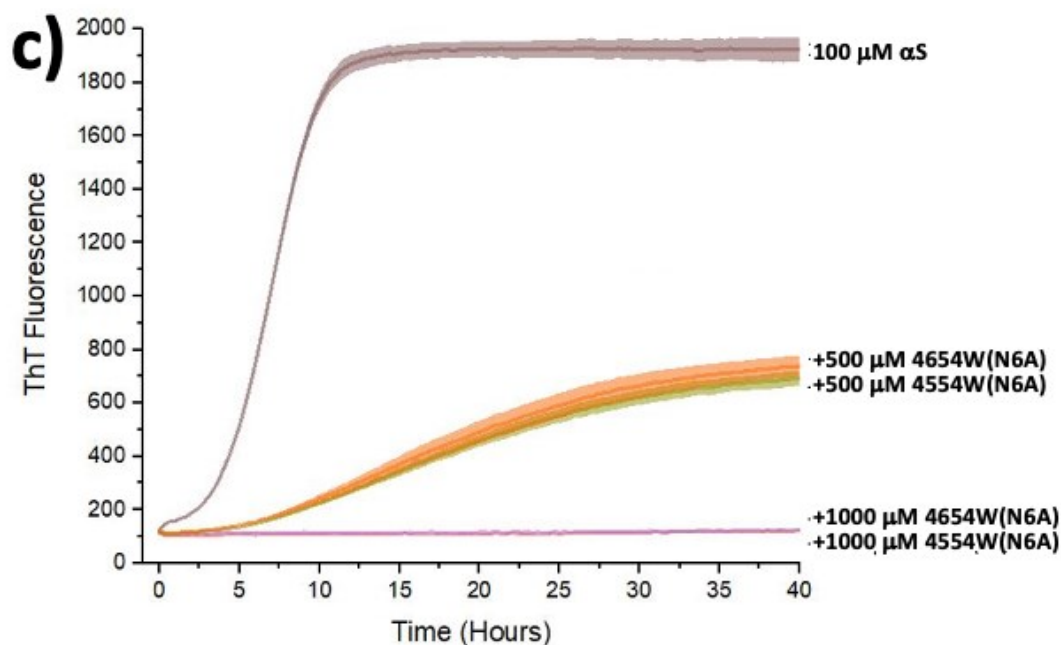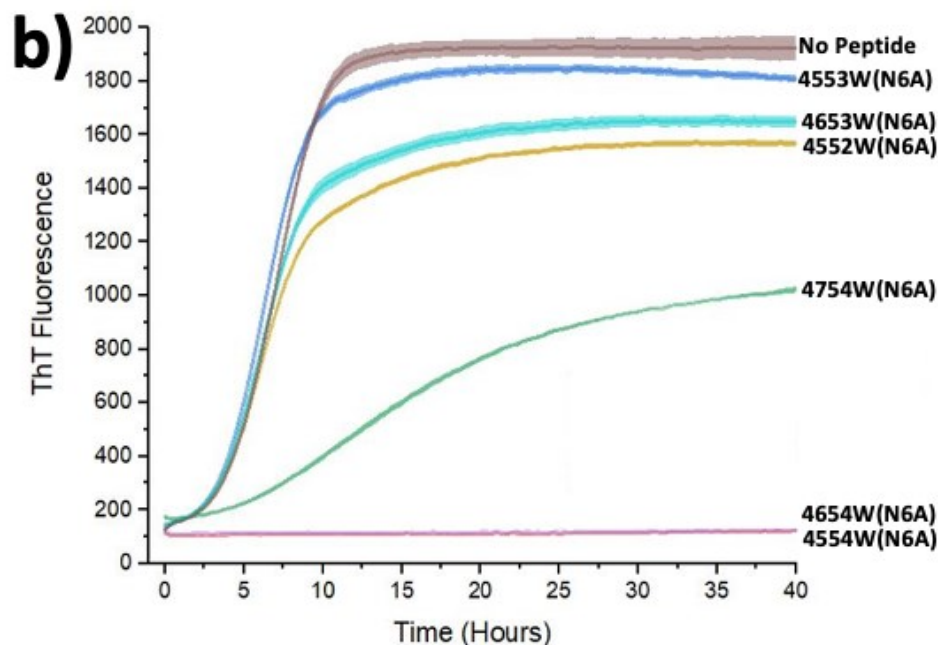
Figure 6.5: a) Truncated peptide variants based on the 4554W(N6A) template **b)** 100 μM αS, 1000 μM Peptide, 200 μM DMPS to show the effect of the truncated peptides on primary nucleation. Notably 4554W(N6A) and 4654(N6A) both completely block aggregation at this concentration over this timescale **c)** 100 μM αS, 1000 μM Peptide, 200 μM DMPS to showing that the dose response of both 4554W(A6) and 4654W(A6) are equal. Suggesting that the lysine in position 1 of the A6 peptide was not required. All profiles show the averages, with standard error, of experiments undertaken in triplicate

143

6.4 Conclusions

Alanine scanning experiments were performed upon 4554W, which was previously been shown to inhibit lipid induced primary nucleation of αS *in vitro* (see chapter 4). Here we report two improvements in the peptide sequence that have permitted improvement in efficacy and concomitant downsizing for the peptide. In particular 4654W(N6A) exhibited improved efficacy in reducing αS aggregation, relative to 4554W, and was no less potent than 4554W(N6A) but 16.4% lower in molecular weight with a mass of 869.5 Da. These changes were removal of K1, since it has been found to be not required for function, and an N6A substitution, which has been shown to greatly increase efficacy, likely by reducing steric hinderance and increasing the hydrophobic interaction along the steric zipper between αS and the peptide.

As a therapeutic peptide 4654W(N6A) shows promise to reduce the number of toxic oligomeric species in patients susceptible to synucleinopathies, hopefully leading the way to the production of novel compounds and therapies for PD and related diseases. The peptide could be further developed into a drug, by creating the retro inverso version of the peptide, and addition of nonnatural amino acids, reducing its degradation by proteasomes. Additional functional motifs could also be included enabling further functionality e.g. cell penetrance and localisation to a specific area.

6.5 Methods

Protein Expression and Purification of Human wt αS (140)

Wild type human α-synuclein was recombinantly expressed and purified, based on, and modified from, a previously published method (Volles and Lansbury, 2007; Pujols et al., 2017). Briefly, the pET21a plasmid containing the human wt αS (1-140), purchased from addgene (deposited by the Michal J Fox Foundation MJFF) was transformed into *E. coli* expression cell line BL21 (DE3). 2XYT overnight cultures containing ampicillin of this human wt αS (1-140) pET21a BL21 (DE3) *E.coli* strain were used to inoculate 1lt 2XYT cultures, containing 100 mg/lt Ampicillin, and grown at 37°C, 200rpm shaking, to OD_{600} = 0.6 - 0.8 and induced with 1mM

isopropyl-1-thio-D-galactopyranoside (IPTG) at 37°C, 200rpm shaking, for 4 hours in an Innova 44 Incubator shaker (New Brunswick Scientific). The bacteria were harvested by centrifugation at 4600g and resuspended in 40ml of 20 mM Tris buffer pH8 containing 1 cOmplete protease inhibitor tablet (Roche) and freeze-thawed at -20°C before lysis, by sonication. The cell debris was discarded by centrifugation at 48400g, and the supernatant was collected and boiled at 95 °C for 10 minutes. The precipitated protein removed by centrifugation at 18500g. The supernatant was collected, and ammonium sulphate added to 30% saturation (0.176 g / ml), left shaking at 20 °C for 1 hour. The precipitated protein, containing the αS, was harvested by centrifugation at 18500g, and resuspended in 50 ml 20 mM Tris buffer pH8 by gentle agitation at 4 °C. This purified by anion exchange chromatography on an AKTA pure purification system (GE Healthcare) with a 5ml HiTrap Q HP (GE Healthcare) pre-packed column, to remove protein impurities and protein bound nucleic acids. The purified fractions were combined and further purified by size exclusion chromatography (SEC) , using a HiLoad 16/60 Superdex 75 pg (GE Healthcare) prepacked purification column, to buffer exchange the αS into the relevant reaction buffer (20 mM sodium phosphate buffer pH 6.5/ 20mM sodium acetate pH5) and ensure that only monomers were collected. Pure monomeric αS eluted between 54 - 60ml.

The concentration of the purified αS was determined in a 2mm path length quarts cuvette, using an extinction coefficient of 4836 M^{-1}cm^{-1} at 280 nm, separated into 1ml aliquots, snap frozen in liquid N$_2$, and stored at -80°C until required.

The purity of αS following SEC was confirmed by SDS-Page gel electrophoresis, and the correct mass was confirmed by mass spectrometry on a Dionex Acclaim RSLC Polar Advantage II (PA2), 2.2 μm, 120 Å, 2.1 x 50 mm (Thermo Fisher Scientific, California, USA). The deconvoluted average mass of the protein was confirmed as 14459.749 m/z, representing the mass of wt Human αS (1-140). A CD spectra scan was performed, to confirm the random coil conformation of the monomeric αS stock.

Production and purification of peptides

The peptides were synthesized in the laboratory using a Liberty Blue microwave peptide synthesizer (CEM).

The liberty blue peptide synthesizer produced the peptides on a Rink amide ChemMatrix resin (PCAS BioMatrix) employing Fmoc solid-phase technique, with repeated steps of coupling-deprotection-washing for each amino acid. The activator solution consisted of 26g PyBOP in 100ml DMF, and the de-protection solution was 20% Piperidine in DMF with the addition of 5% Formic acid to prevent aspartamide formation of the peptide.

The peptide was removed from the matrix by incubating in cleavage solution (95% Trifluoroacetic acid (TFA), 2.5% Triisopropylsilane, and 2.5% water), on a shaker at 25 °C, for 4 hours. The resin was removed by filtration, and the peptide precipitated using ice cold ether, with vortexing and centrifugation at 7000g for 3 rounds. The pellet was left overnight at room temperature to completely dry and purified by HPLC with a Jupiter 4 μm Proteo C-18 90 Å reverse phase prep column.

The fractions of the HPLC peaks were examined by mass spectroscopy, using a microTOF (Bruker Daltonics) to confirm which fractions contained the purified peptide. Fractions, containing the peptide were pooled, and lyophilised. The dry weight of the purified peptides was measured to 0.1 μg accuracy using a Sartorius SE2 Ultra Micro Balance and stored at -80°C.

Microplate ThT Kinetic Assays

ThT kinetic assays to determine the effect of inhibitors on the lipid induced primary nucleation, fibril elongation and secondary nucleation of αS were performed in a CLARIOstar fluorescence microplate reader (BMG Labtech), under quiescent conditions (without shaking), at 37 °C (or 30 °C for lipid induced primary nucleation) in black, clear bottomed 96 well half area polystyrene plates with Non-bonding surface (Corning #3881) covered with Aluminium Thermowell Sealing Tape (Corning #6570). The focal height was set to 4.9 mm, and gain to 800, with an excitation filter of 440-15 nm and emission filter of 480-15nm and a

Dichroic cut-off of 460 nm. Well measurements were taken by spiral average of 4 mm using the bottom optic, with 50 flashes per well and a cycle time of 1200 seconds. The outer wells of the plate were not used.

Lipid preparation for induced Primary Nucleation Method

The mass of dry DMPS lipid powder was determined using an ultra-micro balance (Sartorius), and dissolved in 20mM sodium phosphate buffer pH 6.5 to a concentration of 2 mM. This was dissolved by shaking, in a 2 ml Eppendorf tube, on a Thermomixer compact (Eppendorf), at 45°C, 1400 rpm for 3 hours. The solution was then freeze thawed five times using dry ice and the thermomixer compact (Eppendorf) at 45 °C and 500 rpm. The preparation of the vesicles was carried out by sonication, using a Soniprep 150 plus sonicator, set to an amplitude of 10.0, for 5 cycles of 30 seconds on and 30 seconds off.

Dynamic Light Scattering (DLS) Measurements

A sample of the vesicles produced at each step were diluted to 100 µM in 20mM phosphate buffer pH 6.5. Their size distribution was measured by DLS, using a Zetasizer Nano ZSP (Malvern Instruments), to ensure a final consistent size of between 20-30 nm was obtained.

Lipid induced Aggregation Kinetic Assay to Primary nucleation

Lipid induced primary nucleation experiments were performed in a CLARIOstar fluorescence microplate reader (BMG Labtech), under quiescent conditions (without shaking), at 30 °C in black, clear bottomed 96 well half area polystyrene plates with Non-bonding surface (Corning #3881) covered with Aluminium Thermowell Sealing Tape (Corning #6570). The experiments were performed in 100 µl aliquots, in triplicate, each containing 100 µM αS, 50 µM ThT, 100 µM DMPS and varying concentrations of 4554W peptide (0 µM, 100 µM and 1mM) in 20mM phosphate buffer pH 6.5.

Seed Fibril Formation for Elongation method

Mature fibrils were produced in a 10 mm Quartz cuvette by incubating 1.5 ml of 400 µM αS monomers in 20mM sodium phosphate buffer (pH6.5) for 48 hours at 40⬜C maximal stirring

(1500rpm), using a PTFE magnetic stirrer, on an RCT Basic Heat Plate (IKA, Staufen, Germany). The mature fibrils were diluted to 200 μM monomer equivalents using 20mM sodium phosphate buffer (pH6.5) (1.5ml) and broken into seeds by 3 rounds of freeze-thawing with liquid N_2 followed by 55°C water bath. The mixture was then sonicated using a Soniprep 150 plus sonicator, set to an amplitude of 10, for 3 cycles of 10 seconds on and 10 seconds off. The final seed fibrils were measured by circular dichroism (10 μM monomer equivalent αS in 20 μM sodium phosphate buffer pH 6.5) to ensure complete conversion to β-sheet, and confirmed by TEM. The seed stock was divided into 500 μl aliquots, frozen in liquid N_2, and stored at -80°C until required.

Seeded Aggregation Kinetic Assay to Measure Elongation

Seeded elongation experiments were performed in a CLARIOstar fluorescence microplate reader (BMG Labtech), under quiescent conditions (without shaking), at 37 °C in black, clear bottomed 96 well half area polystyrene plates with Non-bonding surface (Corning 3881) covered with Aluminium Thermowell Sealing Tape (Corning 6570). The experiments were performed in 100 μl aliquots, in triplicate, each containing 100 μM αS, 50 μM ThT, 15μM (monomer equivalents) preformed fibril 'seeds' and varying concentrations of 4554w peptide (0 μM, 100 μM and 1mM) in 20mM phosphate buffer pH 6.5.

Formation of Seeds for Secondary Nucleation

Seed fibrils for inducing secondary nucleation were produced by incubating 25 μM ⍺S monomer in 20 mM sodium acetate, 50 μM ThT and 0.01% sodium azide, split into 100 ⍰l aliquots in a black, clear bottomed 96 well half area polystyrene plates with Non-bonding surface (Corning 3881), with each well containing a single 4 mm glass bead (Hecht Karl ref. 41401004), covered with Aluminium Thermowell Sealing Tape (Corning 6570). The plate was incubated at 37 °C in a CLARIOstar fluorescence microplate reader (BMG Labtech) at 500rpm for 96 hrs. The aliquots were pooled into a 2 ml Eppendorf tube and sonicated using a Soniprep 150 plus, set to an amplitude of 10, for 5 cycles of 1 seconds on and 5 seconds off. The seeds were flash frozen in liquid N_2 and stored at -80 °C until required.

Seeded Aggregation Kinetic Assay to Measure Secondary Nucleation/ Fibril Amplification

Seeded elongation experiments were performed in a CLARIOstar fluorescence microplate reader (BMG Labtech), under quiescent conditions (without shaking), at 37 °C in black, clear bottomed 96 well half area polystyrene plates with Non-bonding surface (Corning 3881) covered with Aluminium Thermowell Sealing Tape (Corning 6570). The experiments were performed in 100 μl aliquots, in triplicate, each containing 100 μM αS, 50 μM ThT, 1 μM (monomer equivalents) preformed fibril 'seeds' and 1mM of peptide in 20mM sodium acetate buffer pH 5.

PICUP cross-linking SDS-PAGE Electrophoresis

Photo-induced cross-linking of unmodified proteins (PICUP) reactions were modified from a previously published protocol (Rahimi, Maiti and Bitan, 2009). Briefly, 20 μl of the end point (20 h) of the lipid-induced primary nucleation assay reaction mixture (100 μM aS, 50 μM ThT, 200 μM DMPS, 0-1000 μM peptide in 20 mM sodium phosphate buffer pH 6.5) was placed in a 1.5ml Eppendorf tube. 2 μl of 1 mM solution of Tris(2,2'bipyridyl)dichloro-ruthenium(II) hexahydrate (RuBpy) in 20 mM sodium phosphate buffer pH 6.5, and 2 μl of 20 mM ammonium persulphate (APS) in 20 mM sodium phosphate buffer pH 6.5 were added to all samples simultaneously. The samples were then irradiated with ambient light for 10 seconds, and the reaction quenched with 10 μl RunBlue LDS Sample Buffer 4X concentrate (Expedeon). The samples were then heated to 95 °C for 5 minutes and fractionated by SDS-Page using a 12% Tricine RunBlue SDS Gel (Expedeon), and RunBlue run Buffer (Expedeon). The protein bands were visualised using Instant Blue (Expedeon) Coomassie stain.

To analyse the gel band intensities the computer program ImageJ was used (http://imagej.nih.gov/ij). The image was first converted to grey scale and the raw integrated density (RID) of each band was measured with ImageJ. The data was then processed in excel to give a relative percentage of the band intensities.

Transmission Electron Microscopy (TEM)

α-Synuclein samples from the end point of the aggregation kinetics were collected. 5 µL of these samples were put onto on glow discharged Formvar/carbon-coated, 200 mesh, copper grids for 1 minute. The samples were dried with filter paper, and washed twice with MiliQ water for 1 second, each time removed with filter paper. The sample was stained by incubating the grids with 5 µL Uranyl Acetate Zero (Agar Scientific) for 30 seconds, followed by removal of the excess stain with filter paper. The grids were left to air-dry for 2 hours. The samples were imaged using a Transmission Electron Microscopy Jeol 2100 Plus (JEOL), operating at an accelerating voltage of 200 kV. Multiple grids were screened in order to obtain representative images of the samples.

Chapter 6:

Supporting information
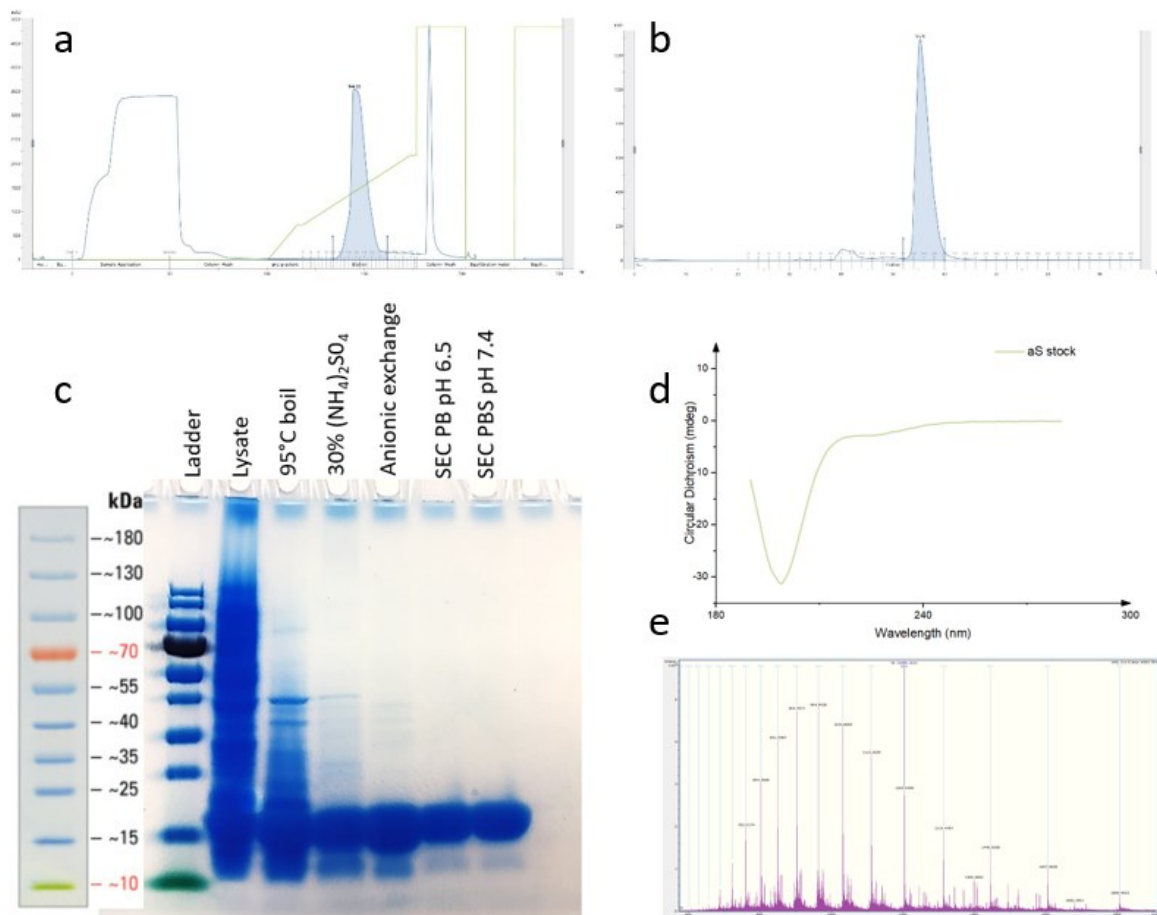
Supplementary Figure 6.1: Overview of the purification of αS used for the experiments. a) Chromatograph of the Hi-Q anionic exchange purification. b) Chromatograph of the Size exclusion chromatography and buffer exchange. c) SDS page gel showing an overview of the entire purification protocol. d) Far-UV circular dichroism spectra of the purified αS showing that the monomeric αS is in a random coil conformation. e) De-convoluted mass spectrum, showing a mass of the protein of 14459.749 m/z, representing the mass of wt Human αS (1-140).

| Peptide	Peptide Sequence	Formula	Monoisotopic mass (Da)
4554W(K1A)	Ac-**A**DGIVNGVKA-NH$_2$	C$_{42}$H$_{73}$N$_{13}$O$_{14}$	983.540
4554W(D2A)	Ac-K**A**GIVNGVKA-NH$_2$	C$_{44}$H$_{80}$N$_{14}$O$_{12}$	996.608
4554W(G3A)	Ac-KD**A**IVNGVKA-NH$_2$	C$_{46}$H$_{82}$N$_{14}$O$_{14}$	1054.613
4554W(I4A)	Ac-KDG**A**VNGVKA-NH$_2$	C$_{42}$H$_{74}$N$_{14}$O$_{14}$	998.551
4554W(V5A)	Ac-KDGI**A**NGVKA-NH$_2$	C$_{43}$H$_{76}$N$_{14}$O$_{14}$	1012.567
4554W(N6A)	Ac-KDGIV**A**GVKA-NH$_2$	C$_{44}$H$_{79}$N$_{13}$O$_{13}$	997.562
4554W(G7A)	Ac-KDGIVN**A**VKA-NH$_2$	C$_{46}$H$_{82}$N$_{14}$O$_{14}$	1054.613
4554W(V8A)	Ac-KDGIVNG**A**KA-NH$_2$	C$_{43}$H$_{76}$N$_{14}$O$_{14}$	1012.567
4554W(K9A)	Ac-KDGIVNGV**A**A-NH$_2$	C$_{42}$H$_{73}$N$_{13}$O$_{14}$	983.540
4554W	Ac-KDGIVNGVK**A**-NH$_2$	C$_{45}$H$_{80}$N$_{14}$O$_{14}$	1040.5978

Supplementary Table 6.1: Sequence and monoisotopic masses for the alanine scan variant peptides.
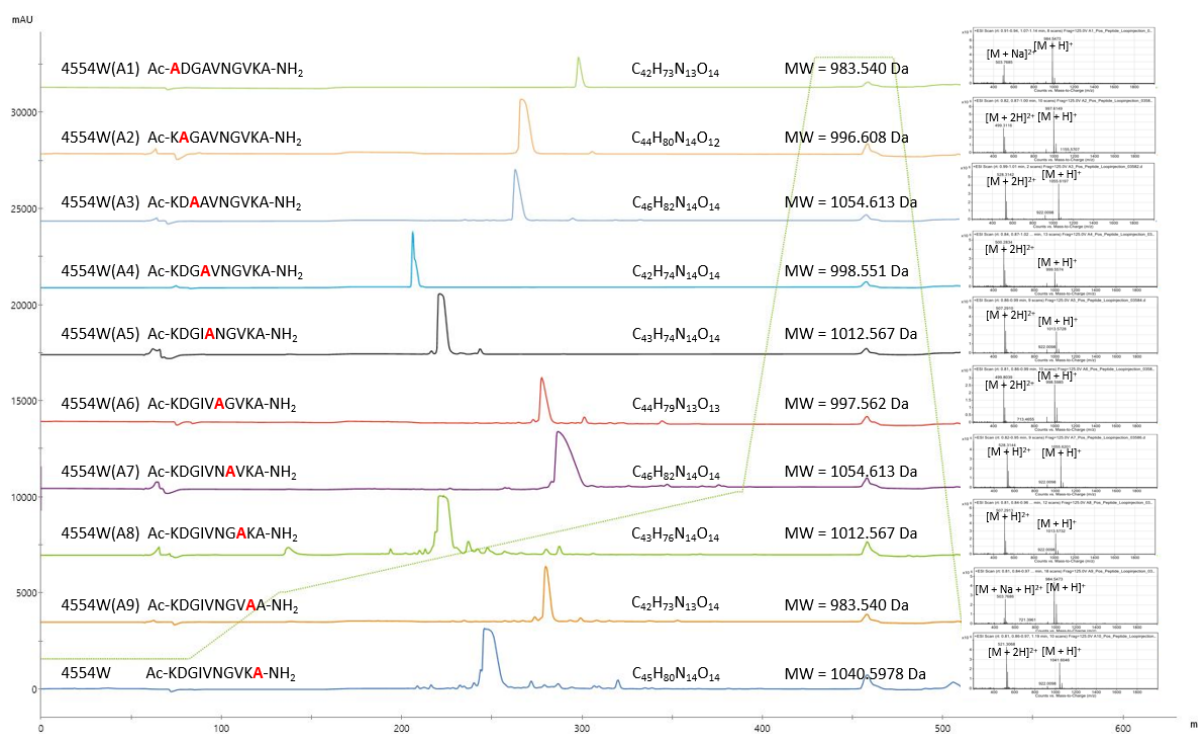
Supplementary Figure 6.2: HPLC traces and corresponding mass spectroscopy for alanine scan variant peptides.

Peptide	Peptide Sequence	Formula	Monoisotopic mass (Da)
4554W(N6A)	Ac-KDGIV**A**GVKA-NH$_2$	C$_{44}$H$_{79}$N$_{13}$O$_{13}$	997.562
4654(N6A)	Ac-DGIV**A**GVKA-NH$_2$	C$_{38}$H$_{67}$N$_{11}$O$_{12}$	869.486
4754(N6A)	Ac-GIV**A**GVKA-NH$_2$	C$_{34}$H$_{62}$N$_{10}$O$_9$	754.459
4553(N6A)	Ac-KDGIV**A**GVK-NH$_2$	C$_{41}$H$_{74}$N$_{12}$O$_{12}$	926.544
4552(N6A)	Ac-KDGIV**A**GV-NH$_2$	C$_{35}$H$_{62}$N$_{10}$O$_{11}$	798.449
4653(N6A)	Ac-DGIV**A**GVK-NH$_2$	C$_{35}$H$_{62}$N$_{10}$O$_{11}$	798.449

Supplementary Table 6.2: Sequence and monoisotopic masses for the truncated variant peptides.
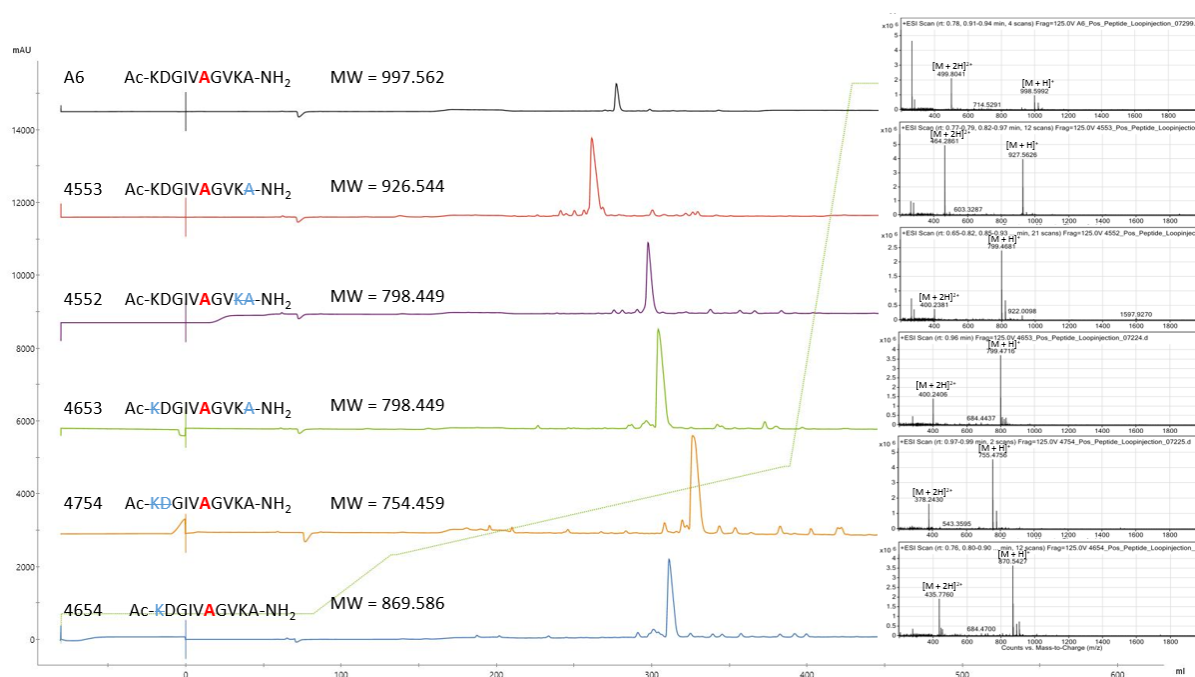
Supplementary Figure 6.3: HPLC traces and corresponding mass spectroscopy for truncated variant peptides.

Supplementary Figure 6.4: Dynamic light scattering size distribution of the DMPS small unilamellar vesicles (SUVs) used for lipid induced nucleation assays, showing a size distribution centred around 30 - 40 nm post sonication.
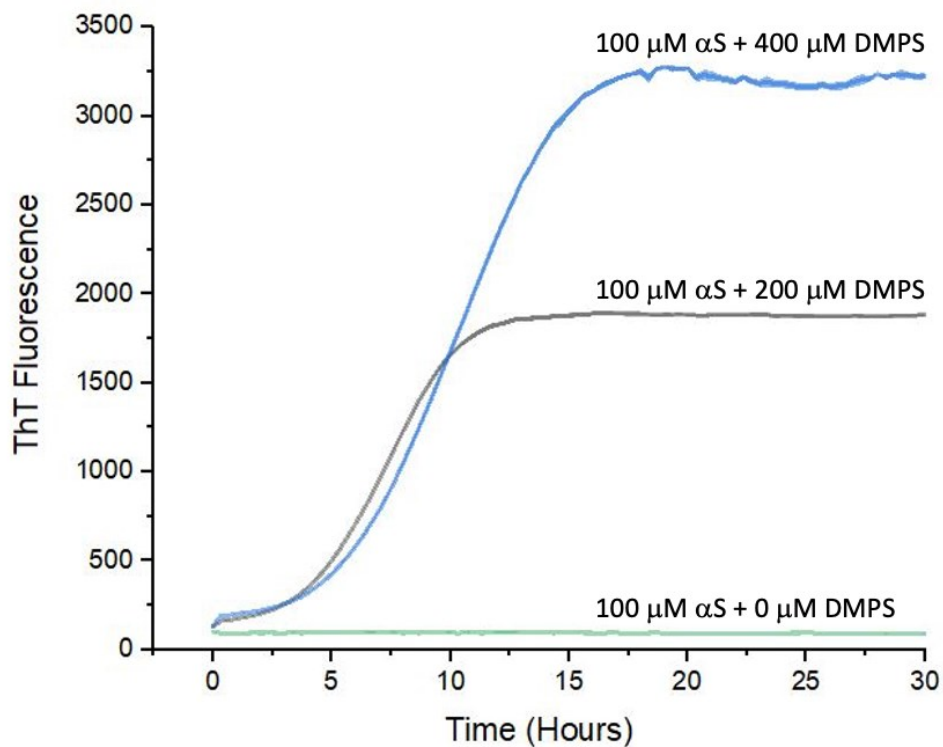
Supplementary Figure 6.5: ThT fluorescence intensity when 100 μM αS is incubated with 0 μM, 200 μM, or 400 μM DMPS vesicles and 50 μM Thioflavin T in 20 mM phosphate buffer (pH 6.5) under quiescent conditions at 30 °C.
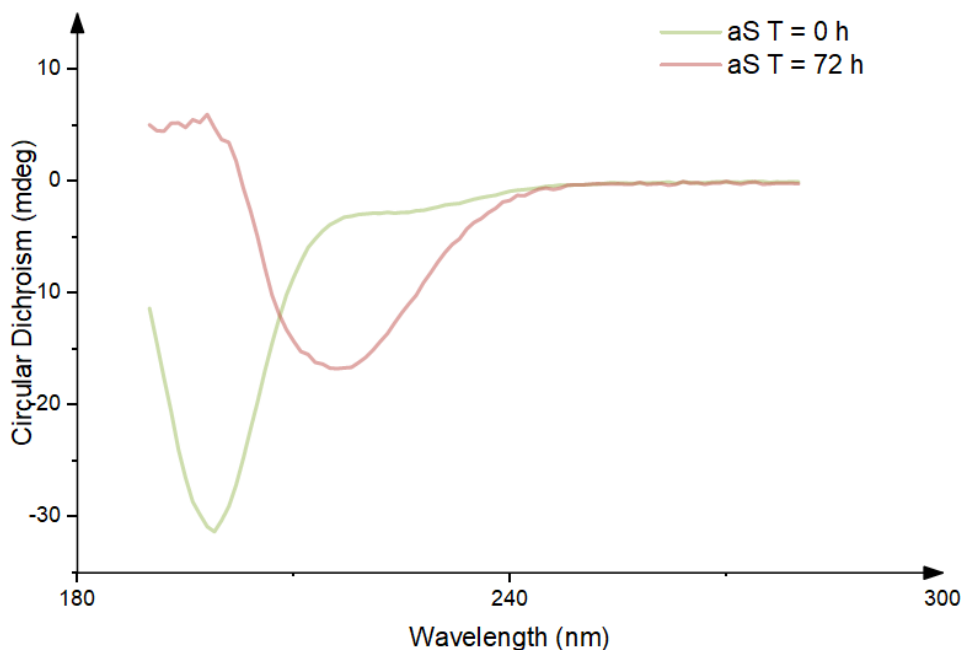
Supplementary Figure 6.6: Circular dichroism spectra of 10 μM seeds formed for ThT assay to probe fibril elongation rates. The αS monomer before aggregation shows a random coil spectra (green). The αS is seen to be fully converted to beta-sheet fibril seeds (red) after 400 μM αS was stirring at 40°C with a teflon bar at 1500rpm for 48 hours, followed by 3 rounds of freeze-thawing in liquid N_2 and 3 rounds of sonication for 10 seconds on 10 seconds off.

Supplementary Figure 6.7: ThT fluorescence experiment measuring seeds only vs seeds and monomer to show seed stability. 100 μM in the presence of 15μM seeds (grey) vs 15 μM seeds without addition of monomer (red), showing that the seeds remained stable.
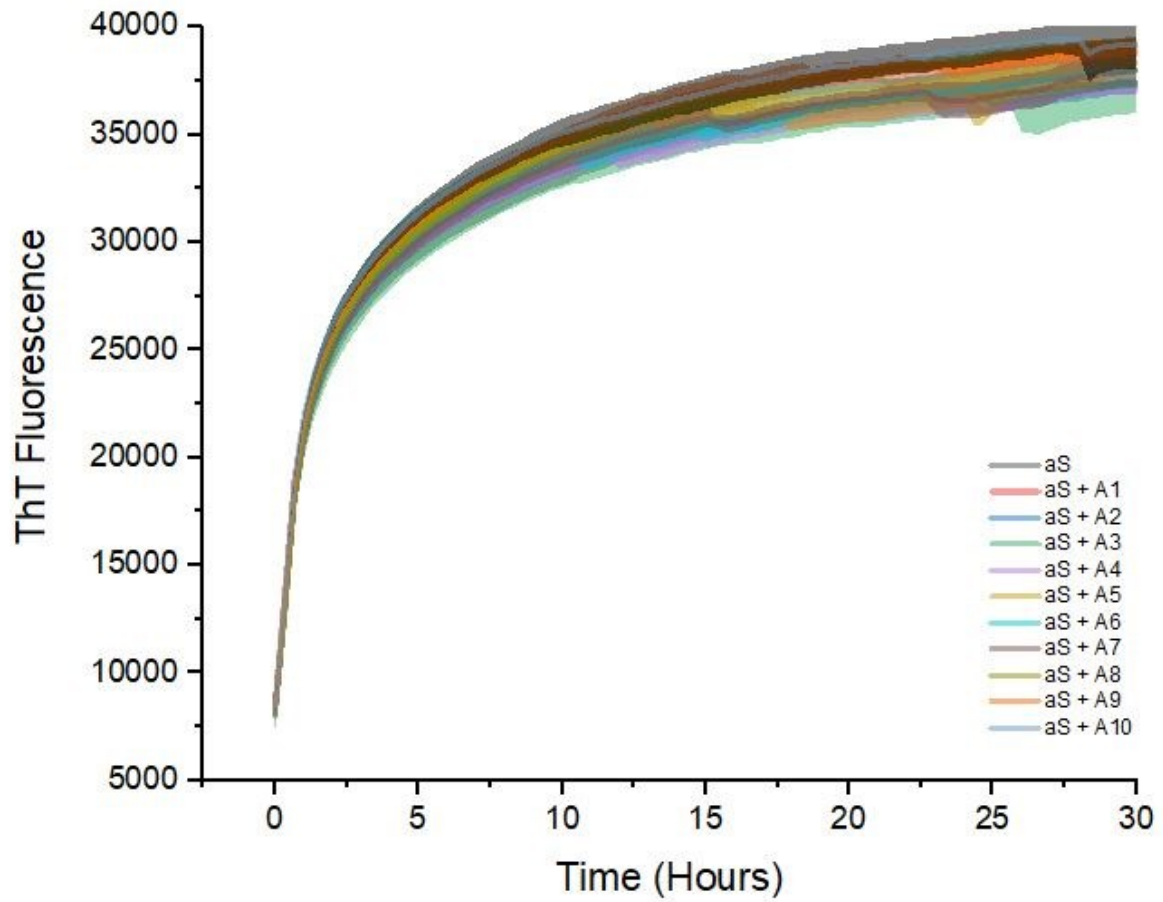
Supplementary Figure 6.8: Effect of 4554W and the alanine scan variants on Fibril elongation, measured by the change in ThT fluorescence intensity when 100 μM monomeric αS was incubated in the presence of 15 μM preformed fibrils and 50 μM ThT in 20 mM sodium phosphate buffer pH 6.5 under quiescent conditions at 37 °C, with 1000 μM of the different 4554W peptide alanine scan variants. No effect on the ThT trace was observed by the addition of the peptides.
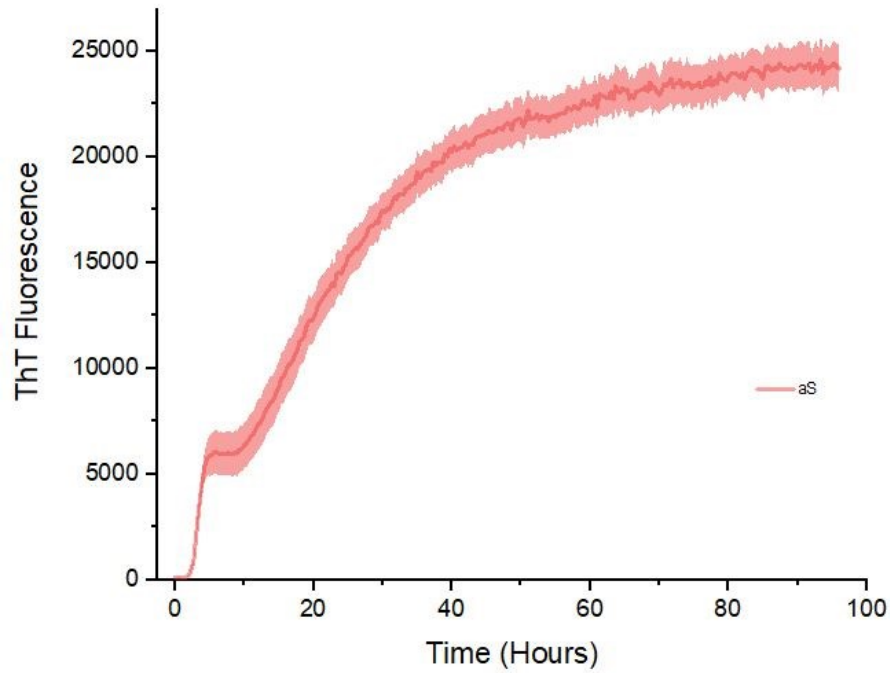
Supplementary Figure 6.9: ThT curve following seed creation for secondary nucleation studies, created in 96 well plates containing glass beads in the wells, with shaking at 500 rpm at a constant temperature of 37 °C.
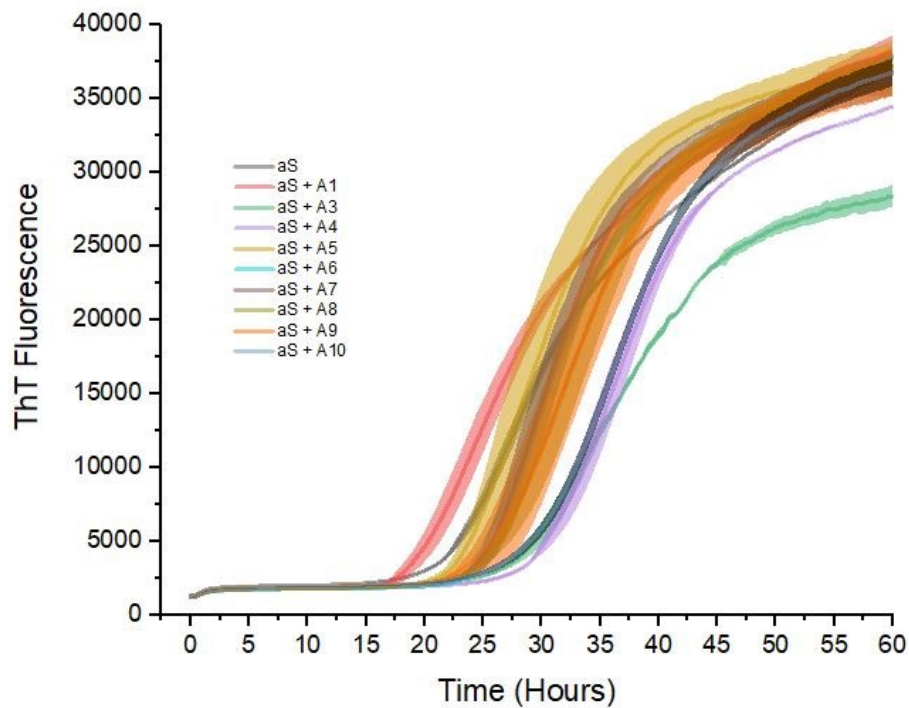
Supplementary Figure 6.10: Effect of 4554W and the alanine scan variants on Fibril amplification/secondary nucleation, measured by the change in ThT fluorescence intensity when 100 μM monomeric αS was incubated in the presence of 1 μM preformed fibril seeds and 50 μM ThT in 20 mM sodium acetate buffer pH 5 under quiescent conditions at 37 °C, with 1000 μM of the different 4554W peptide alanine scan variants. No effect on the ThT trace was observed by the addition of the peptides

158

Chapter 7:

Thesis Conclusions

7.1 Optimising αS production

Producing a consistent quantity and quality of αS was vital for the research presented within this thesis. Three different methods were analysed with varying results (Chapter 3). Ultimately it was found that the most productive, and rapid method utilised wild type αS expressed in *E. coli* using the pET21a vector with no fusions or tags that had to be tolerated or later removed. The methodology involved a heating step, followed by an ammonium sulphate crash, anionic exchange and finally size exclusion chromatography. This method consistently produced excellent yields ($\approx$ 20 mg / l) of purified monomeric αS in the required buffer for the experiments. It would be suggested that any future experiments with αS utilise this purification protocol.

7.2 Developing a cell based αS toxicity protocol in a relevant cell line

A cell-based toxicity assay was developed using the human neuroblastoma SH-SY5Y cell line in 96 well plates, allowing numerous replicates over varying conditions on the same plate. The most efficient technique tested was to use lyophilised αS 'aged' for 24 hours at a concentration of 800 μM under quiescent conditions. This duration produced αS oligomers similar to those found to be toxic to this cell line by others in the literature. The 'aged' αS mixture was added to undifferentiated SH-SY5Y culture for 24 hours, at a final concentration of 100 μM (equivalent to concentrations found inside human dopaminergic neurons) before measuring viability by MTT reduction. This technique gave a dose response to αS toxicity, reaching maximal death in the 100-120 μM range. This technique was used to measure cell death rescue in the presence of increasing concentrations of 4554W.

Although a successful dose response was observed, the total maximal death achieved was low, reaching ~20% cell death relative to the PBS control. This suggested that there could be further improvements to this technique in order to elicit a stronger response. In light of the recent discoveries highlighting the importance of lipid vesicles for the misfolding, and primary nucleation of αS into toxic species, future work should be undertaken that includes vesicles in the solution mixtures added to cells. In this case it may be found that αS does not require an 'aging' process before being added to the cells, since the aggregation time for primary

nucleation to plateau, using the same condition using in this thesis (i.e. about 12-15 hours) would be ideal for a 24 hour incubation on the cells.

7.3 Determining the mechanism of action of 4554W

The 4554W peptide was previously selected by an intracellular screening assay and shown to inhibit the aggregation of αS in solution, as measured by ThT fluorescence and CD. Due to the nature of selection this did not highlight the precise mode of action by which the peptide functioned. By varying the aggregation conditions of αS it was possible to split the aggregation process into three distinct pathways i) heterogeneous primary nucleation, ii) fibril elongation and iii) secondary nucleation. Performing these experiments with varying concentrations of 4554W concluded that this peptide inhibited lipid induced heterogeneous primary nucleation but presented no effect of fibril elongation rates or secondary nucleation. Circular dichroism experiments measuring the binding of αS to vesicle membranes, under varying concentrations of 4554W and DMPS SUVs, showed that the peptide did not inhibit binding of αS to the vesicles, as measured by its conversion to an α-helix upon binding. This suggested that the peptide exerted its effect on aggregation after the αS had already bound to the membrane. A cell toxicity assay on human neuroblastoma SH-SY5Y showed that 4554W can rescue a relevant cell line from αS mediated toxicity.

7.4 Optimisation of 4554W by alanine scan and truncation.

Following from the experiments showing that 4554W inhibits lipid induced primary nucleation, an alanine scan was performed to determine the key residues involved in the interaction. The experiment highlighted that the residues D2, G3, I4, V5, G7, V8 and K9 were all necessary for the function of 4554W, since mutating these to alanine knocked out the function, allowing αS to aggregate normally. The substitution of residues N6 and K1 to alanine was found to increase the inhibitory effect of the peptide on αS aggregation.

A PICUP protein crosslinking experiment was performed on the aggregation mixtures of the increasing concentrations of 4554W(N6A), showed that the population of oligomers above 40kDa, as run on an SDS-PAGE gel, had decreased. This suggested that the peptide must be acting upon a low-n (monomer/dimer/trimer) oligomer.

A truncation assay was therefore performed on the 4554W(N6A) variant of the peptide to determine the importance of the N and C-terminal residues. Residues D2, K9 and A10 were all shown to be important for the interaction, as removing these decreased the efficacy of the peptide. Residue 1 was found to be not required for the peptide function, as its removal presented no decrease in the inhibition of αS aggregation (mirroring the alanine scan experiment that shown increased function when residue size was decreased). Therefore, peptide 4654W(N6A) was the superior peptide due to it increased efficacy compared to 4554W, and its decreased size, which is predicted to allow easier access to the site of action.

Further work should be performed to explore the possibility of elongating the C-terminus of 4654W(N6A) since this may offer further increased inhibition of αS aggregation. Once a fully optimised peptide is achieved further improvements can be explored such as producing a retro-inverso version of the peptide, i.e substituting the amino acids to the D- isomers, reducing the peptides susceptibility to proteases within cells, and additional motifs could be explored and added to improve function, i.e cell permeability. Eventually the peptide could be tested *in vivo* using specifically developed PD animal models such as c. elegans, zebrafish or mice.

7.5 Novel helical polymorphs of αS are populated in the presence of lipid vesicles.

"In the field of observation, chance favours the prepared mind" – Louis Pasteur (1854)

Upon viewing the aggregates from the lipid induced heterogeneous primary nucleation assays by transmission electron microscopy a range of previously unobserved helical polymorphs were discovered, much larger than any of the previously reported fibril structures. These become populated after the apparent ThT aggregation of the sample has plateaued where no additional ThT binding has occurred, suggesting that they may be formed by mature, double stranded fibrils stacking together along a vertical axis. A range of sizes were observed and named 'ribbons', 'waves', 'helices' and 'compact helices'. The respective increases in size from 'ribbons' to 'compact helices' suggest that these are likely composed from the same building blocks (mature fibrils), but with increasing fibril structure.

These interesting structures require further research to determine their potential importance in αS pathology, starting with CryoEM to determine the structural makeup of the large polymorphs. It would also be interesting to determine how they differ between early onset αS variants.

7.6 Further potential for peptides in amyloid diseases

4554W, and related improvements such as 4654W(N6A) presented the capacity to successfully inhibit the large PPIs involved in the primary nucleation of αS. Therefore, highlighting that peptides may represent a powerful tool for preventing the onset of synucleinopathies and related diseases. Although once the disease has set in it is believed to propagate through the brain in a prion-like mechanism. It could therefore be interesting to develop an independent line of peptide enquiry looking at those which are able to bind the outer surface of mature fibrils in order to prevent secondary nucleation on the fibril surfaces, as this is believed to be a key mechanism in propagation of the disease. This would allow synergistic treatments to be tailored to different aggregation stages, allowing greater control on disease onset and progression.

Thesis References

Acharya, S., Safaie, B.M., Wongkongkathep, P., Ivanova, M.I., Attar, A., Klarner, F.G., Schrader, T., Loo, J.A., Bitan, G. and Lapidus, L.J., 2014. Molecular Basis for Preventing alpha-Synuclein Aggregation by a Molecular Tweezer*. *Journal of Biological Chemistry,* 289(15), pp. 10727-10737.

Agerschou, E.D., Flagmeier, P., Saridaki, T., Galvagnion, C., Komnig, D., Heid, L., Prasad, V., Shaykhalishahi, H., Willbold, D., Dobson, C.M., Voigt, A., Falkenburger, B., Hoyer, W. and Buell, A.K., 2019. An engineered monomer binding-protein for alpha-synuclein efficiently inhibits the proliferation of amyloid fibrils. *Elife,* 8, p. 31.

Anderson, J.P., Walker, D.E., Goldstein, J.M., de Laat, R., Banducci, K., Caccavello, R.J., Barbour, R., Huang, J.P., Kling, K., Lee, M., Diep, L., Keim, P.S., Shen, X.F., Chataway, T., Schlossmacher, M.G., Seubert, P., Schenk, D., Sinha, S., Gai, W.P. and Chilcote, T.J., 2006. Phosphorylation of Ser-129 is the dominant pathological modification of alpha-synuclein in familial and sporadic Lewy body disease. *Journal of Biological Chemistry,* 281(40), pp. 29739-29752.

Appel-Cresswell, S., Vilarino-Guell, C., Encarnacion, M., Sherman, H., Yu, I., Shah, B., Weir, D., Thompson, C., Szu-Tu, C., Trinh, J., Aasly, J.O., Rajput, A., Rajput, A.H., Stoessl, A.J. and Farrer, M.J., 2013. Alpha-synuclein p.H50Q, a novel pathogenic mutation for Parkinson's disease. *Movement Disorders,* 28(6), pp. 811-813.

Bartels, T., Choi, J.G. and Selkoe, D.J., 2011. alpha-Synuclein occurs physiologically as a helically folded tetramer that resists aggregation. *Nature,* 477(7362), pp. 107-U123.

Benitez, B.A., Davis, A.A., Jin, S.C., Ibanez, L., Ortega-Cubero, S., Pastor, P., Choi, J., Cooper, B., Perlmutter, J.S. and Cruchaga, C., 2016. Resequencing analysis of five Mendelian genes and the top genes from genome-wide association studies in Parkinson's Disease. *Molecular Neurodegeneration,* 11, p. 12.

Bhatt, M.A., Messer, A. and Kordower, J.H., 2013. Can Intrabodies Serve as Neuroprotective Therapies for Parkinson's Disease? Beginning Thoughts. *Journal of Parkinsons Disease,* 3(4), pp. 581-591.

Braak, H., Del Tredici, K., Rub, U., de Vos, R.A.I., Steur, E. and Braak, E., 2003. Staging of brain pathology related to sporadic Parkinson's disease. *Neurobiology of Aging,* 24(2), pp. 197-211.

Breydo, L., Wu, J.W. and Uversky, V.N., 2012. alpha-Synuclein misfolding and Parkinson's disease. *Biochimica Et Biophysica Acta-Molecular Basis of Disease,* 1822(2), pp. 261-285.
Brown, J.W.P., Buell, A.K., Michaels, T.C.T., Meisl, G., Carozza, J., Flagmeier, P., Vendruscolo, M., Knowles, T.P.J., Dobson, C.M. and Galvagnion, C., 2016. beta-Synuclein suppresses both the initiation and amplification steps of alpha-synuclein aggregation via competitive binding to surfaces. *Scientific Reports,* 6, p. 10.

Brown, J.W.P., Meisl, G., Knowles, T.P.J., Buell, A.K., Dobson, C.M. and Galvagnion, C., 2018. Kinetic barriers to alpha-synuclein protofilament formation and conversion into mature fibrils. *Chemical Communications,* 54(56), pp. 7854-7857.

Bruzzoni-Giovanelli, H., Alezra, V., Wolff, N., Dong, C.Z., Tuffery, P. and Rebollo, A., 2018. Interfering peptides targeting protein-protein interactions: the next generation of drugs? *Drug Discovery Today,* 23(2), pp. 272-285.

Buell, A.K., 2019. The growth of amyloid fibrils: rates and mechanisms. *Biochemical Journal,* 476, pp. 2677-2703.

Buell, A.K., Galvagnion, C., Gaspar, R., Sparr, E., Vendruscolo, M., Knowles, T.P.J., Linse, S. and Dobson, C.M., 2014. Solution conditions determine the relative importance of nucleation and growth processes in alpha-synuclein aggregation. *Proceedings of the National Academy of Sciences of the United States of America,* 111(21), pp. 7671-7676.

Burre, J., Sharma, M. and Sudhof, T.C., 2015. Definition of a Molecular Pathway Mediating alpha-Synuclein Neurotoxicity. *Journal of Neuroscience,* 35(13), pp. 5221-5232.
Burre, J., Sharma, M., Tsetsenis, T., Buchman, V., Etherton, M.R. and Sudhof, T.C., 2010. alpha-Synuclein Promotes SNARE-Complex Assembly in Vivo and in Vitro. *Science,* 329(5999), pp. 1663-1667.

Burre, J., Vivona, S., Diao, J.J., Sharma, M., Brunger, A.T. and Sudhof, T.C., 2013. Properties of native brain alpha-synuclein. *Nature,* 498(7453), pp. E4-E6.

Cascella, R., Perni, M., Chen, S.W., Fusco, G., Cecchi, C., Vendruscolo, M., Chiti, F., Dobson, C.M. and De Simone, A., 2019. Probing the Origin of the Toxicity of Oligomeric Aggregates of alpha-Synuclein with Antibodies. *Acs Chemical Biology,* 14(6), pp. 1352-1362.

Celej, M.S., Sarroukh, R., Goormaghtigh, E., Fidelio, G.D., Ruysschaert, J.M. and Raussens, V., 2012. Toxic prefibrillar alpha-synuclein amyloid oligomers adopt a distinctive antiparallel beta-sheet structure. *Biochemical Journal,* 443, pp. 719-726.

Chandra, S., Chen, X.C., Rizo, J., Jahn, R. and Sudhof, T.C., 2003. A broken alpha-helix in folded alpha-synuclein. *Journal of Biological Chemistry,* 278(17), pp. 15313-15318.

Chartier-Harlin, M.C., Dachsel, J.C., Vilarino-Guell, C., Lincoln, S.J., Lepretre, F., Hulihan, M.M., Kachergus, J., Milnerwood, A.J., Tapia, L., Song, M.S., Le Rhun, E., Mutez, E., Larvor, L., Duflot, A., Vanbesien-Mailliot, C., Kreisler, A., Ross, O.A., Nishioka, K., Soto-Ortolaza, A.I., Cobb, S.A., Melrose, H.L., Behrouz, B., Keeling, B.H., Bacon, J.A., Hentati, E., Williams, L., Yanagiya, A., Sonenberg, N., Lockhart, P.J., Zubair, A.C., Uitti, R.J., Aasly, J.O., Krygowska-Wajs, A., Opala, G., Wszolek, Z.K., Frigerio, R., Maraganore, D.M., Gosal, D., Lynch, T., Hutchinson, M., Bentivoglio, A.R., Valente, E.M., Nicholso, W.C., Pankratz, N., Foroud, T., Gibson, R.A., Hentati, F., Dickson, D.W., Destee, A. and Farrer, M.J., 2011. Translation Initiator EIF4G1 Mutations in Familial Parkinson Disease. *American Journal of Human Genetics,* 89(3), pp. 398-406.

Chartier-Harlin, M.C., Kachergus, J., Roumier, C., Mouroux, V., Douay, X., Lincoln, S., Levecque, C., Larvor, L., Andrieux, J., Hulihan, M., Waucquier, N., Defebvre, L., Amouyel, P., Farrer, M. and Destee, A., 2004. alpha-synuclein locus duplication as a cause of familial Parkinson's disease. *Lancet,* 364(9440), pp. 1167-1169.

Chatani, E. and Yamamoto, N., 2018. Recent progress on understanding the mechanisms of amyloid nucleation. *Biophysical reviews,* 10(2), pp. 527-534.

Chen, L. and Feany, M.B., 2005. alpha-Synuclein phosphorylation controls neurotoxicity and inclusion formation in a Drosophila model of Parkinson disease. *Nature Neuroscience,* 8(5), pp. 657-663.

Chen, S.W., Drakulic, S., Deas, E., Ouberai, M., Aprile, F.A., Arranz, R., Ness, S., Roodveldt, C., Guilliams, T., De-Genst, E.J., Klenerman, D., Wood, N.W., Knowles, T.P.J., Alfonso, C., Rivas, G., Abramov, A.Y., Valpuesta, J.M., Dobson, C.M. and Cremades, N., 2015. Structural characterization of toxic oligomers that are kinetically trapped during alpha-synuclein fibril formation. *Proceedings of the National Academy of Sciences of the United States of America,* 112(16), pp. E1994-E2003.

Cheruvara, H., Allen-Baume, V.L., Kad, N.M. and Mason, J.M., 2015. Intracellular Screening of a Peptide Library to Derive a Potent Peptide Inhibitor of alpha-Synuclein Aggregation. *Journal of Biological Chemistry,* 290(12), pp. 7426-7435.

Chiti, F. and Dobson, C.M., 2006. Protein misfolding, functional amyloid, and human disease. *Annual Review of Biochemistry.* Palo Alto: Annual Reviews, pp. 333-366.
Choi, W., Zibaee, S., Jakes, R., Serpell, L.C., Davletov, B., Crowther, R.A. and Goedert, M., 2004. Mutation E46K increases phospholipid binding and assembly into filaments of human alpha-synuclein. *Febs Letters,* 576(3), pp. 363-368.

Cohen, S.I.A., Arosio, P., Presto, J., Kurudenkandy, F.R., Biverstal, H., Dolfe, L., Dunning, C., Yang, X.T., Frohm, B., Vendruscolo, M., Johansson, J., Dobson, C.M., Fisahn, A., Knowles, T.P.J. and Linse, S., 2015. A molecular chaperone breaks the catalytic cycle that generates toxic A beta oligomers. *Nature Structural & Molecular Biology,* 22(3), pp. 207-213.

Cookson, M.R., 2009. alpha-Synuclein and neuronal cell death. *Molecular Neurodegeneration,* 4, p. 14.

Costa, J., Lunet, N., Santos, C., Santos, J. and Vaz-Carneiro, A., 2010. Caffeine Exposure and the Risk of Parkinson's Disease: A Systematic Review and Meta-Analysis of Observational Studiess. *Journal of Alzheimers Disease,* 20, pp. S221-S238.

Craik, D.J., Fairlie, D.P., Liras, S. and Price, D., 2013. The Future of Peptide-based Drugs. *Chemical Biology & Drug Design,* 81(1), pp. 136-147.

Cremades, N., Cohen, S.I.A., Deas, E., Abramov, A.Y., Chen, A.Y., Orte, A., Sandal, M., Clarke, R.W., Dunne, P., Aprile, F.A., Bertoncini, C.W., Wood, N.W., Knowles, T.P.J., Dobson, C.M.

and Klenerman, D., 2012. Direct Observation of the Interconversion of Normal and Toxic Forms of alpha-Synuclein. *Cell,* 149(5), pp. 1048-1059.

Crowther, R.A., Daniel, S.E. and Goedert, M., 2000. Characterisation of isolated alpha-synuclein filaments from substantia nigra of Parkinson's disease brain. *Neuroscience Letters,* 292(2), pp. 128-130.

da Silveira, S.A., Schneider, B.L., Cifuentes-Diaz, C., Sage, D., Abbas-Terki, T., Iwatsubo, T., Unser, M. and Aebischer, P., 2009. Phosphorylation does not prompt, nor prevent, the formation of alpha-synuclein toxic species in a rat model of Parkinson's disease. *Human Molecular Genetics,* 18(5), pp. 872-887.

Dauer, W. and Przedborski, S., 2003. Parkinson's disease: Mechanisms and models. *Neuron,* 39(6), pp. 889-909.

Delamarre, A. and Meissner, W.G., 2017. Epidemiology, environmental risk factors and genetics of Parkinson's disease. *Presse Medicale,* 46(2), pp. 175-181.

den Jager, W.A., 1969. Sphingomyelin in Lewy inclusion bodies in Parkinson's disease. *Archives of neurology,* 21(6), pp. 615-619.

Dettmer, U., 2018. Rationally Designed Variants of alpha-Synuclein Illuminate Its in vivo Structural Properties in Health and Disease. *Frontiers in Neuroscience,* 12, p. 14.

Dettmer, U., Newman, A.J., von Saucken, V.E., Bartels, T. and Selkoe, D., 2015. KTKEGV repeat motifs are key mediators of normal alpha-synuclein tetramerization: Their mutation causes excess monomers and neurotoxicity. *Proceedings of the National Academy of Sciences of the United States of America,* 112(31), pp. 9596-9601.

Dong, C.H., Hoffmann, M., Li, X., Wang, M.J., Garen, C.R., Petersen, N.O. and Woodside, M.T., 2018. Structural characteristics and membrane interactions of tandem alpha-synuclein oligomers. *Scientific Reports,* 8, p. 11.

Dorsey, E.R., Constantinescu, R., Thompson, J.P., Biglan, K.M., Holloway, R.G., Kieburtz, K., Marshall, F.J., Ravina, B.M., Schifitto, G., Siderowf, A. and Tanner, C.M., 2007. Projected number of people with Parkinson disease in the most populous nations, 2005 through 2030. *Neurology,* 68(5), pp. 384-386.

Doty, R.L., 2012. Olfactory dysfunction in Parkinson disease. *Nature Reviews Neurology,* 8(6), pp. 329-339.

Du, H.N., Tang, L., Luo, X.Y., Li, H.T., Hu, J., Zhou, J.W. and Hu, H.Y., 2003. A peptide motif consisting of glycine, alanine, and valine is required for the fibrillization and cytotoxicity of human alpha-synuclein. *Biochemistry,* 42(29), pp. 8870-8878.

Dutheil, F., Beaune, P., Tzourio, C., Loriot, M.A. and Elbaz, A., 2010. Interaction Between ABCB1 and Professional Exposure to Organochlorine Insecticides in Parkinson Disease. *Archives of Neurology,* 67(6), pp. 739-745.

Fabelo, N., Martin, V., Santpere, G., Marin, R., Torrent, L., Ferrer, I. and Diaz, M., 2011. Severe Alterations in Lipid Composition of Frontal Cortex Lipid Rafts from Parkinson's Disease and Incidental Parkinson's Disease. *Molecular Medicine,* 17(9-10), pp. 1107-1118. Fanning, S., Selkoe, D. and Dettmer, U., 2020. Parkinson's disease: proteinopathy or lipidopathy? *Npj Parkinsons Disease,* 6(1), p. 9.

Fares, M.B., Ait-Bouziad, N., Dikiy, I., Mbefo, M.K., Jovicic, A., Kiely, A., Holton, J.L., Lee, S.J., Gitler, A.D., Eliezer, D. and Lashuel, H.A., 2014. The novel Parkinson's disease linked mutation G51D attenuates in vitro aggregation and membrane binding of alpha-synuclein, and enhances its secretion and nuclear localization in cells. *Human Molecular Genetics,* 23(17), pp. 4491-4509.

Fauvet, B., Mbefo, M.K., Fares, M.B., Desobry, C., Michael, S., Ardah, M.T., Tsika, E., Coune, P., Prudent, M., Lion, N., Eliezer, D., Moore, D.J., Schneider, B., Aebischer, P., El-Agnaf, O.M., Masliah, E. and Lashuel, H.A., 2012. alpha-Synuclein in Central Nervous System and from Erythrocytes, Mammalian Cells, and Escherichia coli Exists Predominantly as Disordered Monomer. *Journal of Biological Chemistry,* 287(19), pp. 15345-15364.

Feigin, V.L., Nichols, E., Alam, T., Bannick, M.S., Beghi, E., Blake, N., Culpepper, W.J., Dorsey, E.R., Elbaz, A., Ellenbogen, R.G., Fisher, J.L., Fitzmaurice, C., Giussani, G., Glennie, L., James, S.L., Johnson, C.O., Kassebaum, N.J., Logroscino, G., Marin, B., Mountjoy-Venning, W.C., Nguyen, M., Ofori-Asenso, R., Patel, A.P., Piccininni, M., Roth, G.A., Steiner, T.J., Stovner, L.J., Szoeke, C.E.I., Theadom, A., Vollset, S.E., Wallin, M.T., Wright, C., Zunt, J.R., Abbasi, N., Abd-Allah, F., Abdelalim, A., Abdollahpour, I., Aboyans, V., Abraha, H.N., Acharya, D., Adamu, A.A., Adebayo, O.M., Adeoye, A.M., Adsuar, J.C., Afarideh, M., Agrawal, S., Ahmadi, A., Ahmed, M.B., Aichour, A.N., Aichour, I., Aichour, M.T.E., Akinyemi, R.O., Akseer, N., Al-Eyadhy, A., Salman, R.A., Alahdab, F., Alene, K.A., Aljunid, S.M., Altirkawi, K., Alvis-Guzman, N., Anber, N.H., Antonio, C.A.T., Arabloo, J., Aremu, O., Arnlov, J., Asayesh, H., Asghar, R.J., Atalay, H.T., Awasthi, A., Quintanilla, B.P.A., Ayuk, T.B., Badawi, A., Banach, M., Banoub, J.A.M., Barboza, M.A., Barker-Collo, S.L., Barnighausen, T.W., Baune, B.T., Bedi, N., Behzadifar, M., Bejot, Y., Bekele, B.B., Belachew, A.B., Bennett, D.A., Bensenor, I.M., Berhane, A., Beuran, M., Bhattacharyya, K., Bhutta, Z.A., Biadgo, B., Bijani, A., Bililign, N., Bin Sayeed, M.S., Blazes, C.K., Brayne, C., Butt, Z.A., Campos-Nonato, I.R., Cantu-Brito, C., Car, M., Cardenas, R., et al., 2019. Global, regional, and national burden of neurological disorders, 1990-2016: a systematic analysis for the Global Burden of Disease Study 2016. *Lancet Neurology,* 18(5), pp. 459-480.

Fitzpatrick, A.W.P., Falcon, B., He, S., Murzin, A.G., Murshudov, G., Garringer, H.J., Crowther, R.A., Ghetti, B., Goedert, M. and Scheres, S.H.W., 2017. Cryo-EM structures of tau filaments from Alzheimer's disease. *Nature,* 547(7662), pp. 185-+.

Forster, J.I., Koglsberger, S., Trefois, C., Boyd, O., Baumuratov, A.S., Buck, L., Balling, R. and Antony, P.M.A., 2016. Characterization of Differentiated SH-SY5Y as Neuronal Screening

Model Reveals Increased Oxidative Vulnerability. *Journal of Biomolecular Screening,* 21(5), pp. 496-509.

Fujiwara, H., Hasegawa, M., Dohmae, N., Kawashima, A., Masliah, E., Goldberg, M.S., Shen, J., Takio, K. and Iwatsubo, T., 2002. alpha-Synuclein is phosphorylated in synucleinopathy lesions. *Nature Cell Biology,* 4(2), pp. 160-164.

Funayama, M., Ohe, K., Amo, T., Furuya, N., Yamaguchi, J., Saiki, S., Li, Y., Ogaki, K., Ando, M., Yoshino, H., Tomiyama, H., Nishioka, K., Hasegawa, K., Saiki, H., Satake, W., Mogushi, K., Sasaki, R., Kokubo, Y., Kuzuhara, S., Toda, T., Mizuno, Y., Uchiyama, Y., Ohno, K. and Hattori, N., 2015. CHCHD2 mutations in autosomal dominant late-onset Parkinson's disease: a genome-wide linkage and sequencing study. *Lancet Neurology,* 14(3), pp. 274-282.

Fusco, G., Chen, S.W., Williamson, P.T.F., Cascella, R., Perni, M., Jarvis, J.A., Cecchi, C., Vendruscolo, M., Chiti, F., Cremades, N., Ying, L.M., Dobson, C.M. and De Simone, A., 2017. Structural basis of membrane disruption and cellular toxicity by alpha-synuclein oligomers. *Science,* 358(6369), pp. 1440-+.

Galvagnion, C., 2017. The Role of Lipids Interacting with alpha-Synuclein in the Pathogenesis of Parkinson's Disease. *Journal of Parkinsons Disease,* 7(3), pp. 433-450.

Galvagnion, C., Buell, A.K., Meisl, G., Michaels, T.C.T., Vendruscolo, M., Knowles, T.P.J. and Dobson, C.M., 2015. Lipid vesicles trigger alpha-synuclein aggregation by stimulating primary nucleation. *Nature Chemical Biology,* 11(3), pp. 229-U101.

Galvagnion, C., Topgaard, D., Makasewicz, K., Buell, A.K., Linse, S., Sparr, E. and Dobson, C.M., 2019. Lipid Dynamics and Phase Transition within alpha-Synuclein Amyloid Fibrils. *The journal of physical chemistry letters*, pp. 7872-7877.

Ghosh, D., Mondal, M., Mohite, G.M., Singh, P.K., Ranjan, P., Anoop, A., Ghosh, S., Jha, N.N., Kumar, A. and Maji, S.K., 2013. The Parkinson's Disease-Associated H50Q Mutation Accelerates alpha-Synuclein Aggregation in Vitro. *Biochemistry,* 52(40), pp. 6925-6927.

Ghosh, D., Sahay, S., Ranjan, P., Salot, S., Mohite, G.M., Singh, P.K., Dwivedi, S., Carvalho, E., Banerjee, R., Kumar, A. and Maji, S.K., 2014. The Newly Discovered Parkinson's Disease Associated Finnish Mutation (A53E) Attenuates alpha-Synuclein Aggregation and Membrane Binding. *Biochemistry,* 53(41), pp. 6419-6421.

Giasson, B.I., Duda, J.E., Murray, I.V.J., Chen, Q.P., Souza, J.M., Hurtig, H.I., Ischiropoulos, H., Trojanowski, J.Q. and Lee, V.M.Y., 2000. Oxidative damage linked to neurodegeneration by selective alpha-synuclein nitration in synucleinopathy lesions. *Science,* 290(5493), pp. 985-989.

Giasson, B.I., Murray, I.V.J., Trojanowski, J.Q. and Lee, V.M.Y., 2001. A hydrophobic stretch of 12 amino acid residues in the middle of alpha-synuclein is essential for filament assembly. *Journal of Biological Chemistry,* 276(4), pp. 2380-2386.

Goedert, M., Jakes, R. and Spillantini, M.G., 2017. The Synucleinopathies: Twenty Years On. *Journal of Parkinsons Disease,* 7, pp. S53-S71.

Golbe, L.I., Diiorio, G., Bonavita, V., Miller, D.C. and Duvoisin, R.C., 1990. A LARGE KINDRED WITH AUTOSOMAL DOMINANT PARKINSONS-DISEASE. *Annals of Neurology,* 27(3), pp. 276-282.

Greenbaum, E.A., Graves, C.L., Mishizen-Eberz, A.J., Lupoli, M.A., Lynch, D.R., Englander, S.W., Axelsen, P.H. and Giasson, B.I., 2005. The E46K mutation in alpha-synuclein increases amyloid fibril formation. *Journal of Biological Chemistry,* 280(9), pp. 7800-7807.

Guerrero-Ferreira, R., Taylor, N.M.I., Arteni, A.-A., Kumari, P., Mona, D., Ringler, P., Britschgi, M., Lauer, M.E., Verasdock, J., Riek, R., Melki, R., Meier, B.H., Böckmann, A., Bousset, L. and Stahlberg, H., 2019. Two new polymorphic structures of alpha-synuclein solved by cryo-electron microscopy. bioRxiv doi:http://dx.doi.org/10.1101/654582.

Guerrero-Ferreira, R., Taylor, N.M.I., Mona, D., Ringler, P., Lauer, M.E., Riek, R., Britschgi, M. and Stahlberg, H., 2018. Cryo-EM structure of alpha-synuclein fibrils. *eLife,* 7.
Gurry, T., Ullman, O., Fisher, C.K., Perovic, I., Pochapsky, T. and Stultz, C.M., 2013. The Dynamic Structure of alpha-Synuclein Multimers. *Journal of the American Chemical Society,* 135(10), pp. 3865-3872.

Halliday, G.M., Holton, J.L., Revesz, T. and Dickson, D.W., 2011. Neuropathology underlying clinical variability in patients with synucleinopathies. *Acta Neuropathologica,* 122(2), pp. 187-204.

Harrison, R.S., Sharpe, P.C., Singh, Y. and Fairlie, D.P., 2007. Amyloid peptides and proteins in review. In: S.G. Amara, E. Bamberg, B. Fleischmann, T. Gudermann, S.C. Hebert, R. Jahn, W.J. Lederer, R. Lill, A. Miyajima, S. Offermanns and R. Zechner, eds. *Reviews of Physiology, Biochemistry and Pharmacology, Vol 159.* Berlin: Springer-Verlag Berlin, pp. 1-77.

Helmer, D. and Schmitz, K., 2016. Peptides and Peptide Analogs to Inhibit Protein-Protein Interactions. *Advances in experimental medicine and biology,* 917, pp. 147-183.

Hodara, R., Norris, E.H., Giasson, B.I., Mishizen-Eberz, A.J., Lynch, D.R., Lee, V.M.Y. and Ischiropoulos, H., 2004. Functional consequences of alpha-synuclein tyrosine nitration - Diminished binding to lipid vesicles and increased fibril formation. *Journal of Biological Chemistry,* 279(46), pp. 47746-47753.

Hong, D.P., Fink, A.L. and Uversky, V.N., 2008. Structural Characteristics of alpha-Synuclein Oligomers Stabilized by the Flavonoid Baicalein. *Journal of Molecular Biology,* 383(1), pp. 214-223.

Hu, C.Y., Fang, Y., Li, F.L., Dong, B., Hua, X.G., Jiang, W., Zhang, H., Lyu, Y. and Zhang, X.J., 2019. Association between ambient air pollution and Parkinson's disease: Systematic review and meta-analysis. *Environmental Research,* 168, pp. 448-459.

Iljina, M., Garcia, G.A., Horrocks, M.H., Tosatto, L., Choi, M.L., Ganzinger, K.A., Abramov, A.Y., Gandhi, S., Wood, N.W., Cremades, N., Dobson, C.M., Knowles, T.P.J. and Klenerman, D., 2016. Kinetic model of the aggregation of alpha-synuclein provides insights into prion-like spreading. *Proceedings of the National Academy of Sciences of the United States of America,* 113(9), pp. E1206-E1215.

Iyer, A., Roeters, S.J., Schilderink, N., Hommersom, B., Heeren, R.M.A., Woutersen, S., Claessens, M. and Subramaniam, V., 2016. The Impact of N-terminal Acetylation of alpha-Synuclein on Phospholipid Membrane Binding and Fibril Structure. *Journal of Biological Chemistry,* 291(40), pp. 21110-21122.

Jiang, P., Gan, M., Ebrahim, A., Castanedes-Casey, M., Dickson, D. and Yen, S.H., 2012. AMPK over-activation leads to accumulation of alpha-synuclein oligomers and decrease of neurites. *Society for Neuroscience Abstract Viewer and Itinerary Planner,* 42.

Jo, E.J., Fuller, N., Rand, R.P., St George-Hyslop, P. and Fraser, P.E., 2002. Defective membrane interactions of familial Parkinson's disease mutant A30P alpha-synuclein. *Journal of Molecular Biology,* 315(4), pp. 799-807.

Johnson, S.M., Wiseman, R.L., Sekijima, Y., Green, N.S., Adamski-Werner, S.L. and Kelly, J.W., 2005. Native state kinetic stabilization as a strategy to ameliorate protein misfolding diseases: A focus on the transthyretin amyloidoses. *Accounts of Chemical Research,* 38(12), pp. 911-921.

Kang, L.J., Moriarty, G.M., Woods, L.A., Ashcroft, A.E., Radford, S.E. and Baum, J., 2012. N-terminal acetylation of alpha-synuclein induces increased transient helical propensity and decreased aggregation rates in the intrinsically disordered monomer. *Protein Science,* 21(7), pp. 911-917.

Kaufmann, T.J., Harrison, P.M., Richardson, M.J.E., Pinheiro, T.J.T. and Wall, M.J., 2016. Intracellular soluble alpha-synuclein oligomers reduce pyramidal cell excitability. *Journal of Physiology-London,* 594(10), pp. 2751-2772.

Kayed, R., Head, E., Thompson, J.L., McIntire, T.M., Milton, S.C., Cotman, C.W. and Glabe, C.G., 2003. Common structure of soluble amyloid oligomers implies common mechanism of pathogenesis. *Science,* 300(5618), pp. 486-489.

Khalaf, O., Fauvet, B., Oueslati, A., Dikiy, I., Mahul-Mellier, A.L., Ruggeri, F.S., Mbefo, M.K., Vercruysse, F., Dietler, G., Lee, S.J., Eliezer, D. and Lashuel, H.A., 2014. The H50Q Mutation Enhances alpha-Synuclein Aggregation, Secretion, and Toxicity. *Journal of Biological Chemistry,* 289(32), pp. 21856-21876.

Khurana, R., Coleman, C., Ionescu-Zanetti, C., Carter, S.A., Krishna, V., Grover, R.K., Roy, R. and Singh, S., 2005. Mechanism of thioflavin T binding to amyloid fibrils. *Journal of Structural Biology,* 151(3), pp. 229-238.

Killinger, B.A., Melki, R., Brundin, P. and Kordower, J.H., 2019. Endogenous alpha-synuclein monomers, oligomers and resulting pathology: let's talk about the lipids in the room. *Npj Parkinsons Disease,* 5, p. 8.

Kitada, T., Asakawa, S., Hattori, N., Matsumine, H., Yamamura, Y., Minoshima, S., Yokochi, M., Mizuno, Y. and Shimizu, N., 1998. Mutations in the parkin gene cause autosomal recessive juvenile parkinsonism. *Nature,* 392(6676), pp. 605-608.

Klucken, J., Shin, Y., Masliah, E., Hyman, B.T. and McLean, P.J., 2004. Hsp70 reduces alpha-synuclein aggregation and toxicity. *Journal of Biological Chemistry,* 279(24), pp. 25497-25502.

Knowles, T.P.J., Waudby, C.A., Devlin, G.L., Cohen, S.I.A., Aguzzi, A., Vendruscolo, M., Terentjev, E.M., Welland, M.E. and Dobson, C.M., 2009. An Analytical Solution to the Kinetics of Breakable Filament Assembly. *Science,* 326(5959), pp. 1533-1537.

Kovalevich, J. and Langford, D., 2013. Considerations for the Use of SH-SY5Y Neuroblastoma Cells in Neurobiology. In: S. Amini and M.K. White, eds. *Neuronal Cell Culture: Methods and Protocols.* Totowa: Humana Press Inc, pp. 9-21.

Krishtal, J., Bragina, O., Metsla, K., Palumaa, P. and Tougu, V., 2017. In situ fibrillizing amyloid- beta 1-42 induces neurite degeneration and apoptosis of differentiated SH-SY5Y cells. *Plos One,* 12(10), p. 16.

Kruger, R., Kuhn, W., Muller, T., Woitalla, D., Graeber, M., Kosel, S., Przuntek, H., Epplen, J.T., Schols, L. and Riess, O., 1998. Ala30Pro mutation in the gene encoding alpha-synuclein in Parkinson's disease. *Nature Genetics,* 18(2), pp. 106-108.

Krumova, P., Meulmeester, E., Garrido, M., Tirard, M., Hsiao, H.H., Bossis, G., Urlaub, H., Zweckstetter, M., Kugler, S., Melchior, F., Bahr, M. and Weishaupt, J.H., 2011. Sumoylation inhibits alpha-synuclein aggregation and toxicity. *Journal of Cell Biology,* 194(1), pp. 49-60.

Lee, H.J., Choi, C. and Lee, S.J., 2002. Membrane-bound alpha-synuclein has a high aggregation propensity and the ability to seed the aggregation of the cytosolic form. *Journal of Biological Chemistry,* 277(1), pp. 671-678.

Lee, J.-E., Sang, J.C., Rodrigues, M., Carr, A.R., Horrocks, M.H., De, S., Bongiovanni, M.N., Flagmeier, P., Dobson, C.M., Wales, D.J., Lee, S.F. and Klenerman, D., 2018. Mapping Surface Hydrophobicity of alpha-Synuclein Oligomers at the Nanoscale. *Nano letters*.

Lesage, S., Anheim, M., Letournel, F., Bousset, L., Honore, A., Rozas, N., Pieri, L., Madiona, K., Durr, A., Melki, R., Verny, C., Brice, A. and French Parkinsons Dis Genet, S., 2013. G51D alpha-Synuclein mutation causes a novel Parkinsonian-pyramidal syndrome. *Annals of Neurology,* 73(4), pp. 459-471.

Lewy, F., 1912. Paralysis agitates. I. Pathologische Anatomie. Handbuch der Neurologie, Vol 3, Lewandowsky M, Abelsdorff G, des. Springer Verlag, Berlin, pp. 920-933.

Li, B.S., Ge, P., Murray, K.A., Sheth, P., Zhang, M., Nair, G., Sawaya, M.R., Shin, W.S., Boyer, D.R., Ye, S.L., Eisenberg, D.S., Zhou, Z.H. and Jiang, L., 2018. Cryo-EM of full-length alpha-

synuclein reveals fibril polymorphs with a common structural kernel. *Nature Communications,* 9, p. 10.

Li, Y.W., Zhao, C.Y., Luo, F., Liu, Z.Y., Gui, X.R., Luo, Z.P., Zhang, X., Li, D., Liu, C. and Li, X.M., 2018. Amyloid fibril structure of alpha-synuclein determined by cryoelectron microscopy. *Cell Research,* 28(9), pp. 897-903.

Liu, S.Y., Chan, P. and Stoessl, A.J., 2017. The underlying mechanism of prodromal PD: insights from the parasympathetic nervous system and the olfactory system. *Translational Neurodegeneration,* 6, p. 9.

Lorenzen, N., Nielsen, S.B., Buell, A.K., Kaspersen, J.D., Arosio, P., Vad, B.S., Paslawski, W., Christiansen, G., Valnickova-Hansen, Z., Andreasen, M., Enghild, J.J., Pedersen, J.S., Dobson, C.M., Knowles, T.P.J. and Otzen, D.E., 2014. The Role of Stable alpha-Synuclein Oligomers in the Molecular Events Underlying Amyloid Formation. *Journal of the American Chemical Society,* 136(10), pp. 3859-3868.

Lou, X.C., Kim, J., Hawk, B.J. and Shin, Y.K., 2017. alpha-Synuclein may cross-bridge v-SNARE and acidic phospholipids to facilitate SNARE-dependent vesicle docking. *Biochemical Journal,* 474, pp. 2039-2049.

Ludtmann, M.H.R., Angelova, P.R., Horrocks, M.H., Choi, M.L., Rodrigues, M., Baev, A.Y., Berezhnov, A.V., Yao, Z., Little, D., Banushi, B., Al-Menhali, A.S., Ranasinghe, R.T., Whiten, D.R., Yapom, R., Dolt, K.S., Devine, M.J., Gissen, P., Kunath, T., Jaganjac, M., Pavlov, E.V., Klenerman, D., Abramov, A.Y. and Gandhi, S., 2018. alpha-synuclein oligomers interact with ATP synthase and open the permeability transition pore in Parkinson's disease. *Nature Communications,* 9, p. 16.

Macdougall, I.C., Rossert, J., Casadevall, N., Stead, R.B., Duliege, A.M., Froissart, M. and Eckardt, K.U., 2009. A Peptide-Based Erythropoietin-Receptor Agonist for Pure Red-Cell Aplasia. *New England Journal of Medicine,* 361(19), pp. 1848-1855.

Madine, J., Doig, A.J. and Middleton, D.A., 2008. Design of an N-methylated peptide inhibitor of alpha-synuclein aggregation guided by solid-state NMR. *Journal of the American Chemical Society,* 130(25), pp. 7873-7881.

Maltsev, A.S., Ying, J.F. and Bax, A., 2012. Impact of N-Terminal Acetylation of alpha-Synuclein on Its Random Coil and Lipid Binding Properties. *Biochemistry,* 51(25), pp. 5004-5013.

Maroteaux, L. and Scheller, R.H., 1991. THE RAT-BRAIN SYNUCLEINS - FAMILY OF PROTEINS TRANSIENTLY ASSOCIATED WITH NEURONAL MEMBRANE. *Molecular Brain Research,* 11(3-4), pp. 335-343.

Mason, J.M., 2010. Design and development of peptides and peptide mimetics as antagonists for therapeutic intervention. *Future Medicinal Chemistry,* 2(12), pp. 1813-1822.

Mbefo, M.K., Paleologou, K.E., Boucharaba, A., Oueslati, A., Schell, H., Fournier, M., Olschewski, D., Yin, G.W., Zweckstetter, M., Masliah, E., Kahle, P.J., Hirling, H. and Lashuel,

H.A., 2010. Phosphorylation of Synucleins by Members of the Polo-like Kinase Family. *Journal of Biological Chemistry,* 285(4), pp. 2807-2822.

Meade, R.M., Fairlie, D.P. and Mason, J.M., 2019. Alpha-synuclein structure and Parkinson's disease - lessons and emerging principles. *Molecular Neurodegeneration,* 14, p. 14.

Meade, R.M., Williams, R.J. and Mason, J.M., 2020. A Series of Helical Alpha-synuclein Fibril Polymorphs Are Populated in the Prescence of Lipid Vesicles.

Meisl, G., Kirkegaard, J.B., Arosio, P., Michaels, T.C.T., Vendruscolo, M., Dobson, C.M., Linse, S. and Knowles, T.P.J., 2016. Molecular mechanisms of protein aggregation from global fitting of kinetic models. *Nature Protocols,* 11(2), pp. 252-272.

Morgan, J., 2015. A seat at the table for people with Parkinson's disease. *The Lancet. Neurology,* 14(11), pp. 1077-1078.
Nuber, S., Rajsombath, M., Minakaki, G., Winkler, J., Muller, C.P., Ericsson, M., Caldarone, B., Dettmer, U. and Selkoe, D.J., 2018. Abrogating Native alpha-Synuclein Tetramers in Mice Causes a L-DOPA-Responsive Motor Syndrome Closely Resembling Parkinson's Disease. *Neuron,* 100(1), pp. 75-+.

Oueslati, A., Fournier, M. and Lashuel, H.A., 2010. Role of post-translational modifications in modulating the structure, function and toxicity of alpha-synuclein: implications for Parkinson's disease pathogenesis and therapies. In: A. Bjorklund and M.A. Cenci, eds. *Recent Advances in Parkinsons Disease: Basic Research.* Amsterdam: Elsevier Science Bv, pp. 115-145.

Parkinson, J., 1817. An Essay on the Shaking Palsy. Sherwood, Neely and Jones, London.
Pasanen, P., Myllykangas, L., Siitonen, M., Raunio, A., Kaakkola, S., Lyytinen, J., Tienari, P.J., Poyhonen, M. and Paetau, A., 2014. A novel alpha-synuclein mutation A53E associated with atypical multiple system atrophy and Parkinson's disease-type pathology. *Neurobiology of Aging,* 35(9), p. 5.

Pasternak, B., Svanstrom, H., Nielsen, N.M., Fugger, L., Melbye, M. and Hviid, A., 2012. Use of Calcium Channel Blockers and Parkinson's Disease. *American Journal of Epidemiology,* 175(7), pp. 627-635.

Peduzzo, A., Linse, S. and Buell, A.K., 2020. The Properties of alpha-Synuclein Secondary Nuclei Are Dominated by the Solution Conditions Rather than the Seed Fibril Strain. *Acs Chemical Neuroscience,* 11(6), pp. 909-918.

Peelaerts, W. and Baekelandt, V., 2016. alpha-synuclein folds: the cards are on the table. *Nature Structural & Molecular Biology,* 23(5), pp. 359-360.

Peelaerts, W., Bousset, L., Van der Perren, A., Moskalyuk, A., Pulizzi, R., Giugliano, M., Van den Haute, C., Melki, R. and Baekelandt, V., 2015. alpha-Synuclein strains cause distinct synucleinopathies after local and systemic administration. *Nature,* 522(7556), pp. 340-+.

Pelletier, J.N., Arndt, K.M., Pluckthun, A. and Michnick, S.W., 1999. An in vivo library-versus-library selection of optimized protein-protein interactions. *Nature Biotechnology,* 17(7), pp. 683-690.

Perni, M., Flagmeier, P., Limbocker, R., Cascella, R., Aprile, F.A., Galvagnion, C., Heller, G.T., Meisl, G., Chen, S.W., Kumita, J.R., Challa, P.K., Kirkegaard, J.B., Cohen, S.I.A., Mannini, B., Barbut, D., Nollen, E.A.A., Cecchi, C., Cremades, N., Knowles, T.P.J., Chiti, F., Zasloff, M., Vendruscolo, M. and Dobson, C.M., 2018. Multistep Inhibition of alpha-Synuclein Aggregation and Toxicity in Vitro and in Vivo by Trodusquemine. *Acs Chemical Biology,* 13(8), pp. 2308-2319.

Perni, M., Galvagnion, C., Maltsev, A., Meisl, G., Muller, M.B.D., Challa, P.K., Kirkegaard, J.B., Flagmeier, P., Cohen, S.I.A., Cascella, R., Chen, S.W., Limboker, R., Sormanni, P., Heller, G.T., Aprile, F.A., Cremades, N., Cecchi, C., Chiti, F., Nollen, E.A.A., Knowles, T.P.J., Vendruscolo, M., Bax, A., Zasloff, M. and Dobson, C.M., 2017. A natural product inhibits the initiation of alpha-synuclein aggregation and suppresses its toxicity. *Proceedings of the National Academy of Sciences of the United States of America,* 114(6), pp. E1009-E1017.

Pieri, L., Madiona, K. and Melki, R., 2016. Structural and functional properties of prefibrillar alpha-synuclein oligomers. *Scientific Reports,* 6, p. 15.

Pissadaki, E.K. and Bolam, J.P., 2013. The energy cost of action potential propagation in dopamine neurons: clues to susceptibility in Parkinson's disease. *Frontiers in Computational Neuroscience,* 7, p. 17.

Polymeropoulos, M.H., Higgins, J.J., Golbe, L.I., Johnson, W.G., Ide, S.E., DiIorio, G., Sanges, G., Stenroos, E.S., Pho, L.T., Schaffer, A.A., Lazzarini, A.M., Nussbaum, R.L. and Duvoisin, R.C., 1996. Mapping of a gene for Parkinson's disease to chromosome 4q21-q23. *Science,* 274(5290), pp. 1197-1199.

Polymeropoulos, M.H., Lavedan, C., Leroy, E., Ide, S.E., Dehejia, A., Dutra, A., Pike, B., Root, H., Rubenstein, J., Boyer, R., Stenroos, E.S., Chandrasekharappa, S., Athanassiadou, A., Papapetropoulos, T., Johnson, W.G., Lazzarini, A.M., Duvoisin, R.C., DiIorio, G., Golbe, L.I. and Nussbaum, R.L., 1997. Mutation in the alpha-synuclein gene identified in families with Parkinson's disease. *Science,* 276(5321), pp. 2045-2047.

Pringsheim, T., Jette, N., Frolkis, A. and Steeves, T.D.L., 2014. The Prevalence of Parkinson's Disease: A Systematic Review and Meta-analysis. *Movement Disorders,* 29(13), pp. 1583-1590.

Pujols, J., Pena-Diaz, S., Conde-Gimenez, M., Pinheiro, F., Navarro, S., Sancho, J. and Ventura, S., 2017. High-Throughput Screening Methodology to Identify Alpha-Synuclein Aggregation Inhibitors. *International Journal of Molecular Sciences,* 18(3), p. 12.

Rahimi, F., Maiti, P. and Bitan, G., 2009. Photo-induced cross-linking of unmodified proteins (PICUP) applied to amyloidogenic peptides. *Journal of visualized experiments : JoVE,* (23).

Rastogi, S., Shukla, S., Kalaivani, M. and Singh, G.N., 2019. Peptide-based therapeutics: quality specifications, regulatory considerations, and prospects. *Drug Discovery Today,* 24(1), pp. 148-162.

Ritz, B., Ascherio, A., Checkoway, H., Marder, K.S., Nelson, L.M., Rocca, W.A., Ross, G.W., Strickland, D., Van den Eeden, S.K. and Gorell, J., 2007. Pooled analysis of tobacco use and risk of Parkinson disease. *Archives of Neurology,* 64(7), pp. 990-997.

Robson, E., Tweedy, C., Manzanza, N., Taylor, J.P., Atkinson, P., Randall, F., Reeve, A., Clowry, G.J. and LeBeau, F.E.N., 2018. Impaired Fast Network Oscillations and Mitochondrial Dysfunction in a Mouse Model of Alpha-synucleinopathy (A30P). *Neuroscience,* 377, pp. 161-173.

Rovere, M., Sanderson, J.B., Fonseca-Ornelas, L., Patel, D.S. and Bartels, T., 2018. Refolding of helical soluble alpha-synuclein through transient interaction with lipid interfaces. *Febs Letters,* 592(9), pp. 1464-1472.
Rutherford, N.J., Moore, B.D., Golde, T.E. and Giasson, B.I., 2014. Divergent effects of the H5OQ and G51D SNCA mutations on the aggregation of alpha-synuclein. *Journal of Neurochemistry,* 131(6), pp. 859-867.

Samii, A., Etminan, M., Wiens, M.O. and Jafari, S., 2009. NSAID Use and the Risk of Parkinson's Disease Systematic Review and Meta-Analysis of Observational Studies. *Drugs & Aging,* 26(9), pp. 769-779.

Sanders, L.H., McCoy, J., Hu, X.P., Mastroberardino, P.G., Dickinson, B.C., Chang, C.J., Chu, C.T., Van Houten, B. and Greenamyre, J.T., 2014. Mitochondrial DNA damage: Molecular marker of vulnerable nigral neurons in Parkinson's disease. *Neurobiology of Disease,* 70, pp. 214-223.

Sawaya, M.R., Sambashivan, S., Nelson, R., Ivanova, M.I., Sievers, S.A., Apostol, M.I., Thompson, M.J., Balbirnie, M., Wiltzius, J.J.W., McFarlane, H.T., Madsen, A.O., Riekel, C. and Eisenberg, D., 2007. Atomic structures of amyloid cross-beta spines reveal varied steric zippers. *Nature,* 447(7143), pp. 453-457.

Serpell, L.C., Berriman, J., Jakes, R., Goedert, M. and Crowther, R.A., 2000. Fiber diffraction of synthetic alpha-synuclein filaments shows amyloid-like cross-beta conformation. *Proceedings of the National Academy of Sciences of the United States of America,* 97(9), pp. 4897-4902.

Shahmoradian, S.H., Lewis, A.J., Genoud, C., Hench, J., Moors, T.E., Navarro, P.P., Castano-Diez, D., Schweighauser, G., Graff-Meyer, A., Godie, K.N., Sutterlin, R., Huisman, E., Ingrassia, A., de Gier, Y., Rozemuller, A.J.M., Wang, J., De Paepe, A., Erny, J., Staempfli, A., Hoernschemeyer, J., Grosseruschkamp, F., Niedieker, D., El-Mashtoly, S.F., Quadri, M., Van Ijcken, W.F.J., Bonifati, V., Gerwert, K., Bohrmann, B., Frank, S., Britschgi, M., Stahlberg, H., Van de Berg, W.D.J. and Lauer, M.E., 2019. Lewy pathology in Parkinson's disease consists of crowded organelles and lipid membranes. *Nature Neuroscience,* 22(7), pp. 1099-+.

Singh, Y., Sharpe, P.C., Hoang, H.N., Lucke, A.J., McDowall, A.W., Bottomley, S.P. and Fairlie, D.P., 2011. Amyloid Formation from an alpha-Helix Peptide Bundle Is Seeded by 3(10)-Helix Aggregates. *Chemistry-a European Journal,* 17(1), pp. 151-160.

Singleton, A.B., Farrer, M., Johnson, J., Singleton, A., Hague, S., Kachergus, J., Hulihan, M., Peuralinna, T., Dutra, A., Nussbaum, R., Lincoln, S., Crawley, A., Hanson, M., Maraganore, D., Adler, C., Cookson, M.R., Muenter, M., Baptista, M., Miller, D., Blancato, J., Hardy, J. and Gwinn-Hardy, K., 2003. alpha-synuclein locus triplication causes Parkinson's disease. *Science,* 302(5646), pp. 841-841.

Smith, G.P. and Petrenko, V.A., 1997. Phage display. *Chemical Reviews,* 97(2), pp. 391-410.
Souza, J.M., Giasson, B.I., Chen, Q.P., Lee, V.M.Y. and Ischiropoulos, H., 2000. Dityrosine cross-linking promotes formation of stable alpha-synuclein polymers - Implication of nitrative and oxidative stress in the pathogenesis of neurodegenerative synucleinopathies. *Journal of Biological Chemistry,* 275(24), pp. 18344-18349.
Spillantini, M.G., Schmidt, M.L., Lee, V.M.Y., Trojanowski, J.Q., Jakes, R. and Goedert, M., 1997. alpha-synuclein in Lewy bodies. *Nature,* 388(6645), pp. 839-840.

Stephens, A.D., Nespovitaya, N., Zacharopoulou, M., Kaminski, C.F., Phillips, J.J. and Schierle, G.S.K., 2018. Different Structural Conformers of Monomeric alpha-Synuclein Identified after Lyophilizing and Freezing. *Analytical Chemistry,* 90(11), pp. 6975-6983.

Stephens, A.D., Zacharopoulou, M. and Kaminski Schierle, G.S., 2018. The Cellular Environment Affects Monomeric alpha-Synuclein Structure. *Trends in biochemical sciences*.
Strohaker, T., Jung, B.C., Liou, S.H., Fernandez, C.O., Riedel, D., Becker, S., Halliday, G.M., Bennati, M., Kim, W.S., Lee, S.J. and Zweckstetter, M., 2019. Structural heterogeneity of alpha-synuclein fibrils amplified from patient brain extracts. *Nature Communications,* 10, p. 12.

Sugeno, N., Takeda, A., Hasegawa, T., Kobayashi, M., Kikuchi, A., Mori, F., Wakabayashi, K. and Itoyama, Y., 2008. Serine 129 phosphorylation of alpha-synuclein induces unfolded protein response-mediated cell death. *Journal of Biological Chemistry,* 283(34), pp. 23179-23188.

Sulzer, D., Cragg, S.J. and Rice, M.E., 2016. Striatal dopamine neurotransmission: Regulation of release and uptake. *Basal Ganglia,* 6(3), pp. 123-148.

Takeda, A., Mallory, M., Sundsmo, M., Honer, W., Hansen, L. and Masliah, E., 1998. Abnormal accumulation of NACP/alpha-synuclein in neurodegenerative disorders. *American Journal of Pathology,* 152(2), pp. 367-372.

Tan, L.C., Koh, W.P., Yuan, J.M., Wang, R.W., Au, W.L., Tan, J.H., Tan, E.K. and Yu, M.C., 2008. Differential effects of black versus green tea on risk of Parkinson's disease in the Singapore Chinese Health Study. *American Journal of Epidemiology,* 167(5), pp. 553-560.

Theillet, F.X., Binolfi, A., Bekei, B., Martorana, A., Rose, H.M., Stuiver, M., Verzini, S., Lorenz, D., van Rossum, M., Goldfarb, D. and Selenko, P., 2016. Structural disorder of monomeric alpha-synuclein persists in mammalian cells. *Nature,* 530(7588), pp. 45-+.

Tornquist, M., Michaels, T.C.T., Sanagavarapu, K., Yang, X.T., Meisl, G., Cohen, S.I.A., Knowles, T.P.J. and Linse, S., 2018. Secondary nucleation in amyloid formation. *Chemical Communications,* 54(63), pp. 8667-8684.

Trexler, A.J. and Rhoades, E., 2012. N-terminal acetylation is critical for forming a-helical oligomer of a-synuclein. *Protein Science,* 21(5), pp. 601-605.

Tuttle, M.D., Comellas, G., Nieuwkoop, A.J., Covell, D.J., Berthold, D.A., Kloepper, K.D., Courtney, J.M., Kim, J.K., Barclay, A.M., Kendall, A., Wan, W., Stubbs, G., Schwieters, C.D., Lee, V.M.Y., George, J.M. and Rienstra, C.M., 2016. Solid-state NMR structure of a pathogenic fibril of full-length human alpha-synuclein. *Nature Structural & Molecular Biology,* 23(5), pp. 409-415.
Twelves, D., Perkins, K.S.M. and Counsell, C., 2003. Systematic review of incidence studies of Parkinson's disease. *Movement Disorders,* 18(1), pp. 19-31.

Valente, E.M., Abou-Sleiman, P.M., Caputo, V., Muqit, M.M.K., Harvey, K., Gispert, S., Ali, Z., Del Turco, D., Bentivoglio, A.R., Healy, D.G., Albanese, A., Nussbaum, R., Gonzalez-Maldonaldo, R., Deller, T., Salvi, S., Cortelli, P., Gilks, W.P., Latchman, D.S., Harvey, R.J., Dallapiccola, B., Auburger, G. and Wood, N.W., 2004. Hereditary early-onset Parkinson's disease caused by mutations in PINK1. *Science,* 304(5674), pp. 1158-1160.

Van Den Eeden, S.K., Tanner, C.M., Bernstein, A.L., Fross, R.D., Leimpeter, A., Bloch, D.A. and Nelson, L.M., 2003. Incidence of Parkinson's disease: Variation by age, gender, and Race/Ethnicity. *American Journal of Epidemiology,* 157(11), pp. 1015-1022.

van Raaij, M.E., van Gestel, J., Segers-Nolten, I.M.J., de Leeuw, S.W. and Subramaniam, V., 2008. Concentration Dependence of alpha-Synuclein Fibril Length Assessed by Quantitative Atomic Force Microscopy and Statistical-Mechanical Theory. *Biophysical Journal,* 95(10), pp. 4871-4878.

Varkey, J., Isas, J.M., Mizuno, N., Jensen, M.B., Bhatia, V.K., Jao, C.C., Petrlova, J., Voss, J.C., Stamou, D.G., Steven, A.C. and Langen, R., 2010. Membrane Curvature Induction and Tubulation Are Common Features of Synucleins and Apolipoproteins. *Journal of Biological Chemistry,* 285(42), pp. 32486-32493.

Volles, M.J. and Lansbury, P.T., 2007. Relationships between the sequence of alpha-synuclein and its membrane affinity, fibrillization propensity, and yeast toxicity. *Journal of Molecular Biology,* 366(5), pp. 1510-1522.

Wang, W., Perovic, I., Chittuluru, J., Kaganovich, A., Nguyen, L.T.T., Liao, J.L., Auclair, J.R., Johnson, D., Landeru, A., Simorellis, A.K., Ju, S.L., Cookson, M.R., Asturias, F.J., Agar, J.N., Webb, B.N., Kang, C.H., Ringe, D., Petsko, G.A., Pochapsky, T.C. and Hoang, Q.Q., 2011. A

soluble alpha-synuclein construct forms a dynamic tetramer. *Proceedings of the National Academy of Sciences of the United States of America,* 108(43), pp. 17797-17802.

Weinreb, P.H., Zhen, W.G., Poon, A.W., Conway, K.A. and Lansbury, P.T., 1996. NACP, a protein implicated in Alzheimer's disease and learning, is natively unfolded. *Biochemistry,* 35(43), pp. 13709-13715.

Winner, B., Jappelli, R., Maji, S.K., Desplats, P.A., Boyer, L., Aigner, S., Hetzer, C., Loher, T., Vilar, M., Campioni, S., Tzitzilonis, C., Soragni, A., Jessberger, S., Mira, H., Consiglio, A., Pham, E., Masliah, E., Gage, F.H. and Riek, R., 2011. In vivo demonstration that alpha-synuclein oligomers are toxic. *Proceedings of the National Academy of Sciences of the United States of America,* 108(10), pp. 4194-4199.

Wolozin, B., Wang, S.W., Li, N.C., Lee, A., Lee, T.A. and Kazis, L.E., 2007. Simvastatin is associated with a reduced incidence of dementia and Parkinson's disease. *Bmc Medicine,* 5, p. 11.
Yedlapudi, D., Joshi, G.S., Luo, D., Todi, S.V. and Dutta, A.K., 2016. Inhibition of alpha-synuclein aggregation by multifunctional dopamine agonists assessed by a novel in vitro assay and an in vivo Drosophila synucleinopathy model. *Scientific Reports,* 6, p. 12.

Yoshino, H., Hirano, M., Stoessl, A.J., Imamichi, Y., Ikeda, A., Li, Y.Z., Funayama, M., Yamada, I., Nakamura, Y., Sossi, V., Farrer, M.J., Nishioka, K. and Hattori, N., 2017. Homozygous alpha-synuclein p.A53V in familial Parkinson's disease. *Neurobiology of Aging,* 57, p. 6.

Zarranz, J.J., Alegre, J., Gomez-Esteban, J.C., Lezcano, E., Ros, R., Ampuero, I., Vidal, L., Hoenicka, J., Rodriguez, O., Atares, B., Llorens, V., Tortosa, E.G., del Ser, T., Munoz, D.G. and de Yebenes, J.G., 2004. The new mutation, E46K, of alpha-synuclein causes Parkinson and Lewy body dementia. *Annals of Neurology,* 55(2), pp. 164-173.

Zavodszky, E., Seaman, M.N.J., Moreau, K., Jimenez-Sanchez, M., Breusegem, S.Y., Harbour, M.E. and Rubinsztein, D.C., 2014. Mutation in VPS35 associated with Parkinson's disease impairs WASH complex association and inhibits autophagy. *Nature Communications,* 5, p. 16.

Zhao, K., Li, Y., Liu, Z., Long, H., Zhao, C., Luo, F., Sun, Y., Tao, Y., Su, X.-D., Li, D., Li, X. and Liu, C., 2020. Parkinson's disease associated mutation E46K of alpha-synuclein triggers the formation of a distinct fibril structure. *Nature communications,* 11(1), p. 2643.

Zimprich, A., Biskup, S., Leitner, P., Lichtner, P., Farrer, M., Lincoln, S., Kachergus, J., Hulihan, M., Uitti, R.J., Calne, D.B., Stoessl, A.J., Pfeiffer, R.F., Patenge, N., Carbajal, I.C., Vieregge, P., Asmus, F., Muller-Myhsok, B., Dickson, D.W., Meitinger, T., Strom, T.M., Wszolek, Z.K. and Gasser, T., 2004. Mutations in LRRK2 cause autosomal-dominant Parkinsonism with pleomorphic pathology. *Neuron,* 44(4), pp. 601-607.

Appendix: Additional Work

Chapter A1: Excitation-Energy-Dependent Molecular Beacon Detects Early Stage Neurotoxic AB Aggregates in the Presence of Cortical Neurons

This declaration concerns the article entitled:

Excitation-Energy-Dependent Molecular Beacon Detects Early Stage Neurotoxic AB Aggregates in the Presence of Cortical Neurons

Publication status (tick one)									
Draft manuscript		**Submitted**		**In review**		**Accepted**		**Published**	**X**

Publication details (reference)	Gulacsy, C.E., Meade, R., Catici, D.A.M., Soeller, C., Pantos, G.D., Jones, D.D., Alibhai, D., Jepson, M., Valev, V.K., Mason, J.M., Williams, R.J. and Pudney, C.R., 2019. Excitation-Energy-Dependent Molecular Beacon Detects Early Stage Neurotoxic A beta Aggregates in the Presence of Cortical Neurons. *Acs Chemical Neuroscience,* 10(3), pp. 1240-1250.

Copyright status (tick the appropriate statement)

I hold the copyright for this material		Copyright is retained by the publisher, but I have been given permission to replicate the material here	**X**

Candidate's contribution to the paper (provide details, and also indicate as a percentage)	The candidate contributed to / considerably contributed to / **predominantly executed** the… Formulation of ideas: 10% - Developed peptide synthesis and purification methodology, and ThT aggregation protocol Design of methodology: 20% - Developed peptide synthesis and purification methodology, and ThT aggregation protocol Experimental work: 20% - Performed peptide synthesis and purification Presentation of data in journal format: 10% - Contributed to manuscript
Statement from Candidate	This paper reports on original research I conducted during the period of my Higher Degree by Research candidature.
Signed		**Date**	19/09/2020

Excitation-Energy-Dependent Molecular Beacon Detects Early Stage Neurotoxic Aβ Aggregates in the Presence of Cortical Neurons

Christina E. Gulácsy,[†] Richard Meade,[†] Dragana A. M. Catici,[†] Christian Soeller,[‖] G. Dan Pantos,[§] D. Dafydd Jones,[⊥] Dominic Alibhai,[#] Mark Jepson,[#] Ventsislav K. Valev,[‡] Jody M. Mason,*[†] Robert J. Williams,*[†] and Christopher R. Pudney*[†]

[†]Department of Biology and Biochemistry, [‡]Department of Physics, and [§]Department of Chemistry, University of Bath, Bath BA2 7AY, United Kingdom

[‖]Biomedical Physics, University of Exeter, Exeter EX4 4QD, United Kingdom

[⊥]School of Biosciences, Cardiff University, Cardiff CF10 3TL, United Kingdom

[#]Wolfson Bioimaging Facility, University of Bristol, Bristol BS8 1TS, United Kingdom

S Supporting Information

ABSTRACT: There is now crucial medical importance placed on understanding the role of early stage, subvisible protein aggregation, particularly in neurodegenerative disease. While there are strategies for detecting such aggregates in vitro, there is no approach at present that can detect these toxic species associated with cells and specific subcellular compartments. We have exploited excitation-energy-dependent fluorescence edge-shift of recombinant protein labeled with a molecular beacon, to provide a sensitive read out for the presence of subvisible protein aggregates. To demonstrate the potential utility of the approach, we examine the major peptide associated with the initiation of Alzheimer's disease, amyloid β-protein (Aβ) at a patho-physiologically relevant concentration in mouse cortical neurons. Using our approach, we find preliminary evidence that subvisible Aβ aggregates are detected at specific subcellular regions and that neurons drive the formation of specific Aβ aggregate conformations. These findings therefore demonstrate the potential of a novel fluorescence-based approach for detecting and imaging protein aggregates in a cellular context, which can be used to sensitively probe the association of early stage toxic protein aggregates within subcellular compartments.

KEYWORDS: Fluorescence, edge-shift, amyloid beta, Alzheimer's, neuron
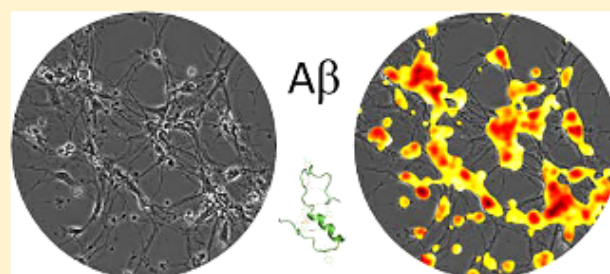
■ INTRODUCTION

Neurodegenerative disorders, such as Alzheimer's disease (AD), are major pathological issues facing aging populations across the world. These diseases typically arise coincident with the appearance and deposition of hallmark protein aggregates, many of which are thought to be toxic to neurons.[1] Amyloid β-protein (Aβ) is the major peptide component of senile plaques found in AD, and the present consensus view is that early stage, subvisible (<1 μm) aggregates composed of small oligomers of Aβ are the likely toxic species.[2,3] Formation of these early stage aggregates are thought to promote further aggregation, leading to fibrillation of the protein.[1] Early stage Aβ aggregates can be tracked in isolation, for example, using fluorescence resonance energy transfer (FRET) based assays,[4] and late-stage fibrillar aggregates can be monitored in cell-based or tissue assays.[5] A range of approaches have been developed for the purpose of capturing increasingly small and early stage protein aggregates, for example, emerging super-resolution,[6] FRET-based sensor[7] and single molecule approaches.[8,9]

However, there is presently no strategy for monitoring and quantifying the extent of prefibrillar, soluble Aβ aggregates associated with cells and in different subcellular compartments. Being able to visualize these early stage toxic species within their cellular context would dramatically enhance our ability to understand the molecular mechanisms underlying the development and progression of AD.

Excitation-energy-dependent changes in fluorophore emission are most commonly reported as the red-edge excitation shift (REES).[10−13] That is, the fluorescence emission spectrum of a fluorophore shows a shift in the peak maximum and inhomogeneous broadening of the spectra upon decreasing excitation energy.[11,12] This shift is observed in situations where, after photoexcitation, the solvent relaxation is slow relative to the emission of the fluorophore. This leads to emission from a lower level excited state, shifting the emission
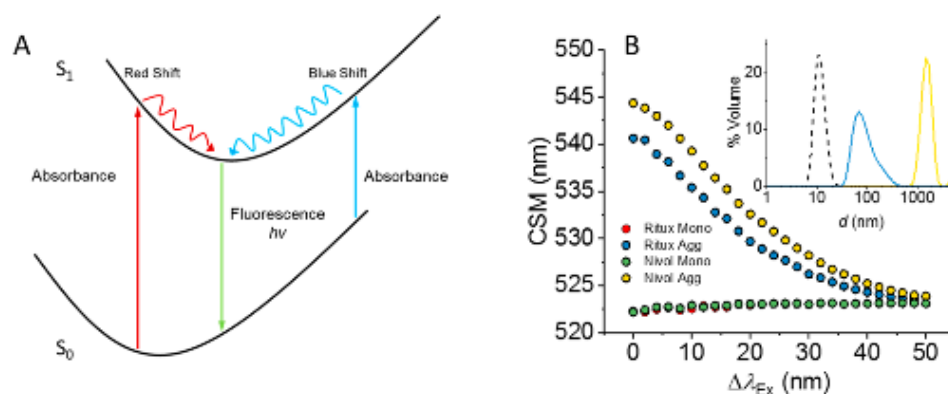
184

Figure 1. (A) Ground and excited electronic states demonstrated by the orientational coordinates of their zero vibrational levels. Relaxation along the potential curve to the energy minimum leads to photoselected emission causing a red-shift, or blue-shift for up-relaxation. (B) Edge-shift measurements of monomeric (red and green) and aggregated (blue and yellow) rituximab and nivolumab labeled with Alexa-488. Inset: DLS profiles for monomeric (black dashed line) and aggregated mAbs (colors as main panel).

to lower energies. When decreasing the excitation energy, discrete emission states are photoselected, resulting in a red-shift of the emission spectrum with respect to excitation wavelength.[10−14] The REES phenomenon has been observed in biomolecules both with intrinsic and extrinsic fluorophores.[14−19] Less commonly observed is a blue-shift in the emission spectrum with decreasing excitation energy, however, this may be explained by upward orientational relaxation of the environment.[20] These concepts are shown in Figure 1A. Experimentally, one measures the combined excitation/emission (EEM) spectrum and plots the change in the center of spectral mass (CSM) of the emission spectra versus the change in excitation wavelength ($\Delta\lambda_{Ex}$).

Edge-shift phenomena have been shown to be accurate probes of subtle protein conformational change (for example, refs [14−18]), and we have recently shown sensitivity to changes in the proteins free energy landscape.[15] Given this sensitivity, we reasoned that early stage, amorphous protein aggregates would similarly reflect highly complex fluorophore environments. As such, an extrinsic fluorophore label, acting as a molecular beacon, might prove sensitive to aggregate formation when measuring edge-shift. Such a probe would then allow the formation of early stage aggregates to be imaged.

Herein, we demonstrate that the fluorescence edge-shift phenomenon can be used to monitor the formation of early stage, subvisible Aβ aggregates (<~1 μm). We detect these species in cultured neurons exposed to nanomolar concentrations of a model peptide fragment[21] responsible for Aβ aggregation (Aβ15−21) as well as near full length peptide (Aβ1−40) and imaged using high resolution microscopy. We find evidence that subvisible Aβ aggregates associate with discrete subcellular compartments of the neuron, likely due to the presence of specific Aβ binding sites or the influence of the local cellular environment on the formation of a particular Aβ species. Moreover, our data point to the importance of considering Aβ aggregation in the presence of a relevant cellular model and that potentially neurons themselves drive the Aβ aggregation type. Our findings present a new approach for monitoring the formation and interaction of toxic Aβ species with a relevant cellular model system, but also point to a new tool that could be used much more widely to augment basic research and drug development into other neurodegenerative diseases that are driven by protein aggregation.

■ RESULTS AND DISCUSSION

Antibodies are particularly prone to aggregation and can easily be driven to early stage aggregates through low temperature incubation. Therefore, we wished to use these species as model systems to explore whether protein aggregation could be detected sensitively by extrinsic fluorophore edge-shift. We have labeled two therapeutic monoclonal antibodies (mAbs), rituximab and nivolumab, with either the fluorophores Alexa-488 or fluorescein via a maleimide linkage to solvent exposed cysteine residues (Figure S1).

Absorption spectra (Figure S1A−C) show that essentially 0.5 mol equiv of either dye binds to the mAbs under the conditions we use. Figure S1D−I shows the emission spectra for each dye-labeled mAb in both monomeric (Figure S1G−I) and aggregated states (Figure S1G−I). The resulting edge-shift data are shown in Figure 1B for the Alexa-488 mAbs and in Figure S2 for the fluorescein labeled mAb. Figure 1B inset shows dynamic light scattering (DLS) data for the mAbs, providing independent evidence that the thermally treated mAbs have formed subvisible aggregates. From Figure 1B, we find that the native, nonaggregated protein displays no edge-shift across the excitation range studied. However, we find on thermal aggregation of the mAbs, for both Alexa-488 and fluorescein, there is a clear blue-shift in the emission spectra (Figures 1B and S2). Moreover, the trend is the same with two different fluorophores, demonstrating our observation is not an artifact of a specific dye structure. The excitation spectra are essentially invariant across the emission range studied, for both the monomeric and aggregated mAbs as shown in Figure S1J−L, demonstrating that the observed edge-shift does not have an artifactual cause.

The monomeric mAb labeled with fluorescein shows some blue-shift in its emission spectra (Figure S2). However, the overall magnitude is far smaller than that observed for the aggregated protein. From Figure 1B, the data show that the magnitude of the blue-shift plateaus as the aggregates tend toward visible particles (>1 μm). Based on the observed changes, the observed edge shift appears to saturate toward aggregates in the ~100mer region. Therefore, these data suggest that the blue-shift is primarily sensitive to the formation of subvisible aggregates and we corroborate this finding below. We note that a recent study has shown that a red edge-shift is observed on aggregation of κ-casein as it forms
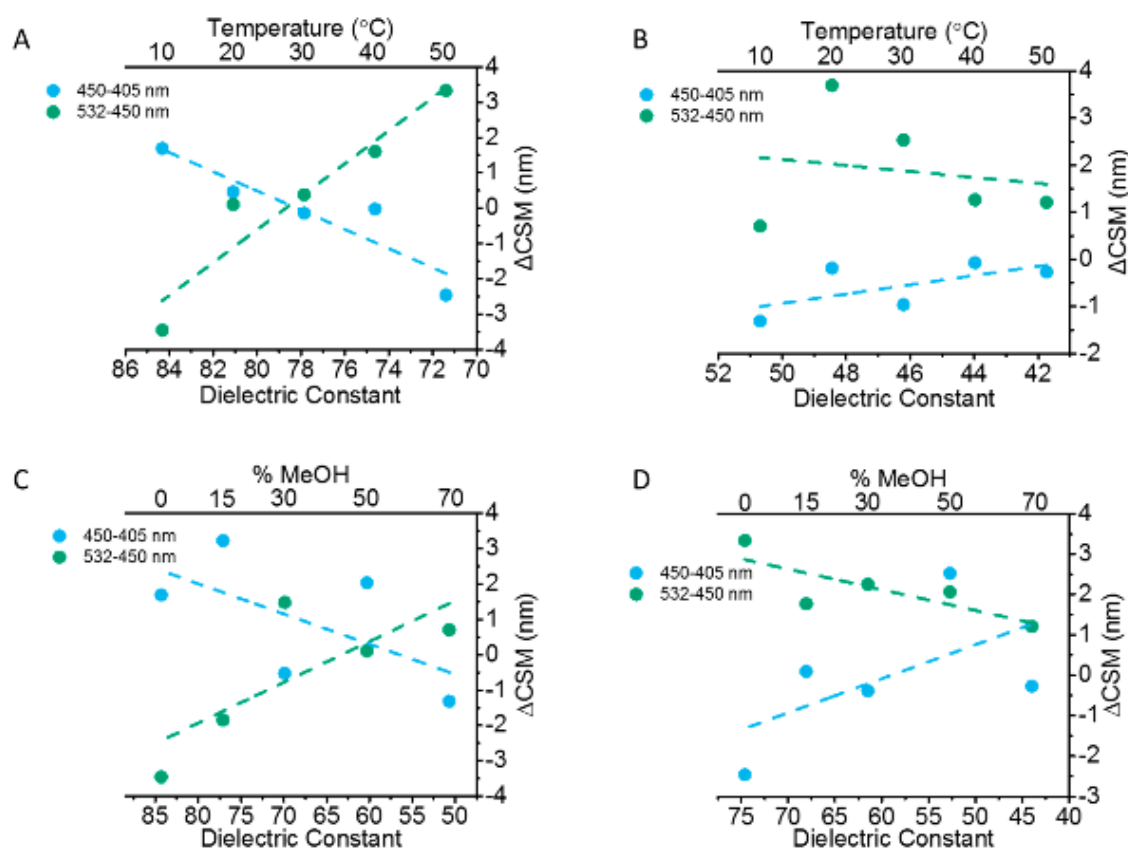
185

Figure 2. Variation in CSM of Alexa-488 versus change in dielectric constant of solvent where dielectric is changed by (A (0% MeOH), B (70% MeOH)), temperature, or (C (10 °C), D (50 °C)) methanol concentration. Alexa-488 emission was measured in water and methanol/water mixtures at 405, 450, and 532 nm. The laser lines were subtracted from the spectra, and a skewed Gaussian was fit to the data. CSM values were calculated from the fitted emission spectra. The difference was then taken between the CSMs of 450 and 405 nm, and 532 and 450 nm to give ΔCSM. The dashed-lines are to aid the eye only.

amyloid fibrils, based on tryptophan emission.[22] The edge-shift phenomenon is sensitive to changes in the dipole moment of the environment, and so we suggest that whether a red or blue shift is observed is based in large part on the specifics of the aggregation type and environment, which controls the dipole moment of the fluorophore. We explore this in more detail below.

Excitation energy-dependent spectral shifts are most commonly observed as a red-shift in emission spectra, though blue-shifts have been previously characterized.[20] Therefore, we turned to free fluorophore solution studies using laser-based excitation to confirm the blue-shift we observe in Figure 1B is responsive to environmental relaxation (Figure 1A), i.e., that it is a bone fide excitation-energy-dependent edge-shift. Figure S3A,B shows that Alexa-488, free in buffered solution, gives both a blue- and red-shift with increasing excitation wavelength. Figure S3C−E shows that these shifts are not attributable to the differential absorption of the excitation light at different excitation wavelengths, and are not due to the bandwidth of the excitation.

Edge-shift phenomena are based on slow dipolar relaxation of the solvent environment. Therefore, altering the solvent dipole should induce a change in the observed excitation energy-dependent edge-shift. Given the potential to observe either a red or a blue shift in excitation energy dependent fluorescence emission, we have conducted solvent studies to determine the dependence of a fluorophore on changes in

environment (dielectric). We altered the solvent dipole by two independent methods, through varying methanol concentration and temperature, and the resulting effect on the observed edge-shift from Figure S3A,B is shown in Figure 2. When using 0% methanol, the dielectric constant was reduced through increasing temperature, and was found to give a blue-shift for the ΔCSM values of 450 and 405 nm. A red-shift was observed for 532 and 450 nm (Figure 2A). However, when changing the solvent system for 70% methanol, a red-shift was observed for the ΔCSM of 450 and 405 nm, and a blue-shift for 532 and 450 nm (Figure 2B). At 10 and 50 °C, the dielectric constants were decreased by increasing methanol concentration. When measuring the ΔCSMs at 10 °C, a blue-shift was observed for 450 and 405 nm, and a red-shift for 532 and 450 nm (Figure 2C). This trend was inverted when the temperature was increased to 50 °C, showing a red-shift and blue-shift for ΔCSMs of 450 and 405 nm, and 532 and 450 nm, respectively (Figure 2D). The dielectric constants of the methanol/water mixtures were calculated as described by Andrenko and Wang[23] and correlated with the experimental data by Gosting and Albright.[24]

We find that both the blue- and red-shift (Figure S3E) are sensitive to changes in the dielectric constant of the solvent (Figure 2). Figure S4 shows that these shifts are not due to differences in the absorption spectrum when varying methanol concentrations. From Figure 2, decreasing the dielectric constant gave rise to an inversion of the blue- and red-shifts.
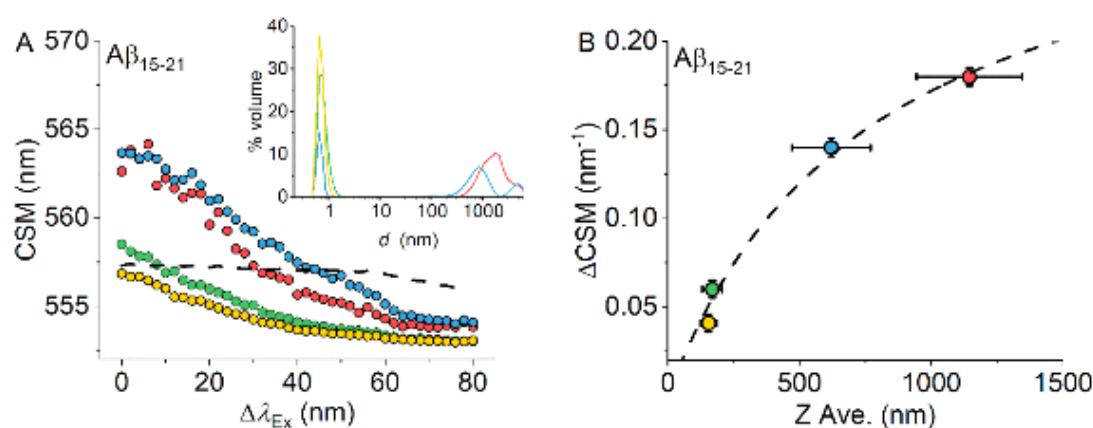
186

Figure 3. (A) Edge-shift measurements demonstrating sensitivity between monomerized and aggregated states (shown as differently colored data points) of fluor-Aβ_{15-21}, and coloration is correlated between the main panel and inset. The black dashed-line shows the data for fluorescein alone. Inset: DLS data for monomerized and aggregated fluor-Aβ_{15-21}. Coloration corresponds to aggregation state shown in the inset. (B) Correlation between the change in CSM (ΔCSM) for fluor-Aβ_{15-21} shown in panel (A). The Z-average hydrodynamic diameter from the DLS data shown in panel (A). Coloration is as in panel (A).

That is, the observed blue-shift becomes a red-shift and the observed red-shift becomes a blue-shift. These data are convincing evidence that the two edge-shifts arise from the same physical phenomenon, i.e., excitation-energy-dependent fluorescence edge-shift, as shown in Figure 1A. Moreover, these data suggest that a plausible mechanism for the large blue-shift, associated with the protein aggregation we observe above, is differences in the dipolar relaxation of the environment around the fluorophore on aggregate formation. We suggest this is because the early stage aggregates are potentially amorphous, and the molecular beacon experiences a range of different molecular (dipolar) environments. This would explain the relative insensitivity to larger, structured aggregates that are essentially a homogeneous repeating unit. Moreover, these data suggest that the same fluorophore can experience either a red or blue shift depending on changes in the local dielectric and this finding validates our finding of a blue edge-shift on protein aggregation (Figure 1B) and the observation of a red-shift for a different protein and fluorophore combination. We stress that our analysis does not at this point allow us to definitively assign the morphology and structure of aggregates, simply that we are detecting subvisible aggregates.

Having established that the observed edge-shift is bone fide and provides a measurement of the presence of subvisible protein aggregates in the mAb model systems, we sought to apply the approach to a biomedically important system where the formation of small soluble aggregates are relevant. Therefore, we synthesized the peptide fragment of Aβ that is responsible for the formation of toxic aggregates of the protein, Aβ_{15-21} (QKLVFFA). This peptide has previously been used as a model for the full length Aβ[25] and has some advantages in the tractability of synthesis. The peptide was synthesized with an N-terminal fluorescein (fluor-Aβ_{15-21}) to monitor the change in edge-shift on aggregation of the peptide. We opted for the fluorescein label since labeling large quantities of peptide with Alexa 488 would be prohibitively expensive for most researchers, and we would like others to be able to adopt this approach.

Figure 3A shows the observed edge-shift for monomerized and aggregated fluor-Aβ_{15-21} peptides and the corresponding raw emission and excitation spectra are shown in Figure S5A,B

and C, respectively. Peptide aggregates were obtained by aging the monomerized sample at room temperature and then separation by FPLC. Similar to the mAbs studied above, the excitation spectra essentially overlay at all emission wavelengths for the monomeric and aggregated protein (Figure S5C). Figure 3A inset shows the corresponding DLS profiles, showing the relative aggregation state of the samples. The ability of fluor-Aβ_{15-21} to form amyloid-like fibrillar aggregates is confirmed by the binding of thioflavin-T (ThT), giving an increase in ThT emission (Figure S6).[26] However, we note that the aggregates we observe, e.g., in Figure 3 are small and we suggest prefibrillar as we discuss below. Similar to the monomeric mAbs labeled with fluorescein, we observe a significant blue-shift associated with the monomeric fluor-Aβ_{15-21}. However, again similar to the fluorophore labeled mAb, the absolute magnitude of the edge-shift is small for the monomer (0.04 nm/nm) compared to the aggregated peptide (0.11 nm/nm).

Figure 3B shows the correlation between the absolute magnitude of the observed edge-shift versus the change in the intensity weighted aggregate size for fluor-Aβ_{15-21}. These data suggest, similar to the mAb data in Figure 1B that the magnitude of the edge-shift increases with the fraction of protein aggregate, but saturates as the aggregates tend toward visible (>1 μm). From Figure 3B it appears the edge-shift is most sensitive to relatively small aggregates, with highest sensitivity to hydrodynamic diameters on the low nanometer range (Figure 3A, inset). Such a size would correspond to low n oligomers of fluor-Aβ_{15-21} ~ 10−100 mers, similar to the approximate size with the mAbs above (Figure 1B). We note that centrifugation does not yield a measurable pellet. The blue-shift appears to saturate (Figure 3B) as the aggregates approach visible sizes (Figure 3A inset), suggesting that the approach is insensitive to large (>1 μm) aggregates that are classically captured by ThT assays. We suggest the reason for this insensitivity is because the late-stage fibrillar form of Aβ is essentially a homogeneous repeating unit, and the edge-shift phenomenon is based on detecting sample heterogeneity where discrete states can be photoselected. The sensitivity to the earliest stages of Aβ aggregates is important since it is the early stage aggregates that are considered to be the toxic species in AD.[3] Again we stress that at present we cannot
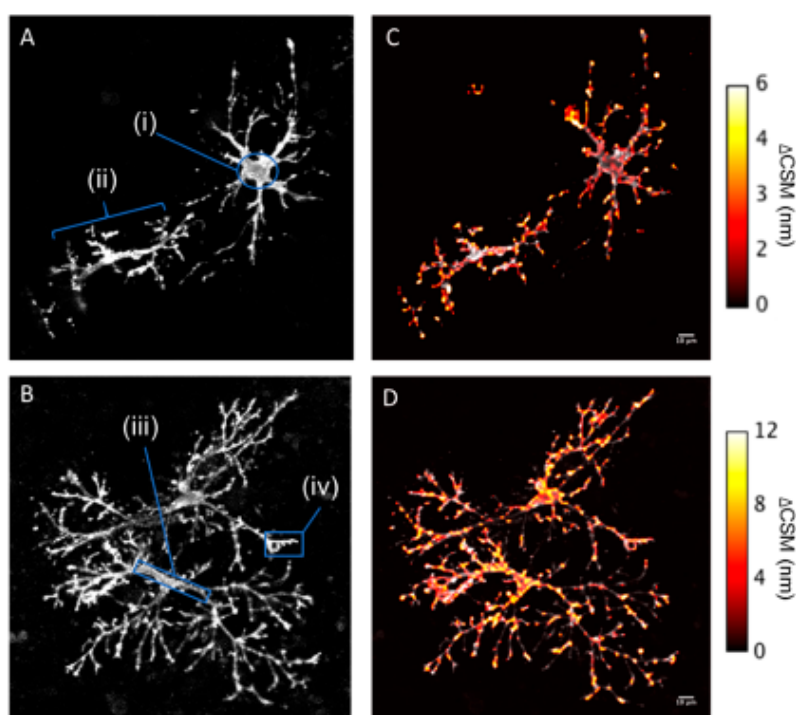
Figure 4. Mouse cortical neurons (A, cell; B, cell 2) treated with 500 nM $A\beta_{15-21}$-fluor, analyzed by high resolution fluorescence microscopy. Labels i−iv show specific morphological features, likely corresponding to the cell body (i), dendrite (ii), periaxonal region (iii), and synapses (iv). (C, D) Corresponding false color map of $\Delta CSM = CSM\ \lambda_{Ex514nm} - CSM\ \lambda_{Ex458\ nm}$ extracted from emission spectra of each image.

definitively determine the aggregation morphology (e.g fibrillary or not) based on the edge-shift value, simply the overall hydrodynamic diameter.

Having established that the observed edge-shift can be used to track subvisible protein aggregates, and that are relevant to $A\beta$ toxicity, we wished to ask if edge-shift could be observed and quantified using a microscope platform and applied to cell studies. We cultured mouse primary cortical neurons (reflecting a key region of the brain affected by AD) for 7 days[27] and incubated the differentiated cells for 24 h with a concentration of fluor-$A\beta_{15-21}$ that is within the range typically used for pathophysiological studies in vitro (500 nM).[28] The presence of fluor-$A\beta_{15-21}$ gave rise to significant morphological changes to the neurons, potentially indicative of neuro-toxicity as expected (Figure S7). The neurons were then washed with phosphate buffered saline (PBS) to remove nonbound fluor-$A\beta_{15-21}$ and fixed with 4% paraformaldehyde. Paraformaldehyde does not affect the absolute magnitude of the observed edge-shift giving, 0.039 nm/nm and 0.036 nm/nm for the untreated and paraformaldehyde treated fluor-$A\beta_{15-21}$, respectively.

Figure 4A (cell 1) and B (cell 2) shows examples of neurons with different morphologies. Cell 1 shows a large discrete cell body, proximal axons, and a dendritic network. Cell 2 shows a much more extensive and elaborate dendritic network, allowing better quantification of the edge-shift with respect to synaptic localization. We note that these assignments are based on the morphology of the cells and not confirmed by cell marker staining, due to the concern that introducing another dye molecule may affect the emission characteristics of the fluor-$A\beta_{15-21}$ through either resonance energy transfer (RET) or direct collisionalquenching. At present, we are not aware of any study that details the optical physics of such interactions

relating specifically to edge-shift phenomena and so we have been reluctant to convolve the present data set with this unknown. That said, our study aims to illustrate the potential of the approach and to establish the routes to and limitations of its use.

To extract the cellular CSM versus λ_{Ex} profile, we monitored the EEM spectra of the fixed cells using a Leica SP8 confocal microscope with spectral detection across the excitation range of 405−514 nm. Figure 4C and D shows the processed EEM data to give the absolute magnitude of the blue-shift as the difference in CSM between λ_{Ex} 458 and 516 nm, and were overlaid as a false color image onto the corresponding fluorescence image from Figure 4A and B. CSMs were calculated on a per pixel basis after smoothing with a Gaussian filter with a 6 pixel fwhm diameter. The coloration is based on the absolute magnitude of the observed blue-shift. The control experiment with fluorescein imaged alone is shown in Figure S8, giving a total edge-shift of ~1 nm between λ_{Ex} 458−516 nm. From Figure 4C and D, we find that the magnitude of the blue-shift varies significantly depending on the cellular morphology. Zoomed in views of the subcellular regions in Figure 4A and B are shown in Figure S9.

The cell body evident in Figure 4A shows essentially no edge-shift, consistent with the measurement from fluorescein alone (Figure S9). A larger edge-shift is observed for the axons and dendrites in both Figure 4C and D (Figure S9). Without staining, it is difficult to definitively identify synaptic structures. However, in many cases, we find that the likely locations of synapses and terminals, based on morphology, is coincident with very high magnitudes of measured edge-shift (Figure S9). Indeed, we selected cell 2 because of its extensive dendritic network where we anticipate a large number of synapses will be located. Cell 2 shows a globally larger edge-shift compared to
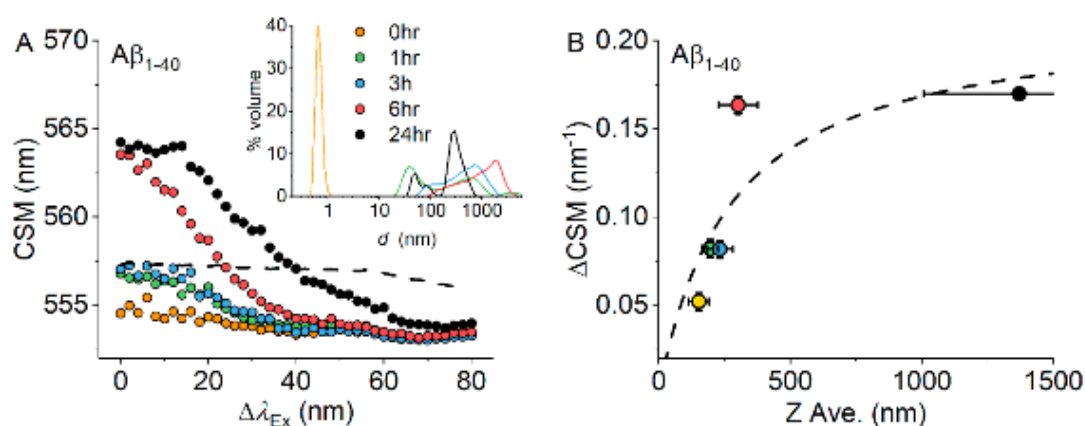
188

Figure 5. (A) Edge-shift measurements demonstrating sensitivity between monomerized and aggregated states of fluor-Aβ_{1-40} that have been aged for different time periods (inset) at 25 °C. The black dashed-line shows the data for fluorescein alone. Inset: DLS data for monomerized and aggregated fluor-Aβ_{1-40}. Coloration corresponds to time points in the inset. (B) Correlation between the change in CSM (ΔCSM) for fluor-Aβ_{1-40} shown in panel (A). The Z-average hydrodynamic diameter from the DLS data shown in panel (A). Coloration is as panel (A).

cell 1, which has a rather less developed dendritic structure. From Figure 3, we find that, for fluor-Aβ_{15-21}, an increase in the blue-shift is commensurate with the formation of subvisible, aggregates. Therefore, the data in Figure 4 suggest that formation and association of early stage fluor-Aβ_{15-21} aggregates are dependent on the cellular environment. Potentially these toxic species associate with dendrites but again we note the caveat of assigning subcellular structures based on morphology. This putative finding would however be consistent with the proposed synaptic binding sites and receptors for Aβ in neurons.[29] The large magnitude edge-shift values do not necessarily correlate with large fluorescence intensity readings in Figure 4, as shown in Figure S9. That is, the extracted edge-shift values are not representing high local concentrations of the fluor-Aβ_{15-21}, but more specifically capturing differences in early stage aggregation state. Given the potential demonstrated with the fluor-Aβ_{15-21} we next examined a similar data set with a longer form of Aβ, fluor-Aβ_{1-40} as shown in Figures 5−7.

Figure 5 shows the observed edge-shift for the fluor-Aβ_{1-40} 40 peptide but now aged over 24 h at 25 °C, starting from the monomerized fluor-Aβ_{1-40}. The corresponding raw excitation/emission spectra are shown in Figure S10. Figure 5A inset shows the corresponding DLS profiles and Figure 5B shows the correlation between the observe edge-shift and the size of aggregate. From Figure 5 the blue shift we observe with fluor-Aβ_{15-21} is essentially recapitulated for fluor-Aβ_{1-40} and even the relationship of aggregate size to the magnitude of edge-shift is qualitatively very similar (cf. Figures 3B and 5B). We note that none of the time points we have tested show any significant emission arising from ThT binding (Figure S11) suggesting that, as with fluor-Aβ_{15-21} above, the edge-shift is only sensitive to the early stage aggregates of Aβ. Moreover, similar to fluor-Aβ_{15-21}, we find that the magnitude of the edge shiftsaturates as the hydrodynamic diameter approaches ~1 μm (Figure 5B). Finally, from Figure S12, we show that fluor-Aβ_{1-40} is cytotoxic (based on MTT absorption to assess cytotoxicity) as one expects and compared to a scrambled version of fluor-Aβ_{15-21} (fluor-FKFQVAL), which does not show any significant edge-shift and is not predicted to aggregate based on sequence analysis.

We have imaged 500 nM fluor-Aβ_{1-40} in the presence of cortical neurons as in Figure 4, but using the fluor-Aβ_{1-40}

samples aged as in Figure 5. The resulting data for 0, 1, and 3 h are shown in Figure 6. At 6 and 24 h we observed only sparse fluorescence emission and we have not analyzed the edge shift values for these data as we were not confident that the signal magnitude would allow us to extract accurate CSM values. From Figure 6 there is clearly association of fluor-Aβ_{1-40} with the neurons as with fluor-Aβ_{15-21} in Figure 4. The magnitude of edge-shift is similar as with fluor-Aβ_{15-21}, but now is red-shifted c.f. blue-shifted. The observed red edge-shift is also in contrast with the solution studies with fluor-Aβ_{1-40} (Figure 5), where a blue-shift is observed on aggregation. As with fluor-Aβ_{15-21} the large magnitude edge-shift values do not necessarily correlate with the highest intensity fluorescence regions. This confirms that the absolute magnitude of emission is not a good reporter of early stage aggregate association on cells. We note that the scrambled fluor-Aβ_{15-21} peptide shows hardly any emission under the same incubation times with the same cultured neurons (Figure S13) and is insufficient to generate a similar false color map of the edge-shift as in Figure 6. These data suggest that the observed edge shift in the presence of cultured neurons is not significantly convolved of nonspecific binding.

The local concentration of fluor-Aβ_{1-40} may be highly variable depending on association with subcellular features and aggregation state. We do not find a significant change in the magnitude of the edge-shift value associated with different concentrations of the monomerized fluor-Aβ_{1-40} (Figure S14), suggesting the observed changes in edge-shift shown in Figure 6 are not artifacts arising from changes in local concentration.

We have also attempted to monitor the signal arising from fluor-Aβ_{1-40} aged in the presence of cells, however we found that the emission signal dissipated after 1 h. Recent evidence has suggested that apoptosis-associated speck-like protein containing a CARD (ASC) specks released by microglia, formed on Aβ deposition, increases the formation of Aβ oligomers and aggregates.[30] Potentially, the partially aggregated fluor-Aβ_{1-40} from Figure 5 gives improved binding in the first instance, at least under the conditions reported. A potential hypothesis therefore is that the sample aged in the presence of neurons are not induced to form aggregates because of a lack of ASC specks.

The observation of a red versus a blue edge-shift is readily explained from our model fluorophore studies shown in Figure
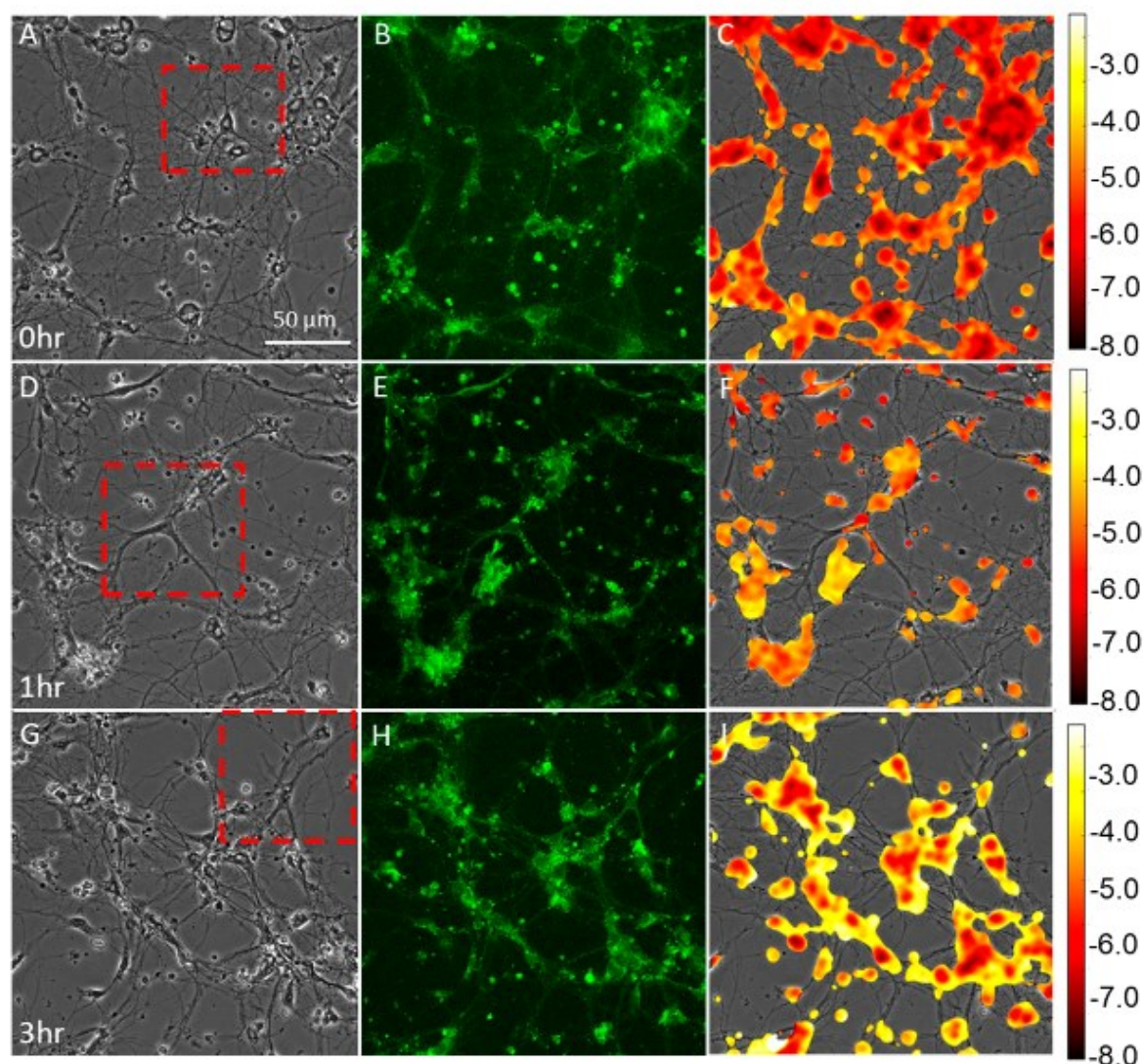
189

Figure 6. Mouse cortical neurons treated with aged 500 nM fluor-Aβ_{15-21} from Figure 5 at 0 h (A), 1 h (D), and 3 h (G). The panels at right of each condition show a corresponding fluorescence emission image ($\lambda_{Ex458\ nm}$; panels B, E, and H) and the extracted edge shift value ($\lambda_{Ex514\ nm}$ − CSM $\lambda_{Ex458\ nm}$; panels C, F, and I) overlaid as a false color map the corresponding image (panel A, D, and G). The scale bar at right corresponds to the ΔCSM values in the edge-shift false color maps.

2 and described above. These data show that a blue shift can transition to a red-shift, purely based on changes in solvent (environment) dielectric constant and this is consistent with the expected physical interpretation of edge shift phenomenon. Specifically, for the corresponding wavelength range studied in Figures 5, the data in Figure 2 suggest a red shift occurs as the dielectric of the environment becomes smaller. That is, in the presence of neurons, the fluorophore molecular beacon is located in a relatively high dielectric environment for fluor-Aβ_{15-21} aggregates and in a relatively low dielectric environment for fluor-Aβ_{1-40} aggregates.

The dielectric constant inside a protein is generally much lower than at the proteins surface[31] and so our data suggest the fluorophore molecular beacon is buried in protein aggregates for fluor-Aβ_{1-40} and rather more solvent exposed for fluor-Aβ_{15-21}. Indeed, recent studies using tryptophan as an intrinsic reporter of protein aggregation find a red edge-shift,[22] corroborating this notion. Taken together, our finding of a red shift for fluor-Aβ_{1-40} in the presence of cells versus a blue-shift in solution potentially suggests an aggregate conformation (dipole environment) that is unique to the combination of fluor-Aβ_{1-40} and the cellular microenvironment. That we find a different aggregate conformation in the presence of neurons versus buffered solution suggests a hypothesis where the cellular environment drives a specific aggregation mechanism that is unique to the full length Aβ. We would stress that this represents a working hypothesis, since only a discrete whole cell study could confidently validate the hypothesis. However, we believe these data are intriguing and provide the rationale for the exploration of the hypothesis.

Membrane association has the potential to alter the environmental relaxation rate of the fluorophore.[32] Therefore, we wished to test if the immediate subcellular environment is the origin of the edge-shift observed for Aβ1−40, instead of a specific conformational state of the aggregate. We have therefore incubated fluor-Aβ_{1-40} with nanodiscs, similar to previous studies[33] and observed the edge-shift at 0 and 6 h as shown in Figure S15. From Figure S15 we find the presence of

190

potentially represent shrunken cell bodies consistent with labeling of apoptotic cell corpses. The colocalization of highly aggregated Aβ with these features points to an important cellular context in which further studies could fruitfully be applied using the edge-shift approach to probe the mechanisms of Aβ induced neuronal cell death.

■ CONCLUSIONS

We have demonstrated the edge-shift in the emission spectra of fluorophore labeled proteins can report on very early stage (subvisible) aggregates. We have applied this finding to whole-cell microscopy experiments to monitor the formation of early stage toxic aggregates of Aβ, at physiological concentrations, in mouse primary cortical neurons. We find that the edge-shift is readily observable in the presence of a relevant cell type, and that the additional information from the microscopy platform potentially allows site specific measurement of the magnitude of the edge-shift. Based on these preliminary studies, our data prompts the hypothesis that Aβ aggregation occurs in a site-specific manner on neuronal cells and that the neurons themselves, or their local environment, potentially drive the formation and specific conformation of the aggregates. We note that, at present, no other approach that we are aware of is able to detect and quantify these subvisible aggregates on a microscopy platform using whole-cells, with a sensitivity that can detect differences in subcellular location.

Clearly, a caveat with the approach is that it relies on labeling the protein of interest. Therefore, while we do not advocate this approach for diagnostic imaging, our findings point the way for studying the underlying cause of Aβ pathology in AD as well as other neurotoxic protein aggregates. Moreover, our study suggests the absolute magnitude of the edge-shift will be sensitive to (i) aggregate size, (ii) distribution of different aggregates, and (iii) morphology of the aggregates. Disentangling these contributions is the next step in developing the utility of this approach and our data point to the potentially very high discriminatory power. A part of this understanding will come from detailed photophysical studies of the edge-shift phenomenon itself. Finally, we see high potential for imaging at the super-resolution level combined with bio-orthogonal labeling strategies to explore different cellular contexts in fine detail. That is, we suggest that building the edge-shift approach into other detection methodologies will significantly enhance the utility of the methods used in isolation. Given that the edge-shift approach has the advantage that it does not require specialist instrumentation, and uses established, readily available fluorescent probes we anticipate this should be an achievable goal in the short term.

■ METHODS

Antibody Labeling. Antibodies (rituximab and nivolumab) were a kind gift from Bath ASU (Corsham, UK). Antibodies were labeled with Alexa Fluor 488 C5-Maleimide from Molecular Probes by Life Technologies or Fluorescein-5-Maleimide from Thermo Scientific. To 1 mL of 50 mM Tris-HCl pH 8.0 buffer, 50 μL of antibody and 10 μL (10 mg/mL) (Alexa 488) or 14 mM (fluorescein-5-maleimide) dye were added, and the mixture was left at 5 °C for 1 h. The protein was then run through a PD-10 desalting column, and the absorbance was measured on a Varian Cary 50 Bio UV−visible spectrophotometer (Varian, Walnut Creek, CA) to monitor antibody tagging. Aggregation was induced thermally for 30 min at 60 °C for nivolumab and 70 °C for rituximab. The antibodies were a kind gift from Bath ASU.

Dynamic Light Scattering (DLS). Aggregation data was obtained in a 50 μL quartz cuvette on a Malvern Zetasizer Nano S (Malvern, Worcestershire, UK) to determine hydrodynamic radius. Samples were left to equilibrate for 2 min at 25 °C then measured in triplicate and averaged for reporting.

Fluorescein Labeled Amyloid β Synthesis. Rink amide ChemMatrix resin was obtained from PCAS Biomatrix, Inc. (St.-Jean-sur-Richelieu, Canada); Fmoc l-amino acids and 2-(1H-benzotriazole-1-yl)-1,1,3,3-tetramethyluronium hexafluorophosphate or benzotriazol-1-yl-oxytripyrrolidinophosphonium hexafluorophosphate were obtained from AGTC Bioproducts (Hessle, UK); all other reagents were of peptide synthesis grade and obtained from Thermo Fisher Scientific (Loughborough, UK). Peptides were synthesized on a 0.1 mmol scale on a PCAS ChemMatrix Rink amide resin using a Liberty Blue microwave peptide synthesizer (CEM; Matthews, NC) employing Fmoc solid-phase techniques with repeated steps of coupling, deprotection and washing (4 × 5 mL dimethylformamide).[34] Coupling was performed as follows: Fmoc amino acid (5 equiv), 2-(1H-benzotriazole-1-yl)-1,1,3,3-tetramethyluronium hexafluorophosphate or benzotriazol-1-yl-oxytripyrrolidino-phosphonium hexafluorophosphate (4.5 equiv), and diisopropylethylamine (10 equiv) in dimethylformamide (5 mL) for 5 min with 35 W microwave irradiation at 90 °C. Deprotection was performed as follows: 20% piperidine in dimethylformamide for 5 min with 30 W microwave irradiation at 80 °C. Following synthesis, the peptide was labeled with 5(6)-carboxyfluorescein using a standard coupling step for 20 min, and then cleaved from the resin with concomitant removal of side-chain-protecting groups by treatment with a cleavage mixture (10 mL) consisting of TFA (95%), triisopropylsilane (2.5%) and H$_2$O (2.5%) for 4 h at room temperature. Suspended resin was removed by filtration, and the peptide was precipitated using three rounds of crashing in ice-cold diethyl ether, vortexing, and centrifuging. The pellet was then dissolved in 1:1 MeCN/H$_2$O and freeze-dried. Purification was performed by RP-HPLC using a Phenomenex Jupiter Proteo (C18) reverse-phase column (4 μm, 90 Å, 10 mm inner diameter × 250 mm long). Eluents used were as follows: 0.1%TFA in H$_2$O (a) and 0.1% TFA in MeCN (b). The peptide was eluted by applying a linear gradient (at 3 mL/min) of 5−70% B over 40 min. Fractions collected were examined by electrospray MS, and those found to contain exclusively the desired product were pooled and lyophilized. Analysis of the purified final product by RP-HPLC indicated a purity of >95%. Prior to running fluorescence measurements, fluorescein labeled Aβ15−21 and Aβ1−40 were monomerized using Zagorski methodology, followed by size exclusion on a PD-10 column to separate monomerized and aggregated material.[35]

Fluorescence Measurements. REES measurements were carried out on a PerkinElmer LS50B luminescence spectrometer (Perkin-nElmer, Waltham, MA) which was temperature regulated ($\pm$1 °C) using a circulating water bath. Samples were allowed 5 min to equilibrate prior to measurements. Measurements were obtained at 20 °C for labeled antibodies and 10 °C for fluorescein labeled amyloid β. Excitation−emission slits were 4.0 nm for Alexa 488 tagged antibodies and fluorescein tagged Aβ. Formaldehyde studies for fluorescein tagged Aβ used excitation−emission slit widths of 6.0 nm. Alexa 488 emission was measured from 480 to 620 nm, with excitation scans taken every 2 nm from 410 to 460 nm. Fluorescein emission was monitored from 535 to 650 nm, with excitation varied every 2 nm from 400 to 520 nm. All measurements were performed in triplicate with the corresponding buffers also measured and subtracted from the spectra for each sample.

For single wavelength excitation measurements, excitation sources were 4.5 mW laser diode modules (405, 450, 532 nm) and fluorescence emission was detected with a compact CCD CCS100 spectrometer (ThorLabs, Newton, NJ).

The center of spectral mass (CSM) was calculated using

$$CSM = \frac{\sum (f_i \lambda_{Em})}{\sum (f_i)} \qquad (1)$$

191

where the measured fluorescence intensity is f_i and the emission wavelength is λ_{Em}. For measurements in buffered solution, the concentration of protein/peptide used was typically between 1 and 2 μM and for microscopy experiments with neurons present, the concentration was 500 nM (buffer in both cases is PBS).

High Resolution Fluorescence Microscopy. REES measurements were carried out on a Leica SP8 confocal microscope, Leica Microsystems with an argon ion laser as the excitation source for 458, 476, 488, 496, and 514 nm with total power of 65 mW. A 50 mW diode laser was used for λ_{Ex} measurements at 405 nm. Measurements were carried out at 37 °C measuring emission from 542.5 to 638.5 nm. As 405 nm gave a high amount of autofluorescence, CSM values were calculated for cells from 458 nm upward where there is effectively no autofluorescence to be convolved in the signal.

Primary Neuronal Cell Culture. Primary cortical neurons were prepared from CD1 mouse embryos in accordance with UK Home Office Guidelines as stated in the Animals (Scientific Procedures) Act 1986 using Schedule 1 procedures approved by the University of Bath Animal Welfare and Ethical Review Body. Primary neurons were prepared essentially as described previously.[22] Cortices were dissected from 15 day old CD1 mouse embryos, and were mechanically dissociated in PBS supplemented with 33 mM glucose, using a fire-polished glass Pasteur pipet. Cells were plated into either 12- or 24-well Nunc tissue culture plates, previously coated with 20 μg/mL poly-D-lysine (Sigma). Neurons were cultured in Neurobasal medium (phenol red free) supplemented with 2 mM glutamine, 100 μg/mL penicillin, 60 μg/mL streptomycin, and B27 (all from Invitrogen), and incubated at 37 °C, in high humidity with 5% CO_2. Under these growth conditions at 7−8 days in vitro (DIV), cells had a well-developed neuritic network and were 99% β-tubulin III positive and <1% GFAP positive.

ASSOCIATED CONTENT

Ⓢ Supporting Information

The Supporting Information is available free of charge on the ACS Publications website at DOI: 10.1021/acschemneuro.8b00322.

> Absorption, emission, and excitation spectra corresponding to the EEM data shown, microscopy image showing whole cells and zoomed in views, scrambled peptide, and nanodisc control experiments (PDF)

AUTHOR INFORMATION

Corresponding Authors

*E-mail: j.mason@bath.ac.uk.
*E-mail: r.j.williams@bath.ac.uk.
*E-mail: c.r.pudney@bath.ac.uk. Tel: +44 (0)1225 385049.

ORCID ●

G. Dan Pantos: 0000-0003-2200-550X
D. Dafydd Jones: 0000-0001-7709-3995
Ventsislav K. Valev: 0000-0001-9951-1836
Jody M. Mason: 0000-0002-4118-1958
Christopher R. Pudney: 0000-0001-6211-0086

Author Contributions

C.E.G., R.M., D.A., D.A.M.C., and R.J.W. conducted experiments. C.E.G., C.S., D.D.J., V.K.V., G.D.P., J.M.M., R.J.W., and C.R.P. designed experiments. All authors interpreted data and contributed to data analysis. All authors wrote the manuscript. All authors have given approval to the final version of the manuscript.

Notes

The authors declare no competing financial interest.

ACKNOWLEDGMENTS

ABBREVIATIONS

Aβ, amyloid-β protein; AD, Alzheimer's disease; CSM, center of spectral mass; EEM, excitation/emission matrix; REES, red-edge excitation-shift; mAb, monoclonal antibody; RET, resonance energy transfer.

REFERENCES

(1) De Strooper, B., and Karran, E. (2016) The Cellular Phase of Alzheimer's Disease. *Cell 164*, 603−615.

(2) Ferreira, S. T., Lourenco, M. V., Oliveira, M. M., and De Felice, F. G. (2015) Soluble amyloid-β oligomers as synaptotoxins leading to cognitive impairment in Alzheimer's disease. *Front. Cell. Neurosci. 9*, 191.

(3) Viola, K. L., and Klein, W. L. (2015) Amyloid β oligomers in Alzheimer's disease pathogenesis, treatment, and diagnosis. *Acta Neuropathol. 129*, 183−206.

(4) Lee, J., Culyba, E. K., Powers, E. T., and Kelly, J. W. (2011) Amyloid-beta forms fibrils by nucleated conformational conversion of oligomers. *Nat. Chem. Biol. 7*, 602−609.

(5) Xu, M., Ren, W., Tang, X., Hu, Y., and Zhang, H. (2016) Advances in development of fluorescent probes for detecting amyloid-β aggregates. *Acta Pharmacol. Sin. 37*, 719.

(6) Young, L. J., Kaminski Schierle, G. S., and Kaminski, C. F. (2017) Imaging Ab(1−42) fibril elongation reveals strongly polarised growth and growth incompetent states. *Phys. Chem. Chem. Phys. 19*, 27987.

(7) Hatai, J., Motiei, L., and Margulies, D. (2017) Analyzing Amyloid Beta Aggregates with a Combinatorial Fluorescent Molecular Sensor. *J. Am. Chem. Soc. 139*, 2136−2139.

(8) Horrocks, M. H., Lee, S. F., Gandhi, S., Magdalinou, N. K., Chen, S. W., Devine, M. J., Tosatto, L., Kjaergaard, M., Beckwith, J. S., Zetterberg, H., Iljina, M., Cremades, N., Dobson, C. M., Wood, N. W., and Klenerman, D. (2016) Single-Molecule Imaging of Individual Amyloid Protein Aggregates in Human Biofluids. *ACS Chem. Neurosci. 7*, 399−406.

(9) Nag, S., Chen, J., Irudayaraj, J., and Maiti, S. (2010) Measurement of the Attachment and Assembly of Small Amyloid-b Oligomers on Live Cell Membranes at Physiological Concentrations Using Single-Molecule Tools. *Biophys. J. 99*, 1969−1975.

(10) Demchenko, A. P. (2002) The red-edge effects: 30 years of exploration. *Luminescence 17*, 19−42.

(11) Itoh, K. (1975) Shift of the emission band upon excitation at the long wavelength absorption edge. II. Importance of the solute−solvent interaction and the solvent reorientation relaxation process. *J. Chem. Phys. 62*, 3431−3438.

(12) Azumi, T., Itoh, K., and Shiraishi, H. (1976) Shift of emission band upon the excitation at the long wavelength absorption edge. III. Temperature dependence of the shift and correlation with the time dependent spectral shift. *J. Chem. Phys. 65*, 2550−2555.

(13) Demchenko, A. P., and Ladokhin, A. S. (1988) Red-edge-excitation fluorescence spectroscopy of indole and tryptophan. *Eur. Biophys. J. 15*, 369−379.

(14) Chattopadhyay, A., and Haldar, S. (2014) Dynamic insight into protein structure utilizing red edge excitation shift. *Acc. Chem. Res. 47*, 12−19.

(15) Catici, D. A. M., Amos, H. E., Yang, Y., van den Elsen, J. M. H., and Pudney, C. R. (2016) The red edge excitation shift phenomenon can be used to unmask protein structural ensembles: implications for NEMO−ubiquitin interactions. *FEBS J. 283*, 2272−2284.

192

(16) Chattopadhyay, A., Rawat, S. S., Kelkar, D. A., Ray, S., and Chakrabarti, A. (2003) Organization and dynamics of tryptophan residues in erythroid spectrin: novel structural features of denatured spectrin revealed by the wavelength-selective fluorescence approach. *Protein Sci. 12*, 2389−2403.

(17) Kelkar, D. A., Chaudhuri, A., Haldar, S., and Chattopadhyay, A. (2010) Exploring tryptophan dynamics in acid-induced molten globule state of bovine α-lactalbumin: A wavelength-selective fluorescence approach. *Eur. Biophys. J. 39*, 1453−1463.

(18) Demchenko, A. P., and Sytnik, A. I. (1991) Solvent reorganizational red-edge effect in intramolecular electron transfer. *Proc. Natl. Acad. Sci. U. S. A. 88*, 9311−9314.

(19) Haldar, S., Chaudhuri, A., and Chattopadhyay, A. (2011) Organization and dynamics of membrane probes and proteins utilizing the red edge excitation shift. *J. Phys. Chem. B 115*, 5693−5706.

(20) Nemkovich, N., and Matseyko, V. T. V. (1980) Intermolecular Up-Relaxation in Phthalimide Solutions at Excitation by Frequency Tuned Dye Laser. *Opt. Spectrosk. 49*, 274−283.

(21) Tjernberg, L. O., Näslund, J., Lindqvist, F., Johansson, J., Karlström, a R., Thyberg, J., Terenius, L., and Nordstedt, C. (1996) *J. Biol. Chem. 271*, 8545−8548.

(22) Chakraborty, H., and Chattopadhyay, A. (2017) Sensing Tryptophan Microenvironment of Amyloid Protein Utilizing Wavelength-Selective Fluorescence Approach. *J. Fluoresc. 27*, 1995−2000.

(23) Wang, P., and Anderko, A. (2001) Computation of dielectric constants of solvent mixtures and electrolyte solutions. *Fluid Phase Equilib. 186*, 103−122.

(24) Albright, P. S., and Gosting, L. J. (1946) Dielectric Constants of the Methanol-Water System from 5 to 55°. *J. Am. Chem. Soc. 68*, 1061−1063.

(25) Tjernberg, L. O., Callaway, D. J. E., Tjernberg, A., Hahne, S., Lilliehook, C., Terenius, L., Thyberg, J., and Nordstedt, C. (1999) A Molecular Model of Alzheimer Amyloid b-Peptide Fibril Formation. *J. Biol. Chem. 274*, 12619−12625.

(26) Levine, H. (1993) Thioflavine T interaction with synthetic Alzheimer's disease β-amyloid peptides: Detection of amyloid aggregation in solution. *Protein Sci. 2*, 404−410.

(27) Cox, C. J., Choudhry, F., Peacey, E., Perkinton, M. S., Richardson, J. C., Howlett, D. R., Lichtenthaler, S. F., Francis, P. T., and Williams, R. J. (2015) Dietary (−)-epicatechin as a potent inhibitor of $\beta\gamma$-secretase amyloid precursor protein processing. *Neurobiol. Aging 36*, 178−187.

(28) Abbott, J. J., Howlett, D. R., Francis, P. T., and Williams, R. J. (2008) Aβ_{1-42} modulation of Akt phosphorylation via α7 nAChR and NMDA receptors. *Neurobiol. Aging 29*, 992−1001.

(29) Shankar, G. M., Li, S., Mehta, T. H., Garcia-Munoz, A., Shepardson, N. E., Smith, I., Brett, F. M., Farrell, M. A., Rowan, M. J., Lemere, C. A., Regan, C. M., Walsh, D. M., Sabatini, B. L., and Selkoe, D. J. (2008) Amyloid-beta protein dimers isolated directly from Alzheimer's brains impair synaptic plasticity and memory. *Nat. Med. 14*, 837−42.

(30) Venegas, C., Kumar, S., Franklin, B. S., Dierkes, T., Brinkschulte, R., Tejera, D., Vieira-Saecker, A., Schwartz, S., Santarelli, F., Kummer, M. P., Griep, A., Gelpi, E., Beilharz, M., Riedel, D., Golenbock, D. T., Geyer, M., Walter, J., Latz, E., and Heneka, M. T. (2017) Microglia-derived ASC specks cross- seed amyloid-β in Alzheimer's disease Genetic and experimental evidence supports a pathogenic role of immune activation in neurodegenerative disorders. *Nature 552*, 355−361.

(31) Li, L., Li, C., Zhang, Z., and Alexov, E. (2013) On the dielectric "constant" of proteins: Smooth dielectric function for macromolecular modeling and its implementation in DelPhi. *J. Chem. Theory Comput. 9*, 2126−2136.

(32) Chattopadhyay, A., and Mukherjee, S. (1999) Red Edge Excitation Shift of a Deeply Embedded Membrane Probe: Implications in Water Penetration in the Bilayer. *J. Phys. Chem. B 103*, 8180−8185.

(33) Mcdowall, J. S., Ntai, I., Hake, J., Whitley, P. R., Mason, J. M., Pudney, C. R., and Brown, D. R. (2017) Steady-State Kinetics of α-Synuclein Ferrireductase Activity Identifies the Catalytically Competent Species. *Biochemistry 56*, 2497−2505.

(34) Fields, G. B., and Noble, R. L. (1999) Solid-phase peptide synthesis utilizing 9-fluorenylmethoxycarbonyl amino acids. *Int. J. Pept. Protein Res. 35*, 161−214.

(35) Zagorski, M. G., Yang, J., Shao, H., Ma, K., Zeng, H., and Hong, A. (1999) Methodological and chemical factors affecting amyloid β-peptide amyloidogenicity. *Methods Enzymol. 309*, 189−203.

193

Chapter A1: Supporting Information

Supplementary information - An excitation-energy-dependent molecular beacon detects early-stage neurotoxic Aβ aggregates in the presence of cortical neurons.

Christina E. Gulácsy[1], Richard Meade[1], Dragana A.M. Catici[1], Christian Soeller[4], G.Dan Panto[§3], D. Dafydd Jones[5], Dominic Alibhai[6], Mark Jepson[6], Ventsislav K. Valev[2], Jody M. Mason[1]*, Robert J. Williams[1]*, Christopher R. Pudney[1]*

[1]Department of Biology and Biochemistry, [2]Department of Physics, [3]Department of Chemistry, University of Bath, Bath, United Kingdom.[4]Biomedical Physics, University of Exeter, Exeter, United Kingdom.[5]School of Biosciences, Cardiff University, Cardiff, United Kingdom. [6]Wolfson Bioimaging Facility, University of Bristol, Bristol United Kingdom.

Supplementary figures
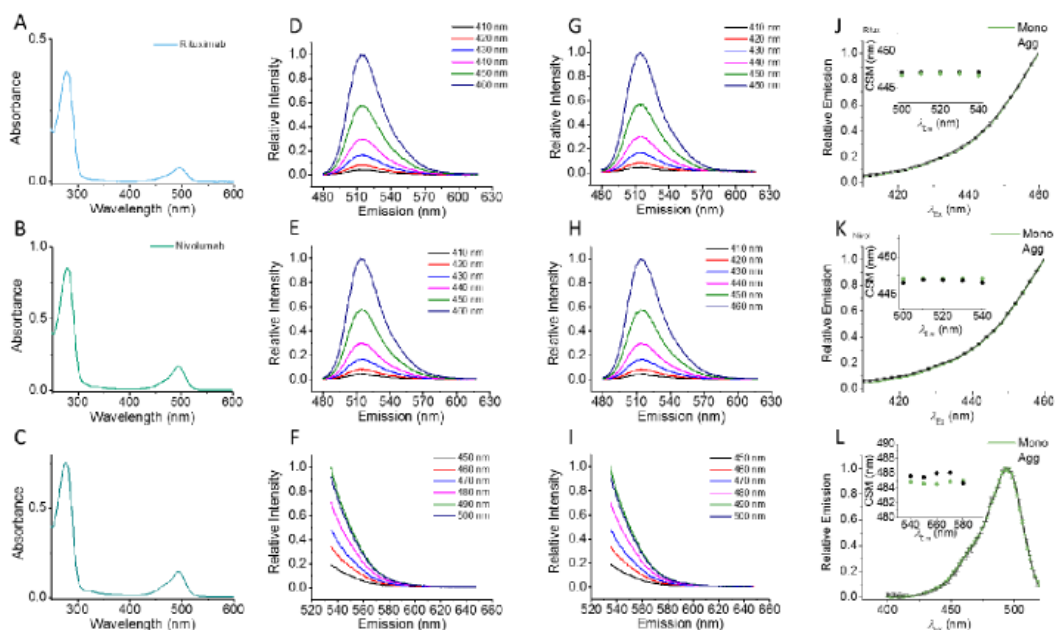
Figure S1. Absorption, emission and excitation spectra of fluorophore labelled antibodies both monomeric and aggregated. Top row show Rituximab-Alexa 488 data, middle row shows Nivolumab-Alexa 488 data and the bottom row shows Rituximab-Fluorescein data. **A-C,** Absorption spectra of Alexa 488 labelled Rituximab (**A**), Nivolumab (**B**) and fluorescein labelled Rituximab (**C**). The ratio of extinction coefficients for the protein (280 nm) and the dye (~500 nm) suggests approximately 0.5 molar equivalents of fluorophore are bound to the antibodies in all cases. **D-F,** Sample EEM spectra for monomeric (assessed by DLS) mAbs. **G-I,** Sample EEM spectra for aggregated (assessed by DLS) mAbs. Note that the Stokes shift of the fluorophore determines how much of the emission spectrum can be present and not be convolved of the excitation light, with this being the reason for the difference in the spectra between Alexa 488 and fluorescein. **J-L,** Comparison of excitation spectra for both monomeric (green line) and aggregated (black line) mAbs. The excitation spectra shown are the average normalized values across the range of emission wavelengths and the error bars on each data point represent the standard deviation of the normalized spectra. That is, the very small error bars illustrate that the excitation spectrum at each emission wavelength essentially overlay and that the excitation spectra for both the monomeric and aggregated proteins overlay. *Inset* is the CSM of the excitation spectra at a range of different emission wavelengths, where CSM is calculated in the same way as described in the main text. The CSM values are essentially invariant at each emission wavelength and this is quantifiable evidence that the excitation spectra are identical. Variation in excitation spectra is, therefore, not the cause of the observed fluorescence edge-shift.
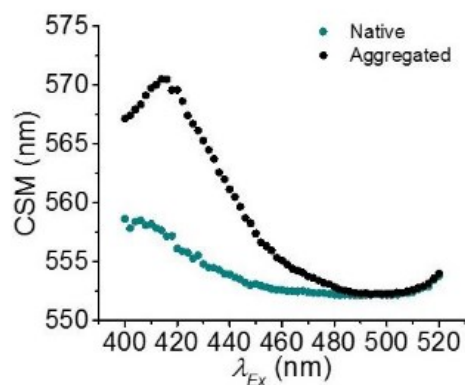
Figure S2. Fluorescein labeled Rituximab shows an excitation-energy-dependent blue-shift when aggregated, similar to the Alexa 488 labelled mAbs.
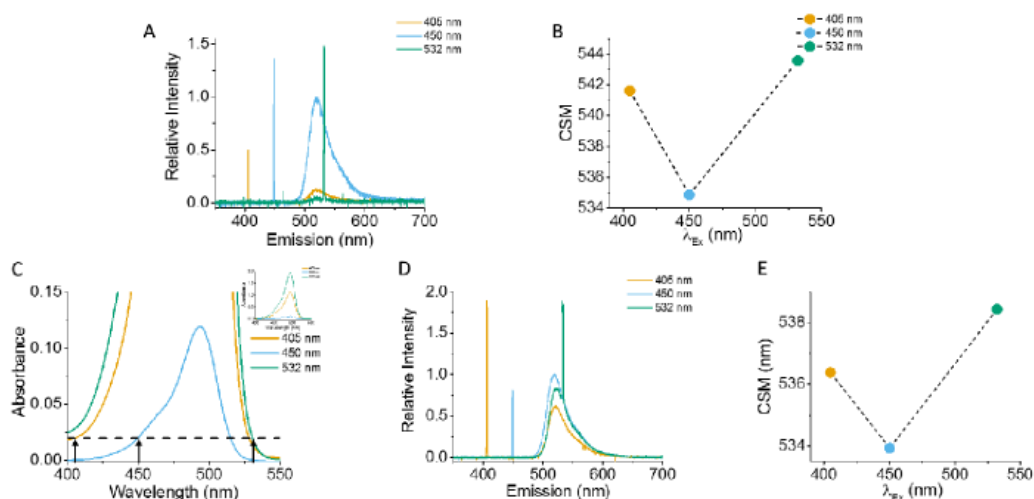

Figure S3. A, Raw emission spectra obtained for λ_{Ex} 405, 450, and 532 nm by 4.9 mW lasers. **B,** Extracted CSM from emission spectra in **A**. CSM values were calculated from emission data fitted with skewed Gaussians following subtraction of laser lines. Following observation of the blue-shift in the laser study, an additional experiment was carried out to determine if the blue-shift was due to the laser intensity. Three solutions of Alexa 488 in water were made in order to match the absorptions at the specified laser wavelengths, as shown by **C**, with arrows indicating matching absorbance at 405, 450, and 532 nm. Subsequent laser emission studies of Alexa 488 from **C** are shown in Panel **D**. **E,** Extracted CSM from emission spectra in **D**. CSM values were calculated from emission spectra from 450 to 650 nm following removal of the 532 nm laser line (530 to 535 nm) of all spectra. The blue-shift was still observed, demonstrating it is not artefactual and the excitation of the fluorophore is unaffected across the emission range studied.
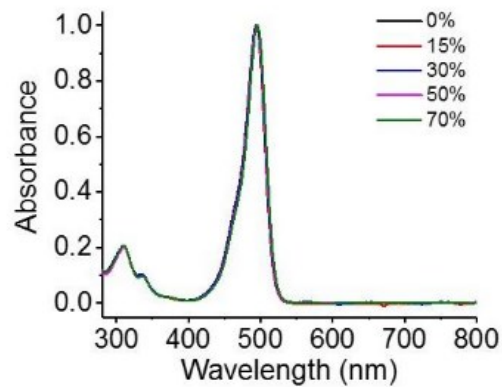
Figure S4. Normalized absorption spectra (normalized for concentration differences only) for Alexa-488 in different percentages of methanol (see key).
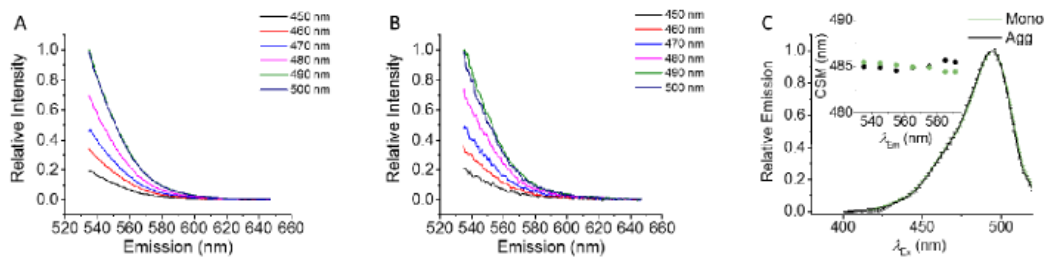
Figure S5. A, Sample EEM spectra for monomeric Aβ$_{15-21}$-fluor. **B,** Sample EEM spectra for aggregated Aβ$_{15-21}$-fluor (aggregation assessed by DLS as in main manuscript). **C,** Comparison of excitation spectra for both monomeric (green line) and aggregated (black line) protein. The excitation spectra shown are the average normalized values across the range of emission wavelengths and the error bars on each data point represent the standard deviation of the normalized spectra. That is, the very small error bars illustrate that the excitation spectrum at each emission wavelength essentially overlay and that the excitation spectra for both the monomeric and aggregated proteins overlay. *Inset* is the CSM of the excitation spectra at a range of different emission wavelengths, where CSM is calculated in the same way as described in the main text. The CSM values are essentially invariant at each emission wavelength and this is quantifiable evidence that the excitation spectra are identical. Variation in excitation spectrum is therefore not the cause of the observed fluorescence edge-shift.
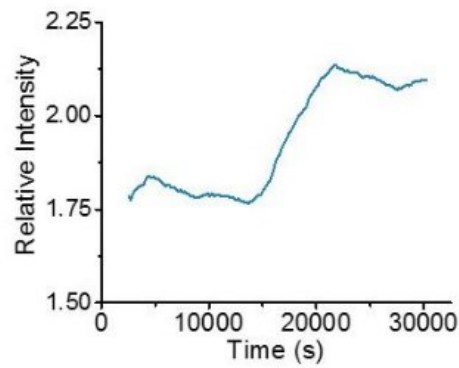
Figure S6. ThT assay of 100 μM Aβ_{15-21}-fluor fluorescein labelled Aβ_{15-21}. The increase in emission is indicative of the formation of fibrillar aggregates. We note that the absolute emission change is relatively small since we anticipate there is a very large amount of resonance energy transfer between the fluorescein and the ThT. This will not affect the aggregation kinetics but will lead to an apparent quenching of the ThT emission. *Conditions*, 90 μM ThT in 50 mM phosphate buffer pH 7, λ_{Em} 482 nm at λ_{Ex} 450 nm.
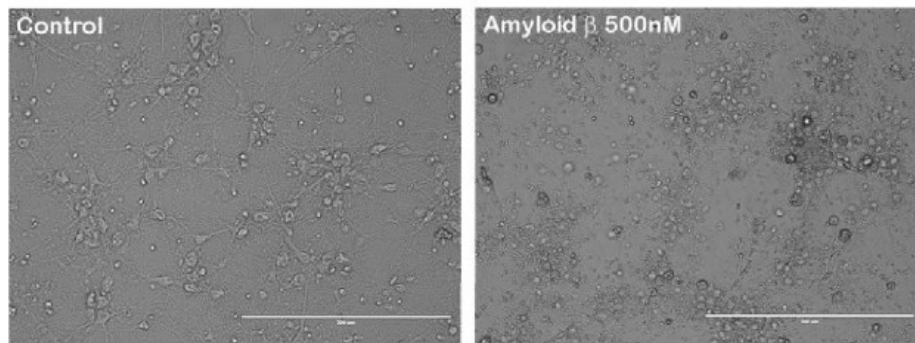
Figure S7. Primary mouse cortical neurons treated for 24 hours with Aβ_{15-21}-fluor (500 nM), washed with PBS, then fixed in paraformaldehyde (4 %). Right images show neurotoxicity compared to control.
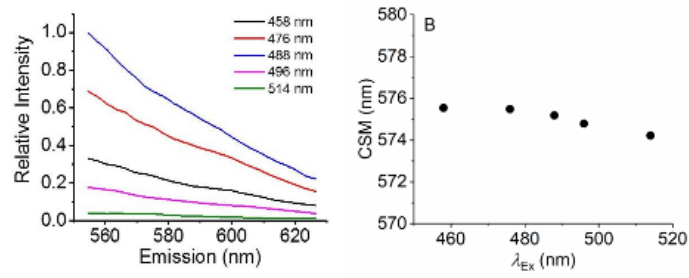
Figure S8. (A) Raw EEM data for fluorescein imaged on the same microscopy platform as the whole cell images in Figure 2. **(B)** The corresponding CSM *versus* λ_{Ex} plot.
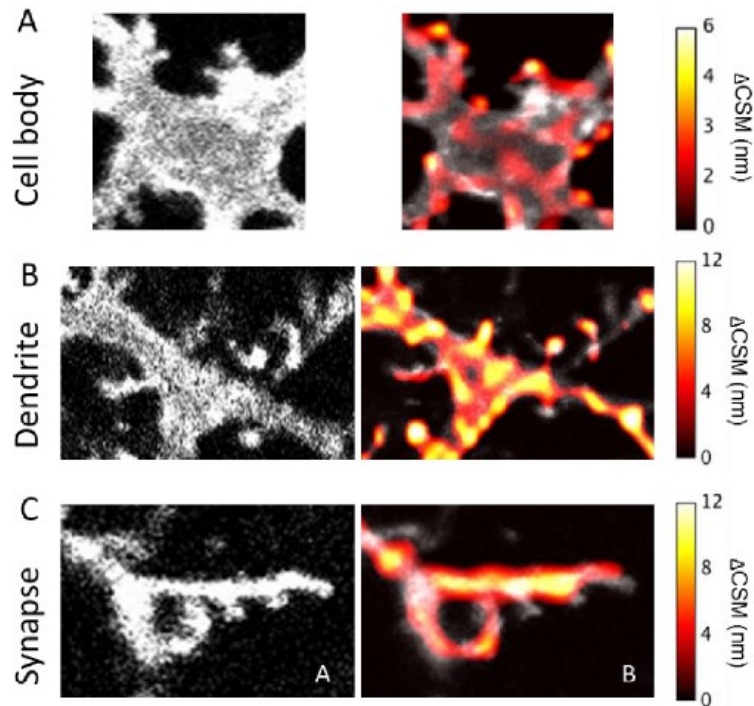
Figure S9. Enlarged image of **A,** the cell body in Figure 2A, **B,** the dendrite in Figure 2B and **C,** the putative synapse in Figure 2B. The left-hand panel in each case shows $A\beta_{15-21}$-fluor emission and the right hand panel shows the extracted edge-shift values.
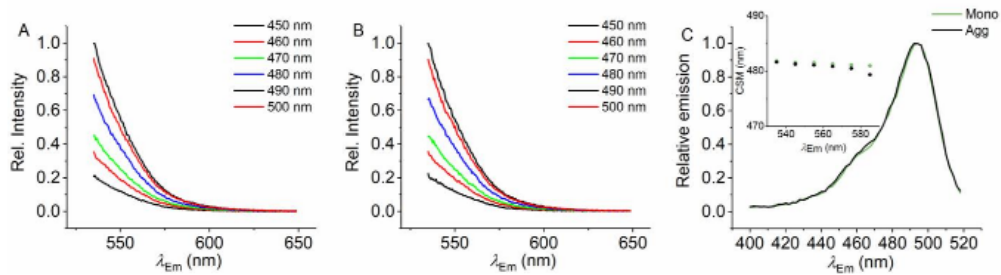
Figure S10. A, Sample EEM spectra for monomeric Aβ$_{1-40}$-fluor (assessed by DLS). **B,** Sample EEM spectra for aggregated Aβ$_{1-40}$-fluor (assessed by DLS). **C,** Comparison of excitation spectra for both monomeric (green line) and aggregated (black line) protein. The excitation spectra shown are the average normalized values across the range of emission wavelengths. *Inset* is the CSM of the excitation spectra at a range of different emission wavelengths, where CSM is calculated in the same way as described in the main text.
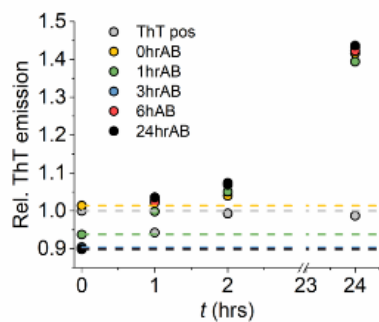
Figure S11. Change in ThT emission as a function of time for flourAβ$_{1-40}$ aged for different times, prior to monitoring ThT emission. We note the change in emission is relative to the background ThT emission and so represents an essentially negligible change in all cases.
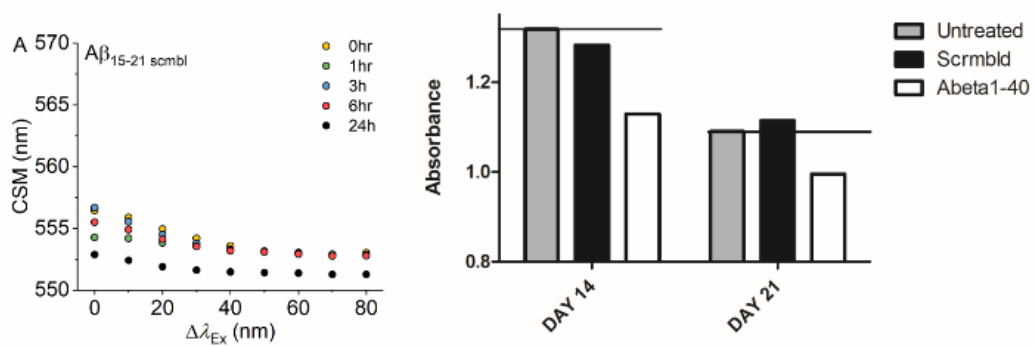
Figure S12. A) Edge-shift measurements for the scrambled flour-Aβ$_{15-21}$ aged for different time periods. Essentially no meaningful change in ΔCSM is observed. **B)** MTT absorbance (595 nm) for cells in the presence of 500nm of each peptide (incubated overnight).
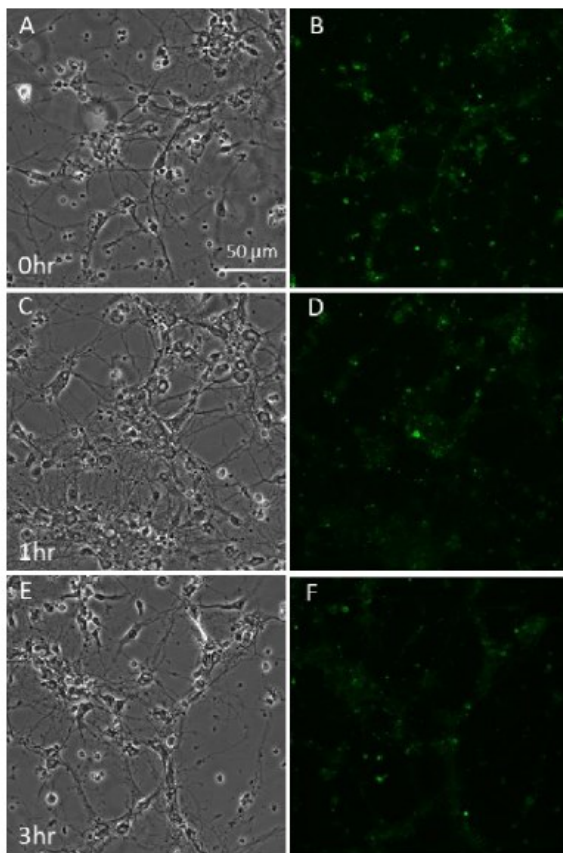

Figure S13. Mouse cortical neurons treated with aged 500 nM fluor-Aβ$_{1-40}$ at 0 hr (A), 1 hr (C) and 3 hrs (E). The panels at right of each condition show a corresponding fluorescence emission image ($\lambda_{Ex458nm}$; panels B, D and F). Image settings are the same for both Figures S13 and Figures 6.
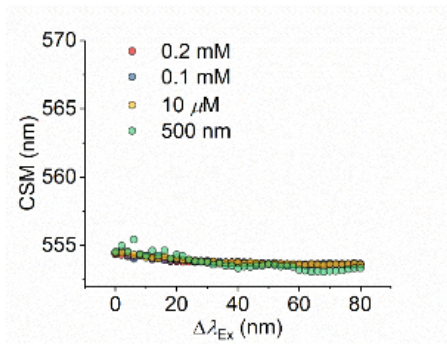
Figure S14. Edge-shift for a range of Aβ1-40 concentrations. Scale bars are the same as Figure 5 for comparison.
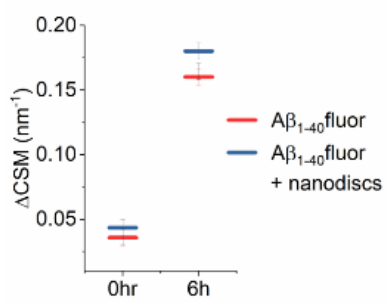

Figure S15. Edge-shift for Aβ$_{1-40}$ in the presence and absence of nanodiscs and aged for 6 hours at 25 °C.